Sympathetic cooling and self-oscillations in a hybrid atom-membrane system

Inauguraldissertation

zur
Erlangung der Würde eines Doktors der Philosophie
vorgelegt der
Philosophisch-Naturwissenschaftlichen Fakultät
der Universität Basel

von

Aline Faber
aus Deutschland

Basel, 2016

Genehmigt von der Philosophisch-Naturwissenschaftlichen Fakultät
auf Antrag von
Prof. Dr. Philipp Treutlein
Prof. Dr. Claus Zimmermann

Basel, den 21. Juni 2016

Prof. Dr. Jörg Schibler
Dekan

Abstract

Hybrid systems combining mechanical oscillators and ultracold atoms provide novel opportunities for cooling, detection and quantum control of mechanical motion with applications in precision sensing, quantum-level signal transduction and for fundamental tests of quantum mechanics.

In this thesis I present experiments performed with a hybrid atom-membrane system, in which the vibrations of a Si_3N_4 membrane in an optical cavity are coupled to the motion of laser-cooled atoms in an optical lattice. The interactions are mediated by the lattice light over a macroscopic distance and enhanced by the cavity.

Via the coupling to the cold atoms, the fundamental vibrational mode of the membrane at $2\pi \times 276\,\text{kHz}$ is cooled sympathetically from room temperature to $0.4(2)\,\text{K}$, even though the mass of the mechanical oscillator exceeds that of the atomic ensemble by a factor of 4×10^{10}. In other systems, sympathetic cooling of molecules with cold atoms or ions has been limited to mass ratios of up to 90. Previous theoretical work has shown that our coupling mechanism is able to cool the membrane vibration into the ground state and to perform coherent state transfers between atomic and membrane motion.

Under certain experimental conditions, the atom-membrane system shows self-oscillations, which arise from an effective delay in the backaction of the atoms onto the light. This retardation drives the system into limit-cycle oscillations if the coupling is large. I study the dependence of this instability on several system parameters and find that a larger atom number and a smaller atom-light detuning make the system less stable. Further, the stability of the coupled system in presence of a delay is investigated theoretically and a modified expression for the sympathetic cooling rate is derived. This model allows to fit the measured atom number dependence with a delay of $\tau = 88(1)\,\text{ns}$. Moreover, direct measurements of the atomic backaction onto the lattice light are presented. These show phase lags exceeding $180°$ in parameter regimes where the instability is observed, proving that the retardation arises within the atomic ensemble. Finally, I present the results of numerical simulations, which show that collective atomic effects within the atomic ensemble in an asymmetric lattice are able to induce the observed phase lag in the atomic backaction.

Contents

Contents

Contents

Introduction

The quantum harmonic oscillator is a well-known quantum mechanical problem, which is part of every physics student's curriculum [1]. Since the discovery of laser cooling techniques [2, 3] quantum mechanical harmonic oscillators have been realized routinely with atoms and ions and are now used for a great variety of quantum mechanics experiments. For more macroscopic massive harmonic oscillators, there is not yet a standard procedure to bring the vibrations into the quantum regime. However, it is a desirable goal. As its mechanical motion can be coupled to electric, magnetic and optical fields, a mechanical oscillator in a low-entropy quantum state can be an extraordinary sensor for small forces [4, 5] or can be functionalized as a signal transducer in a quantum circuit [6, 7, 8, 9]. Further, macroscopic quantum mechanical oscillators allow tests of quantum mechanics in a radically new parameter regime [10, 11].

The relatively young research field of optomechanics develops techniques to gain coherent quantum control over mechanical motion using the radiation pressure force [12]. Various mechanical systems are being investigated including cantilevers with mirrors [13, 14], membranes in optical [15, 16, 17] or microwave [18, 19, 20, 21] cavities, torroidal resonators [22], levitated particles [23, 24, 25, 26], photonic crystal nanobeams [27], clouds of atoms [28, 29, 30, 31], piezo-electric mechanical oscillators [32] or nanobeams [33, 34]. By now, several milestones have been achieved such as ground state cooling [32, 27, 18, 17, 35], strong coupling between light and mechanics [36, 22, 37], the observation of radiation pressure noise [38] or squeezing of light [39, 40] and the mechanical motion [20, 21, 41].

One branch of the mechanics community aims at coupling mechanical oscillators to microscopic quantum systems [42, 43]. Such hybrid quantum systems are of particular interest for precision sensing and quantum-level signal transduction as advantages of different physical systems can be combined. Diverse combinations including mechanics coupled to NV-centers [44, 45, 46, 47, 48, 49], semiconductor quantum dots [50, 51], superconducting qubits [32, 52, 53] or atoms [28, 29, 54, 55, 56] are being explored. Besides optomechanical coupling, also coupling via strain or magnetic field gradients is investigated.

Ultracold atoms are an extremely well-controlled quantum system. The preparation of the motional quantum ground state is state of the art in atom and ion experiments [57, 2, 3]. The internal state of atoms can be coherently manipulated and detected on a single quantum level [58]. By now, even interactions between
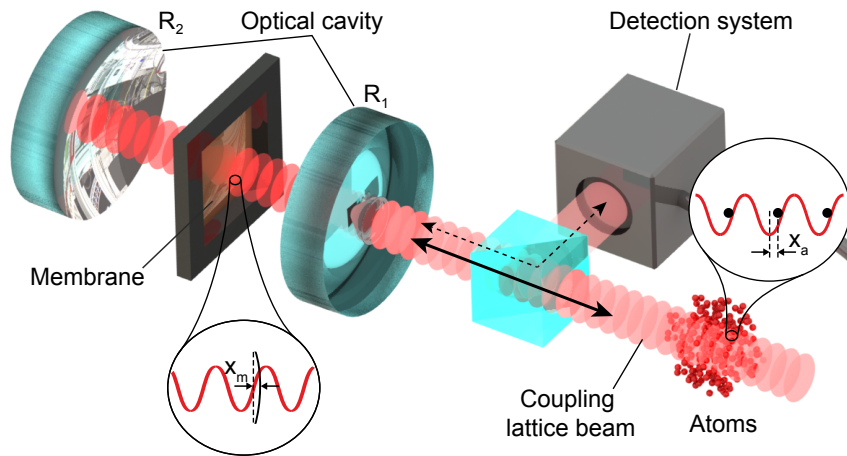
Figure 1: Illustration of the hybrid atom-membrane system. The membrane oscillator is placed inside a single-sided Fabry-Pérot-cavity. A laser beam from the right drives the system and mediates the interactions. It is reflected off the cavity and creates a lattice potential for the atoms. Figure courtesy of Tobias Kampschulte.

the atoms can be engineered [59]. Cold atoms have been used extensively to test the prediction of quantum mechanics e.g. via the well-known realization of Bose-Einstein-condensation [60, 61]. They are used to define our time standard in atomic clocks [62], as sensitive detectors of fields and forces [63, 64], quantum simulators [65, 59] or elements of quantum information circuits [66, 67]. The abilities to control cold atoms on the quantum level makes them a promising partner in a hybrid system providing novel opportunities for the coherent manipulation of mechanical motion. Proposals exist for sympathetic cooling [68, 69, 70, 71], creating atom-membrane entanglement [72, 71] and controlling the oscillator on the single quantum level [73].

First experiments have shown coupling between atoms and mechanics but the effects were too weak to manipulate the mechanical vibration significantly. In [54] and [56] a mechanical oscillator with a magnetic tip was coupled to the spins of an atomic ensemble. In [28] coupling between a cantilever and a BEC was realized via surface forces. All three experiments show a modification of atomic properties by the oscillator but not the backaction of the atoms onto the oscillator. In [29] our group coupled a membrane oscillator to the motion of an atomic ensemble via optical forces and showed, for the first time, a modification of the membrane damping rate in presence of the atomic ensemble. Still, the atomic damping was too weak to observe a reduction of the membrane temperature.

This thesis describes experiments with an improved atom-membrane hybrid system, in which the vibrations of a Si_3N_4 membrane in an optical cavity are coupled to the motion of laser-cooled atoms. The interaction is mediated by laser light over a macroscopic distance. Figure 1 illustrates how a laser beam from the right drives the system. The back mirror of the cavity is almost perfectly reflective so that most

of the light leaves the cavity through the input port and interferes with the ingoing light. If the light is detuned from the atomic transition, the standing wave forms a lattice potential for the atoms, in which they oscillate with axial frequency Ω_a. A displacement of the membrane inside the cavity detunes the coupling light from the cavity and induces a phase shift of the reflected light. The vibrations of the membrane in the cavity at frequency Ω_m thus displace the lattice potential wells periodically. If $\Omega_\mathrm{a} \approx \Omega_\mathrm{m}$, this leads to a resonant coupling between membrane and atom motion. Vice versa, if the atoms move back and forth in the potential wells, they modulate the power in the lattice beams and by this the radiation pressure force on the membrane. The presence of the cavity enhances the coupling in both directions compared to the experiment presented in [29]. If we apply laser-cooling to the atoms, we can extract energy from the coupled system.

With this setup we could, for the first time, exploit a hybrid atom-membrane system for a useful task. We sympathetically cooled the fundamental membrane vibration from room temperature to $650(230)\,\mathrm{mK}$ [55] and later slightly further down to $0.4(2)\,\mathrm{mK}$ via the coupling to the atoms. The cooling is limited by technical noise on the laser and the cavity piezos.

Under certain experimental conditions, the atom-membrane system shows self-oscillations, which arise from an effective delay in the backaction of the atoms onto the light. Most likely this effective delay is caused by collective effects within the atomic ensemble. It drives the system into limit cycle oscillations if the coupling is large, demonstrating impressively the ability of the atomic ensemble to influence the motional state of the oscillator.

Our experiments are a first big step towards a strongly coupled hybrid atom-membrane system. With further improvements on the membrane and atomic side such as cryogenic pre-cooling of the membrane, using a low-noise laser and increasing the atomic optical depth, coherent quantum control of the mechanical oscillator via an atomic ensemble will be in reach in the not too distant future.

Thesis outline

I start in chapter 1 with a theoretical description of the hybrid system. Subsequently, I present and characterize the optomechanical system, chapter 2, and the atomic system, chapter 3. In chapter 4 the results of several sympathetic cooling experiments are presented. After that, in chapter 5, I investigate the self-oscillation phenomenon. Finally, I give an outlook on ongoing and future work in chapter 6.

Contributions to publications

1. A. Jöckel, A. Faber, T. Kampschulte, M. Korppi, M. T. Rakher, and P. Treutlein. *Sympathetic cooling of a membrane oscillator in a hybrid mechanical-atomic system.* Nature Nanotechnology **10**, 55-59 (2015).

2. B. Vogell, T.Kampschulte, M.T.Rakher, A.Faber, P.Treutlein, K.Hammerer and P.Zoller. *Long distance coupling of a quantum mechanical oscillator to the internal states of an atomic ensemble.* New Journal of Physics **17**, 043044 (2015).

Prizes

1. Quantum Nano-and Micromechanics Conference, 2013, Monte Verità-Ascona, Switzerland, Award for Best Contribution

Chapter 1

Theory of atomic and membrane oscillators coupled with light

This chapter reviews the theoretical background of our atom-membrane system. The parameters which will be used later on in this thesis will be introduced and all important relations will be presented.

The chapter starts with a look at the atomic side of our coupled system. I investigate the forces an electromagnetic field exerts on a neutral atom and discuss the two most relevant applications of these forces for this thesis, namely optical cooling [2, 74] and trapping [75]. Thereafter, I will introduce the transfer matrix formalism method [76, 77, 78], which allows to describe both, the forces on the atom as well as the backaction of the atom onto the light field in a unified picture. In our earlier works [29, 55, 43] we always treated these two aspects of the atom-light interaction separately.

In the second part, the key parameters and relations for a membrane-in-the-middle optomechanical system are presented. A detailed description of optomechanical coupling in a membrane-in-the-middle (MIM) system is given for instance in [79] or [80]. Here, I will give only a short summary of the relevant quantities.

In the last section, the transfer matrix model is extended to describe the coupled atom-membrane system using the results from the first two parts. The sympathetic cooling rate will be derived from the coupled equations of motion and the quantum limits of sympathetic cooling will be discussed.

1.1 Atom-light interaction

This section treats the effects which the interaction with laser light has on a neutral atom. Within a semiclassical model I will sketch the derivation of the atomic polarizability, an important quantitiy for the remaining course of this thesis. Further, I present the two important forces for laser cooling and trapping of atoms, the radiation pressure and the dipole force, which we exploit to prepare cold atomic ensembles in an optical lattice. A rigorous derivation of these forces from the semi-
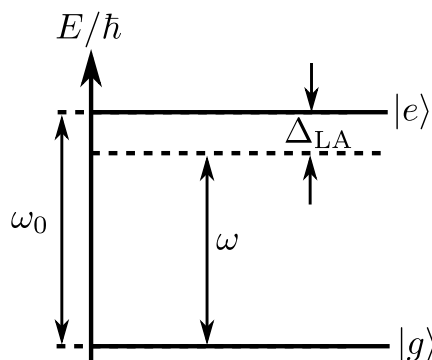
Figure 1.1: Schematic of a two-level atom. Ground state $|g\rangle$ and excited state $|e\rangle$ are separated by the transition frequency ω_0. Laser light at frequency ω is detuned from the atomic transition by $\Delta_{\mathrm{LA}} = \omega - \omega_0$.

classical theory is presented in various textbooks and review papers [2, 74, 75, 81]. I will only summarize the results that are relevant for this thesis.

1.1.1 Polarizability of a two-level atom

In the following, the atom-light interaction will be treated within a semiclassical model, in which the light is described as a classical field and the atom as a quantized two-level system. Even though the electronic structure of the real Rubidium atom is much more complicated [82], this model is very powerful. Doppler cooling of ^{87}Rb is performed on the $|F = 2, m_F = 2\rangle \leftrightarrow |F' = 3, m'_F = 3\rangle$ transition. Driven by circularly polarized light, this so called cycling transition forms an effective two-level system. For optical dipole trapping with linearly-polarized far-detuned laser light, the interaction of light with the complicated level structure can be described by the two-level results with a modified transition strength. Thus, many results of the simple two-level model are directly applicable to the real atom.

The two-level model specifically refers to an atom with ground state $|g\rangle$ and excited state $|e\rangle$ with a transition frequency of $\omega_0 = (E_e - E_g)/\hbar$ as depicted in figure 1.1 and an atomic Hamiltonian $\hat{H}_A = \hbar\omega_0 |e\rangle \langle e|$. The ingoing classical laser field $\boldsymbol{E} = \boldsymbol{E_0} \cos(\omega t)$ is detuned by $\Delta_{\mathrm{LA}} = \omega - \omega_0$ from the atomic transition. In dipole approximation the interaction can be described by the following Hamiltonian [2, 74]

$$\hat{H}_I = -\hat{\boldsymbol{d}} \cdot \boldsymbol{E} \,, \tag{1.1}$$

where $\hat{\boldsymbol{d}} = -e\hat{\boldsymbol{r}}$ is the dipole operator and $e = 1.6 \times 10^{-19}\,\mathrm{C}$ the charge of the electron. One can define the Rabi frequency of the interaction

$$\Omega_{\mathrm{R}} = \frac{\boldsymbol{d}_{eg} \cdot \boldsymbol{E_0}}{\hbar} \,, \tag{1.2}$$

where $\boldsymbol{d}_{eg} = \langle e| e\hat{\boldsymbol{r}} |g\rangle$ the dipole matrix element. In presence of spontaneous emission, the dynamics of the interaction can be described by the following master equa-

tion for the atomic density operator [83]

$$\frac{d\hat{\rho}}{dt} = \frac{1}{i\hbar}[\hat{H}_A + \hat{H}_I, \hat{\rho}] + \Gamma \langle e| \hat{\rho} |e\rangle |g\rangle \langle g| - \frac{\Gamma}{2}(|e\rangle \langle e| \hat{\rho} + \hat{\rho} |e\rangle \langle e|), \qquad (1.3)$$

where Γ is the decay rate of the atomic population in the excited state induced by the coupling of the atom to the vacuum modes of the electromagnetic field. Taking this coupling to the vacuum modes explicitly into account, one can show that Γ is connected to the dipole matrix element $\boldsymbol{d}_{eg}$ via [84]

$$\Gamma = \frac{\omega_0^3 |\boldsymbol{d}_{eg}|^2}{3\pi\epsilon_0 \hbar c^3}. \qquad (1.4)$$

Inserting the Hamiltonian from equation 1.1 into equation 1.3 leads to four coupled differential equations for the entries of the atomic density matrix. Within the rotating wave approximation, which is applicable if $(|\Delta_{\mathrm{LA}}|, \Omega_{\mathrm{R}}) \ll \omega$ and in a rotating reference frame, the so called optical Bloch equations read [2]:

$$\dot{\rho}_{ee} = \frac{i}{2}(\Omega_{\mathrm{R}}^* \rho_{eg} - \Omega_{\mathrm{R}} \rho_{ge}) - \Gamma \rho_{ee},$$

$$\dot{\rho}_{gg} = -\frac{i}{2}(\Omega_{\mathrm{R}}^* \rho_{eg} - \Omega_{\mathrm{R}} \rho_{ge}) + \Gamma \rho_{ee},$$

$$\dot{\rho}_{eg} = \frac{i}{2}\Omega_{\mathrm{R}}(\rho_{ee} - \rho_{gg}) - \left(\frac{\Gamma}{2} - i\Delta_{\mathrm{LA}}\right) \rho_{eg},$$

$$\dot{\rho}_{ge} = -\frac{i}{2}\Omega_{\mathrm{R}}^*(\rho_{ee} - \rho_{gg}) - \left(\frac{\Gamma}{2} + i\Delta_{\mathrm{LA}}\right) \rho_{ge} = \dot{\rho}_{eg}^*. \qquad (1.5)$$

Setting the left side of the equations to zero and using that the total population of the atom is conserved, $\rho_{gg} + \rho_{ee} = 1$, one can find the steady state populations and coherences

$$\rho_{ee}^{\mathrm{st}} = \frac{|\Omega_{\mathrm{R}}|^2}{\Gamma^2 + 4\Delta_{\mathrm{LA}}^2 + 2|\Omega_{\mathrm{R}}|^2},$$

$$\rho_{gg}^{\mathrm{st}} = 1 - \frac{|\Omega_{\mathrm{R}}|^2}{\Gamma^2 + 4\Delta_{\mathrm{LA}}^2 + 2|\Omega_{\mathrm{R}}|^2},$$

$$\rho_{eg}^{\mathrm{st}} = \frac{\Omega_{\mathrm{R}}(2\Delta_{\mathrm{LA}} - i\Gamma)}{\Gamma^2 + 4\Delta_{\mathrm{LA}}^2 + 2|\Omega_{\mathrm{R}}|^2},$$

$$\rho_{ge}^{\mathrm{st}} = \frac{\Omega_{\mathrm{R}}^*(2\Delta_{\mathrm{LA}} + i\Gamma)}{\Gamma^2 + 4\Delta_{\mathrm{LA}}^2 + 2|\Omega_{\mathrm{R}}|^2}. \qquad (1.6)$$

The steady state solution of the density matrix allows to calculate the average value of the induced atomic dipole moment in the steady state [74, 85]

$$\langle \hat{\boldsymbol{d}}^{\mathrm{st}} \rangle = \mathrm{Tr}(\rho^{\mathrm{st}}\hat{\boldsymbol{d}}) = 2\,\mathrm{Re}(-\rho_{eg}^{\mathrm{st}}\boldsymbol{d}_{ge})$$

$$= \mathrm{Re}\left(-2\frac{|\boldsymbol{d}_{ge}|^2}{\hbar}\frac{2\Delta_{\mathrm{LA}} - i\Gamma}{\Gamma^2 + 4\Delta_{\mathrm{LA}}^2 + 2|\Omega_{\mathrm{R}}|^2}\boldsymbol{E_0}\right)$$

$$\stackrel{!}{=} \mathrm{Re}(\alpha\boldsymbol{E_0}). \qquad (1.7)$$

In the last line of equation 1.7 the complex polarizability of the atom, α, [85, 78] has been introduced. It will be the the basis for the derivations presented in the succeeding section 1.1.6. In the limit of large detuning ($|\Delta_{\mathrm{LA}}| \gg \Gamma$) and low saturation ($|\Omega_{\mathrm{R}}| \ll |\Delta_{\mathrm{LA}}|$) and using equation 1.4, it can be written as

$$\alpha \simeq -\frac{|\boldsymbol{d}_{ge}|^2}{\hbar} \frac{1}{\Delta_{\mathrm{LA}}} \left[1 + i \frac{\Gamma/2}{(-\Delta_{\mathrm{LA}})} \right] = \frac{\Gamma/2}{(-\Delta_{\mathrm{LA}})} \frac{3}{4\pi^2} \epsilon_0 \lambda^3 \left[1 + i \frac{\Gamma/2}{(-\Delta_{\mathrm{LA}})} \right] . \qquad (1.8)$$

1.1.2 Scattering rate, scattering cross section and optical depth

According to equation 1.5, the excited state of the atom decays at a rate Γ. The steady state scattering rate is given by the product of this decay rate and the average excited state population

$$\Gamma_{\mathrm{sc}} = \Gamma \rho_{ee}^{\mathrm{st}} = \frac{\Gamma}{2} \cdot \frac{s_0}{1 + (2\Delta_{\mathrm{LA}}/\Gamma)^2 + s_0} . \qquad (1.9)$$

Here $s_0 = 2|\Omega_{\mathrm{R}}|^2/\Gamma^2$ is the so called saturation parameter. Using equation 1.4 and $I = \epsilon_0 c |\boldsymbol{E_0}|^2/2$ it can be written as

$$s_0 = \frac{I}{I_{\mathrm{sat}}} \quad \text{with} \quad I_{\mathrm{sat}} = \frac{\hbar \omega_0^3 \Gamma}{12\pi c^2} . \qquad (1.10)$$

If a laser beam with intensity I_0 travels along the x-direction through a thin sheet of thickness dx of atoms with number density n, a fraction of the photons get scattered out of the beam and the intensity reduces by

$$dI = -\hbar \omega \Gamma_{\mathrm{sc}} n dx \approx -\frac{\sigma_0}{1 + (2\Delta_{\mathrm{LA}}/\Gamma)^2 + s_0} n I dx . \qquad (1.11)$$

The approximation holds for $\omega \approx \omega_0$, which is fulfilled within the rotating wave approximation. The parameter $\sigma_0 = 3\lambda^2/2\pi$ is called the resonant scattering cross-section of the transition. We exploit this reduction of the intensity to image atomic clouds as described in more detail in section 3.5. In the low saturation regime ($s_0 \ll 1$) the intensity dependence of the scattering cross section can be neglected. The solution of the differential equation 1.11 is then a simple exponential function known as Lambert-Beer's law and the intensity behind the atomic medium I_1 becomes

$$I_1 = I_0 e^{-OD} , \qquad (1.12)$$

with the optical depth

$$OD = \frac{OD_{\mathrm{res}}}{1 + (2\Delta_{\mathrm{LA}}/\Gamma)^2} \quad \text{and} \quad OD_{\mathrm{res}} = \sigma_0 \int_d n \mathrm{d}x . \qquad (1.13)$$

Here, d is the extension of the atomic ensemble. We will see in section 1.3 that the optical depth is a crucial parameter on the atomic side for a strong atom-membrane coupling.

1.1.3 Laser cooling

If an atom absorbs a laser photon and emits it into a direction different to the one of the incited photon, the momentum of the atom is altered. Averaged over many absorption and reemission cycles this effect can be exploited to manipulate the velocity of the atom along the laser axis. If the laser is red-detuned with respect to the atomic transition ($\Delta_{\mathrm{LA}} < 0$), preferentially atoms which move towards the laser beam absorb the light due to the Doppler shift [86]. As the momentum kick upon absorbtion is always directed opposite to the motion of the atom, and the momentum kick upon emission is not directed, scattering of many laser photons leads to a reduction of the atomic velocity, the so called Doppler cooling. Via Ehrenfest's theorem $F = \langle \hat{F} \rangle = \mathrm{d}\langle \hat{p} \rangle / \mathrm{d}t$, the steady state mean value of the force on the atom F can be calculated from the Hamiltonian and the steady state solutions of the density operator presented above. For a beam configuration of two counter propagating laser beams in the low saturation regime $s_0 \ll 1$, often referred to as one dimensional optical molasses, one finds for the Doppler cooling force [2, 74]

$$F = -\beta v\,, \quad \text{with} \quad \beta = -\frac{8\hbar k^2 \Delta_{\mathrm{LA}} s_0}{\Gamma(1 + (2\Delta_{\mathrm{LA}}/\Gamma)^2 + s_0)^2}\,. \tag{1.14}$$

The momentum diffusion generated by the random photon emission processes limits the minimal temperature achievable with this cooling process to the Doppler temperature $T_{\mathrm{D}} = \hbar\Gamma/2k_B = 146\,\mu\mathrm{K}$ (for $^{87}\mathrm{Rb}$ [82]). However, the minimal temperatures observed in laser cooling labs are typically lower than the Doppler temperatures. These sub-Doppler temperatures cannot be explained within the two-level model. The multilevel structure of the real atom has to be taken into account. One finds that a slowly moving multilevel atom in a light field with spatially varying polarization experiences additional damping forces. These forces are based on optical pumping between the atomic levels [2, 81]. For a one-dimensional configuration of two counterpropagating beams in the low saturation regime $s_0 \ll 1$ with σ^+ and σ^- polarization acting on the $|J_g = 1\rangle \leftrightarrow |J_e = 2\rangle$ transition (J is the quantum number for the total angular momentum of the atom, see [87] chapter 6) of a slowly moving atom ($kv \cdot \tau_P \ll 1$, τ_P is the optical pumping time) the force on the atom can be written as [81]

$$F = -\alpha v\,, \quad \text{with} \quad \alpha = -\frac{120}{17}\frac{\Delta_{\mathrm{LA}}\Gamma}{5\Gamma^2 + 4\Delta_{\mathrm{LA}}^2}\hbar k^2\,. \tag{1.15}$$

In presence of sub-Doppler cooling forces the temperature limit is given by the atomic recoil temperature $T = \hbar^2 k^2/k_{\mathrm{B}}m = 360\,\mathrm{nK}$ (for $^{87}\mathrm{Rb}$ [82]). A realistic optical molasses generated by three pairs of counter propagating σ^+ and σ^- polarized laser beams as the one in our lab always provides both Doppler and sub-Doppler cooling.

The optical forces presented above allow to damp the motion of the atoms but do not provide spatial confinement. In a magneto-optical trap (MOT) the Doppler cooling force is made position-dependent via the Zeemann effect. A magnetic field with a linear gradient creates a position dependent Zeeman shift. This shift makes

it more likely for an atom to scatter cooling light if it is further away from the center of the trap [2]. The Doppler cooling force is then position- and velocity-dependent. For the one-dimensional, circularly polarized beam configuration described above and a magnetic field with a linear gradient along the axis of the beams $B(x) = Ax$ acting on the $|J_g = 0\rangle \leftrightarrow |J_e = 1\rangle$ transition, one finds the following expression for the combined cooling and trapping force

$$F = -\beta v - Kz\,, \quad \text{with } \beta \text{ as above} \quad \text{and} \quad K = \frac{\mu' A}{\hbar k}\beta\,. \tag{1.16}$$

Here $\mu' = (g_e m_e - g_g m_g)\mu_B$ is the difference between ground and excited state magnetic moment, m_e and m_f are the projections of the total angular momentum on the quantization axis and g_g and g_e the Landé-g-factors of ground and excited state ([87] chapter 14). The typical MOT consists of a pair of Anti-Helmholtz coils, which generate linear magnetic fields gradients in all three spatial directions, and three pairs of counter propagating beams with σ^+ and σ^- polarization. Such a MOT is the main building block of all laser cooling experiments.

1.1.4 Optical dipole traps

In addition to spontaneous emission, which is the physical mechanism behind the spontaneous scattering forces, the atom can also emit a photon into the laser mode via stimulated emission. If the laser field at the position of the atom consists of several k-vectors, this process can also change the momentum of the atom and thus exert a force on the atom, the optical dipole force. As the laser cooling force, the dipole force can by obtained by calculating the mean force on a two level atom via Ehrenfest's theorem in the presence of an intensity gradient of the laser field. It is a conservative force and can therefore be written as the spatial derivative of a potential $\boldsymbol{F} = -\boldsymbol{\nabla}U_{\text{dip}}$. This dipole potential, which is the shift of the energy of the atomic state in presence of the light, can also be determined directly by diagonalizing the atomic Hamiltonian $\hat{H}_A + \hat{H}_I$. If the laser is far-detuned ($|\Delta_{\text{LA}}| \gg \Gamma$), the light shift can be calculated perturbatively using second-order time-independent perturbation theory [75]. For the dipole potential of an alkali atom, interacting with linearly polarized light of a frequency close to the D$_2$-line of ^{87}Rb ($|\omega - \omega_{0,\text{D2}}| \ll |\omega - \omega_{0,\text{D1}}|$) with a detuning which is much larger than the energy splitting of the hyperfine excited states one finds [75]

$$U_{\text{dip}} = \frac{\pi c^2 \Gamma}{\omega_0^3} \frac{I}{\Delta_{\text{LA}}} = \frac{\hbar \Gamma^2 I}{12 I_{\text{sat}} \Delta_{\text{LA}}}\,. \tag{1.17}$$

If the intensity of the light I is position-dependent, there is a force. Our coupling lattice is generated by two counterpropagating, unequally strong, linearly polarized beams. The beams propagate along the x-direction, have Gaussian radial intensity profiles and no significant divergence over length of the the atomic ensemble. The total intensity reads

$$I(r, x) = I_1 e^{-\frac{2r^2}{w_0^2}} |\sqrt{R}\, e^{i(kx+\Phi)} + e^{-ikx}|^2\,, \quad \text{with} \quad I_1 = \frac{2P_0}{\pi w_0^2}\,. \tag{1.18}$$

Here P_0 is the power in the stronger beam coming from the right, R is the lattice reflectivity, w_0 is the waist of the laser beams and Φ is an additional phase on the beam from the left. Inserting equation 1.18 into equation 1.17 gives a dipole potential of

$$U_{\mathrm{dip}}(r,x) = e^{-\frac{2r^2}{w_0^2}} \left[V_{\mathrm{d}} - V_{\mathrm{m}} \sin^2(kx + \Phi/2) \right], \qquad (1.19)$$

where

$$V_{\mathrm{m}} = 4\sqrt{R} V_0, \quad V_d = (1 + \sqrt{R})^2 V_0 \quad \text{and} \quad V_0 = \frac{\hbar \Gamma^2}{12 \Delta_{\mathrm{LA}}} \frac{I_0}{I_{\mathrm{sat}}}. \qquad (1.20)$$

For red (blue) detunings $\Delta_{\mathrm{LA}} < 0$ ($\Delta_{\mathrm{LA}} > 0$) the axial dipole force $F = -\mathrm{d}U_{\mathrm{dip}}(r,x)/\mathrm{d}x$ pulls the atom towards the maxima (minima) of the intensity distribution. For small displacements around the maxima (minima) the dipole potential can be approximated by a harmonic potential $U_{\mathrm{dip}}(r,x) \simeq V_d + \frac{1}{2}m\Omega_{\mathrm{a}}^2 x^2 \pm \frac{1}{2}m\Omega_{\mathrm{r}}^2 r^2$ with axial and radial trapping frequencies

$$\Omega_{\mathrm{a}}(r) = \sqrt{\frac{2|V_{\mathrm{m}}|k^2}{m}} e^{-\frac{r^2}{w_0^2}} \equiv \Omega_{\mathrm{a}}(0) e^{-\frac{r^2}{w_0^2}},$$

$$\Omega_{\mathrm{r}} = \sqrt{\frac{4|V_d|}{mw_0^2}} \quad \text{for} \quad \Delta_{\mathrm{LA}} < 0 \quad \text{and}$$

$$\Omega_{\mathrm{r}} = \sqrt{\frac{4(V_d - V_m)}{mw_0^2}} \quad \text{for} \quad \Delta_{\mathrm{LA}} > 0. \qquad (1.21)$$

The plus holds for red and the minus for blue detuning. Note that in the blue case the radial potential is anti-trapping. The axial trapping frequency at the center of the trap, $\Omega_{\mathrm{a}}(0)$, depends on the incoming laser power P_0, the detuning Δ_{LA} and the reflectivity R, which vary between different measurement in our lab. It can be written as

$$\Omega_{\mathrm{a}}(0) = \epsilon \sqrt[4]{R} \sqrt{\frac{P_0}{|\Delta_{\mathrm{LA}}|}} \quad \text{with} \quad \epsilon = \sqrt{\frac{4}{3} \frac{\hbar \Gamma^2 k^2}{m\pi w_0^2 I_{\mathrm{sat}}}}. \qquad (1.22)$$

In far-detuned optical dipole traps the radiation pressure force is negligible compared to the dipole force. However, the finite scattering rate introduced in equation 1.9 presents a heating mechanism and limits the lifetime of the atoms in the trap. For a far-detuned dipole trap of linear polarized light close to the ^{87}Rb D$_2$ line as described above, one finds a scattering rate of

$$\Gamma_{\mathrm{sc}}(r,z) = \frac{\pi c^2}{\hbar \omega_0^3} \left(\frac{\Gamma}{\Delta_{\mathrm{LA}}} \right)^2 I(r,z). \qquad (1.23)$$

Note that this value is a factor 2/3 lower than the two-level results of equation 1.9 due to a lower transition matrix element [75, 2].

In every scattering event (absorption or emission) the atom can gain one recoil energy $E_{\mathrm{rec}} = \hbar^2 k^2 / 2m$. In [75] they find that the average energy increase per

scattering event in a three-dimensional trap is $2E_{\text{rec}}$. For a simple estimate of the trap lifetime one can assume that the atom at the bottom of the trap needs to scatter $U_{\text{dip}}(0,0)/2E_{\text{rec}}$ photons to gain enough energy to leave the trap. If it scatteres photons at a rate $\Gamma_{\text{sc}}(0,0)$ and the energy increase is distributed equally over the three different spatial axes, it will leave the trap after the time [75]

$$t_{\text{LT}} \approx 3\frac{1}{\Gamma_{\text{sc}}(0,0)}\frac{U_{\text{dip}}(0,0)}{2E_{\text{rec}}} \,. \tag{1.24}$$

For this lifetime estimate only heating due to scattering events is considered. Additional heating due to fluctuations of the dipole potential from technical and shot noise on the laser intensity is not taken into account.

1.1.5 Temperature, density distribution and ballistic expansion

The phase-space distribution $f(\boldsymbol{r},\boldsymbol{p})$ describes the probability density for an atom to be at position $\boldsymbol{r}$ and to move with a momentum $\boldsymbol{p}$. If the cloud is in thermal state with a temperature T, the phase space density is determined by the Boltzmann factor [88]

$$f(\boldsymbol{r},\boldsymbol{p}) = Ce^{-\frac{E(\boldsymbol{r},\boldsymbol{p})}{k_{\text{B}}T}} \,, \quad \text{with} \quad C = \left(\int\int e^{-\frac{E(\boldsymbol{r},\boldsymbol{p})}{k_{\text{B}}T}}\,\mathrm{d}^3p\mathrm{d}^3r\right)^{-1} . \tag{1.25}$$

Here $E(\boldsymbol{r},\boldsymbol{p}) = \boldsymbol{p}^2/2m + V(\boldsymbol{r})$ is the total energy of the atom. Integrating the probability distribution over the entire space yields a Gaussian velocity distribution $f(\boldsymbol{v}) = C'exp(-m|\boldsymbol{v}|^2/2k_{\text{B}}T)$ with width $\Delta v = \sqrt{k_{\text{B}}T/m}$. Integrating over the momentum space gives the number density of the atomic ensemble. In presence of a three dimensional harmonic potential $V(x,y,z) = \frac{1}{2}m(\Omega_{\text{x}}^2x^2 + \Omega_{\text{y}}^2y^2 + \Omega_{\text{z}}^2z^2)$ the atomic number density is Gaussian as well

$$n(x,y,z) = n_0 e^{-\frac{1}{2}\left(\frac{x^2}{\sigma_{\text{x},0}^2}+\frac{y^2}{\sigma_{\text{y},0}^2}+\frac{z^2}{\sigma_{\text{z},0}^2}\right)} . \tag{1.26}$$

where

$$n_0 = N\Omega_{\text{x}}\Omega_{\text{y}}\Omega_{\text{z}}\left(\frac{m}{2\pi k_{\text{B}}T}\right)^{3/2} \quad \text{and} \quad \sigma_{\text{i},0} = \sqrt{\frac{k_{\text{B}}T}{m\Omega_{\text{i}}^2}} \,. \tag{1.27}$$

After a sudden release of the atoms from the trap, the cloud will fall down and expand isotropically. If the expansion is ballistic, meaning that interactions between the atoms are negligible, the density distribution at a time t after the release can be found by a convolution of the initial density distribution 1.27 with the velocity distribution [89, 90]. If both distributions are Gaussian, one finds a new Gaussian distribution with width

$$\sigma_{\text{i}}(t) = \sqrt{\sigma_{\text{i},0}^2 + \frac{k_{\text{B}}T}{m}t^2} \,. \tag{1.28}$$

Hence, by measuring the width of the atomic density distributions at different times after a sudden turn-off of the trapping potential, the so called times of flight (TOF), one can learn about the temperature of the atomic ensemble.

1.1.6 Atoms as optical element - Transfer matrix formalism

In the previous part of this section we got introduced to the interaction of an atom with an electromagnetic field. I derived the atomic complex linear polarisability α given in equation 1.8, which plays an important role in the following description of atoms as linear scatterers.

One-dimensional problems of linear scatterers interacting with light can be described with the so called transfer matrix approach [76, 77, 78]. Using this description will allow us to treat the coupled atom-membrane system in a straightforward way.

In this section I will introduce the transfer matrix formalism and apply it to re-derive the light forces on an atomic scatterer and the backaction of the scatterer onto the light field for the specific beam configuration of our coupling lattice (one far-detuned beam impinging onto the atoms from each side). In section 1.3 I will refer to these results when I describe the coupling between atoms and membrane.

Transfer matrix Formalism

Throughout this chapter I will treat the atom as a two-level system. In the end I will comment on how the result has to be modified for a real ^{87}Rb atom. The lattice light is detuned from the atomic transition and therefore generates a potential for the atoms. If it is blue-detuned ($\Delta_{\mathrm{LA}} = \omega - \omega_0 > 0$), the atoms will be attracted to the intensity minima. If it is red-detuned ($\Delta_{\mathrm{LA}} < 0$), they will accumulate at the intensity maxima. In both cases, the atoms will form a stack of pancake-shaped clouds. In general the light-mediated interactions between the different atomic pancakes have to be taken into account [78]. Such a general treatment will be done in section 5.7. If the detuning is large compared to the atomic linewidth Γ, the pancake-pancake interactions are strongly suppressed [78]. As this is the case in most of our sympathetic cooling experiments, I neglect the interactions for the moment and assume that all the atoms sit in one pancake. This pancake will be modeled as an infinitisimally thin plane of linearly polarizable material, see figure 1.2. The spatial part of the 1D wave equation for a monochromatic plane wave $E(x,t) = \mathrm{Re}[E(x)e^{-i\omega t}]$ incident normally on a polarizable plane at $x = x_{\mathrm{a}}$ reads [76, 77, 78]

$$\begin{aligned}
\left(\frac{\partial^2}{\partial x^2} + k^2\right) E(x) &= -k^2\eta\frac{\alpha}{\epsilon_0}\delta(x - x_{\mathrm{a}})E(x) \\
&= -2k\zeta\delta(x - x_{\mathrm{a}})E(x)\,,
\end{aligned} \tag{1.29}$$

where $k = \omega/c$ is the wave vector, $\delta(x - x_{\mathrm{a}})$ is the Dirac-delta-function and $\eta = N/\sigma_{\mathrm{L}}$ is the area density of atoms in the plane with σ_{L} being the transverse mode area of the beam and N the number of atoms in the pancake. In the second line the dimensionless scattering parameter $\zeta = k\eta\frac{\alpha}{2\epsilon_0}$ got introduced. In the large detuning
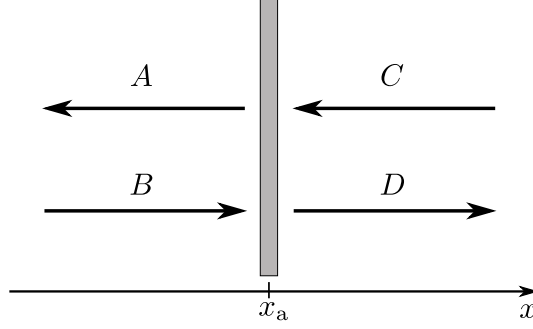
Figure 1.2: Sketch of the atomic ensemble at position x_a, which is modeled as thin sheet of polarizable material interacting with plane waves incident from both sides.

$(\Delta_\mathrm{LA} \gg \Gamma)$ and low saturation regime $(s_0 \ll 1)$ one finds with equation 1.8

$$\zeta = -\frac{N}{2} \frac{\sigma_0}{\sigma_\mathrm{L}} \frac{\Gamma/2}{\Delta_\mathrm{LA} + i\Gamma/2} \,. \tag{1.30}$$

Here $\sigma_0 = 3\lambda^2/2\pi$ is the resonant scattering cross-section and Γ the full-width-half-maximum atomic linewidth. The solutions of the wave equation 1.29 on the left and the right side of the thin sheet are superpositions of plane waves, see figure 1.2

$$
\begin{aligned}
E_{x<x_\mathrm{a}}(x) &= A_0 e^{-ikx} + B_0 e^{ikx} = A(x) + B(x)\,, \\
E_{x>x_\mathrm{a}}(x) &= C_0 e^{-ikx} + D_0 e^{ikx} = C(x) + D(x)\,,
\end{aligned}
\tag{1.31}
$$

with complex amplitudes $A_0, B_0, C_0, D_0 \in \mathbb{C}$.

Integrating eqn. 1.29 over x leads to the following boundary conditions

$$
\begin{aligned}
E|_{x\to x_\mathrm{a}^-} &= E|_{x\to x_\mathrm{a}^+}\,, \\
\left.\frac{\partial E}{\partial x}\right|_{x\to x_\mathrm{a}^-} - \left.\frac{\partial E}{\partial x}\right|_{x\to x_\mathrm{a}^+} &= 2k\zeta\, E|_{x=x_\mathrm{a}}\,.
\end{aligned}
\tag{1.32}
$$

Inserting the ansatz 1.31 into the boundary conditions 1.32 leads to simple algebraic relations between the mode amplitudes on each side of the sheet

$$
\begin{aligned}
A_0 &= \mathfrak{r} B_0 e^{2ikx_\mathrm{a}} + \mathfrak{t} C_0\,, \\
D_0 &= \mathfrak{t} B_0 + \mathfrak{r} C_0 e^{-2ikx_\mathrm{a}}\,,
\end{aligned}
\tag{1.33}
$$

and respectively the fields at the position of the beam splitter

$$
\begin{aligned}
A(x_\mathrm{a}) &= \mathfrak{r} B(x_\mathrm{a}) + \mathfrak{t} C(x_\mathrm{a})\,, \\
D(x_\mathrm{a}) &= \mathfrak{t} B(x_\mathrm{a}) + \mathfrak{r} C(x_\mathrm{a})\,,
\end{aligned}
\tag{1.34}
$$

with complex reflection and transmission coefficients

$$\mathfrak{r} = \frac{i\zeta}{1 - i\zeta} \quad \text{and} \quad \mathfrak{t} = \frac{1}{1 - i\zeta}\,. \tag{1.35}$$

The atomic cloud thus acts as a beam splitter at position $x = x_\mathrm{a}$ with complex reflectivity $\mathfrak{r}$ and transmission $\mathfrak{t}$. This can also be written in a matrix notation with transfer matrix M_BS or scattering matrix S_BS

$$
\begin{aligned}
\begin{bmatrix} A(x_\mathrm{a}) \\ B(x_\mathrm{a}) \end{bmatrix} &= M_\mathrm{BS} \begin{bmatrix} C(x_\mathrm{a}) \\ D(x_\mathrm{a}) \end{bmatrix} = \begin{bmatrix} 1 + i\zeta & i\zeta \\ -i\zeta & 1 - i\zeta \end{bmatrix} \begin{bmatrix} C(x_\mathrm{a}) \\ D(x_\mathrm{a}) \end{bmatrix}, \\
\begin{bmatrix} A(x_\mathrm{a}) \\ D(x_\mathrm{a}) \end{bmatrix} &= S_\mathrm{BS} \begin{bmatrix} B(x_\mathrm{a}) \\ C(x_\mathrm{a}) \end{bmatrix} = \begin{bmatrix} \mathfrak{r} & \mathfrak{t} \\ \mathfrak{t} & \mathfrak{r} \end{bmatrix} \begin{bmatrix} B(x_\mathrm{a}) \\ C(x_\mathrm{a}) \end{bmatrix}.
\end{aligned}
\tag{1.36}
$$

For more complex systems, for instance several atomic stacks, the relations between the in- and outgoing mode amplitudes can easily be derived from a multiplication of the transfer matrices of the elements of the system, making this formalism very elegant.

Force on the atoms

The force of the light on the atomic ensemble can be calculated from the Maxwell-stress tensor [91]

$$
T_{xx}(x,t) = -\frac{\epsilon_0}{2}(|E(x,t)|^2 + c^2|B(x,t)|^2).
\tag{1.37}
$$

The force is the rate of extraction of momentum from the electromagnetic field by the medium. It is given by the surface integral of the stress tensor over the surface of a volume which encloses the atomic medium [77, 78]

$$
F_\mathrm{a}(x_\mathrm{a}) = \oint_S \langle T_{xx} \rangle \mathrm{d}S = \sigma_\mathrm{L}(\langle T_{xx}(x \to x_\mathrm{a}^+) \rangle - \langle T_{xx}(x \to x_\mathrm{a}^-) \rangle).
\tag{1.38}
$$

The parentheses $\langle \rangle$ stand for the average over one optical oscillation period, which is much shorter than the timescale of the atomic motion. In the last step the infinitesimal thin volume $V = \sigma_\mathrm{L} dL$ around the atomic pancake was chosen. Plugging in the plane wave solution 1.31 and averaging over one optical period ($\langle |E(x,t)|^2 \rangle = 1/2|E(x)|^2$) gives

$$
F_\mathrm{a}(x_\mathrm{a}) = \frac{\epsilon_0 \sigma_\mathrm{L}}{2}(|A(x_\mathrm{a})|^2 + |B(x_\mathrm{a})|^2 - |C(x_\mathrm{a})|^2 - |D(x_\mathrm{a})|^2).
\tag{1.39}
$$

In the following I will consider the case of two incident plane waves, one from the right $C(x) = C_0 \exp(-ikx)$ and one from the left $B(x) = B_0 \exp(ikx + i\Phi)$ with $C_0, B_0 \in \mathbb{R}$. The beam from the left carries an additional phase Φ which might be imprinted onto the beam by an electro-optic modulator (EOM) in the beam path or the motion of the membrane ($\Phi = (4/\kappa)Gx_\mathrm{m}$, see section 1.2) if the beam is reflected off the membrane-cavity system. These two cases will appear later in the experimental parts of this thesis. For most of this theoretical section I will use the general expression Φ. The zero-point of the coordinate axis has been chosen so that the global phase of this beam is zero at $x = 0$. This ensures that the restoring force

from the lattice pulls the atoms to the zero-point of the coordinate system in the absence of the additional phase Φ, which is convenient. Further, I treat the general case of different amplitudes coming from left and right. A situation like this occurs in our coupled system: A beam impinges on the atoms from the right and is almost completely transmitted because the atomic reflectivity is small. Then it travels to the membrane-cavity system and is reflected back to the atoms. Due to optical losses the amplitude of the backreflected beam is reduced.

For a rigorous treatment of the coupled atom-membrane-system the entire system including the membrane has to be modeled within the transfer matrix formalism. This will be done in the last section of this chapter. I anticipate already here that, if the atomic reflectivity is small ($|\mathfrak{r}|^2 \ll 1$), the resulting force on the atoms as well as the backaction from the atoms onto the light will be equal to the one generated by the two individual beams described in this paragraph. This means that for small atomic reflectivities higher-order effects such as atom-atom interactions via the reflection at the membrane-cavity system can be neglected.

The intensity of the beam configuration reads

$$I(x) = I_0 + I_1 + 2\sqrt{I_0 I_1}\cos(2kx + \Phi)\,, \tag{1.40}$$

where $I_1 = \epsilon_0 c C_0^2/2$ and $I_0 = \epsilon_0 c B_0^2/2$ are the beam intensities. We see that the coordinate system has been chosen so that the intensity maximum, where the atoms accumulate in the red-detuned case, lies at $x = 0$ if all additional phases of the beam from the left are zero as mentioned above. The outgoing fields at $x = x_\mathrm{a}$ can be calculated from the ingoing fields via equation 1.34.

Inserting these relations into equation 1.39 gives the following force on the sheet of atoms

$$
\begin{aligned}
F_\mathrm{a}(x_\mathrm{a}) &= 2\sigma_\mathrm{L}\frac{I_0 - I_1}{c}\frac{\mathrm{Im}\,\zeta}{|1 - i\zeta|^2} - 4\sigma_\mathrm{L}\frac{\sqrt{I_0 I_1}}{c}\frac{\mathrm{Re}\,\zeta}{|1 - i\zeta|^2}\sin(2kx_\mathrm{a} + \Phi) \\
&\quad + 2\sigma_\mathrm{L}\frac{I_0 - I_1}{c}\frac{|\zeta|^2}{|1 - i\zeta|^2}\,.
\end{aligned}
\tag{1.41}
$$

The first term in expression 1.41 describes the "radiation pressure" force on a resting atom due to absorption of light in the atomic ensemble. It is independent of the position of the atoms and points towards the weaker beam. If the motion of the atom is taken into account, the Doppler cooling force 1.14 can be re-derived from this term.

The second position-dependent term is the "gradient" or "dipole" force, which generates the trapping potential for the atoms and the atom-membrane coupling. It is caused by absorption of light from one beam followed by stimulated emission into the other beam. Note that for red detuning $\mathrm{Re}\,\zeta > 0$, so that the dipole force attracts the particles towards the position of highest intensity, whereas for blue detuning $\mathrm{Re}\,\zeta < 0$ so that the atoms are expelled from the region of highest intensity as expected.

The third term is generated by incoherent reflection at the atomic cloud.

Parameter	Value
Atom number N	10^7
Beam waist w_0	$280\,\mu\mathrm{m}$
Beam area σ_L	$\pi w_0^2/2$
Laser-atom detuning Δ_LA	$-2\pi \times 1\,\mathrm{GHz}$
Atomic linewidth Γ	$2\pi \times 6\,\mathrm{MHz}$
Scattering parameter ζ	$0.0358 + 0.0001i$
$|\zeta|^2$	0.0013

Table 1.1: Typical parameters in our experiment. Note, that ζ here refers to the polarisability of the entire ensemble wheres in [78] ζ refers to the polarisability of one pancake. At a radius of w_0 the intensity of the beam has dropped by a factor of e^{-2} compared to the maximal value in the center of the beam.

The derivation above has been done for an atomic cloud resting at $x = x_\mathrm{a}$. In [77], Xuereb *et al.* treat the more general case of a moving atom for which Doppler shifts have to be taken into account. I find that in our parameter regime of large detuning $\Delta_\mathrm{LA} \gg \Gamma_\mathrm{a}$ and small velocities $v \ll c$ all velocity dependent terms, which they derive, are small compared to the three velocity independent terms given in equation 1.41.

If $|\zeta| \ll 1$ and $|\Delta_\mathrm{LA}|/\Gamma_\mathrm{a} \gg 1$ as in our experiment, see table 1.1, the second term in equation. 1.41 is the dominant one and $|1 - i\zeta|^2 \approx 1$. Further, the first and third term have no spatial dependence. They only cause a small constant displacement of the position in direction of the stronger beam. Therefore, I will neglect these two terms in the following. For small atomic displacements and small additional phases (caused for instance by a small displacement of the membrane) the sine in equation 1.41 can be expanded

$$\begin{aligned}
F_\mathrm{a}(x_\mathrm{a}) &\simeq -8k\sigma_L \frac{\sqrt{I_0 I_1}}{c} \operatorname{Re}\zeta \left(x_\mathrm{a} + \frac{\Phi}{2k} \right) \\
&= -8k\sigma_L \frac{\sqrt{I_0 I_1}}{c} \operatorname{Re}\zeta \left(x_\mathrm{a} + \frac{2G x_\mathrm{m}}{\kappa k} \right) .
\end{aligned} \tag{1.42}$$

Here the last line treats the case in which the additional phase comes from a motion of a membrane inside a cavity. The first line treats the more general case, in which the additional phase could also come from an EOM in the beam path or an additional propagation distance. For $\Delta_\mathrm{LA} \gg \Gamma_\mathrm{a}$ the force can be rewritten in the following way

$$F_\mathrm{a}(x_\mathrm{a}) = -Nm\Omega_\mathrm{a}^2 \left(x_\mathrm{a} + \frac{\Phi}{2k} \right), \quad \text{with} \quad \Omega_\mathrm{a} = \left(2k \frac{\sqrt{I_0 I_1}}{c} \frac{\sigma_0}{m} \frac{\Gamma}{\Delta_\mathrm{LA}} \right)^{1/2}. \tag{1.43}$$

This result is equal to the derivative of the dipole potential of a two-level atom presented in [75]. The axial trapping frequency of the dipole potential presented in section 1.1.4 equation 1.19 is a factor of 2/3 lower. There the specific case of a

real ^{87}Rb atom interacting with far-detuned, linearly polarized laser light is treated, for which the effective dipole matrix element is lower by a factor of 2/3 compared to the two-level value. In the full expression in equation 1.41 an additional factor $|1-i\zeta|^2$ appears in the dipole force term because the atomic backaction onto the light makes the trapping potential a little less stiff. This is neglected in the perturbative calculations of section 1.1.4 and [75]. Hence, the derivation presented here is more general.

To sum up, we see that the dominant term in the force from the light onto the atoms consists of two parts. One part is the restoring force, which generates a trap for the atoms. The second part arises if one of the beams carries an additional phase, which moves the position of the intensity maximum and therefore the point to which the restoring force pulls the atoms. This part can be used to couple to the motion of the atoms from the outside via phase shifts on the lattice light.

Backaction onto the light field

Of particular interest for our experiments is the backaction of the atoms onto the light field. Equation 1.34 tells us how the optical fields that leave the interaction volume look like. From this equation and the relation $I = \epsilon_0 c |E|^2 / 2$ the intensity of field A, which travels e.g. back to the membrane or the EOM, can be calculated

$$
\begin{aligned}
I_A(x_\mathrm{a}) &= \frac{1}{|1-i\zeta|^2} I_1 + \frac{|\zeta|^2}{|1-i\zeta|^2} I_0 - \frac{2\sqrt{I_0 I_1}}{|1-i\zeta|^2} \operatorname{Re}\zeta \sin(2kx_\mathrm{a} + \Phi) \\
&\quad - \frac{2\sqrt{I_0 I_1}}{|1-i\zeta|^2} \operatorname{Im}\zeta \cos(2kx_\mathrm{a} + \Phi) \\
&= |\mathfrak{t}|^2 I_1 + |\mathfrak{r}|^2 I_0 - \frac{2\sqrt{I_0 I_1}}{|1-i\zeta|^2} \operatorname{Re}\zeta \sin(2kx_\mathrm{a} + \Phi) \\
&\quad - \frac{2\sqrt{I_0 I_1}}{|1-i\zeta|^2} \operatorname{Im}\zeta \cos(2kx_\mathrm{a} + \Phi) .
\end{aligned}
\tag{1.44}
$$

This intensity consists of four terms. The transmitted part of the beam from the right, the incoherent reflection of the beam from the left, a position dependent part caused by the stimulated emission processes which are responsible for the dipole potential and a term describing the incoherent scattering out of the beam due to absorption. The first two terms are independent of the position of the atoms, x_a, and the additional phase of beam B, Φ. For the physics we are interested in, they are therefore not very interesting. If beam A impinges on a membrane-cavity system, this constant intensity leads to a shift in the membrane steady-state position and eventually causes optomechanical effects (if the light is detuned from the cavity, see section 1.2). For the motional atom-membrane coupling, this light will not be relevant. I will therefore neglect the first two terms in the following. Further, in the regime of large detuning $|\Delta_\mathrm{LA}|/\Gamma_\mathrm{a} \gg 1$ and small atomic polarizability $|\zeta| \ll 1$,

absorption effects can be neglected so that the intensity reduces to

$$I_A(x_\mathrm{a}) \simeq -2\sqrt{I_0 I_1}\,\mathrm{Re}\,\zeta\,\sin(2kx_\mathrm{a} + \Phi) \approx -4k\sqrt{I_0 I_1}\,\mathrm{Re}\,\zeta\left(x_\mathrm{a} + \frac{\Phi}{2k}\right). \qquad (1.45)$$

In the last step I assumed that the atomic amplitude x_a and the additional phase Φ are small. We see that if the atomic position or the additional phase are modulated periodically, the intensity of beam A is modulated as well. The corresponding power modulation reads

$$P_A = \sigma_\mathrm{L} I_A = -4k\sigma_\mathrm{L}\sqrt{I_0 I_1}\,\mathrm{Re}\,\zeta\left(x_\mathrm{a} + \frac{\Phi}{2k}\right) = \frac{c}{2}F_\mathrm{a}. \qquad (1.46)$$

I will repetitively use this result throughout the thesis. Note that here I use the symbol P_A for the power modulation not for the total power (all four terms in equation 1.44) as only the power modulation matters for the atom-membrane coupling. I will point out that I refer to the modulation of the power whenever the symbol will appear later on. Summing up, I note that the transfer matrix formalism gives us an elegant tool to calculate the relevant features of the atom-light interaction, namely the force on the atoms and the backaction onto the light field. It allows to describe dispersive as well as absorbtive effects in a joint manner via the complex polarisability parameter ζ.

1.2 Membrane-in-the-middle optomechanics

1.2.1 Mechanical resonators

Concept of effective mass and equation of motion

For any mechanical oscillator of interest, in our case a nanomechanical membrane, the vibrational eigenfrequencies and the corresponding vibrational modes can be calculated from the linear theory of elasticity [92]. In the context of optomechanics the focus typically lies on the vibration of one particular eigenmode with eigenfrequency Ω_m and eigenmode $\vec{u}(\vec{r}, t) = x(t)\vec{u}(\vec{r})$, which dissipates mechanical energy with a damping rate Γ_m. If only the global vibration of the mode is of interest, it is enough to describe the dynamics of $x(t)$ in a one-dimensional description. Planar vibrating structures like membranes have eigenmodes of the form $x_\mathrm{m}(x, y, t) = \Psi(x, y)x_0\cos(\Omega_\mathrm{m}t)$, where x and y are locations in the plane, $x_\mathrm{m}(x, y, t)$ is the out-of-place displacement, x_0 is the global amplitude and $\Psi(x, y)$ the transversal mode shape corresponding to the eigenfrequency Ω_m, that is normalized so that $\max(\Psi) = 1$.

The mechanical amplitude is usually probed with a laser beam with a certain planar intensity profile $I(x, y)$. Thus, to be able to compare to the experiment, the best suited global amplitude is not $x(t) = x_0\cos(\Omega_\mathrm{m}t)$ but the mean amplitude seen by the probe beam

$$x_\mathrm{m}(t) = \frac{\int_A x_\mathrm{m}(x, y, t)I(x, y)\mathrm{d}A}{\int_A I(x, y)\mathrm{d}A} \approx \Psi(x_1, y_1)x_0\cos(\Omega_\mathrm{m}t), \qquad (1.47)$$

where A is the area of the vibrating structure and the last equation holds for a small probe beam at location x_1, y_1. An effective mass M can be attributed to the global amplitude so that the vibrational energy of the 1D system description equals the actual vibrational energy of the planar oscillator.

$$U(t) = \frac{1}{2}M\Omega_m^2 x_m^2(t) \equiv \frac{1}{2}M_{Phys}\Omega_m^2 \frac{\int_A x_m(x,y,t)^2 dA}{A} \,. \tag{1.48}$$

From this equation one finds for the effective mass

$$M = M_{phys}\frac{\int_A \Psi(x,y)^2 dA}{A}\left(\frac{\int_A I(x,y)dA}{\int_A \Psi(x,y)I(x,y)dA}\right)^2 \approx \frac{M_{phys}}{4}\frac{1}{\Psi(x_1,y_1)^2}\,, \tag{1.49}$$

where the last equation again holds for a point-like probe beam.

The temporal evolution of the global displacement of the planar structure can then be described by the simple equation of motion of a damped, harmonic oscillator

$$M\ddot{x}_m(t) + M\Gamma_m\dot{x}_m(t) + M\Omega_m^2 x_m(t) = F_{ext}(t)\,, \tag{1.50}$$

where $F_{ext}(t)$ is the sum over all external forces.

Susceptibility, noise spectra, fluctuation dissipation theorem

Equation 1.50 can be solved easily in frequency space. Using the Fourier transform $x(\Omega) = \int_{-\infty}^{\infty} x(t)e^{-i\Omega t}dt$ it can be rewritten as

$$-M\Omega^2 x_m(\Omega) + i\Omega M\Gamma_m x_m(\Omega) + M\Omega_m^2 x_m(\Omega) = F_{ext}(\Omega)\,. \tag{1.51}$$

Rearranging the terms gives

$$\begin{aligned}
x_m(\Omega) &= \chi(\Omega)F_{ext}(\Omega)\,, \quad \text{with} \\
\chi(\Omega) &= [M(\Omega_m^2 - \Omega^2 + i\Omega\Gamma_m)]^{-1} \\
&\approx \left[2M\Omega_m\left(\Omega_m - \Omega + i\frac{\Gamma_m}{2}\right)\right]^{-1}\,.
\end{aligned} \tag{1.52}$$

Here the susceptibility $\chi(\Omega)$ has been introduced, which describes how the membrane reacts to a force. In the last line the Lorentzian approximation $\Omega_m^2 - \Omega^2 \approx 2\Omega_m(\Omega_m - \Omega)$ is applied, which is valid if $\Gamma_m \ll \Omega_m$. In the lab typically not $x_m(t)$ or $x_m(\Omega)$ is measured but the single-sided power spectral density (PSD) of the membrane motion $S_x(\Omega)$, which is related to the displacement $x_m(t)$ via [12, 79]

$$\int_0^\infty S_x(\Omega)\frac{d\Omega}{2\pi} = \langle x_m(t)^2\rangle\,, \tag{1.53}$$

where $\langle x_m(t)^2\rangle$ is the variance of the mechanical displacement, which is also called the mean squared membrane amplitude. The susceptibility from equation 1.52 connects the power spectral density of an external force to the power spectral density of the membrane displacement [93]

$$S_x(\Omega) = |\chi(\Omega)|^2 S_F(\Omega)\,. \tag{1.54}$$

If the oscillator is resting on a support at a finite temperature T_{bath}, it is driven by a fluctuating force F_{th}. The single-sided power spectral density of F_{th} is given by the fluctuation- dissipation theorem [94, 95]

$$S_{F,\text{th}}(\Omega) = \frac{4k_{\text{B}}T_{\text{bath}}}{\Omega}\, \text{Im}[\chi(\Omega)^{-1}] \approx 4k_{\text{B}}T_{\text{bath}}M\Gamma_{\text{m}}\,. \tag{1.55}$$

Inserting 1.55 into 1.54 gives

$$S_{\text{x}}(\Omega) = \frac{k_{\text{B}}T_{\text{bath}}\Gamma_{\text{m}}}{M\Omega_{\text{m}}^2} \frac{1}{(\Omega_{\text{m}} - \Omega)^2 + (\Gamma_{\text{m}}/2)^2}\,. \tag{1.56}$$

Using equation 1.53 and 1.56, the root mean squared membrane amplitude of a membrane driven by the thermal force can be calculated to

$$x_{\text{th}} = \sqrt{\langle x_{\text{m,th}}(t)^2\rangle} = \sqrt{\frac{k_{\text{B}}T_{\text{bath}}}{M\Omega_{\text{m}}^2}}\,. \tag{1.57}$$

Integrating the power spectral density over all frequencies gives the mean potential energy of the oscillator

$$\begin{aligned}\langle U \rangle &= \frac{M}{2}\int_0^\infty \Omega^2 S_x(\Omega)\frac{\text{d}\Omega}{2\pi} \\ &\approx \frac{M}{2}\Omega_{\text{m}}^2 \int_0^\infty S_x(\Omega)\frac{\text{d}\Omega}{2\pi} = \frac{k_{\text{B}}T_{\text{bath}}}{2}\,.\end{aligned} \tag{1.58}$$

Once more, the approximation holds for $\Gamma_{\text{m}} \ll \Omega_{\text{m}}$. Optomechanical damping (section 1.2.4, equation 1.94) and sympathetic cooling via the atoms (section 1.3.3, equation 1.127) lead to an increased damping rate Γ_{eff} in the denominator of equation 1.56. This reduces the mean potential energy of the oscillator. If quantum effects are negligible, one can then attribute the following effective temperature to the oscillator

$$T_{\text{eff}} \simeq \frac{M}{k_{\text{B}}}\Omega_{\text{m}}^2 \int_0^\infty S_{\text{x}}(\Omega)\frac{\text{d}\Omega}{2\pi} = \frac{\Gamma_{\text{m}}}{\Gamma_{\text{eff}}}T_{\text{bath}}\,. \tag{1.59}$$

A quantum mechanical harmonic oscillator in a thermal state at temperature T_{eff} occupies the state $|n\rangle$ with probability $p_n = \exp(-n\hbar\Omega_{\text{m}}/k_{\text{B}}T_{\text{eff}})/Z$ (with $Z = \sum_n \exp(-n\hbar\Omega_{\text{m}}/k_{\text{B}}T_{\text{eff}})$). The average phonon occupation number of the oscillator also referred to as thermal phonon number is given by

$$\bar{n}_{\text{th}} = \frac{1}{e^{\hbar\Omega_{\text{m}}/k_{\text{B}}T_{\text{eff}}} - 1} \approx \frac{k_{\text{B}}T_{\text{eff}}}{\hbar\Omega_{\text{m}}}\,, \tag{1.60}$$

where the last equation holds for large temperatures $k_{\text{B}}T_{\text{eff}} \gg \hbar\Omega_{\text{m}}$.

Mechanical quality factor

If the oscillator motion is excited to a large amplitude $x_m \gg x_{th}$, the thermal force F_{th} in the equation of motion 1.50 can be neglected. The general solution of equation 1.50 in the time domain is then given by

$$x_m(t) = x_0 e^{-\frac{\Gamma_m}{2}t} \cos(\Omega_m t + \phi_0) \,, \tag{1.61}$$

with x_0 and ϕ_0 set by the initial conditions. This trajectory describes an oscillating signal with decaying amplitude, which we use extensively in the lab to determine the damping rate of the oscillator. If the rate at which the amplitude or correspondingly the potential energy $U(t) = M\Omega_m^2 x_m(t)^2/2$ decays is low, the oscillator is well-isolated from undesired dissipation channels. Often not the decay rate Γ_m but the dimension-free mechanical quality factor Q is used to describe the quality of the mechanical oscillation. It is defined via the energy loss per oscillation period $T = 2\pi/\Omega_m$

$$Q = 2\pi \times \left(\frac{U}{\Delta U}\right) = \frac{2\pi}{1 - e^{-\Gamma_m T}} \approx \frac{\Omega_m}{\Gamma_m} \,. \tag{1.62}$$

Here the last approximation is valid for good oscillators $Q \gg 1$.

1.2.2 Membrane-in-the-middle of a cavity

Membrane reflection and transmission coefficient

The transmission and reflection coefficient of a dielectric slab with refractive index n and thickness d can be calculated with the transfer matrices $M_{n1,n2}$ corresponding to Fresnel's equations at an interface in between materials with n_1 and n_2 and M_P of propagation in a homogeneous medium ([96] chapter 7.1, adapted to the notation of section 1.1.6)

$$M_{n1,n2} = \frac{1}{2n_1} \begin{bmatrix} n_1 + n_2 & n_1 - n_2 \\ n_1 - n_2 & n_1 + n_2 \end{bmatrix} \quad M_P = \begin{bmatrix} e^{inkd} & 0 \\ 0 & e^{-inkd} \end{bmatrix} \,. \tag{1.63}$$

The optical properties of the entire slab are derived from the product of the corresponding transfer matrices of the air-material interface, the propagation in the material and the material-air interface $M_m = M_{1,n} M_P M_{n,1}$. From the matrix product one can read off the complex transmission $\tilde{t}_m = M_m(2,2)^{-1}$ and reflection coefficient $\tilde{r}_m = M_m(1,2)/M_m(2,2)$ of the slab [96]

$$
\begin{aligned}
\tilde{t}_m &= \frac{2n}{2n\cos(nkd) + (1 + n^2)i\sin(nkd)} \,, \\
\tilde{r}_m &= \frac{(1 - n^2)i\sin(nkd)}{2n\cos(nkd) + (1 + n^2)i\sin(nkd)} \,.
\end{aligned}
\tag{1.64}
$$
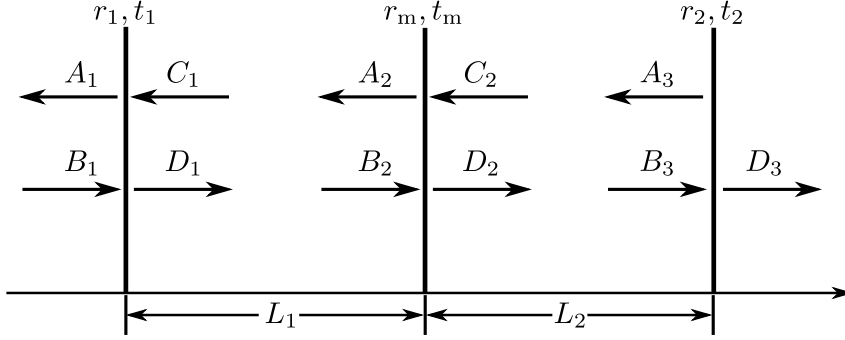
Figure 1.3: Schematic drawing of the MIM system. Laser light enters the system from the left.

Cavity fields, cavity resonances, coupling strength

Figure 1.3 shows a schematic drawing of an entire membrane-in-the-middle (MIM) system. Calculating the exact scattering matrix of the dielectric mirrors is demanding, see [79] section 3.1.2. However, in order to derive the transmission and reflection coefficient of the total MIM system up to a global phase in the absence of absorption, it is sufficient to know the absolute values of mirror reflectivities and to take into consideration that the scattering matrix must be unitary to provide energy conservation. If it is unitary, the scattering matrix of the mirrors 1 and 2 can be written in the form [97]

$$S_i = e^{i\phi} \begin{bmatrix} r_i & t_i \\ -t_i^* & r_i^* \end{bmatrix} \quad i = 1,2 \quad r_i, t_i \in \mathbb{C} \,. \tag{1.65}$$

In the following, I will drop the global phase factor $e^{i\phi}$ as it can be absorbed into the phase of the ingoing light B_1. Further I will rewrite the scattering matrix of the dielectric slab in the same notation

$$S_m = \begin{bmatrix} r_m & t_m \\ -t_m^* & r_m^* \end{bmatrix} \quad \text{with} \quad |r_m| = |\tilde{r}_m|, |t_m| = |\tilde{t}_m| \tag{1.66}$$

The product of the transfer matrices $M_r = M_m M_{L,2} M_2$ with

$$M_i = \frac{1}{t_i^*} \begin{bmatrix} t_i t_i^* + r_i r_i^* & -r_i \\ r_i^* & -1 \end{bmatrix}, M_{L,j} = \begin{bmatrix} e^{ikL_j} & 0 \\ 0 & e^{-ikL_j} \end{bmatrix} \quad i = (1,2,m), j = (1,2) \tag{1.67}$$

relates the amplitudes that enter and leave the right subcavity A_2, B_2 and D_3. From M_r amplitude reflection and transmission coefficients of the right subcavity can be read off

$$
\begin{aligned}
t_r &= \frac{D_3}{B_2} = \frac{t_m^* t_2^* e^{ikL_2}}{1 - r_2 r_m^* e^{2ikL_2}} \,, \\
r_r &= \frac{A_2}{B_2} = r_m - \frac{|t_m|^2 r_2 e^{2ikL_2}}{1 - r_2 r_m^* e^{2ikL_2}} \,.
\end{aligned}
\tag{1.68}
$$
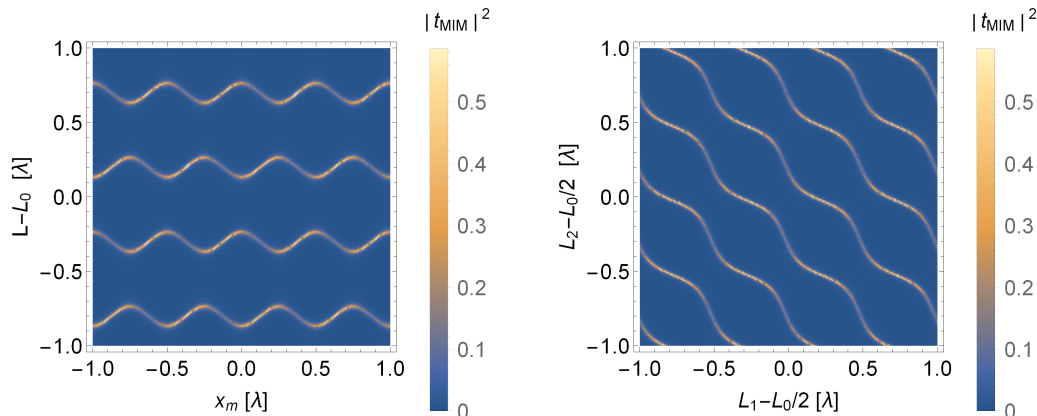
Figure 1.4: Simulation of the cavity transmission $|t_{\mathrm{MIM}}|^2$ for a) varying length of the total cavity $L = L_1 + L_2$ around the macroscopic length L_0 and membrane position $x_{\mathrm{m}} = (L_1 - L_2)/2$ and for b) varying length of the subcavities around their macroscopic length $L_0/2$. $L_0 = 1\,\mathrm{mm}$, $|r_1| = 0.90$ and $|r_2| = 0.99$.

Replacing the right subcavity by an element with reflection and transmission coefficent r_{r} and t_{r}, one finds analogously for the reflectivity and transmission of the total MIM system

$$
\begin{aligned}
t_{\mathrm{MIM}} &= \frac{D_3}{B_1} = \frac{t_1^* t_{\mathrm{r}}^* e^{ikL_1}}{1 - r_{\mathrm{r}} r_1^* e^{2ikL_1}} \,, \\
r_{\mathrm{MIM}} &= \frac{A_1}{B_1} = r_1 - \frac{|t_1|^2 r_{\mathrm{r}} e^{2ikL_1}}{1 - r_{\mathrm{r}} r_1^* e^{2ikL_1}} \,.
\end{aligned}
\tag{1.69}
$$

The amount of transmitted light through the cavity, which is proportional to $|t_{\mathrm{MIM}}|^2$, is a quantity we can easily access in the lab. It carries a lot of information about the optical properties of the system. Figure 1.4 a) illustrates the cavity transmission $|t_{\mathrm{MIM}}|^2$ for small variations in the total length of the cavity $L = L_1 + L_2$ around the macroscopic length L_0 and in the membrane position with respect to the middle of the cavity $x_{\mathrm{m}} = (L_1 - L_2)/2$ for $L_0 = 1\,\mathrm{mm}$, $|r_1| = 0.90$ and $|r_2| = 0.99$. Plot b) shows the transmission for variations of the lengths of the subcavities, which leads to a rotation of the plot by $45°$.

For a given laser frequency $\omega = kc$ and membrane position x_{m}, the length L_{c} at which the laser light is resonant with the cavity can be found by maximizing $|t_{\mathrm{MIM}}|^2$. Using equation 1.69 one finds that the $|t_{\mathrm{MIM}}|^2$ is maximal if

$$
\cos\left(\frac{L\omega}{c}\right) - |r_{\mathrm{m}}| \cos\left(\frac{2x_{\mathrm{m}}\omega}{c}\right) = 0 \,.
\tag{1.70}
$$

Solving equation 1.70 for L one finds

$$L_c = \frac{\lambda}{2} \left[q - \frac{1}{2}[1 - (-1)^q] + \frac{(-1)^q}{\pi} \arccos[|r_m| \cos(2kx_m)] \right] , \qquad (1.71)$$

where $q \in \mathbb{N}$. Similarly, by solving equation 1.70 for ω, one can find the resonant cavity frequencies ω_c in case of a fixed cavity length [98, 79, 80]. As $x_m \ll L$ the ω dependence of the second term in 1.70 can be neglected compared to the ω dependence of the first term. To simplify the calculation, ω in the second term can be replaced by a rough value of the laser frequency $\omega = kc$.

$$\omega_c = \omega_{FSR} \left[q - \frac{1}{2}[1 - (-1)^q] + \frac{(-1)^q}{\pi} \arccos[|r_m| \cos(2kx_m)] \right] . \qquad (1.72)$$

The derivative of 1.72 with respect to x_m, the frequency shift per membrane displacement, is the crucial parameter for optomechanical coupling as we will see in the next paragraph. One finds

$$
\begin{aligned}
G = -\frac{d\omega_c}{dx_m} &= (-1)^q \frac{2\omega |r_m| \sin(2kx_m)}{L\sqrt{1 - |r_m|^2 \cos^2(2kx_m)}} \\
&\approx (-1)^q G_{max} \sin(2kx_m) ,
\end{aligned}
\qquad (1.73)
$$

with

$$G_{max} = \frac{2\omega |r_m|}{L} . \qquad (1.74)$$

The approximation in equation 1.73 holds for small membrane reflectivities $|r_m|^2 \ll 1$.

Cavity linewidth and finesse

Two other important cavity parameters are the energy decay rate κ and the cavity finesse F. The linewidth sets the timescale at which light can enter or leave the cavity, and the finesse measures how often a photon circulates inside the cavity before it leaves. The two quantities are connected via the free spectral range $\omega_{FSR} = \pi c/L$

$$F = \frac{\omega_{FSR}}{\kappa} . \qquad (1.75)$$

In an asymmetric MIM system the values of κ and F depend on the position of the membrane. In principle, all information is contained in the transmission spectra $|t_{MIM}(\omega, x_m)|^2$. For $F \gg 1$ the transmitted intensity (see equation 1.69) near a cavity resonance can be approximated by a Lorentzian

$$|t_{MIM}(\omega)|^2 = \frac{\left(\frac{\kappa}{2}\right)^2}{(\omega_c - \omega)^2 + \left(\frac{\kappa}{2}\right)^2} . \qquad (1.76)$$

Using this approximation we can find an analytic expression for $\kappa = \kappa_0$ in the case where $r_m = 1$, in which all the light stays in the first subcavity. In the more realistic

case of a finite membrane reflectivity $r_m < 1$ but unity reflectivity of the back mirror $r_2 = 1$, the only loss channel is still through the incoupling mirror. However, the rate at which photons are lost from the cavity is modified as the photons spend only a part of their time in the first subcavity. Multiplication of κ_0 with the fraction of light in the first subcavity $|D_1|^2/(|D_1|^2 + |D_2|^2)$ gives the following simple expressions for the cavity linewidths at the position of maximal and minimal cavity linewidth κ, i.e. the slopes of the sinusoidal curves in figure 1.4 a)

$$
\begin{aligned}
\kappa_{\max} &= \frac{\omega_{\mathrm{FSR}}(1 - r_1)(1 + r_m)}{\pi\sqrt{r_1}}, \\
\kappa_{\min} &= \frac{\omega_{\mathrm{FSR}}(1 - r_1)(1 - r_m)}{\pi\sqrt{r_1}}.
\end{aligned}
\tag{1.77}
$$

From these results, we interpolate the following expression for the general membrane-position-dependent linewidth

$$
\kappa = \frac{\omega_{\mathrm{FSR}}(1 - r_1)\left(1 + r_m \frac{G(x_m)}{G_{\max}}\right)}{\pi\sqrt{r_1}}
\tag{1.78}
$$

and the cavity finesse

$$
F = \frac{\pi\sqrt{r_1}}{(1 - r_1)\left(1 + r_m \frac{G(x_m)}{G_{\max}}\right)}.
\tag{1.79}
$$

In the lab it is relatively easy to determine the cavity finesse at a certain membrane position via the width of the cavity transmission 1.76. If the maximal finesse of the cavity is known, one can use the finesse measurement to determine the coupling strength at this membrane position

$$
G(x_m) = \frac{F_{\max} - F - F_{\max} r_m}{F r_m} G_{\max} \quad \text{with} \quad F_{\max} = \frac{\pi\sqrt{r_1}}{(1 - r_1)(1 - r_m)}.
\tag{1.80}
$$

Phase of reflected light

One more important parameter for coupling the cavity-membrane system to the outside world is the phase shift of the reflected light with respect to the ingoing light. In [12] they use input-output theory [99, 100] to derive the complex reflection amplitude $\mathcal{R}$ of an electromagnetic wave at an optical cavity. For a single-sided cavity with intensity decay rate κ one finds [12]

$$
\mathcal{R} = \frac{-\kappa/2 - i\Delta}{\kappa/2 - i\Delta},
\tag{1.81}
$$

where $\Delta = \omega - \omega_c$ is the laser cavity detuning. From this one can read off the phase shift

$$
\Phi = \arctan\left(\frac{\kappa\Delta}{(\kappa/2)^2 - \Delta^2}\right) \approx 0
\tag{1.82}
$$

and its derivative by the detuning

$$\begin{aligned}
\frac{d\Phi}{d\Delta} &= \frac{\kappa}{(\kappa/2)^2 + \Delta^2} \\
&\approx \frac{4}{\kappa} \,.
\end{aligned} \tag{1.83}$$

The approximations hold for $|\Delta| \ll \kappa$ as in our experiment. If the membrane moves inside the cavity, it causes a small change of the cavity laser detuning by $\Delta = G x_{\mathrm{m}}$, see equation 1.73. Thus, if the laser is resonant with the cavity for $x_{\mathrm{m}} = 0$, the membrane motion induces a phase shift of $\Phi = 4 G x_{\mathrm{m}}/\kappa$ on the reflected light. This phase shift can be exploited to detect the membrane motion (section 1.2.6) or to couple to a distant atomic ensemble (section 1.3).

1.2.3 Optomechanical Hamiltonian and coupling strength

A detailed introduction into the field of cavity optomechanics is given in [12]. In the following two paragraphs, I will summarize those results which are relevant for this thesis. The optomechanical coupling between the membrane inside the cavity and the optical field can be described by the following Hamiltonian

$$\hat{H} = \hbar\omega_{\mathrm{c}}(x_{\mathrm{m}})\hat{a}^\dagger\hat{a} + \hbar\Omega_{\mathrm{m}}\hat{b}^\dagger\hat{b}\,, \tag{1.84}$$

where $\hat{b}^\dagger(\hat{a}^\dagger)$ and $\hat{b}(\hat{a})$ are the phonon (photon) creation and annihilation operators of the vibrational (optical) mode. The cavity resonance frequency ω_{c} depends on the membrane amplitude according to equation 1.72. For small membrane displacements the resonance frequency can be expanded in x_{m}

$$\omega_{\mathrm{c}}(x_{\mathrm{m}}) = \omega_{\mathrm{c}}(x_{\mathrm{m}} = 0) - G x_{\mathrm{m}} + \dots. \tag{1.85}$$

using the coupling strength G defined in equation 1.73. Inserting the expansion the Hamiltonian reads

$$\hat{H} = \hbar\omega_{\mathrm{c}}(x_{\mathrm{m}} = 0)\hat{a}^\dagger\hat{a} + \hbar\Omega_{\mathrm{m}}\hat{b}^\dagger\hat{b} + \hat{H}_{\mathrm{int}}\,, \tag{1.86}$$

with the interaction Hamiltonian

$$\hat{H}_{\mathrm{int}} = -\hbar G\hat{a}^\dagger\hat{a}\hat{x}_{\mathrm{m}} = -\hbar g_0\hat{a}^\dagger\hat{a}(\hat{b}^\dagger + \hat{b})\,. \tag{1.87}$$

In the last equation the relation $\hat{x}_{\mathrm{m}} = x_{\mathrm{m},0}(\hat{b}^\dagger + \hat{b})$ with membrane zero point amplitude $x_{\mathrm{m},0} = \sqrt{\hbar/2M\Omega_{\mathrm{m}}}$ is used to define the optomechanical single photon coupling rate $g_0 = G x_{\mathrm{m},0}$. From the interaction Hamiltonian the radiation pressure force can be derived by taking the derivative with respect to $\hat{x}_{\mathrm{m}}$

$$\hat{F}_{\mathrm{rad}} = -\frac{\mathrm{d}\hat{H}_{\mathrm{int}}}{\mathrm{d}\hat{x}_{\mathrm{m}}} = \hbar G\hat{a}^\dagger\hat{a}\,. \tag{1.88}$$

For the optomechanical effects described in this thesis it is sufficient to investigate the dynamics of the classical averaged quantities $\alpha(t) = \langle \hat{a}(t) \rangle$ and $x_{\mathrm{m}}(t) = \langle \hat{x}_{\mathrm{m}}(t) \rangle$ under the mean radiation pressure force

$$F_{\mathrm{rad}} = \hbar G |\alpha|^2 \, . \tag{1.89}$$

I refer to [12, 101, 102] for a theoretical description of the optomechanical coupling in the quantum regime.

1.2.4 Optical spring effect and optomechancial damping

From the radiation pressure force (see above) and input-output theory, one can derive the following set of nonlinear differential equations of motion for α and x_{m} [12]

$$
\begin{aligned}
\dot{\alpha} &= -\frac{\kappa}{2}\alpha + i(\Delta + G x_{\mathrm{m}})\alpha + \sqrt{\kappa}\alpha_{\mathrm{in}} \, , \\
M\ddot{x}_{\mathrm{m}} &= -M\Omega_{\mathrm{m}}^2 x_{\mathrm{m}} - M\Gamma_{\mathrm{m}}\dot{x}_{\mathrm{m}} + \hbar G |\alpha|^2 + F_{\mathrm{th}} \, ,
\end{aligned}
\tag{1.90}
$$

where α_{in} is the incoming light amplitude. In our and in many other experiments the cavity is driven by a strong laser beam. The equations of motion can then be linearized around the steady state solution in absence of the coupling by setting $\alpha = \bar{\alpha} + \delta\alpha$. Setting $\dot{\bar{\alpha}}$ and x_{m} to zero, one finds an expression for the steady state number of photons inside the cavity $\bar{n}_{\mathrm{c}} = |\bar{\alpha}|^2$

$$\bar{n}_{\mathrm{c}} = \frac{\kappa}{\frac{\kappa^2}{4} + \Delta^2} \frac{P_{\mathrm{in}}}{\hbar\omega_{\mathrm{c}}} \tag{1.91}$$

where $P_{\mathrm{in}} = \hbar\omega|\alpha_{\mathrm{in}}|^2$ is the ingoing power. Using this result leads to new equations of motion for the field amplitude fluctuations $\delta\alpha$ around the steady state solution and the oscillator amplitude x_{m} with respect to a slightly shifted steady state position. The radiation pressure from the steady state field shifts the oscillator's steady state by $\hbar G \bar{n}_{\mathrm{c}}/M\Omega_{\mathrm{m}}^2$. In the linearized equations of motion the coupling strength G is enhanced by the steady state field amplitude $\bar{\alpha}$ [12]

$$
\begin{aligned}
\delta\dot{\alpha} &= -\frac{\kappa}{2}\delta\alpha + i\Delta\delta\alpha + iG\bar{\alpha}x_{\mathrm{m}} \, , \\
M\ddot{x}_{\mathrm{m}} &= -M\Omega_{\mathrm{m}}^2 x_{\mathrm{m}} - M\Gamma_{\mathrm{m}}\dot{x}_{\mathrm{m}} + \hbar G(\bar{\alpha}^*\delta\alpha + \bar{\alpha}\delta\alpha^*) + F_{\mathrm{th}} \, .
\end{aligned}
\tag{1.92}
$$

By Fourier transforming these equations of motion, a modified expression for the membrane susceptibility can be derived analog to the derivation of expression 1.52 presented in section 1.2.1. For sufficiently weak laser drive $G\bar{\alpha} \ll \kappa$ and $\Gamma_{\mathrm{m}} \ll \Omega_{\mathrm{m}}$, the modified susceptibility can be written as [12]

$$\chi_{\mathrm{opt}}^{-1}(\Omega) = 2\Omega_{\mathrm{m}}M\left(\Omega_{\mathrm{m}} + \delta\Omega_{\mathrm{m}} - \Omega + i\frac{\Gamma_{\mathrm{m}} + \Gamma_{\mathrm{opt}}}{2}\right) \, , \tag{1.93}$$

with the optomechanical frequency shift $\delta\Omega_\mathrm{m}$ and damping rate Γ_opt:

$$
\begin{aligned}
\delta\Omega_\mathrm{m} &= g_0^2 \bar{n}_\mathrm{c} \left[\frac{\Delta + \Omega_\mathrm{m}}{(\Delta + \Omega_\mathrm{m})^2 + \kappa^2/4} + \frac{\Delta - \Omega_\mathrm{m}}{(\Delta - \Omega_\mathrm{m})^2 + \kappa^2/4} \right], \\
\Gamma_\mathrm{opt} &= g_0^2 \bar{n}_\mathrm{c} \left[\frac{\kappa}{(\Delta + \Omega_\mathrm{m})^2 + \kappa^2/4} - \frac{\kappa}{(\Delta - \Omega_\mathrm{m})^2 + \kappa^2/4} \right].
\end{aligned}
\tag{1.94}
$$

Note that I use a different sign convention in the Fourier transform compared to reference [12], which changes the sign of the imaginary part of the susceptibility. I use $x(\Omega) = \int_{-\infty}^{\infty} x(t) e^{-i\Omega t} \mathrm{d}t$. As mentioned at the end of section 1.2.1, the modified susceptibility changes the PSD of the membrane amplitude, $S_x(\Omega)$. This modifies its mean potential energy and can be attributed to an effective temperature

$$
T_\mathrm{opt} = \frac{\Gamma_\mathrm{m}}{\Gamma_\mathrm{m} + \Gamma_\mathrm{opt}} T_\mathrm{bath}.
\tag{1.95}
$$

In the lab we typically measure the optomechanical frequency shift and damping rate as function of the ingoing power P_in. For this, it is convenient to express them as

$$
\begin{aligned}
\delta\Omega_\mathrm{m} &= c_4 P_\mathrm{in} \quad \text{and} \\
\Gamma_\mathrm{opt} &= \Gamma_\mathrm{m} c_2 P_\mathrm{in},
\end{aligned}
\tag{1.96}
$$

where $c_4 = \delta\Omega_\mathrm{m}/P_\mathrm{in}$ and $c_2 = \Gamma_\mathrm{opt}/\Gamma_\mathrm{m} P_\mathrm{in}$ are constants which are independent of P_in.

1.2.5 T_bath in presence of laser noise

For small ingoing laser power P_tot the bath temperature in equation 1.95 is given by the room temperature $T_\mathrm{bath} \approx T_0$. For finite laser power, noise on the laser intensity and frequency at Ω_m couples to the membrane motion via the radiation pressure force and limits the minimum temperature [103, 104]. Laser frequency noise is converted into additional intensity noise via the cavity response, see equation 1.91. To take this heating mechanism into account, we attribute an additional effective temperature T_L to this random driving process and add it to the room temperature $T_\mathrm{bath} = T_0 + T_\mathrm{L}$. The effective temperature T_L can be found by comparing the PSD of the radiation pressure force noise generated by the intracavity intensity fluctuations to the PSD of a thermal force from a bath at temperature T_0 [98]

$$
T_\mathrm{L} = T_0 \frac{S_\mathrm{F,int}(\Omega_\mathrm{m}) + S_\mathrm{F,freq}(\Omega_\mathrm{m})}{S_\mathrm{F,th}(\Omega_\mathrm{m})},
\tag{1.97}
$$

with $S_\mathrm{F,th}(\Omega_\mathrm{m}) = 4M\Gamma_\mathrm{m} k_\mathrm{B} T_0$ and radiation pressure force power spectral densities generated by laser intensity and frequency noise $S_\mathrm{F,int}(\Omega_\mathrm{m})$ and $S_\mathrm{F,freq}(\Omega_\mathrm{m})$. Using

equations 1.89 and 1.91 and assuming $\Omega_\mathrm{m} \ll |\Delta| \ll \kappa$ the force power spectral densities can be written as

$$
\begin{aligned}
S_{\mathrm{F,int}}(\Omega_\mathrm{m}) &= (\hbar G \bar{n}_\mathrm{c})^2 S_\mathrm{I}(\Omega_\mathrm{m}) \,, \\
S_{\mathrm{F,freq}}(\Omega_\mathrm{m}) &= (\hbar G \bar{n}_\mathrm{c})^2 \left(\frac{8\Delta}{\kappa^2}\right)^2 S_{\dot{\phi}}(\Omega_\mathrm{m}) \,,
\end{aligned}
\tag{1.98}
$$

where $S_\mathrm{I}(\Omega_\mathrm{m})$ and $S_{\dot{\phi}}(\Omega_\mathrm{m})$ are the power spectral densities of the relative laser intensity and frequency noise, which we can measure in the lab.

Both noise terms depend quadratically on the ingoing laser power so that the resulting bath temperature can be written as

$$
T_\mathrm{bath} = T_0(1 + c_3 P_\mathrm{in}^2) \,,
\tag{1.99}
$$

with $c_3 = T_\mathrm{L}/(T_0 P_\mathrm{in}^2)$.

1.2.6 Displacement sensing

To detect the motion of the membrane, we exploit the fact that it slightly changes the cavity resonance frequency, which modifies the phase of the reflected beam Φ. In section 1.2.2 we found $\Phi = 4\Delta/\kappa$ with $\Delta = Gx_\mathrm{m}$ for a resonantly driven cavity and small membrane displacements.

In our new cavity-membrane setup we detect this phase shift via the beat signal with a strong local oscillator beam in a homodyne detection scheme. The back-reflected signal from the cavity and the local oscillator beam are overlapped on a $50 : 50$ beamsplitter, see figure 2.5. The signals from the outgoing ports are sent to two photodiodes whose outputs are subtracted. If the phase of the local oscillator beam is locked to the point where the slope of the interference fringe is maximal, the difference signal becomes

$$
\epsilon_\mathrm{Diff} = 4\sqrt{P_\mathrm{c}P_\mathrm{LO}}\,\Phi \,.
\tag{1.100}
$$

Here P_c is the power which probes the cavity and P_LO is the power of the local oscillator beam, which can be much larger than P_c.

In the old cavity-membrane setup the phase shift was detected via the Pound-Drever-Hall (PDH) error signal [105]

$$
\epsilon_\mathrm{PDH} = -2\sqrt{P_\mathrm{c}P_\mathrm{sb}}\,\Phi \,,
\tag{1.101}
$$

where $P_\mathrm{sb} = \xi P_\mathrm{c}$ is the power in each PDH sideband and P_c the power in the carrier which probes the cavity. One easily sees that both signals are proportional to x_m through Φ and that the local oscillator scheme allows to generate a much larger signal for a given power in the detection beam $P_\mathrm{det} = P_\mathrm{c} + 2P_\mathrm{sb}$.

In both cases, the optical power gets converted into a voltage via a photodiode, thus creating a voltage proportional to x_m, which we detect with a spectrum analyzer. This device measures the PSD of this voltage $S_V(\Omega)$, which is proportional to

the PSD of the membrane displacement $S_x(\Omega)$. Integrating the spectrum analyzer signal over all frequencies gives the detected temperature $T_{\text{det}} = \int_0^\infty S_V(\Omega)\mathrm{d}\Omega/2\pi$, which equals the membrane temperature T_{m} up to a constant

$$T_{\text{det}} = c_1 T_{\text{m}} \,. \tag{1.102}$$

We calibrate c_1 via the assumption that the membrane is at room temperature if no light is impinging onto the membrane.

Combining the results of the previous paragraphs, namely the equations 1.102, 1.95, 1.96 and 1.99, the detected optomechanical temperature in presence of laser noise can be expressed as a function of the ingoing power

$$T_{\text{det}} = \frac{c_1 T_0 (1 + c_3 P_{\text{in}}^2)}{1 + c_2 P_{\text{in}}} \,. \tag{1.103}$$

Operating the spectrum analyzer in zero span mode with a bandwidth larger than the linewidth of the membrane, $BW \gg \Gamma_{\text{tot}}$, allows to probe the membrane power spectrum versus time. We often perform measurements in this temporally resolved mode as it gives direct access to the membrane damping rate without any calibration. In thermal equilibrium, the oscillator is driven by a fluctuating thermal force. As a consequence, the membrane amplitude fluctuates on a timescale of $1/\Gamma_{\text{tot}}$. Therefore, precise measurements of the PSD, which is given by the mean value of the membrane displacement, see equation 1.53, have to be performed for a time much longer than Γ_{tot}^{-1}. A finite measurement time leads to an error in the PSD measurement. In [98] section 1.1.2 it was found by numerical simulations that the resulting uncertainty on the measured temperature is

$$\Delta T = \frac{T}{\sqrt{N(1 + \tau\Gamma_{\text{tot}}/2)}} \,. \tag{1.104}$$

Here τ is the measurement time, N is the number of traces over which the measurement was averaged and T is the measured temperature.

1.2.7   Minimal phonon occupation number and optomechanical co-operativity

To perform experiments in the quantum regime, the harmonic oscillator must be close to or in its quantum ground state. In the classical model presented above the temperature $T_{\text{opt}} = T_{\text{bath}}\Gamma_{\text{m}}/(\Gamma_{\text{m}} + \Gamma_{\text{opt}})$ can be reduced to arbitrary low values if the optomechanical damping rate Γ_{opt} is increased. However, at low oscillator temperatures fluctuations of the radiation-pressure force due to photon shot noise and the coupling to the thermal bath set a limit to the minimally achievable temperature, which is not taken into account in the simple classical model.

A rigorous quantum mechanical treatment of the optomechanical cooling process as presented in [101, 106, 107, 12] results in a minimally achievable phonon

occupation number of [12]

$$\bar{n}_{\mathrm{f}} = \frac{\Gamma_{\mathrm{opt}}\bar{n}_{\mathrm{min}} + \Gamma_{\mathrm{m}}\bar{n}_{\mathrm{th}}}{\Gamma_{\mathrm{opt}} + \Gamma_{\mathrm{m}}}\,, \tag{1.105}$$

where $\bar{n}_{\mathrm{min}}$ is the minimal occupation number in absence of thermal decoherence ($\Gamma_{\mathrm{m}} = 0$). In the bad cavity regime ($\kappa \gg \Omega_{\mathrm{m}}$) the phonon occupation becomes minimal for $\Delta = -\kappa/2$ (where $\Gamma_{\mathrm{opt}}(\Delta = -\kappa/2) = 8\bar{n}_{\mathrm{c}}g_0^2\Omega_{\mathrm{m}}/\kappa^2$) resulting in [12]

$$\bar{n}_{\mathrm{min}} = \frac{\kappa}{4\Omega_{\mathrm{m}}} \gg 1\,, \tag{1.106}$$

In the so-called resolved-sideband regime ($\kappa \ll \Omega_{\mathrm{m}}$) the occupation becomes minimal for $\Delta = -\Omega_{\mathrm{m}}$ ($\Gamma_{\mathrm{opt}} = 4\bar{n}_{\mathrm{c}}g_0^2/\kappa$) where [12]

$$\bar{n}_{\mathrm{min}} = \left(\frac{\kappa}{4\Omega_{\mathrm{m}}}\right)^2 \ll 1\,. \tag{1.107}$$

One easily sees that in the bad cavity regime the ground state $\bar{n}_{\mathrm{f}} \approx 0$ cannot be reached even in the absence of any coupling to the thermal environment. We will see in the following section that ground state cooling in the bad cavity regime still is possible if sympathetic cooling from the atoms is present, which adds additional cooling but no additional noise.

For large damping $\Gamma_{\mathrm{opt}} \gg \Gamma_{\mathrm{m}}$ and in the resolved sideband regime ($\kappa \ll \Omega_{\mathrm{m}}$) the final occupation number from equation 1.105 can be written as [12]

$$\bar{n}_{\mathrm{f}} = \bar{n}_{\mathrm{min}} + \frac{1}{C_{\mathrm{opt}}}\,. \tag{1.108}$$

Here C_{opt} is the optomechanical multiphoton quantum cooperativity

$$C_{\mathrm{opt}} = \frac{4g_0^2\bar{n}_c}{\kappa\Gamma_{\mathrm{m}}n_{\mathrm{th}}}\,, \tag{1.109}$$

Equation 1.108 shows that optomechanical ground state cooling is possible if the cavity is in the resolved sideband regime, and if in addition the optomechanical cooperativity C_{opt} is larger than one.

1.3   Hybrid atom-membrane system

In this final theoretical section I combine the results of the last two sections to describe the hybrid atom-membrane system. Concretely, I will derive classical equations of motion for the membrane displacement and the atomic displacement. From these equations of motion an expression for the sympathetic cooling rate of the membrane will be derived. Further I will present the corresponding Hamiltonian and the atom-membrane coupling strength and briefly discuss the quantum limits of sympathetic cooling.
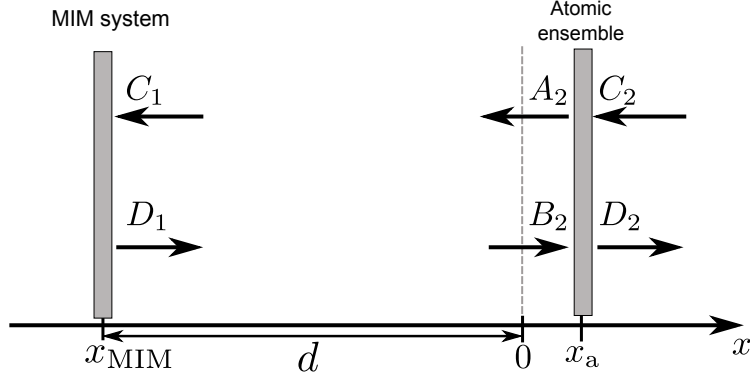
Figure 1.5: Schematic of the coupled atom-membrane system. Atoms and MIM system are modeled as beamsplitter elements. The system is driven by a single laser beam from the right.

1.3.1 Coupled equations of motion

Figure 1.5 shows a schematic of the coupled atom-membrane system. Atomic and membrane system are modeled as beamsplitters with certain complex reflection and transmission coefficients separated by a distance d. The system is pumped with one single laser $C_2(x) = C_{20}\exp(-ikx)$ from the right. Based on the knowledge from section 1.2.2, I model the membrane-in-the-middle system as an object with unity reflection amplitude (see equation 1.81), which shifts the phase of the reflected light by the membrane position dependent phase $\Phi = 4Gx_\mathrm{m}/\kappa$ (see equation 1.83). The position x_m is the displacement of the membrane with respect to its steady state position in the cavity, which is not explicitly drawn in the figure. Within this model the field, which is reflected off the MIM system, can be written as

$$D_1(x_\mathrm{MIM}) = \eta C_1(x_\mathrm{MIM})e^{i\Phi}\,. \tag{1.110}$$

Here x_MIM is the position of the cavity incoupling mirror. Further, the coupling efficiency to the cavity TEM_{00} mode $\eta \leq 1$ is included. I assume that light which is not coupled into the TEM_{00} mode is scattered off the cavity in a divergent optical mode and does not get back to the atoms.

The ingoing field B_2 at the position of the atoms x_a is then related to the outgoing field A_2 by

$$B_2(x_\mathrm{a}) = \eta t^2 e^{i\Phi}e^{2ikd}e^{2ikx_\mathrm{a}}A_2(x_\mathrm{a}) = \eta t^2 e^{i\Phi}e^{2ikx_\mathrm{a}}A_2(x_\mathrm{a})\,, \tag{1.111}$$

where t is the amplitude transmission of the optical path between atoms and cavity. In the second equation the distance between the two systems has been set to $d = n\lambda/2$, $n \in \mathbb{N}$ to place an intensity maximum at the zero point of the coordinate system $x_\mathrm{a} = 0$.

As in section 1.1.6, I model the atomic ensemble as a beamsplitter with reflectivity $\mathfrak{r}$ and transmission $\mathfrak{t}$ given by equation 1.35. I assume that the reflectivity of the

atoms is small $|\mathfrak{r}| \ll 1$, which is a reasonable assumption in our system. Inserting equation 1.111 into the first line of equation 1.34 relates the field $A_2(x_a)$ to the ingoing field $C_2(x_a)$

$$
\begin{aligned}
A_2(x_a) &= \frac{\mathfrak{t}C_2(x_a)}{1 - \mathfrak{r}\eta t^2 e^{i\Phi} e^{2ikx_a}} \\
&\approx \mathfrak{t}C_2(x_a)(1 + \mathfrak{r}\eta t^2 e^{i\Phi} e^{2ikx_a}).
\end{aligned} \tag{1.112}
$$

In the second line the fraction is expanded in the small parameter $\mathfrak{r}$ up to first order. Terms scaling with $\mathfrak{r}^2$ or higher and with this interaction effects of the atomic ensemble with itself via the MIM system are neglected.

In this approximation the field $B_2(x_a) = [A_2(x_a) - \mathfrak{t}C_2(x_a)]/\mathfrak{r}$ becomes independent of $A_2(x_a)$,

$$
B_2(x_a) \approx \eta t^2 e^{i\Phi} e^{2ikx_a} \mathfrak{t}C_2(x_a). \tag{1.113}
$$

Thus, we recover the situation from section 1.1.6. To calculate the force onto the atoms and the modulation of the power in the beam which propagates towards the membrane, we can directly use the results from section 1.1.6 for incoming fields, $C(x) = C_0 \exp(-ikx)$ from the right and $B(x) = B_0 \exp(ikx + \phi)$ from the left, setting $B_0 = \eta t^2 \mathfrak{t}C_0$ or correspondingly $I_0 = \eta^2 t^4 I_1 \equiv RI_1$. In the last equation, I dropped the atomic transmission coefficient $\mathfrak{t}$, which is very close to one ($\mathfrak{t} \approx 1$) if $\mathfrak{r} \ll 1$. For small atomic and membrane displacements x_a and x_m the force onto the atoms is then given by equation 1.43. Using $\Phi = 4Gx_m/\kappa$ it can be written as

$$
F_a = -Nm\Omega_a^2 x_a - Kx_m, \tag{1.114}
$$

with coupling spring constant

$$
K = Nm\Omega_a^2 \frac{2G}{\kappa k}. \tag{1.115}
$$

The motion of the atoms creates a modulation of the power of the beam traveling towards the membrane given by equation 1.46. This power modulation induces a force on the membrane because it alters the radiation pressure force 1.89 inside the cavity. Inserting equation 1.46 and 1.91 into equation 1.89 results in the following force on the membrane

$$
F_m = -\eta^2 t^2 K x_a - \eta^2 t^2 Nm\Omega_a^2 \left(\frac{2G}{\kappa k}\right)^2 x_m. \tag{1.116}
$$

For the power which is coupled into the cavity, the cavity incoupling efficiency η and the optical path transmission between atom and membrane t are taken into account. The first term in equation 1.116 is the force from the atoms. The second term results from an interaction of the membrane with itself via the reflection at the atomic ensemble. It has the form of a restoring force. For our parameters the intrinsic restoring force of the membrane $F_{m,res} = -M\Omega_m^2 x_m$ is much larger than

this second term ($M\Omega_{\mathrm{m}}^2 \approx 350 \,\mathrm{N/m} \gg Nm\Omega_{\mathrm{a}}^2(2G/\kappa k)^2 \approx 0.0016 \,\mathrm{N/m}$). I will therefore neglect this second term in the following.

Inserting these forces into the equations of motion for the atomic and membrane displacement gives the following set of coupled differential equations

$$
\begin{aligned}
Nm\ddot{x}_{\mathrm{a}} &= -\Gamma_{\mathrm{a}}Nm\dot{x}_{\mathrm{a}} - Nm\Omega_{\mathrm{a}}^2 x_{\mathrm{a}} - Kx_{\mathrm{m}}\,, \\
M\ddot{x}_{\mathrm{m}} &= -\Gamma_{\mathrm{m}}M\dot{x}_{\mathrm{m}} - M\Omega_{\mathrm{m}}^2 x_{\mathrm{m}} - \eta^2 t^2 Kx_{\mathrm{a}} + F_{\mathrm{th}}\,.
\end{aligned}
\tag{1.117}
$$

Here F_{th} is the fluctuating thermal force originating in the coupling of the membrane to the environment. As the atomic temperature is negligibly small, the corresponding atomic term is neglected. Γ_{a} and Γ_{m} are the damping rates of the atomic and membrane motion.

1.3.2   Coupling Hamiltonian and coupling strength

A quantized description of the coupled system explicitly modeling the atom-light and membrane-light interaction has recently been published [69]. In their work Vogell *et al.* show that the atom-membrane interaction can be described by the Hamiltonian

$$
\hat{H} = \hbar g_{\mathrm{N}} \left(\hat{b}_{\mathrm{m}} + \hat{b}_{\mathrm{m}}^{\dagger} \right) \left(\hat{b}_{\mathrm{a}} + \hat{b}_{\mathrm{a}}^{\dagger} \right)\,,
\tag{1.118}
$$

with coupling constant

$$
g_{\mathrm{N}} = |r_{\mathrm{m}}|\Omega_{\mathrm{a}}\sqrt{\frac{Nm\Omega_{\mathrm{a}}}{M\Omega_{\mathrm{m}}}}\frac{2F}{\pi}\,.
\tag{1.119}
$$

Here $\hat{b}_{\mathrm{m}}$ ($\hat{b}_{\mathrm{a}}$) and $\hat{b}_{\mathrm{m}}^{\dagger}$ ($\hat{b}_{\mathrm{a}}^{\dagger}$) are annihilation and creation operators of the membrane (atomic mode). The coupling constant is connected to the spring constant $g_{\mathrm{N}} = Kx_{\mathrm{m},0}x_{\mathrm{a},0}/\hbar$, where $x_{\mathrm{m},0} = \sqrt{\hbar/2M\Omega_{\mathrm{m}}}$ and $x_{\mathrm{a},0}[N] = \sqrt{\hbar/2Nm\Omega_{\mathrm{a}}}$ are the quantum mechanical zero point amplitudes of the membrane and atomic center-of-mass-motion, respectively. Note that the derivation in [69] is done for the point of maximal optomechanical coupling. If the membrane is placed at a position where the optomechanical coupling strength G is smaller than G_{max}, the atom-membrane coupling constant is reduced by the same factor. The coupled equations of motion presented above can alternatively be derived from the Hamiltonian description. Using equation 1.21 and 1.74, the coupling constant can be rewritten as a product of the atomic and the membrane coupling to light

$$
g_{\mathrm{N}} = \frac{4\sqrt{N}\bar{n}_{\mathrm{c}}g_0 g_1}{\kappa}\,.
\tag{1.120}
$$

Here $g_0 = Gx_{\mathrm{m},0}$ is the optomechanical single photon coupling rate introduced in equation 1.87 and g_1 is the single atom, single photon atom-light coupling rate

$$
g_1 = \frac{V_1}{\hbar}kx_{\mathrm{a},0}[N=1]\,,
\tag{1.121}
$$

where $V_1 = V_{\mathrm{m}}/\bar{n}_{\mathrm{c}}$ is the depth of the lattice potential per intra-cavity photon.

1.3.3 Sympathetic cooling

Analog to the derivation of the optomechanical damping rate sketched in section 1.2.4, one can derive a sympathetic damping rate from the coupled equations of motion 1.117. Fourier transforming the equations leads to

$$
\begin{aligned}
\tilde{x}_{\mathrm{a}}(\Omega) &= \chi_{\mathrm{a}}(\Omega)[-K\tilde{x}_{\mathrm{m}}(\Omega)]\,, \\
\tilde{x}_{\mathrm{m}}(\Omega) &= \chi_{\mathrm{m}}(\Omega)[\tilde{F}_{\mathrm{th}} - \eta^2 t^2 K\tilde{x}_{\mathrm{a}}(\Omega)]\,,
\end{aligned}
\tag{1.122}
$$

with the mechanical susceptibilities

$$
\begin{aligned}
\chi_{\mathrm{a}}(\Omega) &\simeq [2Nm\Omega_{\mathrm{a}}(\Omega_{\mathrm{a}} - \Omega + i\Gamma_{\mathrm{a}}/2)]^{-1}\,, \\
\chi_{\mathrm{m}}(\Omega) &\simeq [2M\Omega_{\mathrm{m}}(\Omega_{\mathrm{m}} - \Omega + i\Gamma_{\mathrm{m}}/2)]^{-1}\,.
\end{aligned}
\tag{1.123}
$$

In the last two lines a Lorentzian approximation as in equation 1.52 was made, which is valid for $\Omega_{\mathrm{a}} \gg \Gamma_{\mathrm{a}}$ and $\Omega_{\mathrm{m}} \gg \Gamma_{\mathrm{m}}$. Note that due to a different sign convention in the Fourier transform $x(\Omega) = \int_{-\infty}^{\infty} x(t)e^{-i\Omega t}\mathrm{d}t$ the signs of the imaginary parts of the susceptibilities here differ from the ones in reference [55]. Eliminating $\tilde{x}_{\mathrm{a}}(\Omega)$ in equation 1.122 one obtains

$$
\tilde{x}_{\mathrm{m}}(\Omega) = \chi_{\mathrm{sym}}(\Omega)\tilde{F}_{\mathrm{th}}(\Omega)\,,
\tag{1.124}
$$

with an effective membrane susceptibility

$$
\begin{aligned}
\chi_{\mathrm{sym}}^{-1}(\Omega) &= \chi_{\mathrm{m}}^{-1}(\Omega) - \eta^2 t^2 K^2 \chi_{\mathrm{a}}(\Omega) \\
&= 2M\Omega_{\mathrm{m}}\left(\Omega_{\mathrm{m}} - \Omega + i\frac{\Gamma_{\mathrm{m}}}{2} - \frac{\eta^2 t^2 g_{\mathrm{N}}^2}{\Omega_{\mathrm{a}} - \Omega + i\Gamma_{\mathrm{a}}/2}\right)\,.
\end{aligned}
\tag{1.125}
$$

For $\Gamma_{\mathrm{a}} \gg g_{\mathrm{N}}, \Gamma_{\mathrm{m}}$, as in our sympathetic cooling experiments, one can replace Ω by Ω_{m} in the last term resulting in

$$
\chi_{\mathrm{sym}}^{-1}(\Omega) = 2M\Omega_{\mathrm{m}}\left(\Omega_{\mathrm{m}} - \delta\Omega_{\mathrm{m}} - \Omega + i\frac{\Gamma_{\mathrm{sym}} + \Gamma_{\mathrm{m}}}{2}\right)\,,
\tag{1.126}
$$

with sympathetic damping rate

$$
\Gamma_{\mathrm{sym}}[N, \Omega_{\mathrm{a}}] = \frac{\eta^2 t^2 g_{\mathrm{N}}^2 \Gamma_{\mathrm{a}}}{(\Omega_{\mathrm{a}} - \Omega_{\mathrm{m}})^2 + (\Gamma_{\mathrm{a}}/2)^2}
\tag{1.127}
$$

and frequency shift

$$
\delta\Omega_{\mathrm{m}} = (\Omega_{\mathrm{a}} - \Omega_{\mathrm{m}})\frac{\Gamma_{\mathrm{sym}}}{\Gamma_{\mathrm{a}}}\,.
\tag{1.128}
$$

The modified membrane susceptibility leads to a modified membrane displacement spectrum $S_x(\Omega) = |\chi_{\mathrm{sym}}(\Omega)|^2 S_{\mathrm{F,th}}$ in analogy to the case of the optomechanical interaction discussed in section 1.2.1. This results in a different membrane temperature $T_{\mathrm{sym}} = T_{\mathrm{bath}}\Gamma_{\mathrm{m}}/(\Gamma_{\mathrm{m}} + \Gamma_{\mathrm{sym}})$. If in addition to the sympathetic damping also optomechanical damping is present, as in our experiments, the membrane temperature becomes

$$
T_{\mathrm{sym}} = T_{\mathrm{bath}}\frac{\Gamma_{\mathrm{m}}}{\Gamma_{\mathrm{m}} + \Gamma_{\mathrm{opt}} + \Gamma_{\mathrm{sym}}}\,.
\tag{1.129}
$$

1.3.4 Ensemble-integrated sympathetic cooling rate

In our sympathetic cooling experiments the coupling lattice potential is overlapped with the molasses cooled cloud with radius R_a, much larger than the waist w_0 of the lattice laser beam. From absorption images we find that the atomic number density n_a in the molasses is approximately constant over the lattice volume. During the molasses phase the presence of the lattice does not seem to change the density distribution significantly. We will see that in section 4.3.

The Gaussian radial intensity distribution of the coupling lattice leads to the Gaussian profile of axial trapping frequencies $\Omega_a(r) = \Omega_a(0)e^{-r^2/w_0^2}$ given in equation 1.21 for atoms at different radial positions r. If the atomic density distribution is constant, as in our experiment, there are atoms at all different radii. They act on the membrane with different sympathetic cooling rates due to their different axial trapping frequencies, see equation 1.127.

To determine the total sympathetic cooling rate of the membrane for a given radial profile of axial frequencies, the contributions to Γ_{sym} from all the atoms have to be added up. To do this, we integrate the single atom sympathetic cooling rate over the lattice beam profile

$$\Gamma_{\text{sym}}^{\text{int}} = 2R_a n_a \int_0^{R_a} \mathrm{d}r\, 2\pi r \Gamma_{\text{sym}}[N=1, \Omega_a(r)] \,. \tag{1.130}$$

With equation 1.21 this can be converted into an integral over frequency

$$\Gamma_{\text{sym}}^{\text{int}} = N_{\text{lat}} \int_{\Omega_a(R_a)}^{\Omega_a(0)} \mathrm{d}\Omega_a \frac{\Gamma_{\text{sym}}[N=1, \Omega_a]}{\Omega_a} \,, \tag{1.131}$$

where $N_{\text{lat}} = 2R_a \pi w_0^2 n_a$ is the number of atoms in the lattice volume. As $R_a \gg w_0$, the lower integration limit can be set to zero $\Omega_a(R_a) \to 0$. Using equation 1.127 and 1.119 one finds

$$\Gamma_{\text{sym}}^{\text{int}} = \frac{4g_{N_r}^2 \eta^2 t^2}{\Gamma_a \pi} \left\{ \left(1 - \frac{\Gamma_a^2}{4\Omega_m^2}\right) \left(\arctan\left[\frac{2\Omega_m}{\Gamma_a}\right] + \arctan\left[\frac{2(\Omega_a(0) - \Omega_m)}{\Gamma_a}\right]\right) \right.$$
$$\left. + \frac{\Gamma_a}{2\Omega_m^2} \left(\Omega_a(0) + \Omega_m \ln\left[\frac{\Gamma_a^2 + 4(\Omega_a(0) - \Omega_m)^2}{\Gamma_a^2 + 4\Omega_m^2}\right]\right) \right\} \,, \tag{1.132}$$

where $N_r = N_{\text{lat}}(\pi \Gamma_a / 2\Omega_m) = \pi^2 R_a w_0^2 n_a \Gamma_a / \Omega_m$ is the number of resonantly coupled atoms and $g_{N_r} = |r_m|\Omega_m \sqrt{\frac{N_r m}{M}} \frac{2F}{\pi}$ the corresponding coupling constant. For $\Gamma_a \ll \Omega_m$, as in our sympathetic cooling experiments, equation 1.132 can be approximated by

$$\Gamma_{\text{sym}}^{\text{int}} \simeq \frac{4g_{N_r}^2 \eta^2 t^2}{\Gamma_a \pi} \left(\arctan\left[\frac{2\Omega_m}{\Gamma_a}\right] + \arctan\left[\frac{2(\Omega_a(0) - \Omega_m)}{\Gamma_a}\right]\right) \,. \tag{1.133}$$

This is a step-like function with step width Γ_a and step height

$$\Gamma_{\text{sym}}^{\text{step}} = \frac{4g_{N_r}^2 \eta^2 t^2}{\Gamma_a} \,. \tag{1.134}$$

1.3.5 Ground state cooling and atom-membrane cooperativity

As in the optomechanical case in section 1.2.4, the description of sympathetic cooling above was fully classical. Quantum noise processes which limit the minimally achievable temperature are neglected. In the fully quantized description presented in [69] the relevant dissipation processes are taken into account. Vogell *et al.* find a minimal phonon occupation number consisting of four terms

$$
\begin{aligned}
\bar{n}_\mathrm{f} &= \frac{\Gamma_\mathrm{m}\bar{n}_\mathrm{th}}{\Gamma_\mathrm{m} + \Gamma_\mathrm{sym}} + \frac{\Gamma_\mathrm{m}^\mathrm{rp}}{\Gamma_\mathrm{m} + \Gamma_\mathrm{sym}} + \left(\frac{\Gamma_\mathrm{a}^\mathrm{cool}}{4\Omega_\mathrm{a}}\right)^2 + \frac{\Gamma_\mathrm{a}^\mathrm{diff}}{\Gamma_\mathrm{a}^\mathrm{cool}} \\
&= n_1 + n_2 + n_3 + n_4 \, .
\end{aligned}
\tag{1.135}
$$

The first term originates from thermal decoherence via the coupling to the thermal bath analog to the second term in equation 1.105 with $\bar{n}_\mathrm{th} = k_\mathrm{B} T_\mathrm{bath}/\hbar\Omega_\mathrm{m}$. The second term comes from radiation pressure noise on the coupling beam, which causes a membrane momentum diffusion rate of $\Gamma_\mathrm{m}^\mathrm{rp} = 4g_0^2\bar{n}_\mathrm{c}/\kappa$ [12][1]. These first two terms can be summarized introducing the total membrane decoherence rate $\Gamma_\mathrm{m}^\mathrm{dec} = \Gamma_\mathrm{m}\bar{n}_\mathrm{th} + \Gamma_\mathrm{m}^\mathrm{rp}$

$$
n_1 + n_2 = \frac{\Gamma_\mathrm{m}^\mathrm{dec}}{\Gamma_\mathrm{m} + \Gamma_\mathrm{sym}} \, .
\tag{1.136}
$$

The third term is caused by the "rotating terms" in the coupling Hamiltonian, which start to play a role if the atomic damping is very strong. The last term comes from scattering of coupling lattice photons by the atoms. This results in a light-induced momentum diffusion of the atoms corresponding to an atomic damping rate of [108]

$$
\Gamma_\mathrm{a}^\mathrm{diff} = (kx_\mathrm{a,0}[N=1])^2 \cdot \Gamma \frac{V_\mathrm{d}}{\hbar\Delta_\mathrm{LA}} \, .
\tag{1.137}
$$

Here $x_\mathrm{a,0}[N=1] = \sqrt{\hbar/2m\Omega_\mathrm{a}}$ is the zero point amplitude of a single atom and V_d the depth of the lattice potential, see equation 1.20. This intrinsic damping rate will always be present on the atomic side even if all additional laser cooling is switched off. The atomic damping rate in the equation of motion 1.117 is the sum of this intrinsic damping rate and all additional damping for instance from laser cooling $\Gamma_\mathrm{a} = \Gamma_\mathrm{a}^\mathrm{diff} + \Gamma_\mathrm{a}^\mathrm{cool}$. For strong laser cooling, as in our laser cooling experiments, the second term dominates $\Gamma_\mathrm{a} \approx \Gamma_\mathrm{a}^\mathrm{cool}$.

For large sympathetic cooling rates $\Gamma_\mathrm{sym} \gg \Gamma_\mathrm{m}$ and resonant atom-membrane coupling $\Omega_\mathrm{a} = \Omega_\mathrm{m}$ and using equation 1.127, the first two terms can be written as

$$
n_1 + n_2 \approx \frac{\Gamma_\mathrm{m}^\mathrm{dec}}{\Gamma_\mathrm{sym}} = \frac{1}{C_\mathrm{qu}} \, ,
\tag{1.138}
$$

where C_qu is the atom-membrane quantum cooperativity

$$
C_\mathrm{qu} = \frac{4\eta^2 t^2 g_\mathrm{N}^2}{\Gamma_\mathrm{a}\Gamma_\mathrm{m}^\mathrm{dec}} \, .
\tag{1.139}
$$

---

[1]Note that the expression given in [69] is too small by a factor 4.

Thus, the atom-membrane cooperativity must be large ($C_{\text{qu}} \gg 1$) to reach a phonon occupation below unity.

If $\Gamma_{\text{a}} \approx \Gamma_{\text{m}}^{\text{dec}}$, an atom-membrane quantum cooperativity above unity ($C_{\text{qu}} \gg 1$) implies strong coupling $g \gg (\Gamma_{\text{a}}/2, \Gamma_{\text{m}}^{\text{dec}}/2)$. In this regime, quantum mechanical state swaps between the atomic and membrane system are possible [12]. In summary, to perform interesting experiments in the quantum regime with the hybrid system it is crucial to have a system with a large quantum cooperativity.

In a parameter regime in which one of two coupled oscillators is very broad and the other one is narrow, meaning $g_{\text{N}} > \Gamma_{\text{m}}$ and $g_{\text{N}} < \Gamma_{\text{a}}$ or vice versa, a large cooperativity allows to observe interference phenomena analog to the electromagnetically-induced transparency (EIT) [12, 109]. The constraint for this is even much weaker than for ground state cooling. To see interference effects, only the non-quantum cooperativity C has to exceed one ($C \gg 1$) [12], which is defined as

$$C = \frac{4\eta^2 t^2 g_{\text{N}}^2}{\Gamma_{\text{a}}\Gamma_{\text{m}}} = \frac{\Gamma_{\text{sym}}}{\Gamma_{\text{m}}} \, . \tag{1.140}$$

If the membrane decoherence rate is dominated by thermal decoherence $\Gamma_{\text{m}}^{\text{dec}} \approx \Gamma_{\text{m}}\bar{n}_{\text{th}}$, the two cooperativities are connected by the thermal bath occupation $C_{\text{qu}} = C/\bar{n}_{\text{th}}$. In a system with $C > 1$ the coupling is not strong enough for quantum state transfers between the coupling partners, but a coherent exchange of energy as in EIT is possible [70].

Using equation 1.121, the atom-membrane quantum cooperativity from equation 1.139 can be written as

$$
\begin{aligned}
C_{\text{qu}} &= 4\eta^2 t^2 \cdot \frac{4 g_0^2 \bar{n}_{\text{c}}}{\Gamma_{\text{m}}^{\text{dec}} \kappa} \cdot \frac{4 g_1^2 \bar{n}_{\text{c}} N}{\Gamma_{\text{a}} \kappa} \\
&= 4\eta^2 t^2 C_{\text{m}} C_{\text{a}} \, ,
\end{aligned} \tag{1.141}
$$

with membrane-light cooperativity C_{m} and atom-light cooperativity C_{a}. Note that C_{m} is equal to the optomechanical quantum cooperativity C_{opt} introduced in equation 1.109 if the radiation pressure noise is negligible.

In the absence of laser cooling ($\Gamma_{\text{a}}^{\text{cool}} = 0$) the atom damping is reduced to the intrinsic damping rate $\Gamma_{\text{a}}^{\text{diff}}$ given in equation 1.137 and the atom-light cooperativity becomes maximal. Using the equations 1.137, 1.20 and 1.23, C_{a} can then be rewritten as

$$
\begin{aligned}
C_{\text{a}} &= \frac{4 g_1^2 \bar{n}_{\text{c}} N}{\Gamma_{\text{a}}^{\text{diff}} \kappa} \\
&= \frac{4\eta^2 t^4}{(1 + \eta t^2)^2} \sigma_0 \frac{N}{\sigma_{\text{L}}} = \frac{4\eta^2 t^4}{(1 + \eta t^2)^2} OD_{\text{res}} \, ,
\end{aligned} \tag{1.142}
$$

with the resonant optical depth OD_{res} defined in equation 1.13. Here $N/\sigma_{\text{L}} = \int_d n \, \mathrm{d}x$ is the atomic area density. Thus, in absence of optical losses ($\eta = t = 1$) the atom-light cooperativity C_{a} equals the resonant optical depth OD_{res}.

Note that for ground state cooling via cavity optomechanical damping, sideband resolution and $C_{\mathrm{opt}} > 1$ is required (see equation 1.108). It can been shown that also feedback cooling to the ground state in an optomechanical system via classical feedback requires $C_{\mathrm{opt}} > 1/8$ [70]. In our sympathetic cooling scheme the ground state cooling criterion is strongly relaxed as only the product of C_{m} and C_{a} has to be larger than one and sideband resolution is not required. The membrane can be ground state cooled even if $C_{\mathrm{opt}} \ll 1$ (which implies $C_{\mathrm{m}} \ll 1$) if it is coupled to an optically dense atomic ensemble with $C_{\mathrm{a}} \gg 1$ so that $4\eta^2 t^2 C_{\mathrm{m}} C_{\mathrm{a}} > 1$. The quantum feedback from the atoms thus outperforms optomechanical damping in the bad cavity regime as well as classical cavity feedback.

Chapter 2

A membrane oscillator in a cavity

This chapter provides a description and characterization of the second-generation membrane-in-the-middle (MIM) system which was used in the second half of this thesis, more precisely, for all experiments on self-oscillations in chapter 5 and several of the sympathetic cooling experiments in chapter 4. It was set up as part of the master's thesis of Thomas Lauber. A lot of details on the assembly process can be found in his thesis [110]. The cavity system used for the measurements in this thesis is not exactly the same as the one described in [110]. It is an almost identical copy, which was built with slight differences in the assembly process. I will point out the differences in the corresponding section of this chapter. The first-generation MIM system, which was used in some of the experiments discussed in chapter 4, has already been treated in details in [111, 98, 55]. I will therefore focus on the description of the second-generation setup and just summarize the characteristics of the first-generation setup at the end. The chapter starts with a short introduction to the central element of the MIM setups - the membrane oscillator.

2.1 Stochiometric SiN Membranes

The mechanical object of interest in our hybrid system is a stochiometric silicon nidride membrane. These membranes are used in a growing number of optomechanics experiments [80, 16, 29, 112, 113, 9, 8, 19]. While the main reason for this are the exceptionally high qualitiy factors of these membranes ($Q > 10^6$) combined with decent optical reflectivities ($r_\mathrm{m} \approx 0.4$ at $780\,\mathrm{nm}$), they are also commercially available, rather cheap and due to their large size relatively easy to handle and functionalize [8, 19, 9].
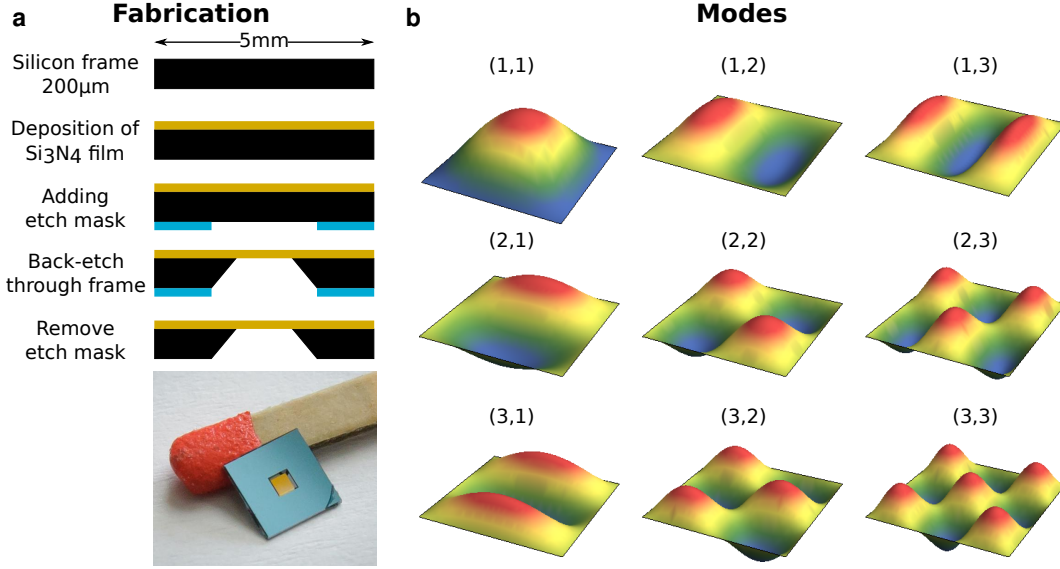
Figure 2.1: a) Membrane production process and photograph of membrane. b) Vibrational wavefunctions of lowest order membrane modes. Figure adapted from [98] .

2.1.1 Production

We purchase our membranes from Norcada Inc.[1]. A short summary of the process used by Norcada to fabricate the membranes and a photograph of the final membrane are shown in figure 2.1 a). To fabricate the membranes, a thin (tens of nm) layer of Si_3N_4 is deposited by low-pressure chemical vapor deposition (LPCVD) onto a silicon wafer. Due to the lattice constant mismatch between the Si and the Si_3N_4 the silicon-nitride layer is under a high tensile stress ($S \approx 1\,\mathrm{GPa}$). Subsequently, a part of the the silicon is etched away from the backside creating a suspended square membrane. Previous experiments of our and other groups [29, 114, 15] used non-stochiometric SiN membranes with relatively low stress $S \approx 100\,\mathrm{MPa}$ [114]. At equal dimensions these low-stress membranes have lower frequencies and therefore a smaller quality factor. They also show higher optical absorption. Taking all that into account makes them less attractive for optomechanical experiments.

2.1.2 Mechanical frequencies

The suspended square membrane can oscillate out of plane like a square drum with frequencies [115]

$$\Omega_{i,j} = \frac{\pi}{l}\sqrt{\frac{S}{\rho}(i^2 + j^2)}, \tag{2.1}$$

---

[1]www.norcada.com

Parameter	Value
Mass density ρ	$2700\,\mathrm{kg/m^3}$[16, 116]
Tensile stress S_0	$930\,\mathrm{MPa}$
Refractive index $\mathrm{Re}\,n$	1.98[79] 2.0[117]
Absorption $\mathrm{Im}\,n$	$< 4 \times 10^{-6}$ at $780\,\mathrm{nm}$[55]
Side length l	$1.5\,\mathrm{mm}$
Thickness d	$39.1(40.6)\,\mathrm{nm}$
Wafer dimensions	$5\,\mathrm{mm} \times 5\,\mathrm{mm} \times 200\,\mu\mathrm{m}$
Effective mass M	$117(140)\,\mathrm{ng}$
Fundamental frequency Ω_m	$2\pi \times 276.3(274)\,\mathrm{kHz}$
Amplitude reflectivity r_m	$0.404(0.4148)$
Quality factor Q	$1.8(3.0) \times 10^6$

Table 2.1: Properties of the membranes in the second (first)-generation setup. The values for l and the wafer dimensions are company specifications. Other numbers without quotations were measured in our lab. The first-generation membrane numbers are adapted from [98]. Ω_m, M and Q refer to the (1,1)-mode. Parameters of the (6,6)-mode can be found in section 2.4.2.

where $\rho = 2700\,\mathrm{kg/m^3}$ [16, 116] is the mass density, S is the tensile stress in the material, l is the side length of the membrane and i and j are integer numbers. Figure 2.1 b) illustrates the corresponding membrane wave functions for the lowest frequency modes. Table 2.1 summarizes the physical parameters of the membranes used for the experiments in this thesis. The tensile stress can be inferred from a measurement of the fundamental mode frequency ($i = j = 1$). I will refer to the fundamental mode frequency as Ω_m in the following.

2.1.3 Q-factor

For quantum-optomechanics experiments it is desirable to have a mechanical oscillator with a large Q-value as this reduces undesired decoherence processes originating from coupling to the environment. A larger Q-value reduces for instance the minimally achievable phonon occupation number given by equation 1.108. With typical Q-values larger than 10^6 stochiometric SiN membranes are at the upper end of the spectrum of mechanical oscillators used in various optomechanical setups [12]. The mechanisms which limit this high oscillation quality and the question of how to further improve it are subject of current research [116, 118, 119, 114, 120, 121, 122, 123, 124, 125]. A major limitation of the mechanical Q-factor is air damping ($Q_\mathrm{at\ air} \approx 1$). When reducing the pressure, the Q-factor typically saturates at pressures around $10^{-6}\,\mathrm{mbar}$ [111]. The biggest limitation of the Q-factor is then in many experiments given by radiation losses through the supporting substrate [114, 120, 116, 123, 122, 16, 102, 121]. The Si frame of the membrane is often glued or clamped to a supporting structure. This leads to a strong coupling between

the vibrational modes of the frame and the support, which broadens the modes of the frame. If the membrane mode of interest lies close to a frame mode, it then couples to the supporting structure via the frame. This creates a dissipation channel for the motion of the membrane mode. A minimization of the clamping often leads to the highest Q-factors [16, 111]. Moreover, symmetric (i,i) modes, especially higher order ones, typically have higher Q-values than antisymmetric modes [123, 116, 98], which can be explained within a theoretical model of the clamping losses [126]. Embedding the membrane into a periodic structure allows to create a phononic bandgap shield, which makes clamping down the membrane a less delicate procedure [120, 123]. The limitation of Q is then ultimately given by internal loss mechanisms [127, 122, 128, 119, 129], which still have not been completely understood. The highest quality factors observed with stochiometric silicon nidride membranes are in the range of several tens of millions. It seems that the Q-factor rises for increasing side length l and decreasing membrane thickness d [98, 116]. Furthermore, it has been observed that higher Q-values are reached in a cryogenic environment [120, 130].

2.2 Cavity design and vacuum setup

The SiN membranes have impressive Q-factors, but their reflectivity ($r_{\mathrm{m}} \approx 0.4$ at 780 nm) is too low to use them as a vibrating end mirror in an optomechanical system. However, placing the membrane inside an optical cavity from highly reflective bulk mirrors, a configuration pioneered by the Harris group in Yale [80, 15, 130], called membrane-in-the-middle (MIM) system, creates a powerful optomechanical system. We make use of this cavity enhancement in our hybrid setup. Theoretical details are presented in section 1.2.

2.2.1 Design criteria

For the designated task of coupling the membrane efficiently to the motion of the atomic ensemble, the membrane cavity system must fulfill a range of requirements:

- The cavity must be asymmetric as all the light shall be reflected back to the atoms. Thus, one mirror of the cavity should have a reflectivity as high as possible.

- The phase shift of the reflected light induced by the membrane motion $\Phi = 4Gx_{\mathrm{m}}/\kappa = 8|r_{\mathrm{m}}|kx_{\mathrm{m}}F/\pi$ (see section 1.2.2) and thus the cavity finesse F is supposed to be high so that the membrane motion has a large effect on the atoms. A high finesse also increases the influence of quantum laser noise on the membrane compared to the influence of undesired technical laser noise. Coupling to the motion of the atoms sets limits to the minimum power outside the cavity because the resonance condition $\Omega_{\mathrm{a}} = \Omega_{\mathrm{m}}$ needs to be fulfilled, see section 1.3. As the membrane has a small but finite absorption, this limits

the maximally acceptable intra-cavity power and therefore the cavity finesse. In [55] we estimate that ground state cooling in our system in presence of absorption is feasible with a finesse around $F = 1000$. The reflectivity of the second cavity mirror is therefore chosen to create a cavity finesse close to this value (based on equation 1.79).

- For optimal performance of the coupling scheme presented in section 1.3, the cavity linewidth κ must be large compared to the frequency of the membrane, so that information gets exchanged quickly between atoms and membrane. For a given cavity finesse, this means that the cavity must be rather short. A large linewidth also serves the purpose of reducing the importance of laser frequency noise, which we found as a limiting factor to the optomechanical behavior of our first-generation system [55, 98].

- The entire cavity setup should be small enough for potential cryogenic pre-cooling of the membrane.

- The cavity system shall be very stable. Our first-generation cavity-membrane system turned out to be too shaky. The cavity was rather long ($L = 27\,\mathrm{mm}$, see section 2.5 or [111, 98] for more details). Most importantly, the membrane was mounted on a stack of attocube positioners[2] with a resonance frequency in the 100 Hz regime. This made the cavity system extremely sensitive to low frequency vibrations. Any acoustic noise in the lab was visible on the cavity-frequency lock signal. It was only possible to run the experiment with several layers of vibration insulation material around the cavity-membrane setup [111]. Still, slamming drawers and doors made the cavity-frequency stabilization fall out of lock, so that all the data presented in [55] had to be taken late at night. Furthermore, the position of the membrane was drifting by significant fractions of the laser wavelength on the timescale of hours, probably caused by the torque resulting from the gravitational force on the membrane positioned at the end of a lever, see figure 4.1 in [98]. Driven by these inconveniences, the second-generation cavity-setup was designed for maximal stability. This was mostly realized by reducing the length scales and giving up degrees of freedom. As in an atom-membrane coupling experiment the coupling laser frequency is typically set by the atomic ensemble, the cavity needs at least one degree of freedom to adjust the cavity resonance frequency to the laser frequency.

2.2.2 Cavity design and vacuum setup

Figure 2.2 a) and b) illustrates the second-generation cavity setup. The bottom mirror ($r_2^2 = 99.99\%, R = 30\,\mathrm{cm}$) is attached to a titanium ground plate. The membrane is glued[3] to a thin[4] aluminium holder, which is separated from the ground

---

[2]Attocube, ANGp101, ANGt101, ANPz101
[3]UV glue (OG 142), Epoxy Technology
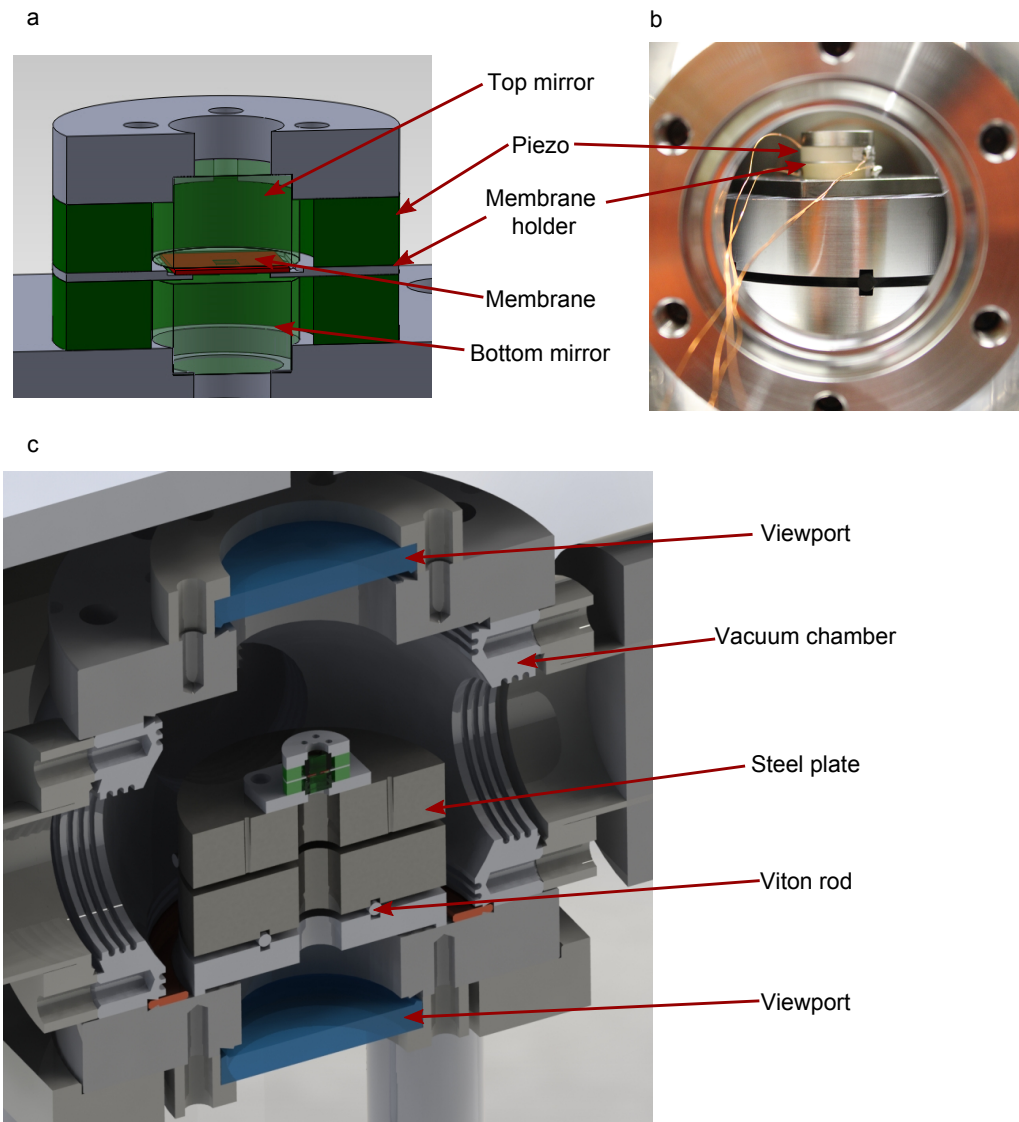[4]Thickness $400\,\mu\mathrm{m}$, $\varnothing 15\,\mathrm{mm}$

Figure 2.2: a) Technical drawing of the cavity system. b) Photograph of the cavity in the vacuum chamber. In the second assembly run the electrical contacts were not soldered on the piezo elements but attached with conducting glue (EJ189, Exopy Technology) as the piezos in the first run potentially had been damaged by the soldering process. c) Technical drawing of the cavity mounting in the vacuum chamber. The cavity is resting on a stack of massive steel cylinders, which are separated by viton rods for vibration insulation. The upper surface is tilted by 2° with respect to the viewports to prevent reflections. The entire block is resting on an aluminum holder, that is attached to the bottom flange of the vacuum chamber.
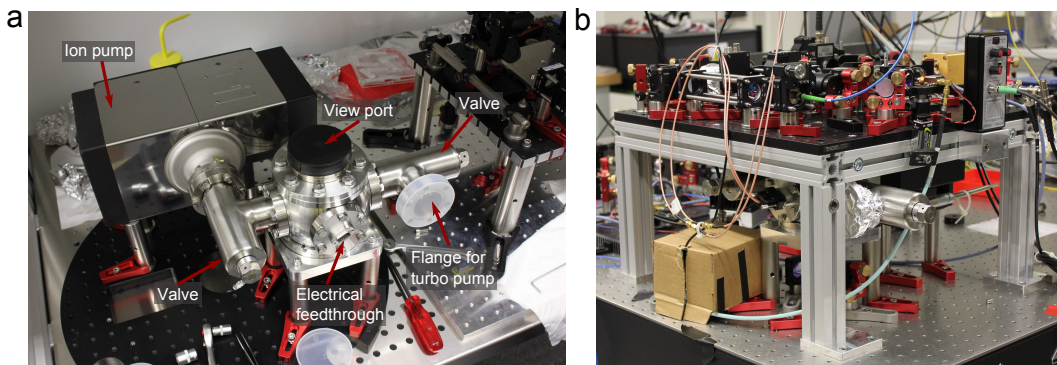
Figure 2.3: a) Vacuum system. The stainless steel chamber (MCF450-SphSq-E2C4, Kimball Physics, produced by Swiss Vacuum) has six ports. AR-coated viewports (CF 40 on CF 63 adapter) are used on the top and bottom port for optical access to the cavity. One of the four ports on the side (CF 40) is used for an electric feed-through to control the piezos, one is blank, one is connected to an ion pump via a valve and the last one is connected to a second valve, which we initially connect to a turbo pump (HiCube 80 Classic, Pfeiffer Vacuum). The vacuum chamber is resting on 10 cm stainless steel feet to provide optical access to the cavity transmission. b) Photograph of the table, carrying the optical setup.

plate by a ring piezo[5] leaving a gap of ≈ 0.5 mm to the bottom mirror. To minimize clamping losses, the membrane is glued only at one edge. A second equal ring piezo on top of the membrane mount carries the top mirror holder[6] and the top mirror ($r_1^2 = 98.54\%, R = 30$ cm) leaving a gap between top mirror and membrane of equal size. The two piezos allow to change the lengths of the two subcavities L_1 and L_2 and with this the total cavity length $L = L_1 + L_2$ as well as the position of the membrane relative to the middle of the cavity $x_\mathrm{m} = (L_1 - L_2)/2$. All components were glued together to maximize the stability of the system[7]. During the gluing procedure the cavity transmission was recorded and the position of the elements fine aligned to achieve a perpendicular alignment of the membrane with respect to the cavity mode. Details on this delicate procedure are given in [110]. As pointed out before, the current cavity is very similar but not identical to the cavity in [110]. In the second assembly run the cavity components were attached via an iris to a mirror holder, which itself was mounted on a three-axis translation stage during the alignment process to improve the precision in positioning. We observe that the incoupling into the cavity has to be re-adjusted whenever one of the piezos is moved. This indicates an imperfect cylindrical symmetry of the cavity system for instance from a residual tilt between the wave fronts of the cavity mode and the membrane.

---

[5]Piezomechanik GmbH, $3\,\mu$m/150V, thickness 3 mm, $\varnothing$15 mm
[6]Titanium, thickness 3 mm, $\varnothing_\mathrm{outer}$15 mm, $\varnothing_\mathrm{inner}$5 mm
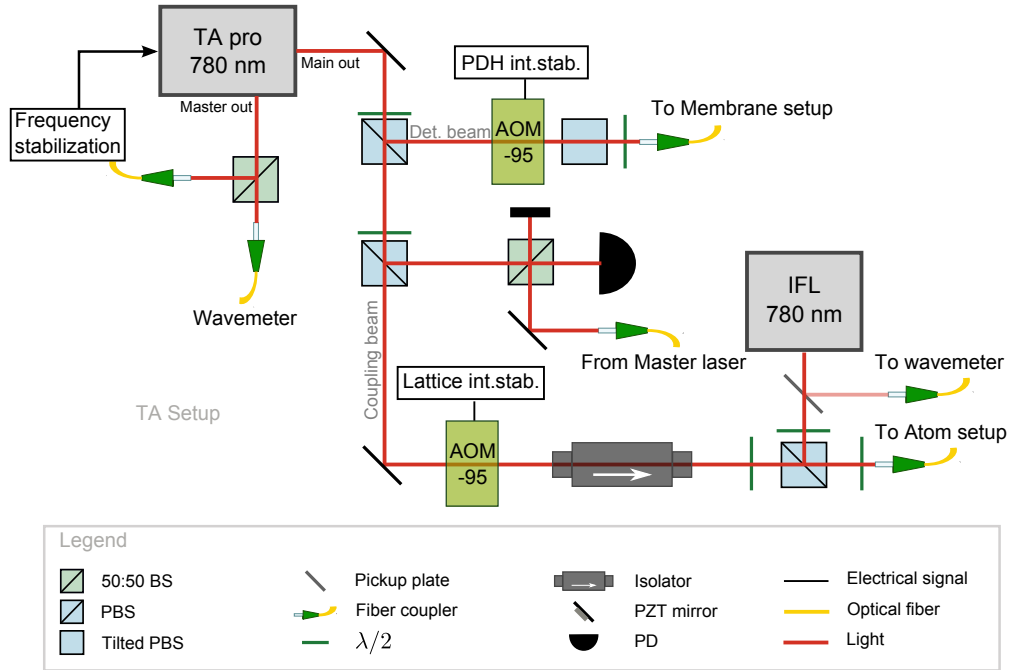[7]Two component epoxy glue, UHU Schnellfest

Figure 2.4: Coupling and detection light preparation setup. Beam shaping elements such as lenses are left away for clarity. AOM: acousto-optic modulator, IFL: interference filter laser, BS: beam splitter, PBS: polarizing beam splitter, PD: photo diode. The green AOM boxes display the rf-frequency in MHz. Further details are given in the text.

Figure 2.2 c) illustrates how the cavity system is mounted inside a vacuum chamber. The entire vacuum system including an ion pump is shown in figure 2.3. Pumping the chamber down from the ambient air pressure with a turbo pump and the ion pump without any baking, we reach a typical pressure of $\approx 10^{-7}$ mbar.

2.3   Optical setup

The following paragraphs introduce the different elements of the optical setup used to interact with the cavity-membrane setup, namely the laser source, the frequency stabilization setup, the detection system and the coupling beam. Except for small modifications the same laser source was used with the first-generation cavity-membrane setup, but the detection system was different. A short summary of the first-generation optical setup will be given in section 4.1.

2.3.1   Light preparation

Two laser beams are required to run the optomechanical system. One couples the membrane to the atomic ensemble. The other one is used to stabilize the cavity to the laser frequency and also to read out the membrane motion. Figure 2.4 shows the optical setup which prepares the two beams. Both beams come from the same 780 nm grating stabilized diode laser[8], which is amplified by a tapered amplifier (TA) within the laser box. Before amplification a fraction of the laser light ($\approx 2\,\mathrm{mW}$) is coupled out of the laser box at the master output. This light is split in two parts. One part is sent to a wavemeter[9] to coarsely determine the atom-laser detuning Δ_{LA}. The other one travels to a frequency stabilization setup, which allows to reduce the laser frequency noise at the membrane frequency by 8 dB acting back on the laser current and piezo. Details on this setup are given in [98], section 4.2.4. The frequency stabilization was in use for the cooling measurements presented in chapter 4 and not in use for the self-oscillation measurements presented in chapter 5.

The main amplified output of the TA ($\approx 1\,\mathrm{W}$) is split into the detection and stabilization beam (from now on referred to as PDH beam) and the coupling beam (sometimes also referred to as lattice beam) at the first polarizing beam splitter cube (PBS). A small fraction of the coupling beam (5 mW) is picked up with a second PBS cube and overlapped with a second laser beam originated from the MOT master laser on a beam splitter (BS). The beat-note signal is recorded on a photodiode[10] (PD). As the MOT master laser is locked to the ^{87}Rb $F = 2 \leftrightarrow F' = 3$ crossover, this allows to measure the detuning Δ_{LA} from the beat signal between the two lasers with a precision much higher than with the wavemeter. The minimal resolution of the wavemeter is 10 MHz and it can drift by about 50 MHz within a few hours. The precision of the detuning measurement via the beat signal is limited only by the small linewidth (100 kHz in $5\,\mu$s [111]) of the diode lasers. Small atom-laser detunings $\Delta_{\mathrm{LA}} < 2\pi \times 1\,\mathrm{GHz}$ are therefore typically adjusted via the beat signal. A lock of the detuning is not required as the laser frequency is stable up to 10 MHz over hours. Both the PDH and the coupling beam powers are stabilized via an acousto-optic modulator[11] (AOM)[12]. The AOMs are driven by the same low noise voltage-controlled oscillator (VCO) and the same deflection order is used to avoid time-dependent interference effects between the two beams inside the cavity. Behind the AOM the lattice beam passes an optical isolator, which protects the laser from lattice back reflections. It is overlapped with a beam from a third laser in the opposite polarization on a PBS cube. This 780 nm laser beam at a slightly different frequency is used as a ruler to mark the membrane position in the cavity as described at the end of section 2.4.1. Finally, all beams are coupled into polarization-maintaining fibers[13].

---

[8]Toptica, TA pro, 1.5 W

[9]WS-7, High Finesse

[10]ZX85-12G-S+, Mini Circuits

[11]Crystal Technology, 3080-120 & 3110-120

[12]See figure 2.6 and table 2.2
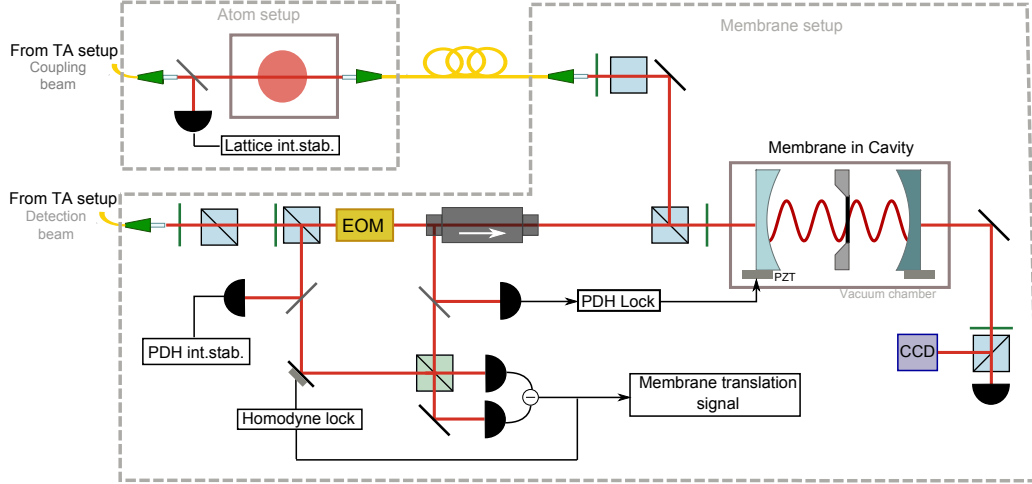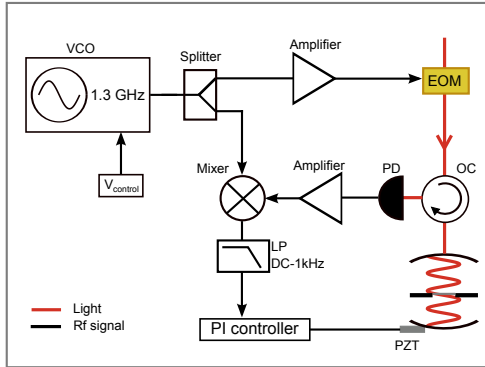
[13]PM780HP, Thorlabs

Figure 2.5: Optics assembly for cavity stabilization, membrane readout and atom-membrane coupling. For a legend see figure 2.4. Details are given in the text.
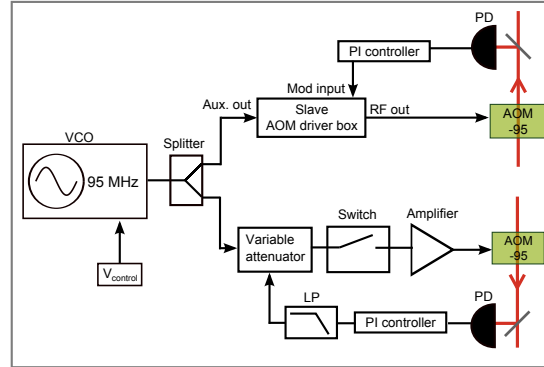

Figure 2.6: a) PDH stabilization rf-setup. VCO: voltage-controlled oscillator, EOM: electro-optic modulator, PD photo diode, LP: low pass filter, OC: optical circulator. We can adjust the phase between the inputs of the mixer by fine tuning the frequency of the VCO by a control voltage. b) Coupling (lower branch) and PDH (upper branch) beam power stabilization rf-setup. AOM: acousto-optic modulator. Part numbers of the electrical components are summarized in table 2.2.

a) Parameter	Value	b) Parameter	Value
VCO	ZX-95-1600W-S+	VCO	ROS-95-419
Splitter	Z-FSC-2-5	Splitter	ZMSC
Amplifier 1	Sat-8 + ZHL 1217 HLN	Variable attenuator	ZAS-3+
EOM	4441 1.3GHz New Focus	Switch	ZASWA-2-50-DR+
PD	ZX85-12G-S+	Amplifier	ZHL-3-5WF+
Amplifier 2	AMF-4F-01200160-04-13P Miteq	PD+PI controller	see [111], section 5.1.2
Mixer	ZEM-4300+	AOM driver box	AOM2-100 (slave mod.)
LP	home built	PD	DET10A/M Thorlabs
PI controller	SIM 960 SRS	PI controller	Noise Eater 3V2 TEM

Table 2.2: Rf-components shown in figure 2.6. a) PDH stabilization. b) Coupling (top) and PDH beam (bottom) power stabilization. If not mentioned otherwise, all components are from Mini Circuit.

2.3.2 PDH-lock

The cavity frequency is stabilized to the laser frequency by Pound-Drever-Hall (PDH) stabilization [105]. In this scheme, optical sidebands, which do not enter the cavity, are modulated onto the carrier light. The phase relation between carrier and sidebands in the reflected light carries information about the deviation between the carrier frequency and the cavity frequency [105]. Demodulated back to DC, this signal can be used to lock the laser-cavity detuning in the range $-\kappa/2 < \Delta < \kappa/2$ around the cavity resonance.

The optics for cavity stabilization and readout of the membrane motion are placed on a small table on top of the vacuum system. Figure 2.3 b) depicts a photograph of this table and figure 2.5 a schematic drawing of the optics assembly. The lower dashed box shows the optics on the little table. Again, beam shaping elements are not shown (see [110] or [111] for details on spatial mode matching into the cavity). The PDH light arrives via a fiber to the left of the dashed box. The beam is split with an aspect ratio of $10 : 1$ into a local oscillator (LO) beam $(1\,\text{mW})$ and the actual PDH beam $(0.1\,\text{mW})$, which probes the cavity. A small fraction is split off the local oscillator beam and sent to a photo diode for intensity stabilization (see figure 2.6). An electro-optic modulator (EOM) modulates the sidebands onto the PDH beam. The beam then enters the cavity, is reflected back and picked up at an optical isolator. A small fraction of this reflected light is picked up and sent to a fast PD to generate the error signal. Figure 2.6 a) shows the electronics of the PDH stabilization circuit. The demodulated error signal [105] is low-pass filtered and sent to a PI controller, which gives feedback to one of the ring piezos of the cavity. The part numbers of the rf components mentioned in this paragraph are summarized in table 2.2. The second ring piezo receives a fixed voltage $(0 - 32\,\text{V})$ from a power supply.

2.3.3 Homodyne detection

In the first-generation cavity setup the membrane motion was detected via the high frequency $(> 100\,\text{kHz})$ part of the PDH error signal, see equation 1.101 and [98], section 4.2.1, or [111], section 6.6. To enhance the signal-to-noise ratio, a balanced

homodyne detection scheme was implemented into the second-generation setup, see equation 1.100. For this, the major part of the cavity backreflection in figure 2.5 is overlapped with the strong LO beam on a 50:50 BS. The outputs of the BS are sent to a balanced PD [14]. One part of the difference signal is low-pass filtered and used to stabilize the phase of the local oscillator via a mirror on a piezo element (PZT). The other part is used to record the membrane signal with a spectrum analyzer[15] or an oscilloscope. Figure 2.12 shows exemplary membrane spectra recorded with the homodyne detection. The signal-to-noise ratio of the peak on the very right is 1000 at a membrane temperature of $\approx 50\,\mathrm{K}$. In a similar measurement taken with the first-generation setup ([98], figure 4.11 a)), the signal to noise ratio was 133 at an even higher membrane temperature of $200\,\mathrm{K}$. Thus, the detection via the strong local oscillator clearly improved the signal-to-noise ratio as expected from equations 1.101 and 1.100.

2.3.4 Coupling and cooling light

The coupling light passes the atomic setup before it enters the cavity system. The upper dashed box in figure 2.5 sketches the relevant optical setup. Before passing the vacuum chamber which contains the atomic ensemble, a part of the coupling beam is picked up for intensity stabilization, see figure 2.6 b). The beam arrives at the membrane setup via a second fiber. The beam is overlapped with the PDH beam at a PBS cube. Thus, coupling and PDH beam are in different polarization modes when they enter the cavity and are split again on the same PBS on their way back. We found that we have to introduce a $\lambda/2$ plate between the PBS and the cavity to suppress back reflections of coupling light into the PDH path. This indicates that the cavity is slightly birefringent. If no atomic ensemble is prepared, the coupling beam can be used for optomechanical cooling experiments, see section 2.4.2.

2.3.5 Cavity transmission

A small amount of light will leak through the highly reflective back mirror of the cavity. We use half of this light to monitor the cavity modes with a CCD camera and the other half to measure the amount of transmitted power with a photodiode, see figure 2.5. This is an important tool to characterize the optical properties of the cavity.

2.4 System characterization and optomechanical performance

In the next two paragraphs the static optical properties and the optomechanical behavior of the second-generation membrane system are characterized before the

---

[14]New Focus, 2107
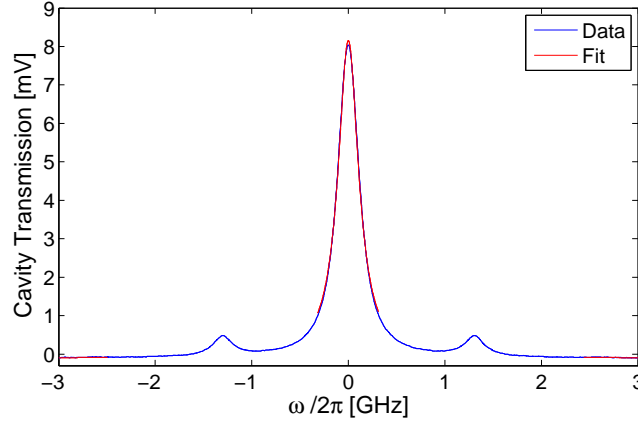[15]FSVR or FSV, Rohde&Schwarz

Figure 2.7: Exemplary cavity transmission signal. The red line shows the result of a Lorentzian fit. The optical sidebands, which are used to calibrate the horizontal axis, are not included into the model. Therefore, the sideband area without the red line is excluded for the fit.

system is compared to the the first-generation setup.

2.4.1 Static optical properties

The optical properties of the membrane cavity system, more precisely the free spectral range ω_{FSR}, the cavity finesse F and the reflectivity of the membrane r_{m} can be determined from the cavity transmission. To measure the free spectral range, the frequency of the laser is tuned over a large range by moving the laser grating until the second next longitudinal mode enters the cavity. The frequency difference between the two modes is measured with the wavemeter to $2\pi \times 330\,\mathrm{GHz}$ resulting in a free spectral range of $\omega_{\mathrm{FSR}} = 2\pi \times 165\,\mathrm{GHz}$. This corresponds to a cavity length of $L = \pi c/\omega_{\mathrm{FSR}} = 0.91\,\mathrm{mm}$, which is close to the design length of $1\,\mathrm{mm}$ meaning that the thickness of the cavity mirror substrates matches the specified value. A measurement of the frequency difference to the second next (n+2) longitudinal mode is necessary as the frequency shift from the membrane of the next longitudinal mode (n+1) has opposite sign (see equation 1.72 and figure 1.4).

To determine the finesse of the cavity, the length of one of the subcavities is scanned over the cavity resonance and the linewidth of the resulting Lorentzian in the transmission of the PDH beam is extracted. The x-axis is calibrated via the known PDH sideband frequency as depicted in an exemplary measurement in figure 2.7. The thinnest FWHM linewidth which we observe is $\kappa = 2\pi \times 232\,\mathrm{MHz}$ corresponding to a maximal finesse of $F = \omega_{\mathrm{FSR}}/\kappa = 711$.

The membrane reflectivity r_{m} and with this the optomechanical coupling strength G can be extracted from a measurement of the transmission spectra in which the lengths of both subcavities L_1 and L_2 are scanned. We can apply voltages between 0
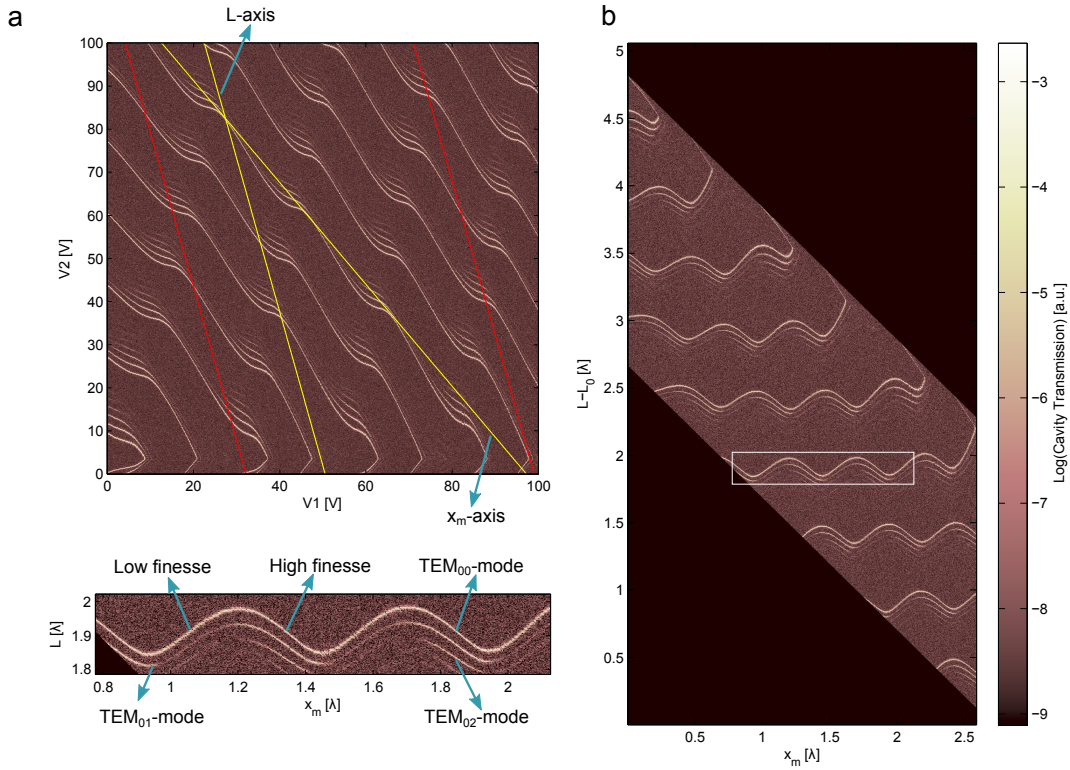
Figure 2.8: Measured cavity transmission spectra. a) Recorded cavity transmission versus the voltages applied to the two ring piezos. The yellow lines indicate the axes along which the membrane position x_m and the cavity length L are varied. b) Data between the red lines in a) in a distorted view, in which the yellow axes from plot a) are perpendicular to each other. $L_0 \approx 0.9\,\mathrm{mm}$ is the macroscopic length of the cavity. c) Zoom into the white box of plot b).
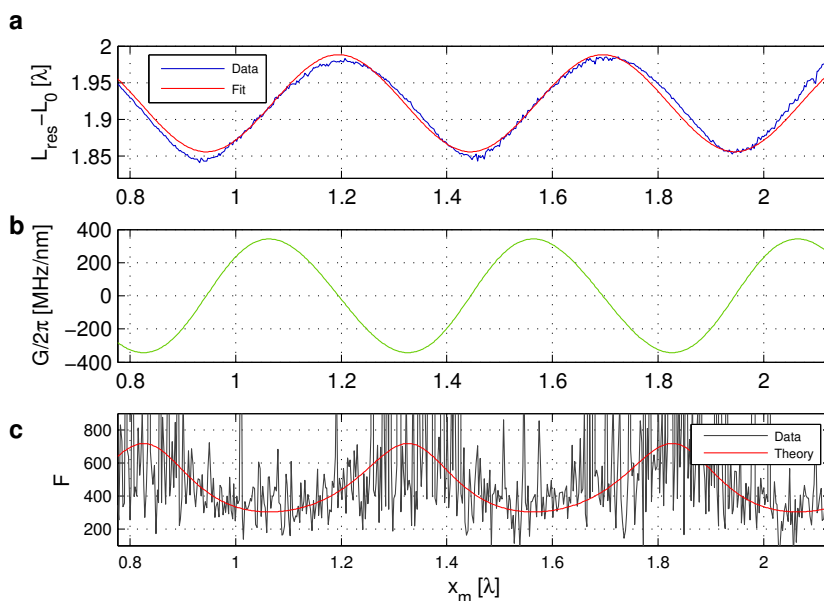
54

Figure 2.9: a) Resonant cavity length extracted from Lorentzian fits to the data in figure 2.8 c) and fit of theoretical expectation 1.71. b) Corresponding coupling strength G from equation 1.73. c) Finesse extracted from the Lorentzian fits and the theoretical expectation 1.79.

and $100\,\mathrm{V}$[16] to the ring piezos corresponding to changes in length of $2\,\mu$m. Figure 1.4 b) and a) in section 1.2 illustrates the expected spectrum as well as the spectrum in which the axes are converted to a change in the total length $L = L_1 + L_2$ and the membrane mostion $x_\mathrm{m} = (L_1 - L_2)/2$. Compared to the theoretical expectation, the measured spectrum in figure 2.8 a) looks very distorted. We suspect the origin of the distortion either in crosstalk between the piezos or in missing cylindrical symmetry of the cavity-membrane system. We also observe that the angle of the ingoing beam has to be re-optimized whenever the piezo voltages are changed. This means that the optical mode in the cavity tilts and suggests that the cavity system is indeed not cylindrically symmetric.

By hand one can find the axes along which the membrane position and the cavity length are varied (yellow lines). If the data is transferred into a coordinate systems in which the two yellow axes are perpendicular to each other, the expected behavior is recovered as shown in figure 2.8 b). From Lorentzian fits to the vertical direction of the spectra in the white box (see equation 1.76), the resonant cavity length and the finesse for varying membrane position can be extracted. Figure 2.9 a) depicts the resonant cavity length versus membrane position together with a fit of formula 1.71, in which the membrane amplitude reflectivity has been fitted to $r_\mathrm{m} = 0.4039(29)$. As expected, this is almost the same value as measured for

---

[16] using HV amplifiers, built in house by electronic workshop, Physics Basel SP908

the membrane in the first-generation setup ($r_{\mathrm{m}} = 0.4148$, see table 2.1), which had the same specified dimension. Using equation 1.64 the membrane thickness corresponding to this reflectivity $d = 39.1\,\mathrm{nm}$ can be determined. Plot b) shows the optomechanical coupling strength $G = \mathrm{d}\omega_{\mathrm{c}}/\mathrm{d}x_{\mathrm{m}}$ (see equation 1.73) corresponding to the fitted reflectivity with maximum value $G_{\max} = 2r_{\mathrm{m}}\omega_{\mathrm{c}}/L = 2\pi \times 342\,\mathrm{MHz/nm}$. Plot c) depicts the dependence of the cavity finesse on the position of the membrane. Due to the coarse resolution of the scan the data quality is very poor. Nevertheless, the theoretically predicted behavior from equation 1.79 is consistent with the data. For the theoretical curve the reflectivity of the input mirror (the only remaining free parameter in formula 1.79) has been set to $r_1^2 = 0.9854$ (slightly higher than the specified value $r_1^2 = 0.98$) to reproduce the maximal finesse of $F = 711$.

The distorted cavity transmission spectra make a reproducible positioning of the membrane difficult, especially on positions of intermediate coupling strength. To simplify this positioning in everyday lab life, we introduced an additional "ruler" laser, depicted in figure 2.4. If a desired membrane position is chosen, the frequency of this laser can be chosen in such a way that it also enters the cavity in the subsequent axial mode. As the frequency separation between successive axial modes in the MIM system depends on the position of the membrane (see figure 2.8, figure 1.4 and equation 1.72), the knowledge about the frequency separation can be used to adjust the desired membrane position again.

2.4.2 Optomechanical behavior

Q-Factor of fundamental mode

In our lab Q-factors of a larger set of membranes are typically determined in a test chamber [111, 131] by means of ringdown measurements, see equation 1.61. The best oscillator is implemented into the main experimental setup. In the test chamber the membranes are already glued to the membrane holder. Roughly one out of ten glued membranes has a Q-factor above 3×10^6. For the fundamental mode of the current membrane a Q-factor of 4.5×10^6 was measured in the test chamber. As the Q-factor might change during the setup of the cavity, for instance by a long-term exposure to ambient air, we check the Q-factor again inside the cavity. As it is technically difficult to run the cavity exactly on resonance with the laser light, small optomechanical damping effects are very hard to avoid. We therefore simply measure the damping rate for a series of ingoing powers P_{in} and extrapolate the linear dependence of $\Gamma_{\mathrm{tot}}(P_{\mathrm{in}}) = \Gamma_{\mathrm{m}} + \Gamma_{\mathrm{opt}}(P_{\mathrm{in}})$ on P_{in} (see equation 1.94) back to the zero power value. The membrane is placed at a position with relatively weak optomechanical coupling during this measurement to improve the sensitivity of the offset measurement. To measure the total damping rate for a given ingoing power, the membrane motion is excited to a large amplitude by a modulation of the voltage on one of the ring piezos. The damping rate is extracted from the ringdown of the membrane amplitude after a sudden stop of this excitation, see equation 1.61. We use the spectrum analyzer in its zero span mode and record the power in a
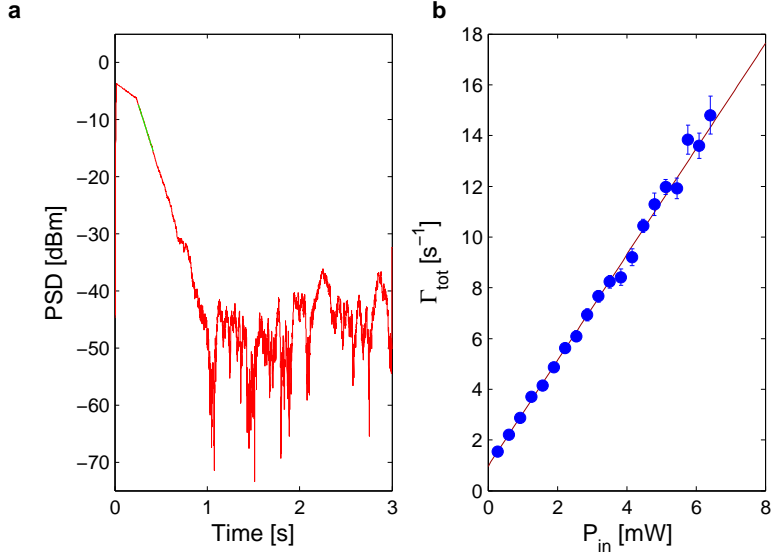
Figure 2.10: a) Exemplary ringdown measurement. The area under the membrane power spectral density S_X is plotted versus time. The membrane motion is excited to a large amplitude. After the stop of the driving, it goes back to the thermal amplitude with rate Γ_{tot}. b) Damping rate $\Gamma_{\text{tot}} = \Gamma_{\text{m}} + \Gamma_{\text{opt}}$ extracted from ringdown measurements versus the ingoing power into the cavity P_{in}.

bandwidth around the membrane frequency versus time to measure the ringdown signal. The bandwidth is chosen large enough to enclose the entire membrane peak ($BW \gg \Gamma_{\text{tot}}$). Figure 2.10 a) depicts an exemplary ringdown signal. Plot 2.10 b) shows the measured total damping rate versus the ingoing power. The offset of a linear fit to the data (red line) yields $\Gamma_{\text{m}} = 0.96(2)\,\text{s}^{-1}$ corresponding to a quality factor of $Q = 1.81(4)$ slightly lower than outside the cavity. The frequency of the fundamental mode also decreased slightly, from $2\pi \times 276.8\,\text{kHz}$ to $2\pi \times 276.3\,\text{kHz}$.

Optomechanical damping and optical spring effect

From the theory of optomechanical coupling we expect to see a power dependent frequency shift, an increased damping rate (equation 1.94) and a corresponding reduction in the mode temperature (equation 1.95). Figure 2.11 summarizes the optomechanical behavior of our MIM system for two mechanical modes, the (1,1)-mode with $\Omega_{\text{m}} = \Omega_{1,1} = 2\pi \times 276.31(1)\,\text{kHz}$ and the (6,6)-mode with $\Omega_{6,6} = 2\pi \times 1657.9\,\text{kHz}$. Unless otherwise noted, membrane properties such as Ω_{m}, Γ_{m} or Q in this thesis refer to the (1,1)-mode. For the measurement the membrane was placed at the location of maximum finesse ($F = 711$) and the laser cavity detuning was set to $\Delta = -0.05\kappa$. Plot a) depicts the damping rate of the 11-mode extracted from ringdown measurements as described above. The slope of the fitted linear dependence 1.96 contains the single-photon optomechanical coupling strength g_0 as only free parameter. The
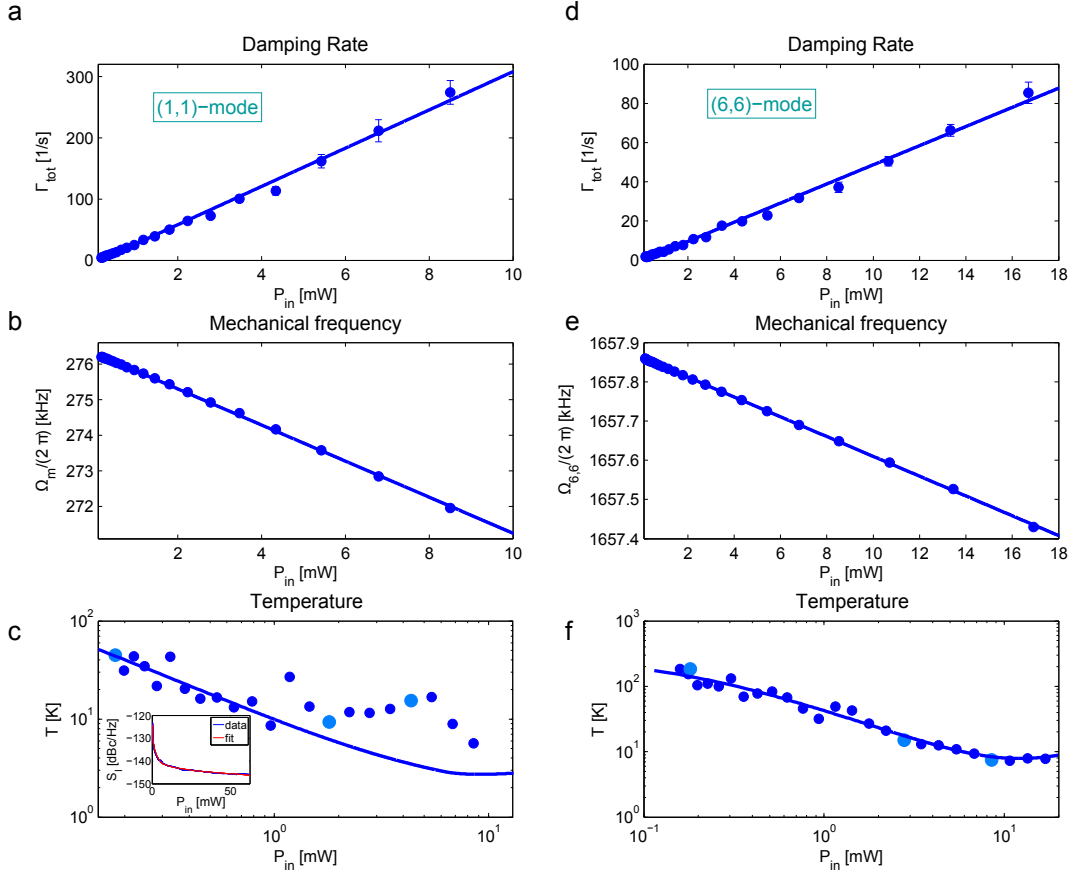
Figure 2.11: Optomechanics of the (1,1)- and (6,6)-modes. a) and d) Damping rate $\Gamma_{\text{tot}} = \Gamma_{\text{m}} + \Gamma_{\text{opt}}$. b) and e) Membrane frequency $\Omega_{\text{m}} = \Omega_{1,1}$ and $\Omega_{6,6}$ respectively. c) and f) Mode temperature T. The inset in plot c) shows the measured laser intensity noise S_{I}. a) - c) (1,1)-mode. d) - f) (6,6)-mode. The light-blue points mark the positions of the exemplary spectra shown in figure 2.12.
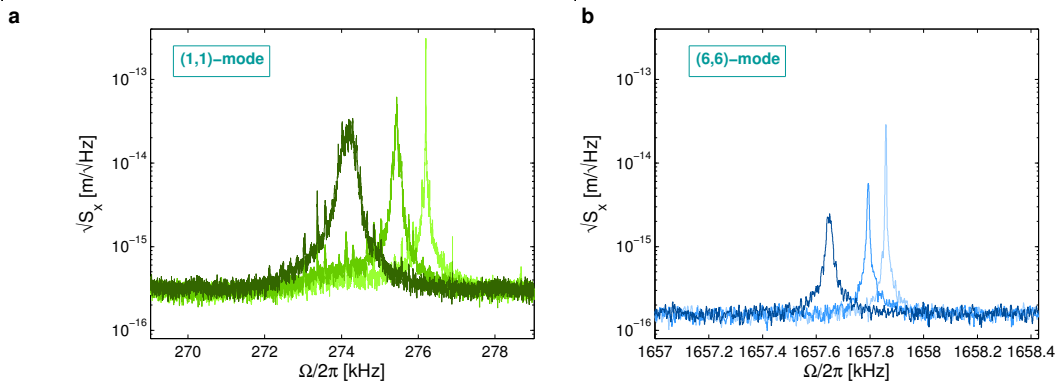

Figure 2.12: Exemplary membrane spectra corresponding to the measurements marked by the light blue dots in figures 2.11 c) and f).
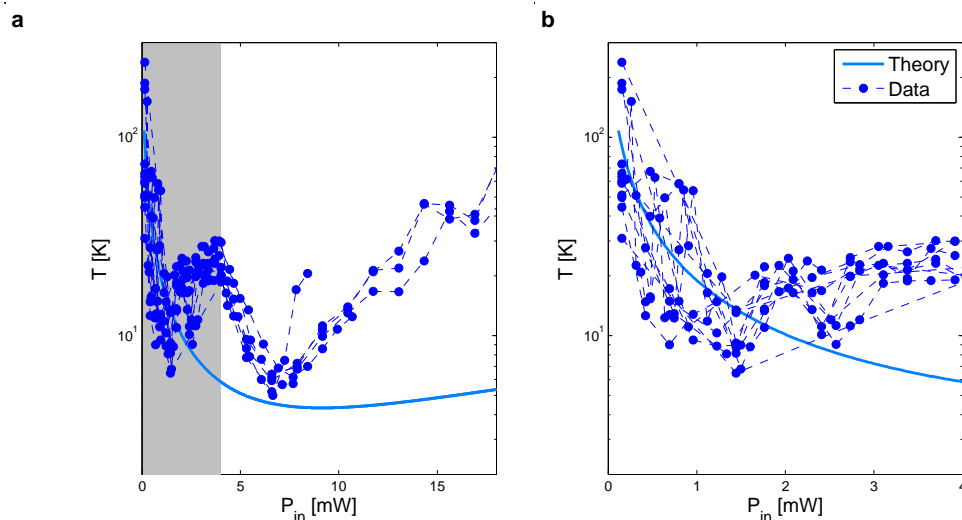
Figure 2.13: Large data collection of optomechanical damping experiments with (1,1)-mode. Plot b) is a zoom into the grey region of plot a). The blue line shows the theoretical expectation.

fit gives a value of $g_0 = 1106(10)\,\mathrm{s}^{-1}$. The data in figure 2.11 b) and c) are extracted from spectrally resolved measurements of the membrane amplitude. Figure 2.12 a) exemplarily shows such spectra for three different powers indicated by the lighter blue data points in figure 2.11 c). Figure 2.11 b) shows the center frequency of the membrane spectrum versus power. The mode frequency displayed above is the offset of a fit of the linear dependence 1.96 to that data. Also here, the fitted slope contains g_0 as only free parameter. I extract $g_0 = 1085(3)\,\mathrm{s}^{-1}$, which is in reasonable agreement with the value from the ringdown measurements. The fact that the frequency shift is even lower than expected from the coupling rate extracted from the damping measurement, indicates that absorption does not play any role in this measurement as it would shift the frequency even further towards low frequencies [114]. I use the average value of the two measurements $g_0 = 1095(5)\,\mathrm{s}^{-1}$ to determine the effective mass of the membrane $M = 117\,\mathrm{ng}$, see section 1.2.1. The discrepancy between M and $M_{\mathrm{phys}}/4 = 60\,\mathrm{ng}$ means that the $60\,\mu\mathrm{m}$ wide cavity mode hits the $1.5\,\mathrm{mm}$ wide membrane $360\,\mu\mathrm{m}$ away from the center, which is very realistic.

The area under the membrane spectrum is proportional to the temperature of the membrane $T = (M\Omega_{\mathrm{m}}^2/k_{\mathrm{B}}) \int_0^\infty S_{\mathrm{x}}(\Omega)d\Omega/2\pi$, see equation 1.59. The measured temperatures are shown in figure 2.11 c) together with the theoretical expectation T_{opt} in presence of independently measured laser intensity noise $S_I(\Omega_{\mathrm{m}})$ shown in the inset and laser frequency noise $S_{\dot{\Phi}}(\Omega_{\mathrm{m}}) = 4\pi^2 \times 256\,\mathrm{Hz}^2/\mathrm{Hz}$ using the equations 1.95 and 1.97. To calibrate the temperature axis, equation 1.103 has been fitted to the first ten data points with the calibration factor c_1 as only free parameter, using the result for g_0 obtained from the fit to the frequency shift to determine c_2. This fit has an uncertainty of 9%. The calibration factor c_1 is also used to calibrate the

spectra in figure 2.12 a). Initially the membrane temperature follows the theoretical expectation. However, for powers larger than $1\,\text{mW}$ the membrane temperature increases occasionally. This is a behavior we repetitively see when laser cooling the (1,1)-mode. Figure 2.13 shows a summary of many damping experiments of this mode. This increase in temperature happens when the optical spring effects takes the membrane signal into a frequency region in which we see certain small spikes on top of the membrane signal in the spectrum as visible in figure 2.12 a). We do not observe any signature of these spikes on the coupling or PDH light. Therefore, we suspect that the spikes originate from electrical noise on the voltages which supply the ring piezos. The piezos slightly shake at the frequencies of the spikes and start to drive the motion of the sensitive membrane whenever the membrane frequency hits the frequency of one of the spikes.

Figure 2.12 shows exemplary spectra of the (6,6)-mode at $\Omega_{6,6} = 2\pi \times 1658\,\text{kHz}$. The noise level at this higher frequency is lower and most importantly no spikes are visible in the spectra. The temperature in figure 2.11 f) follows the theoretical expectation nicely. The temperature has been calibrated in the same way as for the (1,1)-mode with the laser intensity noise $S_I(\Omega_\text{m}) = -139.6(3)\,\text{dBc/Hz}$ as an additional fit parameter. The fitted temperature uncertainty is 7%. Plot d) and e) show the optomechanical damping and the optical spring effect of the (6,6)-mode. From the offset in plot d) one can extract the intrinsic damping rate of the (6,6)-mode $\Gamma_{\text{m},6,6} = 0.81(18)\,\text{s}^{-1}$ and the corresponding Q-factor $Q_{6,6} = 1.28(29) \times 10^7$. The offset of plot e) gives the mode frequency. From the slopes in plot d) and e) single photon coupling rates of $g_0 = 179(1)\,\text{s}^{-1}$ and $242.3(3)\,\text{s}^{-1}$ are derived. The discrepancy is larger than for the (1,1)-mode measurements. It can be explained by an increase of the small laser-cavity detuning from $\Delta = -0.05\kappa$ to $\Delta = -0.09\kappa$ in-between the measurements. This is not unlikely because the cavity was taken out of lock in between measurements, but the detuning was measured only once at the beginning of the day. As the first measurement was temporally much closer to the detuning measurement, I use $g_0 = 179\,\text{s}^{-1}$ to determine the effective mass of the (6,6)-mode $M_{6,6} = 772\,\text{ng}$. The large effective mass shows that we hit the (6,6)-mode much less centered, which is not surprising as the width of the maximum is six times smaller. If the pointing was better, the (6,6)-mode would be the more favorable mode to use in this cavity system due to the large Q-factor and the absence of electronic noise at higher frequencies.

2.5 Comparison with first-generation setup

Table 2.3 displays the optical and optomechanical properties of the first-generation membrane setup. The data are adopted from [98] table 4.1. The properties have been measured in a very similar manner, as presented above. The last column summarizes the corresponding values of the second-generation setup. Comparing the two systems I draw the following conclusions:

- The new cavity is a factor of 29 shorter and has a 2.4 times higher finesse.

Parameter	Value 1st generation setup	Value 2nd generation setup
Cavity length L	26.1(4) mm	0.91 mm
Mirror curvature R	30 mm	30 mm
Mirror reflectivity r_1^2	96.6 %	98.54 %
Mirror reflectivity r_2^2	99.99 %	99.99 %
Mirror diameter	1/4"	1/4"
Free spectral range ω_{FSR}	$2\pi \times 5.75(8)$ GHz	$2\pi \times 165$ GHz
Linewidth (FWHM) κ	$2\pi \times (19...41)$ MHz	$2\pi \times (232...543)$ MHz
Finesse F	140...300	304...711
Coupling strength G_{max}	$2\pi \times 9.75(15)$ MHz/nm	$2\pi \times 342$ MHz/nm
Coupling rate g_0	$28.7\,\mathrm{s}^{-1}$	$1095(5)\,\mathrm{s}^{-1}$

Table 2.3: Summary of MIM system parameters for first-and second-generation cavity setup. The parameters from the first-generation setup are adapted from [98]. The coupling rate g_0 refers to the fundamental mode. The parameters of the membranes themselves are summarized in table 2.1.

This brings it closer to the desired cavity finesse of $F = 1000$ and reduces the influence of laser frequency noise on the membrane motion, which is beneficial.

- The reduced size of the entire MIM system, which now occupies a volume $< (25\,(\mathrm{mm}))^3$ [98], is a large step in the direction of a cryo-compatible cavity system.

- The compact and monolithic design of the new cavity massively improves the passive stability of the system. One can now run the experiment at small cavity detunings $\Delta \approx -0.05\kappa$ without the use of any vibration insulation material. Acoustic noise is not visible on the PDH error signal any more. The cavity stabilization stays in lock even if doors are slammed or if mechanical work is done at the same optical table.

- In order to reduce the mechanical degrees of freedom of the cavity system, the possibility to adjust the angle of the membrane with respect to the cavity mode was removed as well. It is very likely that during the cavity assembly an undesired tilt of the membrane was created, which now creates a strange distortion of the cavity transmission spectra and makes the cavity incoupling efficiency dependent on the membrane position. Even though this does not affect the performance of the system, it causes a lot of inconveniences in characterizing the cavity. One should certainly consider to re-implement this degree of freedom back in the next-generation backup.

- The current limitation to the optomechanical performance of the new cavity system is given by a set of noise peaks visible on the membrane spectrum, which drive the membrane motion whenever the optical spring effect moves the membrane frequency on top of one of the peaks. Most likely, the noise

is on the voltages which supply the cavity ring piezos. During the course of this thesis we were not able to find the exact origin of the noise peaks. If it remains unknown, proper electrical filtering must be implemented in the future to improve the performance of the system.

- Finally, the optical read-out of the cavity system has been improved by the implementation of a homodyne detection scheme with a local oscillator.

Chapter 3

Preparation of cold and dense atomic clouds

This chapter describes and characterizes the atomic side of the hybrid system. In the first part of the chapter I am giving an overview of our cold atom apparatus. The basic building blocks of the setup, namely the vacuum system, the magnetic field coils and the laser system were planned during the PhD thesis of Andreas Jöckel and were set up by him together with me. Many details of these elements are given in Andreas' PhD thesis [98]. I am just summarizing the important aspects here. During this thesis our imaging system was developed further and extended, which I am treating in more detail.

In the second part, I am characterizing two experimental sequences: the standard MOT-molasses sequence, which we used in most of the sympathetic cooling (chapter 4) and self-oscillation (chapter 5) experiments, and a sequence which allows to generate very dense atomic clouds. We use the latter sequence to load a far-detuned dipole trap [132], which will be used as a storage medium in a quantum memory experiment [133, 134] or for future membrane coupling experiments. This sequence is also applied in two of the sympathetic cooling experiments presented in chapter 4.

3.1 ^{87}Rubidium

The experiments in our lab are performed with ^{87}Rb atoms. Rubidium is an alkali metal. A very useful collection of its properties relevant for atomic physics experiments is given in [82]. Rb is a solid at our ambient lab conditions ($T_{\text{lab}} = 22\,^{\circ}$C). As its melting point is only at 39.5°C [82], the vapor pressure at room temperature is relatively high (2.5×10^{-7} mbar [82]). This allows to generate gases with a Rb pressure high enough for optical cooling and trapping without heating the container. Further and even more importantly, as it is an alkali atom, the electronic structure of Rubidium has a closed cycle transition ($|F = 2, m_F = \pm 2\rangle \leftrightarrow |F' = 3, m'_F = \pm 3\rangle$), which is a prerequisite for laser cooling.
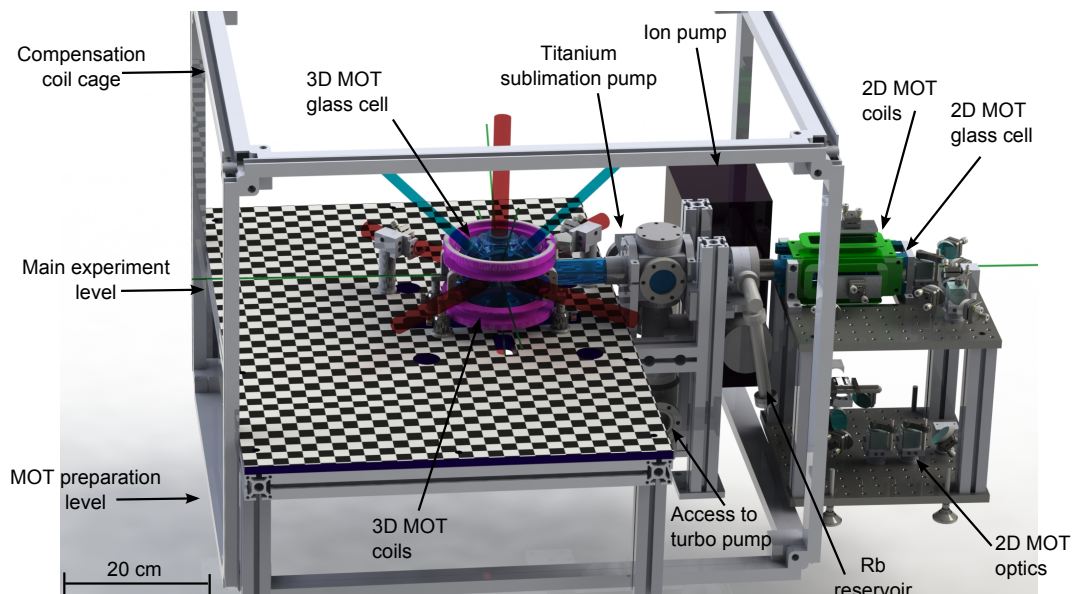
Figure 3.1: Overview of the atomic setup. The schematic shows the vacuum system, the surrounding mechanical construction, the magnetic field coils, the ^{87}Rb reservoir and the ion pump. The titanium sublimation pump is hidden behind the cube which connects the 2D and 3D MOT glass cells. Its position is indicated. The figure is adapted from [98].

3.2   Vacuum system and magnetic fields

Figure 3.1 gives an overview of the mechanical construction of our cold atom apparatus, showing the vacuum system, the magnetic field coils and the mechanical construction, which holds the vacuum system and the optical elements.

We use a two-chamber system consisting of the the main experimental 3D MOT cell[1] and a 2D MOT cell[2] to combine large MOT loading rates with ultra-high vacuum in the main chamber [135, 136, 98]. The two chambers are connected only by a small differential pumping tube [98]. An ion pump[3] and a titanium sublimation pump are connected to the 3D MOT side of the system to maintain the vacuum. The 2D MOT chamber hidden under the green coils on the right side of figure 3.1 contains a macroscopic piece of Rb[4], which fills this chamber with a Rb pressure of about 2×10^{-7} mbar. A pressure gauge[5] on the 3D MOT side placed at the connection piece between the two chambers reads a pressure of $p \approx 10^{-9}$ mbar. The measured lifetime of ≈ 8 s of the atoms in a conservative potential of depth $230\,\mu$K generated by a far-detuned dipole trap [132] is consistent with this pressure [137].

---

[1]Precision Glassblowing, www.precisionglassblowing.com
[2]Precision Glassblowing
[3]Varian/Agilent, VacIon Plus 40 starcell
[4]1 g Rb of natural isotope abundance, Sigma-Aldrich
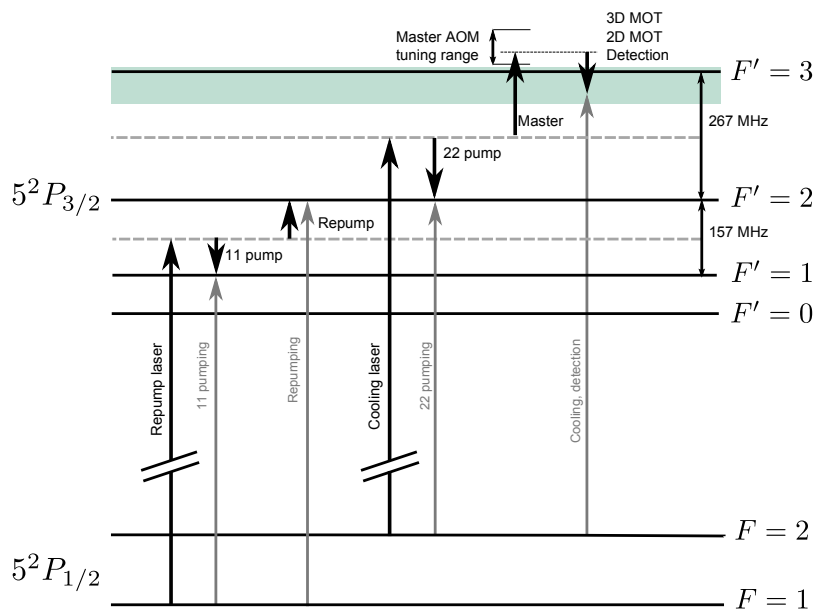[5]Leybold Ionivac IE514 Extractor

Figure 3.2: ^{87}Rb D$_2$-line transitions used for laser cooling, optical pumping and detection. The figure illustrates the frequencies of the repumper and cooling master laser and shows how the different AOMs in the laser system shift the frequencies to the desired transitions. The frequency of the master AOM is tunable over a range of ± 23 MHz allowing the 3D MOT, 2D MOT and detection beams to cover detunings between -11Γ and $+4\Gamma$. All other AOM frequencies are fixed.

To confine the Rb atoms spatially in a MOT, magnetic field gradients are required as discussed in section 1.1.3. Further, the possibility to apply small homogeneous magnetic fields is needed to define quantization axes, induce Zeemann shifts or compensate the earth magnetic field. The magnetic field gradients for the 3D and 2D MOT are generated by sets of Anti-Helmholz pairs (magenta and green structures in figure 3.1). To avoid large currents, the coils are placed close to the vacuum chambers. The 3D MOT coils generate field gradients of 0.66 G/A cm (1.4 G/A cm) along the horizontal (vertical) axis. Short-circuiting the 3D MOT coils over a 200 V Zener diode allows to switch off the gradient in 80 μs, much faster than the turn-off time of tens of ms in absence of the diode. The 2D MOT coils generate 8.7 G/A cm (8.6 G/A cm) along the horizontal (vertical) axis and run permanently.

To enable the generation of small, homogeneous magnetic fields, the entire setup is placed inside a large coil cage consisting of three pairs of Helmholtz coils, see figure 3.1. These compensation coils can generate fields of (0.41, 0.69 0.66) G/A in the three spatial directions with rise times of (1.1, 1.5, 2.2) ms. The current supplies for the compensation fields include PID controllers and allow to actively stabilize the magnetic fields if desired [98].

3.3 Laser system

For laser cooling, manipulating and detecting ^{87}Rb atoms, several laser beams with different frequencies are required. An overview of these frequencies is given in figure 3.2. In our setup two lasers provide cooling and detection light on the $F = 2 \leftrightarrow F' = 3$ transition, repumping light on the $F = 1 \leftrightarrow F' = 2$ transition and pumping light on the $F = 2 \leftrightarrow F' = 2$ and $F = 1 \leftrightarrow F' = 1$ transition. The laser system used to prepare the different beams is based on previous laser systems utilized in our group [138, 139]. Figure 3.3 shows its main components. Beam shaping elements such as lenses are not shown for clarity. Two grating-stabilized diode lasers[6] [140], the cooling master and the repumper laser, are locked using standard Doppler-free saturation spectroscopy [141, 142] to the atomic transition of a Rb vapor. A major fraction of the master laser beam passes an acousto-optic modulator (AOM)[7] in double pass configuration, which enables fast modifications of the cooling and detection light frequency via the experimental control in a range of $+4\Gamma$ to -11Γ detuning around the cycling transition. Subsequently, the master beam is amplified by a slave diode laser[8] [143] and a tapered amplifier chip[9] to 1.1 W.

A series of beam splitters and AOMs distribute and shift the beams as illustrated in figure 3.3 to prepare two beams containing cooling and repumping light for the 2D and 3D MOT, one beam containing repump light only and two beams for detection and pumping. Behind the optical fibers, in total 100 mW (308 mW) are available for cooling and in total 2.2 mW (6 mW) for repumping in the 3D (2D) MOT. Further 4.5 mW are available for detection, 500 μW for 22 pumping and 100 μW for 11 pumping per imaging beam. Mechanical shutters in all beam paths allow to completely switch off the light via the computer control on the timescale of ms. A small fraction of the cooling master light is picked up and coupled to a fiber directly behind the laser output. This light is used to determine precisely the frequency of the coupling lattice laser as described in section 2.3.1.

3.4 Coupling lattice potential

A crucial ingredient for coupling experiments between atoms and membrane is the coupling lattice potential. After our first experiments on sympathetic cooling we changed the cavity-membrane system, which also slightly changed the coupling lattice. In the following I am describing the lattice in the form in which it was used for most of measurements on self-oscillations (chapter 5) and sympathetic cooling (chapter 4). A characterization of the prior lattice used for the first sympathetic cooling experiments in chapter 4 is given in [98], section 3.7.4. I am only summarizing its properties here.

---

[6]homebuilt, output power 25 mW
[7]Crystal Technologies
[8]homebuilt, output power 45 mW
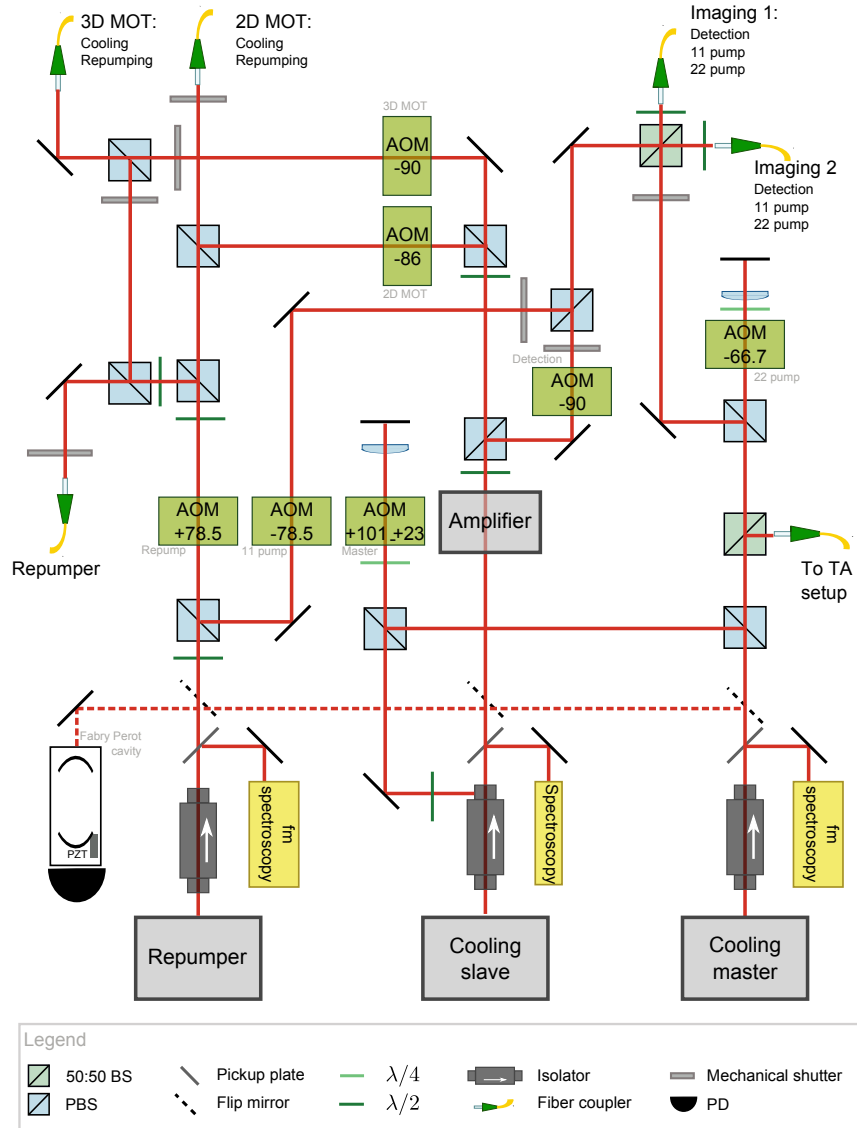[9]Toptica, BoosTA nominally 1.5W output power

Figure 3.3: Laser system for the preparation of cooling, pumping and detection light. The numbers on the AOM boxes display the AOM frequency shift in MHz. A series of pick-up mirrors and a Fabry-Pérot-Cavity with $\nu_{FSR} \approx 750\,\mathrm{MHz}$ allow to check whether the laser are running single mode. Further details are given in the text.
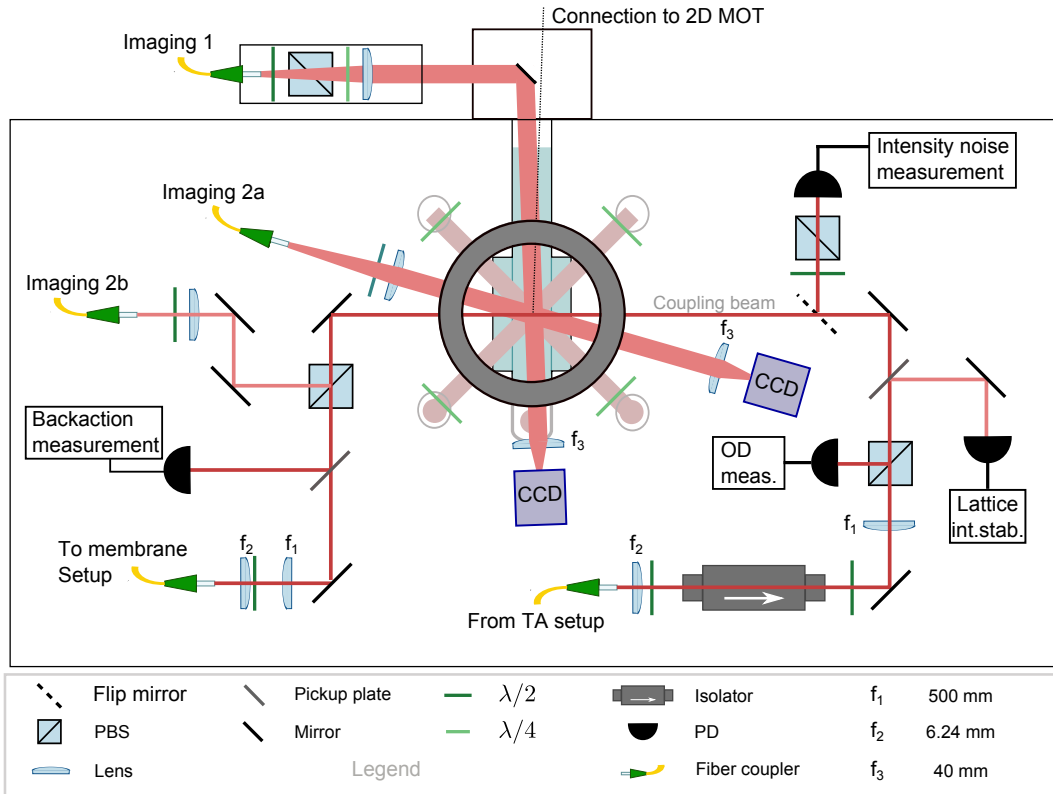
Figure 3.4: The schematic shows the MOT beams (lightest red), the three imaging beams (medium red) and the coupling beam (darkest red). Most beam shaping elements are omitted for clarity. The optical isolator behind the lattice fiber prevents undesired multiple reflections. When taking the second-generation membrane-cavity system into operation, we found that reflections from the $\lambda/2$ plate at the fiber outcoupler drive the membrane motion via delayed feedback (see chapter 5). Before entering the chamber, the polarization of the lattice light is cleaned by a PBS cube and a small fraction of the light is picked up for intensity stabilization as described in section 2.3.4 and illustrated in the figures 2.4 and 2.6. The light from the second imaging fiber is either used in the *Imaging 2a* or *2b* path.

The 780 nm diode laser, which provides the lattice light, and the initial preparation of the coupling lattice beam were presented in section 2.3.1. The beam is brought to the atomic system via a fiber as depicted in figure 3.4. It is focused down to $w_0 = 280\,\mu$m ($1/e^2$ radius) at the position of the atoms. We measure an intensity transmission through the glass cell of $t^2_{\text{cell}} = 0.95$. Behind the cell, the beam is collimated and coupled into a fiber which transports the light to the membrane cavity system, see figure 2.5. Typically, $R = 30\%$ of the power is reflected back to the atoms by the membrane-cavity system, resulting in a single-path amplitude transmission of $t = \sqrt[4]{R} = 0.74$, if the coupling efficiency to the cavity is good $\eta \approx 1$. This value varies slightly from day to day. Good mode-matching between the ingoing and the reflected beam is guaranteed by the use of the fiber.

The lattice laser is detuned by Δ_{LA} from the $|F = 2, m_F = 2\rangle \leftrightarrow |F' = 3, m'_F = 3\rangle$ transition of the ^{87}Rb D$_2$ line. Therefore it forms a potential for the atoms, in which they oscillate with an axial center frequency of $\Omega_{\text{a}}(0) = \epsilon\sqrt[4]{R}\sqrt{P_0/|\Delta_{\text{LA}}|}$ (see eqaution 1.22). The parameter ϵ can be determined from sympathetic cooling experiments using the fact that the axial atomic frequency equals the membrane frequency $(\Omega_{\text{a}}(0) = \Omega_{\text{m}})$ at the minimal power at which sympathetic cooling occurs. This connection will be discussed in section 4.3. Using the sympathetic cooling measurement presented in section 5.5.2 (figure 5.19) I find $\epsilon = 2\pi \times (7.75 \pm 0.65) \times 10^{11}\,Hz^{3/2}W^{-1/2}$, which agrees very well with the expected value of $\epsilon = 2\pi \times (7.5) \times 10^{11}\,Hz^{3/2}W^{-1/2}$ from the model presented in section 1.1.4 equation 1.22.

The prior optical lattice used for the initial sympathetic cooling experiments (chapter 4) was not transferred to the first cavity-membrane setup via a fiber but propagating in free space, see [98] figure 4.2. This resulted in a slightly higher power reflectivity $R = 0.51$ but a deformed mode shape of the backreflected beam ($w_x^{\text{in}} = 287\,\mu$m, $w_y^{\text{in}} = 282\,\mu$m, $w_x^{\text{re}} = 265\,\mu$m, $w_y^{\text{re}} = 301\,\mu$m). To a good approximation, the trapping frequencies in this case can be calculated from the mean width of the incoming and reflected beam $w_0 = 284\,\mu$m. Also for this lattice, the calculated value $\epsilon = 2\pi \times (7.4) \times 10^{11}\,Hz^{3/2}W^{-1/2}$ is in reasonable agreement with the calibrated value of $\epsilon = 2\pi \times (6.3 \pm 0.1) \times 10^{11}\,Hz^{3/2}W^{-1/2}$, which in this case was determined in a parametric heating experiment [98].

We load the optical lattice simply by overlapping it with the MOT. As the atom-laser detunings we use are rather small ($\Delta_{\text{LA}} = 2\pi(1-8)\,$GHz for the experiments in chapter 4 and $\Delta_{\text{LA}} = 2\pi(0.5-3)\,$GHz in chapter 5) the scattering rates introduced in equation 1.23 are large and limit the lifetime of the atoms in the lattice potential to a few tens of ms according to equation 1.24 ($t_{\text{LT}} = 52(10)\,$ms for $P_0 = 7.8(1.6)\,$mW, $\Delta_{\text{LA}} = 2\pi \times 5(1)\,$GHz, $R = 0.3$ corresponding to $\Omega_{\text{a}}(0) = \Omega_{\text{m}}$). To compensate for the losses, the large laser-cooled cloud (either in MOT or molasses configuration) is overlapped with the lattice potential also during the coupling experiments. This provides permanent refilling of the trap but makes it extremely difficult to determine the exact properties, especially temperature and density, of the atoms in the lattice volume. For the molasses configuration we found that one can explain the coupling experiments very well if it is assumed that temperature and density of the atoms in the lattice volume are not significantly influenced by the lattice potential but given

by the bare temperature and density of the molasses (see chapter 4).

3.5 Absorption imaging of dense atomic clouds

The optical depth of the atomic ensemble, the number of atoms, their spatial distribution and temperature are measured using absorption imaging [90]. If the atoms are illuminated by resonant laser light, they will scatter a fraction of the light out of the beam, which can be detected by a camera. The shape of this shadow gives information about the spatial distribution of the atoms and the amount of scattered photons about the optical depth. If the scattering cross section is known, the number of atoms can be calculated from the camera images. In this section I will present our imaging system and describe the principle of absorption imaging of dense atomic clouds.

3.5.1 Main imaging system

Figure 3.4 illustrates our imaging system. It allows to observe the cloud from two different sides. The primary imaging beam (*Imaging 1*) probes the atoms perpendicularly to the coupling lattice direction. The light from the laser system shown in figure 3.3 arrives via a fiber at a small bread board mounted on top of the titanium sublitation pump. The polarization of the light is cleaned by a PBS before a $\lambda/4$ plate turns it into circular polarization. A planoconvex lens creates a slightly diverging beam, which has a $1/e^2$-radius of $w_{I1} = 6.88$ mm at the position of the atoms. A 1/2" mirror inside the vacuum system directs the light towards the atoms. Behind the vacuum chamber, a $f_3 = 40$ mm achromatic lens images the plane at which the atoms are located onto a CCD camera[10]. We use this imaging axis to investigate the axial distribution of the atoms in the coupling lattice and also to determine the properties of the entire laser cooled cloud quantitatively as the CCD camera has a large camera chip (see table 3.1 for technical details on the cameras).

The second imaging beam (*Imaging 2a*) propagates with an angle of 22° to the coupling lattice direction. A second $f_4 = 40$ mm achromatic lens images the atoms onto a second CCD camera[11] with a smaller chip. We mostly use this imaging axis to align the coupling lattice to the center of the MOT.

During the imaging sequence a small magnetic field $(1\,G)$ is applied along the propagation axis of the respective imaging beam using the compensation coils (see figure 3.1) to set a quantization axis. Thus, the imaging light has either σ_+ or σ_- polarization with respect to the quantization axis, and the atoms will scatter light on the $|F = 2, m_F = \pm 2\rangle \leftrightarrow |F' = 3, m_F' = \pm 3\rangle$ cycling transition. The imaging usually takes place after a certain time of flight (TOF) period, in which all trapping and cooling light is switched off, see section 1.1.5. During TOF and imaging the

---

[10]AVT Manta G-145B MOD RCG
[11]AVT Guppy Pro F-031B

Parameter	Manta	Guppy
Number of pixels	1388×1388	656×492
Pixel area A_{px}	$6.45 \times 6.45\,\mu\mathrm{m}^2$	$5.6 \times 5.6\,\mu\mathrm{m}^2$
Quantum efficiency QE	0.17	0.3
Gain G_e	$3.7/e^-$	$4.1/e^-$
Well capacity	$17000\,e^-$	$16000\,e^-$
ND filter transmission t_{ND}	0.17	0.17
Magnification M	0.39775	0.3726
Imaging intensity	$\approx 0.2\,I_{\mathrm{sat}}$	$\approx 0.2\,I_{\mathrm{sat}}$
Field of view	$22.5 \times 16.8\,\mathrm{mm}^2$	$9.9 \times 7.4\,\mathrm{mm}^2$
Resolution	$14\,\mu\mathrm{m}$	$14\,\mu\mathrm{m}$
Typical imaging pulse length	$100\,\mu\mathrm{s}$	$100\,\mu\mathrm{s}$

Table 3.1: Parameters of the CCD cameras (top) and the imaging optics (bottom) for primary (left) and secondary imaging system. All parameters besides pixel area and number of pixels have been measured in our lab. For details on the measurement of the camera parameters see [98], section 3.5.

repump beams are turned on to prepare the atoms in the $F = 2$ hyperfine state and keep them on the cycling transition.

3.5.2 Imaging along the coupling lattice

During the course of this thesis a major challenge was to determine the properties of the atoms in the coupling lattice when they are surrounded by the large laser-cooled atomic cloud. Therefore a third imaging beam (*Imaging 2b* in figure 3.4) spatially mode-matched with the coupling lattice beam was implemented. The beam is overlapped with the optical lattice at a PBS, separated off at the subsequent PBS on the other side of the vacuum chamber and sent to a photodiode. The beam has a waist of $w_{\mathrm{I2b}} = 305\,\mu\mathrm{m}$ at the position of the atoms, which is only slightly larger than the waist of the coupling lattice beam ($w_0 = 280\,\mu\mathrm{m}$). The detection with the PD gives information about the amount of light the atoms scatter out of the beam integrated over the entire probe beam area. Note that the polarization of this imaging beam is a mixture of σ_+ and σ_- light with respect to the quantization axis along the direction of propagation of the beam. The scattering cross section will therefore deviate from the two-level value σ_0 of the cycling transition [82]. A quantized determination of atom numbers in this situation is difficult because optical pumping redistributes atoms among different m_{F}-levels. One can roughly calibrate the effective scattering cross section as I will describe in chapter 3.5.4. However, the signal can be used to compare the number of atoms in the lattice volume in different experimental situations.

3.5.3 Principle of absorption imaging

The amplitude and the phase of light can be altered if it propagates through a medium with refractive index n_{ref}. For a gas of atoms with number density n the refractive index is connected via $n_{\mathrm{ref}} = \sqrt{1 + n\alpha/\epsilon_0}$ [144] to the atomic polarizability α introduced in equation 1.8. We image on the $|F = 2, m_F = 2\rangle \leftrightarrow |F' = 3, m'_F = 3\rangle$ transition of the ^{87}Rb D$_2$-line, which is a closed cycle transition and can therefore be described as a two-level system. For small polarizabilities $\alpha \ll 1$ the refractive index can be written as [90]

$$n_{\mathrm{ref}} = 1 + \frac{n\lambda\sigma_0}{4\pi}\left(\frac{i - \delta}{1 + \delta^2 + \frac{I}{I_{\mathrm{sat}}}}\right), \tag{3.1}$$

where $\delta = 2\Delta_{\mathrm{LA}}/\Gamma$ is the detuning from the atomic transition in units of half linewidths, $\sigma_0 = 3\lambda^2/2\pi = 2.9 \times 10^{-13}\mathrm{m}^2$ the resonant scattering cross section of the cycling transition [82] and $I_{\mathrm{sat}} = \hbar\omega\Gamma/2\sigma_0 = 1.67\,\mathrm{mW/cm}^2$ the saturation intensity of the transition [82].

As we already saw in section 1.1.6, the imaginary part of n_{ref} is responsible for the absorption of light and the real part of n_{ref} describes the dispersive behavior. Applying Maxwell's equations (see section 1.1.6) to a thin slice of polarizable matter of density n, one can derive the reduction of a beam intensity dI after propagation through a distance dx in the medium [90, 144]

$$\begin{aligned} dI &= -2k\,\mathrm{Im}\,n_{\mathrm{ref}}\,I dx \\ &= -\frac{\sigma_0}{1 + (2\Delta_{\mathrm{LA}}/\Gamma)^2 + I/I_{\mathrm{sat}}}I\,n(x)\mathrm{d}x, \end{aligned} \tag{3.2}$$

where $n(x)$ is the atomic density at position x. Note that this equals equation 1.11, which we found by simple arguments about the scattering of laser light. Furthermore, one finds that the phase of the light behind the slice differs from the phase it would have in absence of the medium by

$$\begin{aligned} d\psi &= 2\pi(\mathrm{Re}\,n_{\mathrm{ref}} - 1)\frac{\mathrm{d}x}{\lambda} \\ &= \frac{(2\Delta_{\mathrm{LA}}/\Gamma)}{2}\frac{\sigma_0}{1 + (2\Delta_{\mathrm{LA}}/\Gamma)^2 + I/I_{\mathrm{sat}}}n(x)\mathrm{d}x. \end{aligned} \tag{3.3}$$

Our imaging system relies on the detection of the intensity reduction by a camera. In principle the phase shift can be also used for imaging [90].

Separating the x and I dependent terms in equation 3.2 and integrating over the atomic ensemble along the x direction gives the atomic area density

$$\frac{\mathrm{d}N}{\mathrm{d}A} \equiv \int_d n(x)\mathrm{d}x = -\int_{I_0}^{I_1}\frac{1 + (2\Delta_{\mathrm{LA}}/\Gamma)^2 + I/I_{\mathrm{sat}}}{\sigma_0\,I}\mathrm{d}I. \tag{3.4}$$

Here $I_0(I_1)$ is the intensity in front of (behind) the atomic ensemble and d the length of the ensemble. One can easily access these intensities by taking two images, one

with and one without atoms. This allows us to determine the area density on a pixel-by-pixel basis.

If the laser polarization deviates from circular or if the atoms are not in the $|F = 2, m_F = 2\rangle$ state during the entire imaging pulse, they also scatter light on transitions with lower dipole matrix elements than the cycling transition. As a consequence the average scattering cross section is reduced and the average saturation intensity increased [82]. Effective parameters $\sigma_{\text{eff}} = \sigma_0/\alpha$ and $I_{\text{sat,eff}} = I_{\text{sat}}\alpha$ are used to account for this. The correction factor α has a minimal value of one if the imaging light is scattered perfectly on the cycling transition.

Inserting these modifications into equation 3.4 and integrating it over the intensity, one finds

$$
\begin{aligned}
\frac{\mathrm{d}N}{\mathrm{d}A} &= \frac{\alpha}{\sigma_0}(1 + 4(\Delta/\Gamma)^2)\ln\left(\frac{I_0}{I_1}\right) + \frac{1}{\sigma_0}\frac{I_0 - I_1}{I_{\text{sat}}} \\
&= (1 + 4(\Delta/\Gamma)^2)\left[\frac{\alpha}{\sigma_0}\ln\left(\frac{I_0}{I_1}\right) + \frac{1}{\sigma_0}\frac{I_0 - I_1}{I_{\text{sat},\Delta}}\right],
\end{aligned}
\tag{3.5}
$$

where the detuned saturation intensity is defined as $I_{\text{sat},\Delta} = (1 + 4(\Delta/\Gamma)^2)I_{\text{sat}}$.

From the atomic area density one can easily calculate the atom number by multiplying it with the pixel area at the atomic position and summing over all pixels

$$
N = \sum_{\text{all pixels}} \frac{A_{\text{px}}}{M}\frac{\mathrm{d}N}{\mathrm{d}A}.
\tag{3.6}
$$

Here A_{px} is the area of a pixel on the camera and M the magnification of the imaging system.

The first term in equation 3.5 depends only on the ratio between the camera counts in absence and in presence of atoms. To determine the second term correctly, the absolute intensities I_0 and I_1 must be known. Thus, the transmission of all the elements between the atoms and camera, the camera quantum gain and the imaging pulse length must be calibrated. The intensity can then be calculated from the camera counts via

$$
I_{0(1)} = \frac{\hbar\omega_0 M N_{\text{cam},0(1)}}{G_e t_{\text{ND}} QE dt_{\text{probe}} A_{\text{px}}},
\tag{3.7}
$$

where $N_{\text{cam},0(1)}$ is the number of counts on the camera, t_{ND} the transmission of potential neutral density (ND) filters in front of the camera, G_e an internal camera gain factor, QE the quantum efficiency of the camera and dt_{probe} the length of the imaging pulse. All these parameters are listed in table 3.1.

To reduce the importance of calibration uncertainties we typically image with low intensities $I_0 \ll I_{\text{sat},\Delta_{\text{LA}}}$. Then the polarizability of the atoms becomes independent of intensity and the last term in equation 3.5 vanishes. The intensity behind the atomic ensemble can then be written as

$$
I_1 = I_0 e^{-OD},
\tag{3.8}
$$

with optical depth

$$OD = \ln\left(\frac{I_0}{I_1}\right) = \frac{\sigma_0/\alpha}{1+(2\Delta_{\text{LA}}/\Gamma)^2}\int_d n(x)\mathrm{d}x$$
$$= \frac{OD_{\text{res}}}{1+(2\Delta_{\text{LA}}/\Gamma)^2}, \tag{3.9}$$

where $OD_{\text{res}} = (\sigma_0/\alpha)\int_d n(x)\mathrm{d}x$ is the optical depth for resonant light, which was already introduced in section 1.1.2. In this low-saturation limit the phase shift in the medium given by equation 3.3 becomes

$$\psi = \frac{(2\Delta_{\text{LA}}/\Gamma)}{2}OD. \tag{3.10}$$

3.5.4 Calibration of α

When imaging with low intensities ($I \ll I_{\text{sat},\Delta}$), the second term in equation 3.5 can be neglected as mentioned above. For $I = I_{\text{sat},\Delta}$ both terms are equal, and for very large intensities the second term dominates. Note that the parameter α affects only the first term of the area density in equation 3.5. In the second term it cancels. The parameter α can thus be determined by imaging a cloud of fixed atom number with varying intensity.

Figure 3.5 a) shows the results of an intensity variation experiment for the primary imaging axis (*Imaging 1* in figure 3.4). A dilute atomic cloud ($OD_{\text{res}} < 1$) is imaged with resonant laser light ($\Delta_{\text{LA}} = 0$) for different powers in the detection beam. The plot shows the total atom number N and the contributions from the first $N_{1.\text{Term}}$ and second term $N_{2.\text{Term}}$ in equation 3.5 versus the intensity of the detection beam. The sum $N_{1.\text{Term}} + N_{1.\text{Term}} = N$ is independent of intensity, meaning that $\alpha_{\text{I1}} = 1 \pm 0.1$. The atoms mostly scatter light on the cycling transition as desired. The error is determined from the scattering of the data points. It gives a systematic uncertainty of 10% in our atom number determination.

As mentioned above, the polarization of the imaging beam along the lattice direction (*Imaging 2b* in figure 3.4) is not adapted to the cycling transition. The corresponding higher value of α_{I2b} can be determined by comparing the optical depths which the *Imaging1* and the *Imaging2b* systems measure when a spherically symmetric cloud as illustrated in figure 3.5 c) is imaged. I find $\alpha_{\text{I2b}} = 1.4 \pm 0.1$.

3.5.5 Imaging very dense clouds

In principle, the theory presented above allows imaging of a medium of arbitrary optical depth with resonant light. In practice, however, there is a minimal intensity level our camera can detect due to the noise level of the camera. Furthermore, in very optically dense clouds multiscattering events will happen, which is not taken into account in our simple model. Both effects modify the detected optical depth and atom number. To circumvent this, we image dense clouds with detuned laser
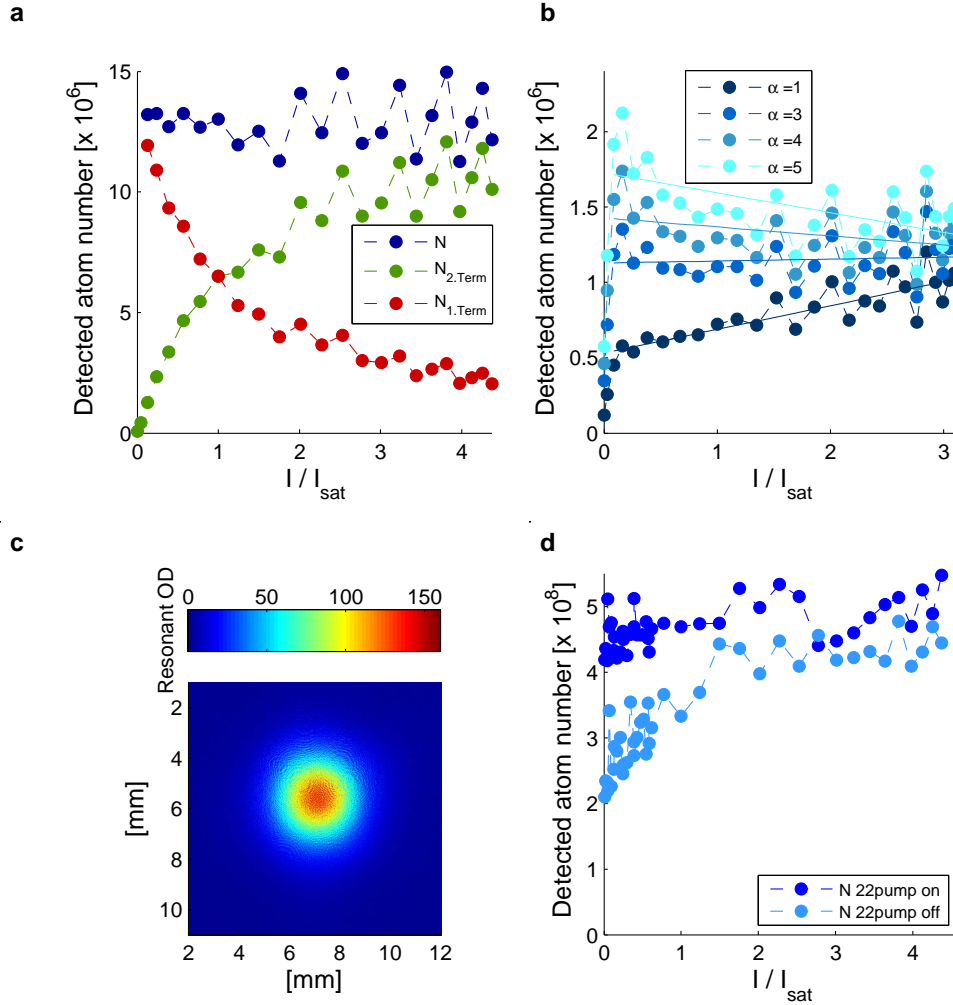
Figure 3.5: a) Total atom number N detected by the *Imaging 1* imaging system and calculated by equation 3.6 and the contributions to N from the first and second term in equation 3.5 as a function of imaging intensity. A dilute cloud was imaged on resonance. b) Similar data recorded with imaging beam with mixed polarization. The total detected atom number N is shown for several values of the correction value α. The lines are guides to the eye. c) Resonant optical depth of the symmetric cloud used to calibrate α of the *Imaging 2b* axis. d) Imaging of an optically dense cloud ($OD_{\mathrm{res}} \approx 70$) with a detuning of $\Delta_{\mathrm{LA}} = -4\Gamma$. The plot shows the atom number detected with the *Imaging 1* imaging system and calculated with equation 3.6 as a function of imaging intensity in absence (light blue) and presence (dark blue) of the pumping pulse.

light ($|\Delta_{\text{LA}}| > 0$, e.g. $\Delta_{\text{LA}} = -6\Gamma$ for $OD_{\text{res}} \approx 100$), so that the measured optical depth $OD = \ln(I_0/I_1)$ becomes smaller than one. Note that there is a finite phase shift $\psi = (\Delta_{\text{LA}}/\Gamma)OD$ for non-zero detunings. The atoms will then act like a lens and refract some light out of the beam. For clouds of large diameter $d \gg \lambda$ as in our case, the refraction angle $2\psi\lambda/(\pi d)$ [90] is still very small, so that all the light is collected by the imaging objects and the atom number is not altered.

When the measured optical depth of a dense atomic ensemble is small, the number of photons scattered per atom is low. However, a few photons (≈ 5 according to simulations done in [139]) need to be scattered to pump the atoms into the cycling transition. If the atoms do not spend most of the imaging time on the cycling transition, the number of detected atoms, which is calculated assuming that the atom scatters all light on the cycling transition ($\alpha = 1$), decreases as depicted in the light blue curve of figure 3.5 d). To account for this problem, without recalibrating α every time we change the imaging intensity or the detuning, we implemented a short 2-2-pumping sequence before the imaging pulse. The 2-2 pumping light pumps the atoms into the desired $|F = 2, m_F = \pm 2\rangle$ state. As this state is a dark state for the pumping light, the pumping pulse can be resonant, short and weak. To account for depumping of the $F = 2$ state by the 2-2 pumper the repump beam is also present during the pumping sequence. The dark blue curve in figure 3.5 d) illustrates how the pumping corrects the detected atom number at low imaging intensities. The average value of the corrected atom number is $N = 4.7 \times 10^8$, the standard deviation is $\Delta N = 3.4 \times 10^7$ corresponding to an uncertainty of 7%. This statistical error characterizes the overall reproducibility of the MOT preparation.

3.6 Experimental control

During each experimental cycle we need to adjust laser parameters and magnetic fields on ms timescales. To perform this, we use a software called *Goodtime* written in the 1990s by Jakob Reichel and developed further by Pascal Böhi [145] and Caspar Ockeloen [146]. It is a C based program that allows us to write script based control sequences. These get complied and are sent to four National instrument (NI) cards[12] which give out digital and analog output signals in separate channels. Each NI card has 48 digital TTL channels, which we use as trigger and switching signals. Furthermore each card has 16 analog (16Bit) and 32 analog (13Bit) channels with $\pm 10\,\text{V}$ output, which we use as control voltages for rf-signal frequencies and amplitudes, as set-points in intensity control circuits or to control the magnetic fields. *Goodtime* also allows us to send settings to devices such as the spectrum analyzer, function generators or the lock-in amplifier, which are connected to the main lab computer via GPIB bus, Ethernet(VISA) or USB [146]. The storage capacity of the NI cards currently limits our timing resolution of $25\,\mu\text{s}$. The major tools for diagnostics on the atomic side are the cameras for absorption imaging. For optimization, debugging and implementations of new experimental sequences, it is essential to have a

---

[12]NI 6535, 2x NI 6733, NI 6723

Parameter	3D MOT	Molasses	2D MOT
Cooling Intensity/I_{sat}	17(8)	17(8)	19.6(11.4)
Detuning/Γ	$-3.5(-3.1)$	$-11(-11)$	-3.1(-2.7)
Repump Intensity/$I_{\text{sat,rep}}$	0.19(0.1)	0.19(0.1)	0.19(0.18)
B-field gradient [G/cm]	24(11)	0(0)	20(20)

Table 3.2: 3D MOT, 2D MOT and molasses parameters for optimized MOT and molasses performance. $I_{\text{sat}} = 1.67\,\text{mW/cm}^2$, $I_{\text{sat,rep}} = I_{\text{sat}}/2$ [82]. The values in parentheses hold for the prior version of the system, which was used for the measurements in chapter 4. They are adapted from [98].

live evaluation of every camera shot on the lab computer. In our lab this is done by a Matlab based software called *MatCam* written by Caspar Ockeloen [146]. The software reads in the camera pictures, computes the atom number, fits a user-chosen distribution to the data and stores the picture, the atom number and the fit results together with all configuration parameters.

3.7 Characterization of experimental sequences

In the following I want to characterize two sequences. The first one is the sequence which we have been using for most coupling experiments between atoms and membrane. The second sequence allows to prepare denser atomic clouds. We use it to load a far-detuned dipole trap [132] which will be used for future membrane coupling and single photon storage experiments [133, 134]. The sequence is also used in two of the sympathetic cooling experiments presented in chapter 4.

3.7.1 Standard MOT and molasses generation

In most coupling experiments between atoms and membrane a rather simple sequence is used. We prepare a large but rather warm MOT and then add a molasses phase, in which the temperature of the cloud is reduced drastically. The data I will show in the following characterizes the atomic system in the status of the year 2015 when the measurements presented in chapter 5 were performed. A part of the data in chapter 4 (Exp. 1, Exp. 4 and Exp. 5) was recorded with an almost identical system, which is characterized in [98]. I will point out the slight differences at the end of the section.

MOT

The laser parameters and the magnetic field gradient during the MOT phase have been optimized for a maximal number of atoms. During the MOT phase the cloud is permanently loaded from the 2D MOT. The 2D MOT parameters have been optimized separately for a maximal loading rate as described in [98]. A maximum

atom number of 5×10^9 and a maximum loading rate $2.7 \times 10^9 \, \mathrm{s}^{-1}$ were reached for the parameters summarized in table 3.2.

Figure 3.6 shows how the number of atoms N, the resonant optical depth OD_{res}, the number density n_0 in the center of the cloud, the axial and vertical temperature $T_{\mathrm{x,y}}$ and the width of the cloud $\sigma_{\mathrm{x,y}}$ evolve with time during the sequence. N and OD are inferred from absorption images using equation 3.9 and 3.6. The widths $\sigma_{\mathrm{x,y}}$ are determined from Gaussian fits to the area density distribution. The density in the center of the cloud n_0 is calculated from the optical depth in the center and the horizontal width using the equations 1.27 and 3.9 under the assumption that the atomic cloud is cylindrically symmetric. The temperature has been derived from a fit of equation 1.28 to the widths measured for different times of flight. It compares the case of two different 3D MOT magnetic field gradients, one with the optimal value $B_{\mathrm{3D\ MOT}} = 24 \, \mathrm{G/cm}$ used for the experiments in chapter 5 (see table 3.2) and one with $B_{\mathrm{3D\ MOT}} = 12 \, \mathrm{G/cm}$ similarly to the value used for the experiments presented in chapter 4. For times larger than 3 s the filled markers in figure 3.6 show the properties of the molasses cooled cloud. For the 24 G/cm measurements the empty markers display how the parameters evolve when the settings are not changed to molasses settings.

One clearly sees that the steeper gradient, which generates a deeper trap (see equation 1.16), allows to load more atoms and to create larger densities and optical depths at the expense of higher temperatures. We attribute the temperature increase to the reabsorption of scattered light in a dense atomic ensemble, which induces a random diffusion mechanism. In [147] Cooper *et al.* model this diffusion process and find that in the high density regime the temperature of a MOT scales as $T \propto n_0^{2/3} N^{1/3}$. Figure 3.7 illustrates that this scaling can be seen in our experiment, at least in an intermediate parameter regime. After 1 s (3 s) for $B_{\mathrm{3D\ MOT}} = 12 \, \mathrm{G/cm}$ ($B_{\mathrm{3D\ MOT}} = 24 \, \mathrm{G/cm}$) the MOT seems to be completely full and the parameters do not change any more. Reabsorption of scattered photons also allows to explain the constant density profile observed in figure 3.6 d) [2, 148, 149, 147]. In the absence of interactions between the atoms one would expect the density to increase with growing atom number as the spatial geometry of the trap is fixed by the magnetic field. However, at a certain density the probability that scattered light gets reabsorbed by other atoms rises, which induces a repulsive force between the atoms and hence limits the density.

Molasses

After 3 s the settings of the experiment shown in figure 3.6 are changed from MOT to molasses cooling. In molasses configuration the magnetic field gradient is switched off and the cooling laser is much further detuned. The exact molasses settings have been chosen in a compromise between low temperature and large atom number (see table 3.2). This change in the cooling settings takes the cloud from the regime of Doppler cooling [2, 74] into the regime of polarization gradient cooling [2, 81], which increases the cooling rate Γ_{a}. Moreover, the large increase in the cooling
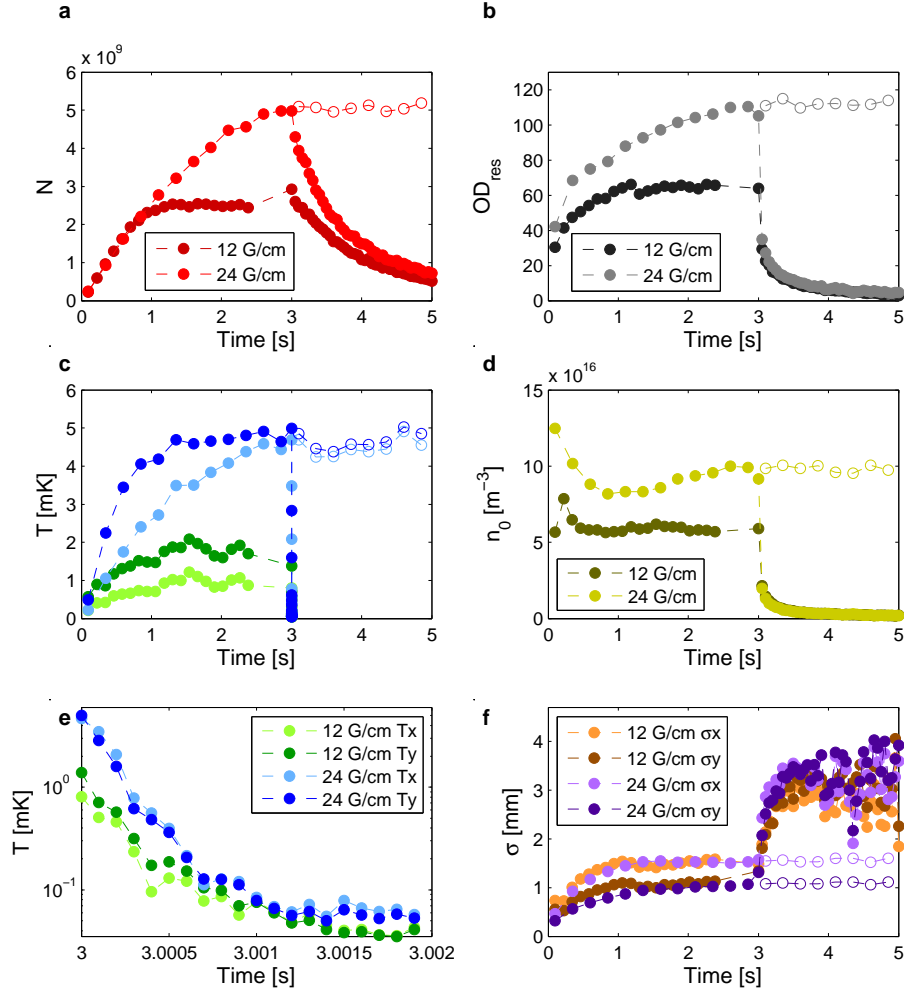
Figure 3.6: Time evolution of a) number of atoms N, b) resonant optical depth OD_{res} in the center of the cloud, c) horizontal and vertical temperature $T_{x(y)}$, d) density in the center of the cloud n_0, e) the temperatures in the early molasses phase (zoom into plot c)), f) horizontal and vertical width $\sigma_{x(y)}$ ($e^{-1/2}$ half width).
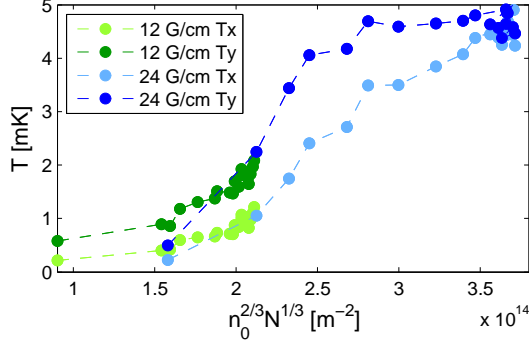
Figure 3.7: Dependence of the MOT temperature on the product of $n_0^{2/3}N^{1/3}$. In [147] a linear dependence is predicted.

light detuning drastically reduces the diffusion process generated by reabsorption of scattered light. Together, this leads to the immediate strong reduction of the temperatures down to $40\,\mu\mathrm{K}(60\,\mu\mathrm{K})$ for $B_{\mathrm{3D\ MOT}} = 12\,\mathrm{G/cm}$ ($B_{\mathrm{3D\ MOT}} = 24\,\mathrm{G/cm}$) visible in figure 3.6 e). A linear fit to the first data points reveals an atomic damping rate of $\Gamma_{\mathrm{a}} = 5.0(8) \times 10^3\,\mathrm{s}^{-1}$ ($\Gamma_{\mathrm{a}} = 5.3(4) \times 10^3\,\mathrm{s}^{-1}$) which is in reasonable agreement with the value expected from equation 1.15 ($\Gamma_{\mathrm{a}} = \alpha/m = 7.5 \times 10^3\,\mathrm{s}^{-1}$). Note that the theoretical value was derived for a simplified level scheme and in the low saturation limit.

Even if the outward directed force from multiple scattering is reduced, the atomic density depicted in figure 3.6 d) decreases when we switch to molasses settings as the confining magnetic potential is switched off. This is accompanied by a sudden increase in the width of the atomic ensemble as visible in figure 3.6 f) and a reduction of the optical depth, figure 3.6 e). Note that these changes happen on a time scale of a few tens of ms, much slower than the reduction of the temperature $1/\Gamma_{\mathrm{a}} \approx 0.2\,\mathrm{ms}$. On top of this fast dynamics, the number of atoms decays exponentially with a lifetime of $\tau_{\mathrm{lt}} = 1.19(2)\,\mathrm{s}$ ($\tau_{\mathrm{lt}} = 1.10(2)\,\mathrm{s}$). In addition, the widths slowly broaden due to the diffusive motion of the atoms in absence of any confining potential [2]. Atoms which diffuse out of the trapping volume are lost. Further we expect to lose atoms by light-assisted collisions [150, 151] and collisions with the background gas [137].

Old molasses settings

As mentioned above, the data presented in figure 3.6 was recorded with the atom setup as it was used in 2015. The slightly different prior settings of the setup, which were used for the first sympathetic cooling measurements in chapter 4, are listed in parenthesis in table 3.2. The main differences are a lower magnetic field gradient and a lower intensity in the cooling beams. With these settings we observed a slightly higher molasses cooling rate $\Gamma_{\mathrm{a}} = 9.0 \times 10^3\,\mathrm{s}^{-1}$ ($9.3 \times 10^3\,\mathrm{s}^{-1}$) for the horizontal (vertical) axis and a shorter molasses lifetime of $\tau_{\mathrm{lf}} = 0.65\,\mathrm{s}$.
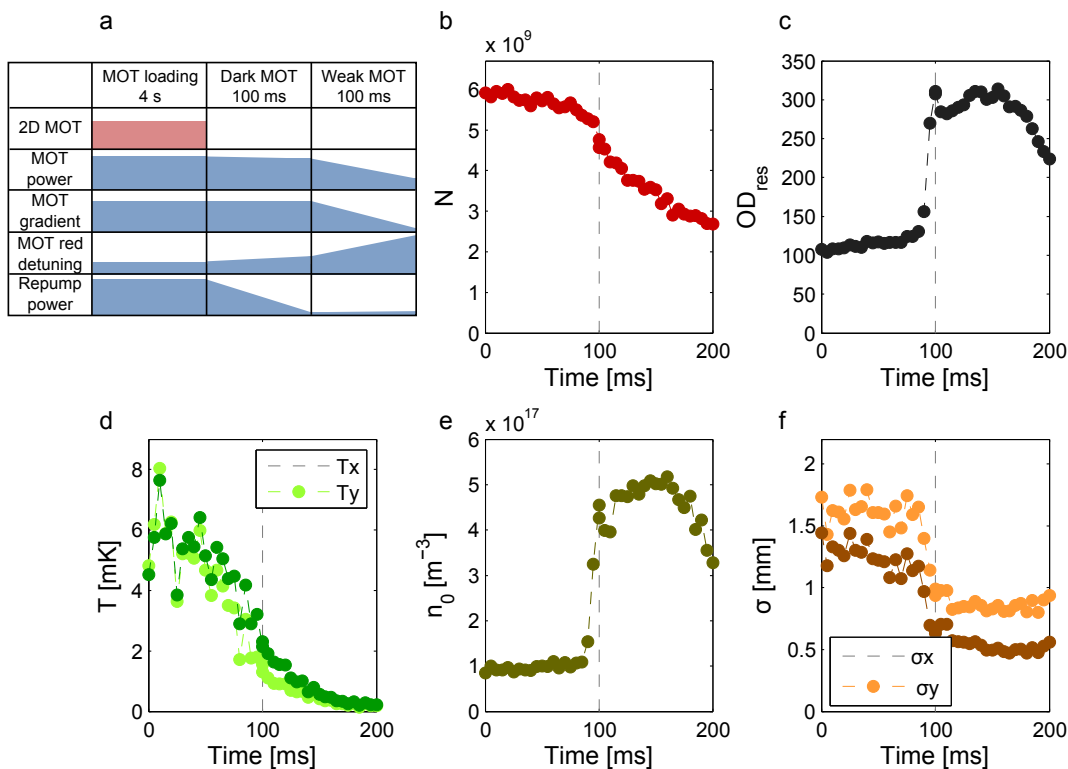
Figure 3.8: a) Overview of the dense MOT sequence. The initial MOT loading is the same as presented in figure 3.6. The plots show the evolution of the cloud properties during the *dark MOT* and *weak MOT* phases. They show b) number of atoms N, c) resonant optical depth OD_{res} in the center of the cloud, d) horizontal and vertical temperature $T_{x(y)}$, e) density in the center of the cloud n_0, f) horizontal and vertical width $\sigma_{x(y)}$ ($e^{-1/2}$ half width).

3.7.2   Preparation of ensembles with very high OD

During the course of this thesis, we realized that the figure of merit for a strong coupling between atoms and membrane on the atomic side is the resonant optical depth OD_{res} and not the overall atom number N in the lattice. Therefore in a second optimization run we optimized on the optical depth rather than on the atom number. We currently use this sequence with slight modifications to load an optical dipole trap. The sequence is also used in two of the sympathetic cooling experiments presented in chapter 4 (Exp. 2 and Exp. 6).

Figure 3.8 a) shows a summary of the optimized sequence. In a first step the MOT is loaded in the same way as presented above (24 G/cm parameter set). After 4 s of loading the 2D MOT is switched off, and a *dark MOT* phase starts. During this phase the red-detuning of the laser cooling beams is slightly increased (from $-3.5\,\Gamma$ to $-4.5\,\Gamma$) and the repump power is drastically reduced (from $0.19\,I_{\text{sat,rep}}$ to $1.2 \times 10^{-3}\,I_{\text{sat,rep}}$). The parameters are changed linearly over the course of 100 ms

as illustrated in figure 3.8 a). Both changes reduce the scattering rate of the cooling light and thus the density limiting reabsorption processes. As the confining magnetic field gradient is still present, the cloud shrinks and the atomic density and resonant optical depth increase as depicted in figure 3.8 f), e) and c). The density increase and the size reduction are initially very moderate. However, shortly before the end of the *dark MOT* phase the atomic depth and the resonant OD quickly jump up and the cloud size reduces. At this time the repump power reaches a critical value. It becomes so low that the rate at which the cooling light depumps the $F = 2$ level starts to compete with the repumping rate of the the repump light. As a consequence the atoms begin to accumulate in the $F = 1$-state, in which they do not scatter cooling light. This massively reduces the outwards directed radiation pressure force so that the density increases drastically. The optical depth increases up to $OD_{\text{res}} = 300$. Although the cloud becomes denser it now also gets colder as visible in figure 3.8 d). The temperature levels off at about 2 mK. We found that we can still reduce the temperature of the cloud without large losses in optical depth, if we add a *weak MOT* phase in which the magnetic field gradient is slowly ramped down, from 24 G/cm to 4 G/cm. Further, we reduce the intensity in the cooling beams to $10 I_{\text{sat}}$ and increase the MOT detuning (from $-4.5\,\Gamma$ to $-11\,\Gamma$). Simultaneously, the repump power slightly increases again (from $1.2 \times 10^{-3} I_{\text{sat,rep}}$ to $3 \times 10^{-3} I_{\text{sat,rep}}$). The adiabatic reduction of the confining magnetic potential reduces the temperature of the cloud. Figure 3.8 shows that we can reach temperatures of $200 \,\mu$K in combination with on optical depth of 225.

Chapter 4

Sympathetic cooling of a membrane oscillator in a hybrid mechanical-atomic system

In this chapter I will present results on sympathetic cooling of the fundamental membrane mode via the atomic ensemble. Prior experiments in our group showed that the damping rate of the membrane can be altered by the presence of the atoms [29]. However, the effect was too small to modify the temperature of the membrane significantly. Our recent sympathetic cooling results are the first realization of an atom-membrane hybrid system in which the coupling can be exploited for something useful, namely to cool the membrane. The initial sympathetic cooling measurements were performed with the first-generation membrane-cavity setup. The results of these measurements are published in [55] and can be found in Andreas Jöckel's PhD thesis [98]. I will summarize them here and in addition show the results of several new measurements performed with the second-generation membrane-cavity setup presented in chapter 2. Concretely, repetitions of the initial measurements with the new setup, a sympathetic cooling measurement in a blue-detuned lattice and the dependence of sympathetic cooling on the atomic density will be presented.

4.1   Experimental setup of the hybrid system

Figure 4.1 shows a schematic of the hybrid setup used for the first sympathetic cooling experiments. It connects the atomic ensemble (chapter 3) and the first-generation membrane-cavity system ([98], chapter 4) via a standing wave generated by a 780 nm laser[1] (see figure 2.4). The light travels through the atomic ensemble and is reflected off the single-sided membrane-cavity system. As the light is detuned from the atomic $F = 2 \leftrightarrow F' = 3$ transition by Δ_{LA}, it generates the lattice potential described in the end of section 3.4. The properties of this membrane-cavity system
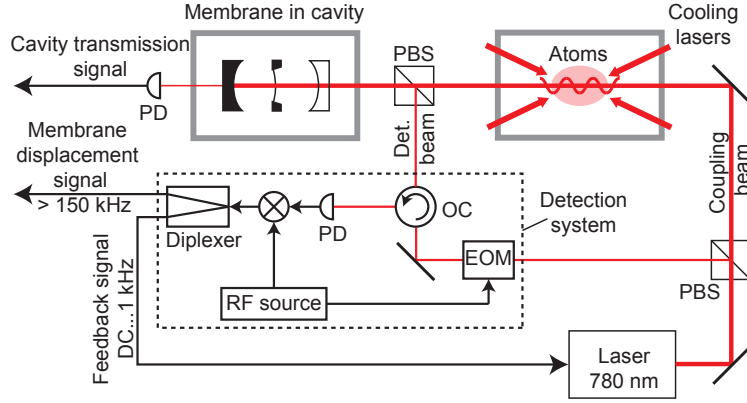
---

[1]Toptica, TA pro, 1.5 W

Figure 4.1: Setup used for the first sympathetic cooling experiments in a hybrid atom-membrane system. Grey boxes: Vacuum chambers. PBS: polarizing beam splitter. EOM: electro-optic modulator. OC: optical circulator. PD: photodiode. A small fraction of the coupling light is split off at a PBS for detection and stabilization via a Pound-Drever-Hall type error signal. The low frequency part of the Pound-Drever-Hall signal is used to lock the frequency of the laser to the cavity frequency. The high frequency part is sent to a spectrum analyzer to determine the power spectral density of the membrane motion $S_x(\Omega)$, see section 1.2.6. Further details are given in the text. Figure courtesy of Tobias Kampschulte.

and its interaction with the laser light are summarized in section 2.5.

The latter measurements are performed with the very similar hybrid setup shown in figure 5.1, in which the atomic ensemble and the second-generation membrane-cavity setup, that is characterized in chapter 2, see figure 2.5, are connected via a fiber. The fiber was implemented because the second-generation setup rests on a separate optical table. The coupling laser is the same for all experiments in this chapter, see section 2.3.1. Further, the atomic ensemble is in principle the same in all experiments. However, changes in the preparation sequence in between the various measurements lead to differences in parameters of the cloud. I will point this out in the text.

In all experiments presented in this chapter the laser is detuned slightly to the red from the cavity resonance ($\Delta < 0, |\Delta| \ll \kappa$) to avoid the optomechanical parametric instability. Thus, a finite amount of optomechanical damping is present in all measurements. We make use of the known optomechanical behavior to calibrate the measured membrane temperature. In all but one time-resolved experiments of this chapter, the MOT is loaded with the lattice running at low incoming power P_0 before the start of the actual experiment so that $\Omega_a(0) < \Omega_m$ and no resonant atom-membrane coupling is present. Only when the atomic cloud is prepared and

the final laser cooling settings are set (molasses or *weak MOT* settings), the coupling is turned on by ramping up the laser power to P_0 so that $\Omega_\mathrm{a}(0) \geq \Omega_\mathrm{m}$. In the spectrally-resolved measurements the lattice is running on the higher power value P_0 continuously. For all experiments we do a control experiment without atoms, in which the cooling laser is set to blue detuning to prevent atom trapping. The parameters of all the experiments are summarized in table 4.1 at the end of the chapter.

4.2 Time-resolved sympathetic cooling with red and blue detuning

In the following I present sympathetic cooling measurements in the time domain. For this the membrane signal is recorded continuously within a bandwidth $BW \gg (\Gamma_\mathrm{tot}, \delta\Omega_\mathrm{m})$ using the zero-span mode of the spectrum analyzer.

4.2.1 Experiment 1 - First observation of sympathetic cooling

In experiment 1, shown in figure 4.2, the membrane is positioned at the slope of the intracavity field, where the optomechanical coupling is the largest. Our asymmetric cavity offers two positions for maximum optomechanical coupling $|G_\mathrm{max}|$, the point of highest and lowest finesse (see figure 2.9). Figure 4.2 a) shows how the membrane temperature evolves with time for a measurement in which the membrane is positioned at the low finesse slope ($F = 140$). The column A corresponds to the end of the MOT loading time. In this preparation part the membrane temperature is already colder than room temperature ($T \approx 30\,\mathrm{K}$) due to the finite optomechanical damping. At the start of the actual experiment the laser cooling settings are changed to molasses cooling and $10\,\mathrm{ms}$ later the lattice power is ramped up linearly to the higher power P_0 so that $\Omega_\mathrm{a}(0) \geq \Omega_\mathrm{m}$ within $1\,\mathrm{ms}$. This simultaneously turns on the sympathetic cooling and increases the optomechanical damping (column B). Due to the additional optomechanical damping the temperature in a control measurement without atoms (blue trace) decreases to $T_\mathrm{opt} = T_\mathrm{bath}\Gamma_\mathrm{m}/(\Gamma_\mathrm{m} + \Gamma_\mathrm{opt}) = 11(2)\,\mathrm{K}$. However, in the measurement with atoms (red trace) the membrane temperature decreases much faster and settles at a much lower temperature of $T_\mathrm{sym} = T_\mathrm{bath}\Gamma_\mathrm{m}/(\Gamma_\mathrm{m} + \Gamma_\mathrm{opt} + \Gamma_\mathrm{sym}) = 1.5(4)\,\mathrm{K}$ due to the additional sympathetic cooling from the atoms. Subsequently, the temperature slowly rises due to the finite lifetime of $0.65\,\mathrm{s}$ of the molasses-cooled cloud. After $0.5\,\mathrm{s}$ of molasses cooling all laser cooling is switched off (column C) and the red curve equilibrates at the level of the blue curve.

The initial slope of the red curve corresponds to the total damping rate of the membrane $\Gamma_\mathrm{tot} = \Gamma_\mathrm{m} + \Gamma_\mathrm{sym} + \Gamma_\mathrm{opt}$. We find $\Gamma_\mathrm{tot} = 111(1)\,\mathrm{s}^{-1}$ from a fit to the data in figure 4.2 a). This value agrees with the the total damping rate inferred from the minimum temperature and the bath temperature $\Gamma_\mathrm{tot} = \Gamma_\mathrm{m}T_\mathrm{bath}/T_\mathrm{sym} = 122(22)\,\mathrm{s}^{-1}$ within one standard deviation. Note that here $T_\mathrm{bath} = 320\,\mathrm{K}$ includes
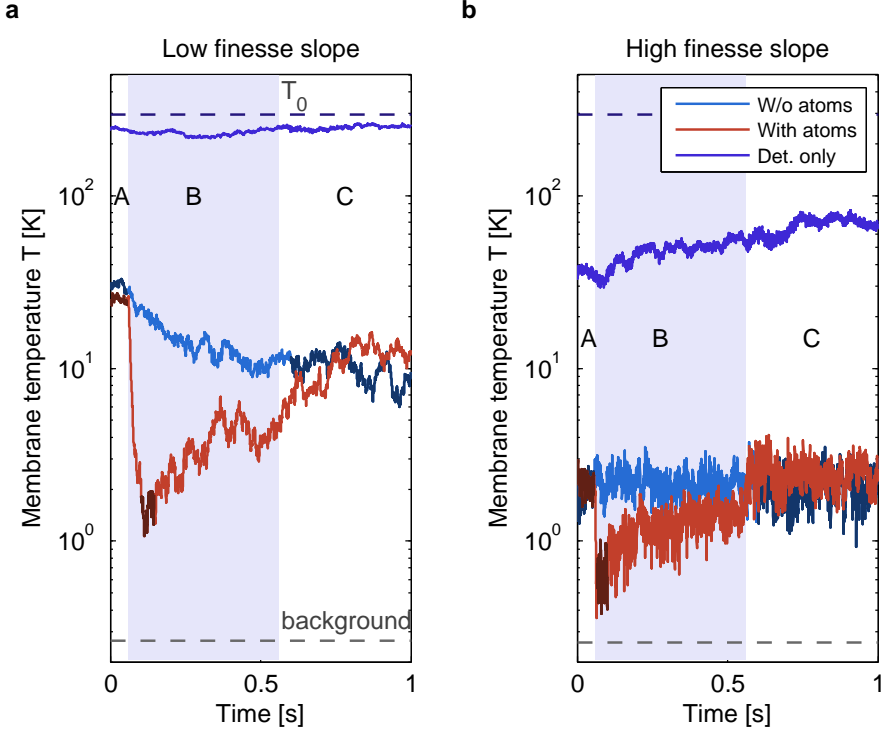
Figure 4.2: Sympathetic cooling in the time domain with the first-generation setup. a) and b) Membrane temperature versus time. A: atoms not resonant ($P_0 = 5.5\,\mathrm{mW}$). B: atoms resonant ($P_0 = 16.5\,\mathrm{mW}$). C: atoms resonant ($P_0 = 16.5\,\mathrm{mW}$), but laser cooling switched off. Red curves: with atoms, blue curves: without atoms, dark blue curve: detection light only, dashed lines: measurement noise floor and room temperature. All measurements were taken with the spectrum analyzer set to a fixed frequency $\approx \Omega_\mathrm{m}$ with bandwidth $BW \gg (\Gamma_\mathrm{tot}, \delta\Omega_\mathrm{m})$ and averaged over 20 experimental runs. The temperatures given in the text are the average values of the darker regions. a) Measurement with $F = 140$, $\Delta_\mathrm{LA} = -2\pi \times 8\,\mathrm{GHz}$ and $BW = 2\pi \times 0.5\,\mathrm{kHz}$. b) Measurement with $F = 300$, $\Delta_\mathrm{LA} = -2\pi \times 8\,\mathrm{GHz}$ and $BW = 2\pi \times 2\,\mathrm{kHz}$.

the laser noise at P_0 and is thus larger than room temperature ($T_0 = 300 \, \mathrm{K}$), see section 1.2.5.

The experiment is repeated at the position of maximum cavity finesse ($F = 300$), see figure 4.2 b). The higher finesse increases both the optomechanical damping rate Γ_{opt} and the sympathetic damping rate Γ_{sym}. In this measurement the optomechanical damping is limited by laser noise. As a consequence the temperature in the blue trace (without atoms) slightly increases to $T_{\mathrm{opt}} = 2.2(8) \, \mathrm{K}$ when we ramp up the lattice power (going from column A to column B). Still, the atoms cool the membrane temperature further down with a total damping rate of $\Gamma_{\mathrm{tot}} = 331(30) \, \mathrm{s}^{-1}$ (inferred from the initial slope) to a minimum temperature of $T_{\mathrm{sym}} = 0.7(2) \, \mathrm{K}$. This corresponds to a minimal phonon occupation of $\bar{n}_{\mathrm{f}} = k_{\mathrm{B}} T_{\mathrm{sym}} / \hbar \Omega_{\mathrm{m}} = 4.9(1.7) \times 10^4$. We can also infer the total damping rate from the bath temperature $T_{\mathrm{bath}} = 640 \, \mathrm{K}$, which is strongly increased by laser noise, and the minimum temperature in presence of atoms T_{sym}. In this way we find $\Gamma_{\mathrm{tot}} = \Gamma_{\mathrm{m}} T_{\mathrm{bath}} / T_{\mathrm{sym}} = 535(191) \, \mathrm{s}^{-1}$, which is slightly higher than the value determined from the initial slope.

From the minimum temperatures in presence and absence of atoms and the bath temperature, the sympathetic cooling rate can be extracted

$$\Gamma_{\mathrm{sym}} = \Gamma_{\mathrm{m}} \left(\frac{T_{\mathrm{bath}}}{T_{\mathrm{sym}}} - \frac{T_{\mathrm{bath}}}{T_{\mathrm{opt}}} \right) . \tag{4.1}$$

We find $\Gamma_{\mathrm{sym}} = 103(26) \, \mathrm{s}^{-1}$ in the low finesse case and $\Gamma_{\mathrm{sym}} = 390(138) \, \mathrm{s}^{-1}$ in the high finesse case. The measured values are in reasonable agreement with the value predicted by equation 1.134, $\Gamma_{\mathrm{sym}} = 130 \, \mathrm{s}^{-1}$ for the low finesse and $\Gamma_{\mathrm{sym}} = 606 \, \mathrm{s}^{-1}$ for the high finesse case. Table 4.1 summarizes the relevant system parameters together with the expected and measured sympathetic cooling rates.

The temperature axis in the low finesse data set was calibrated by the known optomechanical behavior. More precisely, equation 1.103 has been fitted to the three signal levels at different lattice powers available in the data without atoms, with the calibration factor c_1 and the parameter c_2 as free parameters, which contains the not precisely known cavity detuning Δ. For the fit the dependence of T_{bath} on the measured laser noise ($S_I(\Omega_{\mathrm{m}}) = -145 \, \mathrm{dBc/Hz}$ and $S_{\dot{\Phi}} = 4\pi^2 \times 256 \, \mathrm{Hz}^2/\mathrm{Hz}$, see equation 1.97) has been taken into account. Due to the small amount of available data points, the resulting uncertainties in the measured temperatures are rather large. The absence of a data point with low damping $\Gamma_{\mathrm{opt}} \approx \Gamma_{\mathrm{m}}$ makes a calibration of the temperature axis of the high finesse data set difficult. Therefore, it was calibrated via the low finesse calibration taking the increase in readout sensitivity with increasing finesse F, given by equation 1.101, into account. For further details on the calibration and the error determination see [98] chapter 5.2 or the supplementary material of [55].

4.2.2 Experiment 2 - Repetition of the results with the new setup

Shortly after taking the measurements presented above, we changed the membrane-cavity system to the more stable second-generation setup and repeated the time-
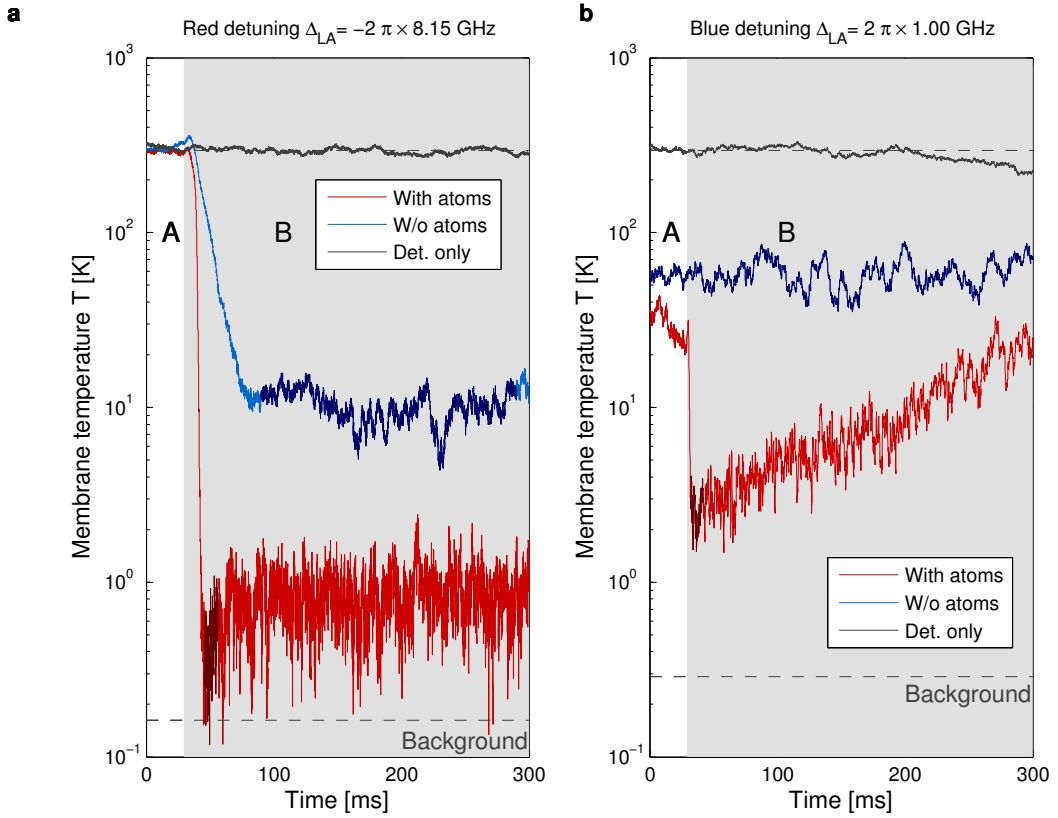
Figure 4.3: Sympathetic cooling in the time domain with the second-generation cavity setup. a) Membrane coupled to *weak MOT*. A: atoms not resonant ($P_0 = 112\,\mu\text{W}$), B: atoms resonant ($P_0 = 19.1\,\text{mW}$). $BW = 2\pi \times 10\,\text{kHz}$, the data is averaged over 15 runs. b) Membrane coupled to molasses via a blue lattice ($\Delta_{\text{LA}} > 0$). A: MOT cooled atoms, lattice resonant ($P_0 = 5.6\,\text{mW}$). B: Molasses cooled atoms, lattice resonant ($P_0 = 5.6\,\text{mW}$). $BW = 2\pi \times 10\,\text{kHz}$, the data is averaged over 20 runs. a) and b) Red trace: with atoms, blue trace: w/o atoms, black trace: detection light only, dashed lines: measurement noise level and average detection light level. The temperatures given in the text are the mean values of the dark colored regions. Temperature uncertainties are determined via equation 1.104.

resolved sympathetic cooling experiment. The result is shown in figure 4.3 a). This time the measurement is performed with a *weak MOT*, with laser and magnetic field parameters very similar to the one described in section 3.7.2. Due to the higher finesse of the new cavity setup and the higher atomic density in the *weak MOT*, we expect a stronger sympathetic cooling effect than before. From linear fits to the initial slopes of the measurements with and without atoms (red and blue trace) one finds $\Gamma_{\rm tot} = 1486(7)\,{\rm s}^{-1}$, $\Gamma_{\rm opt} + \Gamma_{\rm m} = 87.2(1)\,{\rm s}^{-1}$ and $\Gamma_{\rm sym} = \Gamma_{\rm tot} - \Gamma_{\rm opt} - \Gamma_{\rm m} = 1399(7)\,{\rm s}^{-1}$ clearly higher than the values seen before. Note that this time the sympathetic cooling rate is determined from the slopes in absence and presence of atoms as both $\Gamma_{\rm tot}$ and $\Gamma_{\rm opt} + \Gamma_{\rm m}$ can be fitted nicely. In the previous experiment 1 this was not the case, especially for the high finesse measurement, so that $\Gamma_{\rm sym}$ was inferred from the minimal temperatures. Further note that for the fit only the membrane signal after the end of the lattice ramp-up time (this time $10\,{\rm ms}$) is taken into account. From the measured atomic density of the *weak MOT* (see table 4.1) and equation 1.134 one expects an even higher value of $\Gamma_{\rm sym} = 3.57 \times 10^4\,{\rm s}^{-1}$ if one assumes that all the atoms are in the $F = 2$ hyperfine state. However, in the *weak MOT* a large part of the atoms stays in the further detuned $F = 1$ hyperfine groundstate and is not coupled resonantly to the membrane as the detuning $\Delta_{\rm LA,F=1} = \Delta_{\rm LA} - 2\pi \times 6.8\,{\rm GHz}$ is too large. The atomic density used for the calculation assuming all atoms are in $F = 2$ is thus probably much too large. Still, the discrepancy could also be a sign for a reduction of the sympathetic cooling rate due to a delay in the coupling as it will be discussed in chapter 5.

The additional membrane cooling factor expected from the damping rates in presence and absence of atoms $(T_{\rm opt}/T_{\rm sym})_{\rm expect} = \Gamma_{\rm tot}/(\Gamma_{\rm m} + \Gamma_{\rm opt}) = 17.0(1)$ matches the observed additional cooling factor $T_{\rm opt}/T_{\rm sym} = 16(2)$ (from $T_{\rm opt} = 10.3\,{\rm K}$ to $T_{\rm sym} = 0.64\,{\rm K}$) within one standard deviation. This means that, in contrast to the optomechanical damping, sympathetic cooling does not add additional noise.

As we saw in figure 2.11 and 2.13, the optomechanical temperature $T_{\rm opt}$ of the new setup does not follow a predictable power dependence due to the presence of electrical noise on the cavity piezos. Therefore, a correct calibration of the temperature axis with only three data points is impossible and only temperature ratios as presented above can be determined with decent precision. To get some idea about the absolute temperatures, I calibrated the vertical axis in both plots of figure 4.3 by setting the average value of the measurement done in absence of the coupling lattice with the detection light alone (black trace) to room temperature. In absence of noise this leads to an overestimation of the membrane temperatures. From the expected cooling factor at the detection light level and the typically small laser and piezo noise heating at this low power level, I estimate that the absolute temperature calibration is good up to a factor of three. Due to this imprecise absolute temperature calibration no strong claims about the minimum temperature in this measurement can be made. Still, the sympathetic cooling and total cooling rate in this experiment are the largest we have observed so far.

4.2.3 Experiment 3 - Sympathetic cooling in a blue-detuned lattice

The sympathetic cooling experiments presented so far were performed with red-detuned lattices ($\Delta_{\mathrm{LA}} < 0$). According to the one-dimensional theory presented in section 1.3, the sympathetic cooling should work equally well in a blue-detuned lattice ($\Delta_{\mathrm{LA}} > 0$). The potential is then anti-trapping in the radial direction but the surrounding laser-cooled cloud continuously refills the lattice. The experiment shown in figure 4.3 b) demonstrates that sympathetic cooling also works in this case. In contrast to the measurements before, this time the lattice power is not ramped up, but stays at a value high enough so that $\Omega_{\mathrm{a}}(0) \geq \Omega_{\mathrm{m}}$ during the experiment. Therefore, already in the preparation phase A, the membrane is slightly cooled sympathetically by the MOT cooled atoms. At the start of phase B the laser cooling settings are switched from MOT to molasses cooling. From the slope I determine $\Gamma_{\mathrm{tot}} = 1082(95)\,\mathrm{s}^{-1}$. Due to the absence of a lattice power ramp, no slope exists in the control measurement without atoms (blue trace). Calculating the optomechanical damping rate from the ingoing power and the measured system parameters (see table 4.1) results in $\Gamma_{\mathrm{opt}} = 39\,\mathrm{s}^{-1}$ and $\Gamma_{\mathrm{sym}} = 1043(95)\,\mathrm{s}^{-1}$. This value also lies below the theoretically expected one of $\Gamma_{\mathrm{sym}} = 4420\,\mathrm{s}^{-1}$, indicating that delay effects, which will be discussed in chapter 5, already play a role here or that the atomic density in the blue-detuned lattice is locally reduced due to the anti-trapping radial potential. The fact that the membrane temperature increases rather immediately after the initial decline when the atoms are slowly lost from the trap, speaks for the second argument.

4.3 Spectrally-resolved sympathetic cooling

4.3.1 Experiment 4 - Studying the resonant behavior

To study the resonant behavior of the sympathetic cooling effect, we repeat experiment 1 and measure the minimal temperature as a function of the ingoing laser power P_0. For this we record the membrane spectrum $S_x(\Omega)$ for $380\,\mathrm{ms}$ starting $12\,\mathrm{ms}$ after the start of the molasses cooling. A variation of P_0 changes the trapping frequency $\Omega_{\mathrm{a}}(0)$ of the atomic ensemble (see equation 1.22). This time the lattice power is kept constant throughout the experiment. Furthermore, the membrane is placed at a position where $G = 0.92\,G_{\mathrm{max}}$ on the low finesse slope, which decreases g_{N} by the same factor. The temperature is determined from the area under the membrane spectrum after subtraction of the background level (see equation 1.59).

Figure 4.4 a) shows the membrane temperature in absence and presence of atoms as function of P_0. For powers larger than $P_0 = 14\,\mathrm{mW}$ the data points taken with atoms lie significantly below the data points taken without atoms. The inset depicts exemplarily the spectra at the thicker data points. The high power spectra are massively broadened due to a jitter in the optical spring effect caused by a fluctuation of the small laser-cavity detuning Δ. As in experiment 1, the temperature axis is calibrated via a fit of the expected optomechanical behavior 1.103 to the detected
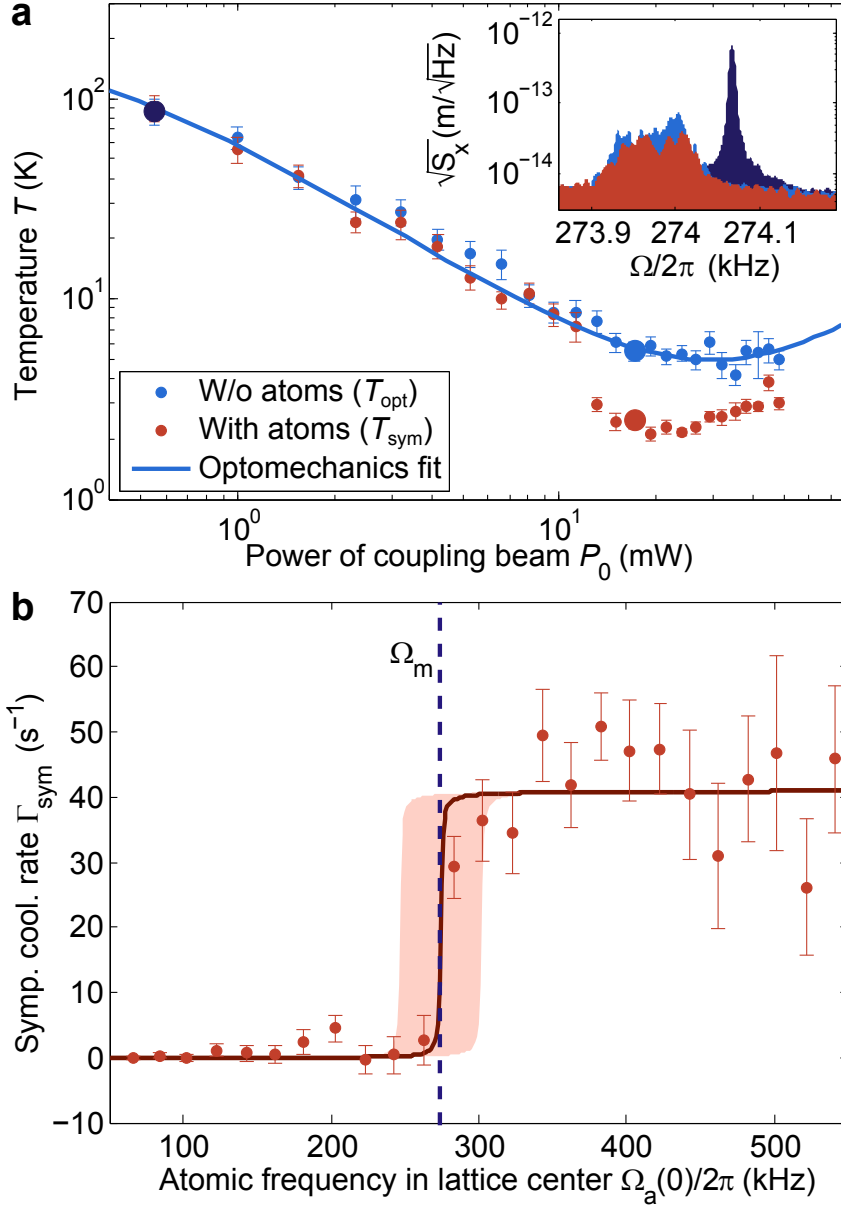
Figure 4.4: Resonant behavior of sympathetic cooling in first cavity setup. a) Membrane fundamental mode temperature as a function of laser power P_0, with atoms in the lattice (T_{sym}) and without atoms (T_{opt}). Blue line: fit of the theory of cavity optomechanical cooling with laser noise but without atoms given by equation 1.103. The data is averaged over 20 identical runs. The errors show the standard error of the mean value (s.e.m.). Inset: membrane displacement spectra $\sqrt{S_x(\Omega)}$ corresponding to the big dots in the main plot. b) Sympathetic cooling rate Γ_{sym} obtained from the data in a) as a function of the atomic frequency in the lattice center, $\Omega_a(0)$. Red line: fit of a theoretical model of Γ_{sym} given in equation 1.132 taking the lattice profile into account. The shaded red region indicates the $\pm 10\%$ uncertainty in $\Omega_a(0)$.

temperature. This time c_1, c_2 and c_3 are fitted, and the calibration factor, the cavity detuning Δ and the noise temperature T_L are determined from the fit results. See [98] section 5.3 or the supplementary material of [55] for more details on the fit. We find that laser amplitude and frequency noise limit the achievable optomechanical cooling factor and extract the effective bath temperature $T_{\text{bath}}(P_0)$ from the fit.

Figure 4.4 b) shows the sympathetic cooling rate $\Gamma_{\text{sym}} = \Gamma_{\text{m}}(T_{\text{bath}}/T_{\text{sym}} - T_{\text{bath}}/T_{\text{opt}})$ calculated from the temperatures versus the independently calibrated atomic center frequency. The sympathetic cooling rate shows a step-like dependence on the atomic center frequency. The behavior can be explained by the extreme inhomogenous broadening of our atomic ensemble caused by the large size of the atomic cloud. If the laser power is so low that even the atoms in the center of the Gaussian beam profile are not resonant with the membrane $\Omega_{\text{a}}(0) < \Omega_{\text{m}}$, no coupling occurs, so $\Gamma_{\text{sym}} = 0$. At the threshold laser power, at which $\Omega_{\text{a}}(0) \approx \Omega_{\text{m}}$, the atoms in the center become resonant and the membrane gets cooled. If $\Omega_{\text{a}}(0) > \Omega_{\text{m}}$, the atoms in the center are off resonant. However, some atoms in the wings of the Gaussian beam profile will now be resonant. Due to the large surrounding molasses cloud ($R_{\text{a}} \gg w_0$, R_{a}: cloud radius, w_0: lattice beam waist), the atoms are distributed over the entire beam profile and sympathetic cooling occurs for all $\Omega_{\text{a}}(0) \gtrsim \Omega_{\text{m}}$. The simple analytical model presented in section 1.3.4, which assumes a constant atomic density in the lattice volume and integrates the sympathetic cooling rate over the entire ensemble, predicts exactly this step-like behavior and allows to model the data very nicely. A fit of equation 1.132 to the data with the atomic density as only free parameter gives $n_{\text{a}} = 4.5(3) \times 10^{15}\text{m}^{-3}$. This is in good agreement with an independent measurement of $n_{\text{a}} = 8.6 \times 10^{15}\text{m}^{-3}$ taken at the start of the molasses phase, when taking into account that a significant part of the atoms gets lost during the 380 ms measurement time.

4.3.2 Experiment 5 - Repetition of the results with the new setup

Here the spectrally-resolved measurement is repeated with the second-generation cavity-membrane system. The only difference on the atomic side is a smaller atom-laser detuning $\Delta_{\text{LA}} = -2\pi \times 3.3\,\text{GHz}$. All the laser-cooling settings are the same (see table 4.1 for a list of parameters). Figure 4.5 shows the results. One sees that in this experiment the membrane reaches its so far lowest observed temperature of $T_{\text{sym}} = 0.4(2)\,\text{K}$ in the measurement at $P_0 = 9.4\,\text{mW}$ with atoms ($T_{\text{opt}} = 2.4(1.2)\,\text{K}$ at this power) corresponding to a phonon occupation of $\bar{n}_{\text{f}} = 3.0(1.5) \times 10^4$. As in experiment 2, the correct modeling of the optomechanical cooling data in the second-generation setup is difficult. The blue line in figure 4.5 a shows the optomechanical temperature which is expected from the observed optical spring effect and the measured laser noise. The left inset shows the measured frequency shift. The transmittance of the optical system between atom and membrane, t^2, was determined by a fit of equation 1.96 to the data in the inset using $P_{\text{in}} = \eta^2(t^2 P_0 + P_{\text{det}})$. To calibrate the temperature axis, the theoretical prediction 1.103 was fitted to the intermediate (piezo noise free) data points with the calibration factor c_1 as only free
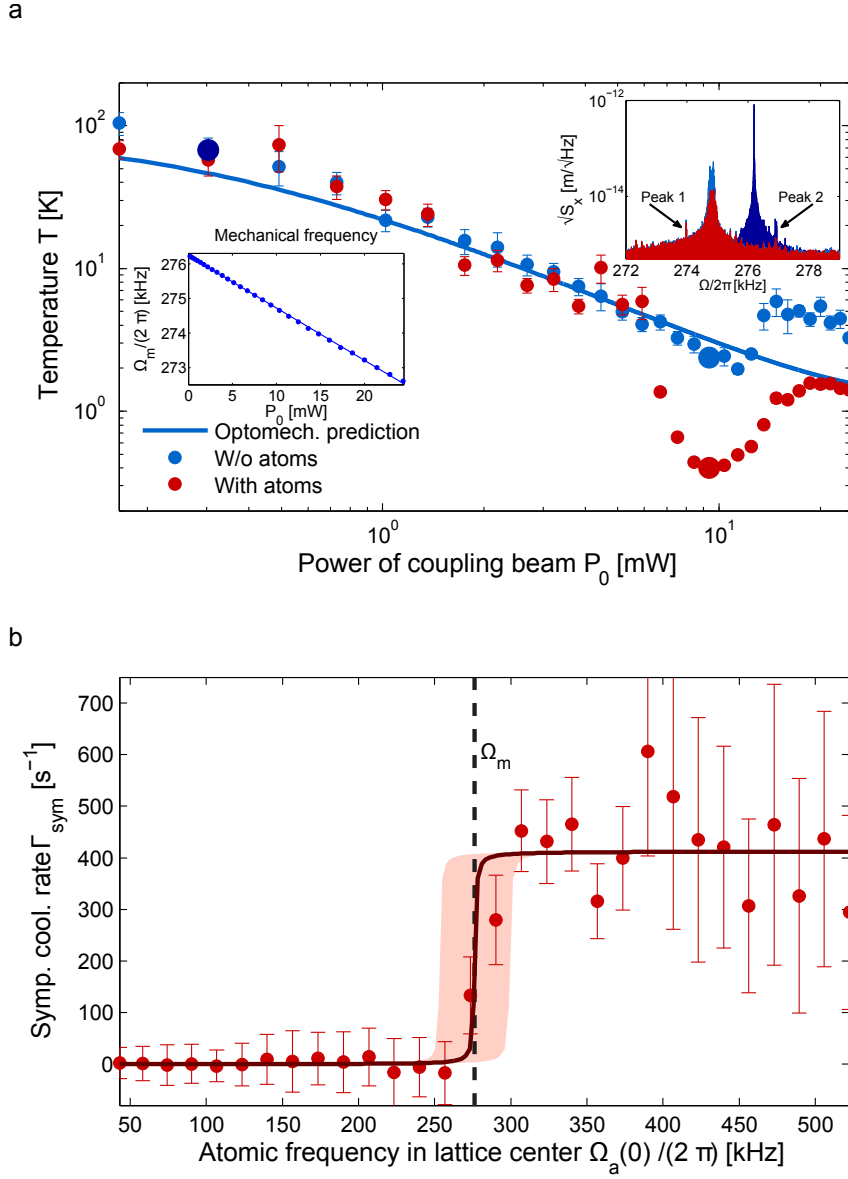
a

b

Figure 4.5: Resonant behavior of sympathetic cooling in the second-generation cavity setup, analog to figure 4.4. a) Membrane temperature with atoms (T_{sym}) and without atoms (T_{opt}) as a function of the ingoing laser power P_0. The solid blue line shows the optomechanical theory prediction. The second inset on the left in a) shows the optomechanical frequency shift of the membrane and a fit of the theoretical model given in equation 1.96. The arrows in the upper right inset mark two noise peaks which are probably responsible for the deviation of the optomechanical data from the theoretical expectation. b) Sympathetic cooling rate Γ_{sym} as a function of the separately calibrated atomic trapping frequency $\Omega_{\mathrm{a}}(0)$ (see section 3.4). Again, the data is averaged over 20 identical runs.

parameter. The fit result depends on the chosen set of data points for the fit, with a variation of about 50% for different sets. This determines the uncertainty of absolute temperature declarations for this experiment. From the calibrated temperature T_{opt} and the optomechanical damping rate Γ_{opt}, which is inferred from the measured frequency shift, the effective bath temperature $T_{\text{bath}} = T_{\text{opt}}(\Gamma_{\text{opt}} + \Gamma_{\text{m}})/\Gamma_{\text{m}}$ can be calculated for every data point. I find that the membrane experiences significant heating in the very low and very large power regime. A closer look at the spectra reveals that in both cases the membrane signal is close to a suspicious noise peak as indicated in the upper inset, which most likely is responsible for the heating.

As in experiment 4, the sympathetic cooling rate is determined from the calibrated temperatures and the corresponding bath temperatures. The result depicted in figure 4.5 b) looks qualitatively identical to the one before. However, the measured sympathetic cooling rates are ten times higher due to the higher finesse of the new cavity. The step-value resulting from a fit of equation 1.132 is $\Gamma_{\text{sym}} = 413(18)\,\text{s}^{-1}$. Given the separately-measured atomic damping rate of $\Gamma_{\text{a}} = 1 \times 10^{4}\,\text{s}^{-1}$, the measured sympathetic cooling rate corresponds to a coupling strength of $g_{\text{N}} = 1.6 \times 10^{3}\,\text{s}^{-1}$ and $N_{\text{r}} = 2.0 \times 10^{4}$ resonantly coupled atoms. As the finesse of the new cavity is larger by a factor of 5 (see table 4.1), we expect an increase in Γ_{sym} of a factor 25 according to equation 1.119 and 1.134. Thus, once more the measured cooling rate is too low, which can be due to a reduced atomic density on that day or due to delay effects (see chapter 5).

4.4 Experiment 6 - Atomic density dependence of sympathetic cooling rate

According to the results of section 1.3.4 (see equation 1.134 and lines above), the sympathetic cooling rate is proportional to the atomic density. To verify this, I repeat experiment 2 with variable atomic density. Again, the second-generation cavity-membrane setup is coupled to the *weak MOT*. The atomic density is varied by changing the length of the MOT loading time (in the range $(10 - 300)\,\text{ms}$) and recorded by absorption images. From the initial slopes after the ramp-up of the lattice power in measurements with and without atoms, the damping rates Γ_{tot}, $\Gamma_{\text{opt}} + \Gamma_{\text{m}}$ and $\Gamma_{\text{sym}} = \Gamma_{\text{tot}} - \Gamma_{\text{opt}} - \Gamma_{\text{m}}$ are inferred. Figure 4.6 shows the result. As a variation of the loading rate not only changes the atomic density but also the width of the atomic ensemble, Γ_{sym} is plotted against the product of the cloud radius R_{a} and the peak density $n_{\text{a}} = n_0$. Here $R_{\text{a}} = \sqrt{2\pi}\sigma_x/2$ is the radius of a top-head density profile with density n_0 with equal optical depth as the actual Gaussian cloud ($\int n_0 e^{-x^2/2\sigma_x^2}\mathrm{d}x \equiv n_0 2R_{\text{a}}$). The data shows a linear dependence of the sympathetic cooling rate on the product of cloud size and density as expected from equation 1.134

$$\Gamma_{\text{sym}} = \epsilon R_{\text{a}} n_{\text{a}} \quad \text{with} \quad \epsilon = 8\eta^2 t^2 g_0^2 \frac{m}{\hbar}\left(\frac{\Omega_{\text{m}}}{k\kappa}\right)^2 \pi^2 w_0^2\,. \tag{4.2}$$
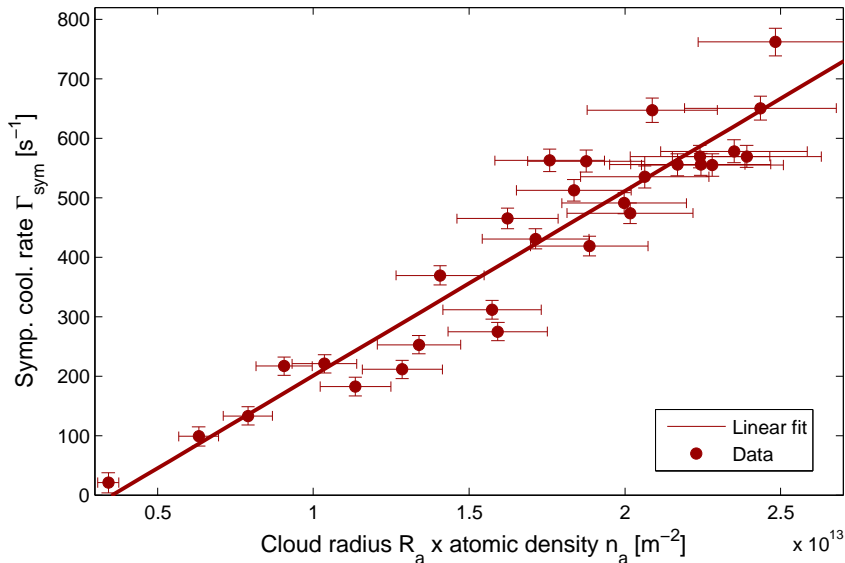
Figure 4.6: Atomic density dependence of sympathetic cooling rate. The sympathetic cooling rate Γ_{sym} extracted from the initial slopes after a sudden change of the lattice power in measurements with and without atoms is plotted versus the product of atomic cloud radius R_{a} and cloud density n_{a} determined from absorption images. The line shows a linear fit to the data.

The data points have a small horizontal offset indicating that the MOT was not well-centered at the position of the coupling lattice.

4.4.1 From rates expected versus observed cooling factor

In our experiments, the optomechanical cooling performance is limited by noise. This can be either laser intensity or frequency noise or electrical noise on the cavity piezos as discussed in section 2.4.2. The noise increases the bath temperature T_{bath} above the room temperature T_0 (see equation 1.99). As a consequence in many experiments the observed optomechanical cooling factor T_0/T_{opt} with respect to room temperature lies below the value $(T_0/T_{\text{opt}})_{\text{expect}} = (\Gamma_{\text{opt}} + \Gamma_{\text{m}})/\Gamma_{\text{m}}$ which can be achieved in absence of noise. The data taken in the last experiment with variable atomic density show that this is not the case for the additional sympathetic cooling. The atomic cooling does not add any additional noise. To see this, in addition to the initial slopes also the minimum temperatures T_{sym} and T_{opt} are evaluated, as in experiments 1 and 2. In figure 4.7 the observed additional cooling-factor from the atoms $T_{\text{opt}}/T_{\text{sym}}$ is plotted against the cooling factor $(T_{\text{opt}}/T_{\text{sym}})_{\text{expect}} = \Gamma_{\text{tot}}/(\Gamma_{\text{opt}} + \Gamma_{\text{m}})$, which is expected from the rates of the inital slopes. The plot shows that expected and observed cooling factors are in very good agreement, meaning that the coupling to the atoms does not add additional noise. As mentioned above, it is difficult to make statements about absolute temperatures with the new cavity system. Relative tem-
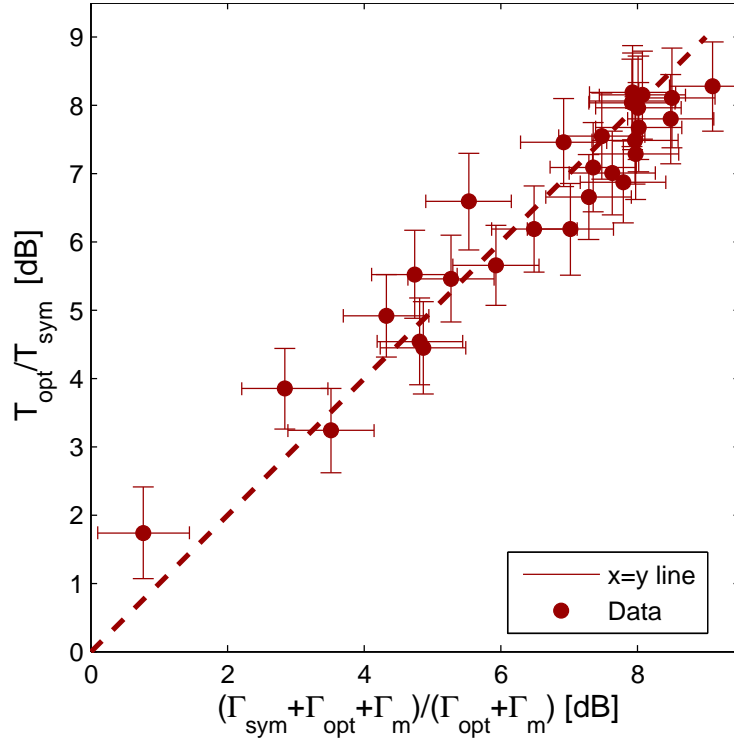
Figure 4.7: The additional cooling factor from the sympathetic cooling $T_{\mathrm{opt}}/T_{\mathrm{sym}}$ extracted from the minimal temperatures in absence and presence of atoms is plotted against the additional cooling factor, which is expected from the slopes of the initial decay of the membrane temperature in presence Γ_{tot} and absence $\Gamma_{\mathrm{opt}} + \Gamma_{\mathrm{m}}$ of atoms. As guide for the eye, the dashed line marks the line on which both cooling factors are equal.
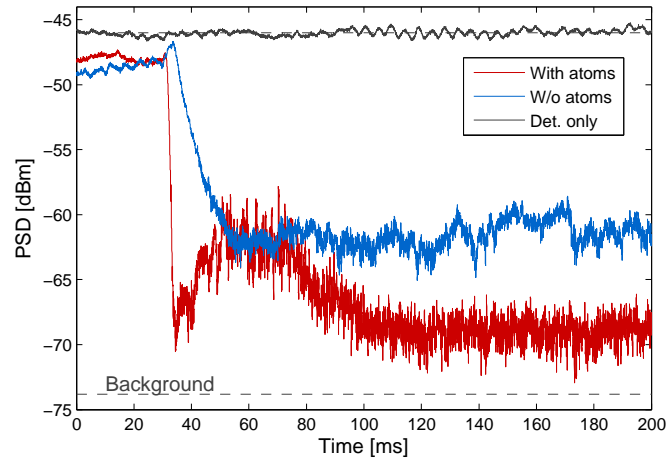
Figure 4.8: Exemplary trace showing the unexpected sudden increase in membrane amplitude after the initial sympathetic cooling.

peratures, like the additional atomic cooling factor, can however be measured with a precision given by equation 1.104 as they do not require an absolute temperature calibration.

Note that for the measurement presented in this section the MOT loading time was varied only within a very small range ((0-300) ms). For longer loading times, occasionally sudden increases in the membrane temperature after the initial temperature decline appeared in the data as exemplary depicted in figure 4.8. This made a meaningful evaluation of the minimum temperature for longer loading times impossible. Looking back in time, these temperature increases were probably the first indications of the delay-induced instability which will be studied in the next chapter.

Parameter	Exp 1a)	Exp 1b)	Exp 2	Exp 3	Exp 4	Exp 5	Exp 6
Which atomic cloud?	old mol	old mol	*weak MOT*	new mol	old mol	old mol	*weak MOT*
Atomic density n_a [$10^{15}\,\mathrm{m^{-3}}$]	8.6	8.6	300	60	≈ 4	≈ 4	0-45
Cloud radius R_a [mm]	3.5	3.5	1.1	1.9	3.5	3.5	0-0.6
Atomic damping rate Γ_a [$\mathrm{s^{-1}}$]	1×10^4	1×10^4	not meas.	0.5×10^4	1×10^4	1×10^4	not meas.
L.-atom det. $\Delta_{\mathrm{LA}}/(2\pi)$ [GHz]	-8	-8	-8.2	+1	-8	-3.3	-4.2
Ingoing power P_0 [mW]	16.5	16.5	19.1	5.6	0-50	0-24	13.5
Power transmission t^2	0.8	0.8	0.47	0.47	0.8	0.41	0.47
Lattice power at start [mW]	5.5	5.5	0.1	5.6	5.5	5.5	0.1
Cavity finesse F	140	300	711	600	140	711	not meas.
Cavity incoupling eff. η^2	0.69	0.69	1	1	0.69	1	1
Coupling strength G	$G_{\max}$	$G_{\max}$	$G_{\max}$	$0.72 G_{\max}$	$0.92 G_{\max}$	$G_{\max}$	$0.7 G_{\max}$
Power in PDH beam [μW]	200	200	100	100	200	100	100
Laser-cavity detuning Δ/κ	-0.013(4)	-0.019(2)	not meas.	-0.07	-0.028(4)	-0.075	-0.118
Opt. cool rate Γ_{opt} [$\mathrm{s^{-1}}$]	**17(3)**	**169(62)**	87.2(1)	**39**	**0-90**	**0-225**	106(15)
Symp. cool rate Γ_{sym} [$\mathrm{s^{-1}}$]	**103(26)**	**390(138)**	1399(7)	1043(95)	**57(5)**	**413(18)**	0-640
Total cool rate Γ_{tot} [$\mathrm{s^{-1}}$]	**122(22)**	**535(191)**	1487(7)	1082(95)	**0-147**	**0-638**	106-746
Coupling constant g_N [$\mathrm{s^{-1}}$]	683(86)	1329(235)		1666(76)	508(22)	1587(35)	
Cooperativity $C = \Gamma_{\mathrm{sym}}/\Gamma_m$	180(46)	684(242)	1457(8)	1087(99)	100(9)	430(19)	667
$\Gamma_{\mathrm{sym,theo}}$ [$\mathrm{s^{-1}}$]	130	606	35700	4420	60	1270	

Table 4.1: Summary of parameters and results of the sympathetic cooling experiments. The damping rates which are printed bold are determined from temperature measurements, taking the increase in the bath temperature T_{bath} due to laser noise into account. The other damping rates are inferred from the slopes in time-resolved measurements. Missing quantities could not be calculated because Γ_a was unknown. $g_N = (\Gamma_a \Gamma_{\mathrm{sym}}/4)^{1/2}$. The expected sympathetic cooling rate $\Gamma_{\mathrm{sym,theo}}$ has been calculated using equation 1.134.

4.5 Conclusion

In this chapter I presented a collection of measurements on sympathetic cooling of the membrane motion. The mechanism was exploited to cool the temperature of the fundamental membrane mode from room temperature ($\bar{n}_{\mathrm{th}} = 2.3 \times 10^7$ phonons) down to a minimal temperature of $T_{\mathrm{sym}} = 0.4(2)\,\mathrm{K}$, corresponding to a phonon occupation of $\bar{n}_{\mathrm{f}} = 3.0(1.5) \times 10^4$. In this measurement the minimal optomechanical temperature was only $T_{\mathrm{opt}} = 2.4(1.2)\,\mathrm{K}$. The membrane was cooled with a sympathetic cooling rate of $\Gamma_{\mathrm{sym}} = 413(18)\,\mathrm{s}^{-1}$, which corresponds to a coupling strength of $g_{\mathrm{N}} = 1.6 \times 10^3\,\mathrm{s}^{-1}$ and $N_{\mathrm{r}} = 2.0 \times 10^4$ resonantly coupled atoms.

Our experiments show for the first time a significant reduction of the membrane temperature via the coupling to an atomic ensemble. The mass ratio of the membrane and the resonantly coupled atoms is $M/(N_{\mathrm{r}}m) = 4 \times 10^{10}$. Impressively, the light-mediated atom-membrane interactions still cool the membrane by a factor 750 below room temperature. Sympathetic cooling with similar cooling factors and final temperatures was observed on large molecular ions in an ion trap [152]. However, in this experiment the mass ratio between the target and coolant species was only ~ 90.

Up to now, we observe sympathetic cooling as a very robust phenomenon. It works with different membrane-cavity setups, various laser-cooling settings and red or blue coupling lattice detuning.

The optomechanical behavior of both membrane-cavity systems used in this chapter is limited by noise, either on the laser intensity and frequency or on the cavity piezos. As some optomechanical coupling is always present in our system, this limits the minimal observable temperature. The sympathetic cooling is limited by the strong inhomogeneous broadening of the atomic ensemble. If the atoms were not smeared out over the lattice profile but localized in the center of the atomic trap, the atom-membrane coupling would be even more efficient. Some measurements might be limited by delay effects, which will be discussed in the next chapter.

In section 1.3.5 I introduced the atom-membrane cooperativity C and the atom-membrane quantum cooperativity C_{qu} as key parameters for the ability of the coupled system to coherently exchange energy between atoms and membrane and to do experiments in the quantum regime. Table 4.1 summarizes settings and results of the various experiments presented in this chapter. The cooperativity C exceeds one in all experiments with a maximum of $C = 1457(8)$ in experiment 2. Our coupled atom-membrane system thus allows to observe interference phenomena analog to EIT. For this the system has to run in a regime in which the optomechanical damping rate Γ_{opt} not too large, as optomechanical damping broadens the effective membrane linewidth and by this reduces C. In principle, this is achievable by reducing Δ_{LA} and with this P_0 and the ingoing power into the cavity. However, we will see in the next chapter that using small detunings on the atomic side can take the system into an unstable regime if the coupling is too large.

The criterion for ground state cooling $C_{\mathrm{qu}} = C/\bar{n}_{\mathrm{bath}} > 1$ is far from being fulfilled, even in experiment 2, where $C_{\mathrm{qu}} = 6.3 \times 10^{-5}$. However, it is shown in

[69] and the supplementary material of [55] that the mechanical ground state can be reached with realistic improvements, most importantly a reduction of the bath temperature to $T_{\mathrm{bath}} = 4\,\mathrm{K}$ in a cryogenic environment, an increase in the atomic density to $n_{\mathrm{a}} = 1 \times 10^{17}\,\mathrm{m}^{-3}$ and a suppression of technical laser noise. Note that in our system optomechanical damping is not only weaker than the sympathetic cooling (see table 4.1) but also unable to provide ground state cooling due to the large cavity linewidth κ. For sympathetic cooling into the ground state on the other hand, the resolved sideband condition $\kappa \ll \Omega_{\mathrm{m}}$ is not required. In the outlook of this thesis I will give an overview over a new setup which is currently being built with the goal to reach the quantum regime.

Chapter 5

Self-oscillations in a delay-coupled atom-optomechanical system

In this chapter I will investigate a dynamical instability which arises in our hybrid system if it is operated in a regime of small coupling lattice detunings and if the number of atoms in the lattice volume is large. The effect was encountered when we attempted to see signatures of mechanically-induced transparency (MIT). The MIT dip in the motional atomic excitation spectrum is expected to broaden in presence of an optomechanical damping rate Γ_{opt}. Thus, in order to achieve a pronounced dip, we pushed the coupling beam to the limits of small atom-laser detuning and small laser power to reduce the power on the membrane and with this Γ_{opt}.

Operating at small atom-light detuning causes an instability, which takes the coupled atom-membrane system into self-oscillations at a large amplitude. This effect is not predicted by the theory presented in chapter 1.3. The instability can be explained by a delay in the coupling between atom and membrane. We learned that any delay in the system, e.g. the finite propagation delay between atoms and membrane, is a potential source of self-oscillations, which limit the sympathetic cooling performance. With a series of experiments we figured out that the propagation delay is of minor importance, but that the main origin of the delay is an effective retardation in the backaction of the atomic ensemble onto the light field. Most likely this retardation is caused by collective effects within the atomic ensemble.

In the following I will present our main experimental observations and discuss the coupled system in presence of a delay. Further, I will present an extended model of the atomic ensemble and numerical simulations, which show that collective effects in the ensemble lead to an effective delay in the atomic backaction.
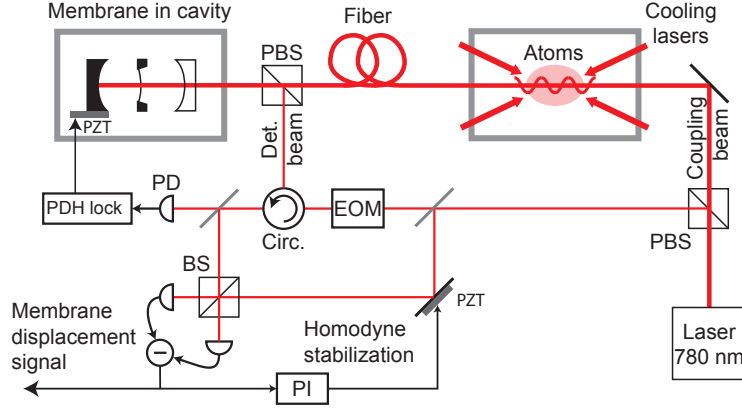
Figure 5.1: Second-generation coupled atom-membrane system. The atoms and the membrane-cavity-system are resting in separate vacuum chambers. A 780 nm diode laser (TA-pro, Toptica) is split into the coupling beam and a detection and locking beam. A large fraction is split off the detection and locking beam and acts as local oscillator for a homodyne measurement. An EOM modulates sidebands onto this beam for Pound-Drever-Hall (PDH) error signal generation. The reflected PDH signal is coupled out at an optical circulator and split in two parts. A smaller part is used to lock the cavity frequency to the laser frequency via a piezo attached to the cavity back mirror. The bigger part is mixed with the local oscillator beam on a beam splitter for homodyne detection of the membrane signal. Figure courtesy of Tobias Kampschulte.

5.1 Experimental setup

The experiments presented in this chapter were performed with the second generation of the hybrid system presented in the chapters 2 and 3. For all experiments the MOT was running in the high-magnetic-field-gradient configuration ($B_{\mathrm{MOT}} = 24\,\mathrm{G/cm}$) characterized in section 3.7.1, which produces large and dense but rather warm atomic clouds (see figure 3.6). Figure 5.1 illustrates the coupled setup. The second-generation membrane-cavity setup and the atomic ensemble are connected via a fiber because the two systems are resting on different optical tables (separation $\approx 10\,\mathrm{m}$).

Throughout the chapter, the membrane has been placed to a position at which the cavity finesse is $F = 570$ (slightly lower than the maximum value $F_{\mathrm{max}} = 711$), the cavity linewidth is $\kappa = 2\pi \times 290\,\mathrm{MHz}$ and the single photon coupling strength is $g_0 = 0.63\,g_{0,\mathrm{max}}$. This was done to avoid large optical spring effects which would bring the membrane frequency in a regime where a series of noise peaks on the membrane displacement spectrum disturb the measurement (see section 2.4.2). In the second-generation membrane-cavity setup, the cavity incoupling efficiency of the incoming mode to the cavity TEM$_{00}$ mode η is almost perfect, $\eta \approx 1$. The power in the coupling beam gets reduced by a factor $t^2 \approx 0.5$ on the way between atoms
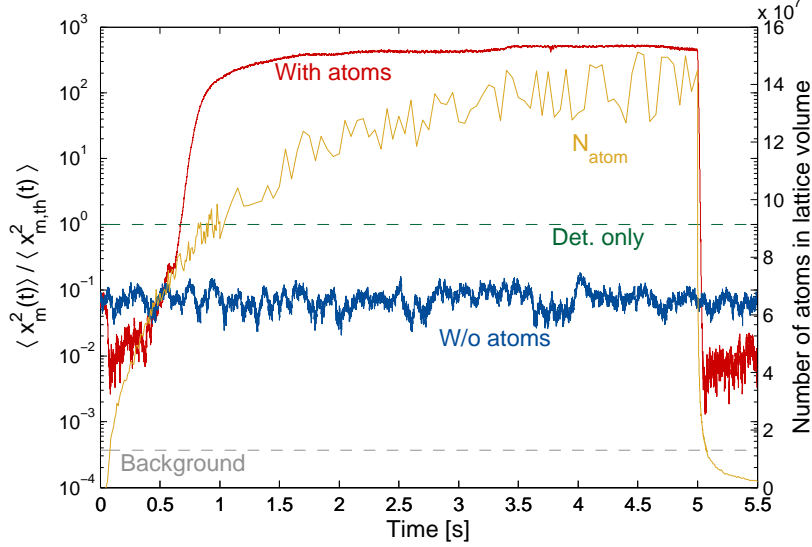
Figure 5.2: Occurrence of self-oscillations. The red, blue, green and gray lines show the mean squared membrane amplitude $\langle x_m^2(t)\rangle$ in units of the room temperature value $\langle x_{m,th}^2(t)\rangle$ (left axis) in different situations versus time during the MOT loading phase (0 s - 5 s) and a subsequent molasses cooling phase (5 s - 5.5 s). Red: with atoms, blue: without atoms, grey: background signal, green: detection light level. The temporal averages of the detection and background signal are shown for better visibility. The yellow trace (right axis) shows the number of atoms in the lattice volume recorded with the on axis imaging beam (*Imaging 2b*). The power reflectivity in the experiment is $R = 24\%$.

and membrane, where t is the single pass amplitude transmission between atoms and membrane. Thus $R = \eta^2 t^4 \approx t^4 \approx 0.25$ of the power gets reflected back to the atoms. Due to the fiber coupling, this factor varies slightly in-between measurements and is therefore specified for each experiment. If not mentioned otherwise, we set the laser-cavity detuning to a small red value, typically $\Delta \approx -0.05\kappa$.

5.2 Experimental observation

5.2.1 Time domain

Figure 5.2 shows the central experimental observation. The data is recorded in an experiment with coupling lattice power, $P_0 = 3.4\,\text{mW}$ and small atom-light detuning $\Delta_{\text{LA}} = -2\pi \times 960\,\text{MHz}$. In contrast to most experiments presented in the previous chapter, the laser power is kept constant throughout the sequence. The power is higher than the threshold power needed for resonant coupling ($\Omega_a(0) = 2\pi \times 396\,\text{kHz} > \Omega_m$, see chapter 4). In the experiment the membrane amplitude during a standard MOT/molasses experiment (see section 3.7.1) is recorded.
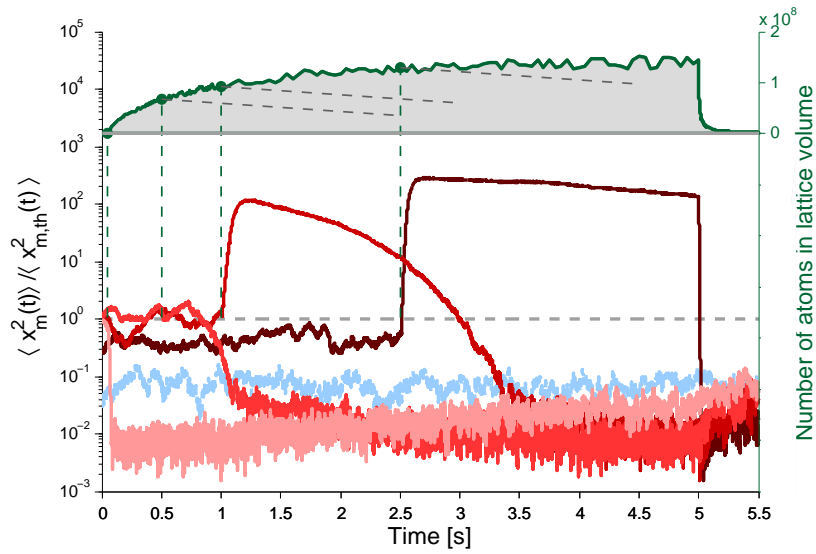
Figure 5.3: Evolution of the mean squared membrane amplitude for several MOT loading times. Loading time = 50 ms, 500 ms, 1 s, 2.5 s from light to dark red. The upper plot shows the atom number in the lattice volume (same data as in figure 5.2). The dashed lines in the upper plot indicate how the atom number in the lattice volume reduces after the stop of the loading. The experiment was performed with laser-cavity detuning $\Delta = -0.06\,\kappa$ and power reflectivity $R = 25\%$.
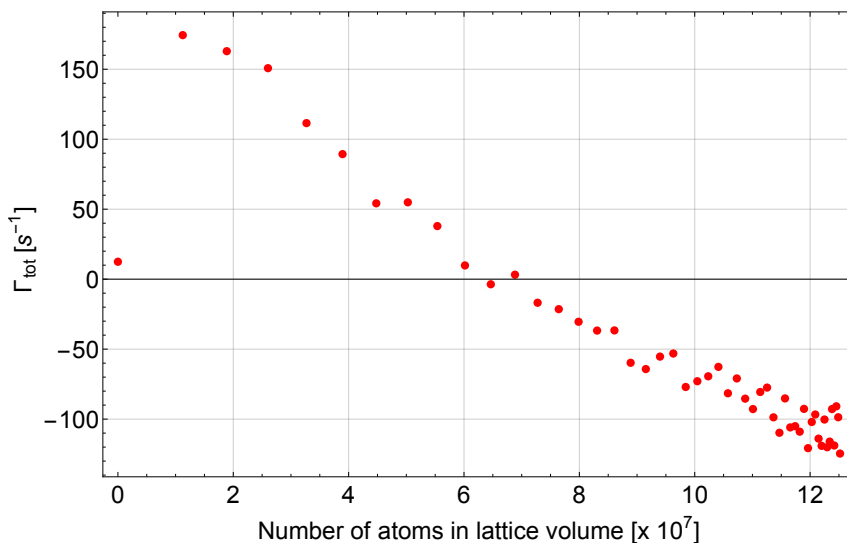
Figure 5.4: Total membrane damping rate $\Gamma_{\text{tot}} = \Gamma_{\text{m}} + \Gamma_{\text{opt}} + \Gamma_{\text{sym}}$, extracted from the initial slope of the membrane amplitude after the sudden turn-on of the lattice power shown in figure 5.3, versus the number of atoms in the lattice volume. The existing theory predicts a linear scaling as $\Gamma_{\text{sym}} \sim N$ (see equation 1.127).

Looking at the red trace (with atoms), one observes that briefly after switching on the MOT, when not very many atoms have been loaded yet[1], the presence of the atoms causes sympathetic cooling. The membrane mean squared amplitude $\langle x_{\text{m}}^2(t) \rangle$ quickly drops below the blue level (without atoms), at which it stays if only optomechanical damping is present in the system. However, for increasing atom number, this sympathetic cooling effect decreases and after a loading time of $0.5\,\text{s}$ the sympathetic cooling stops and loading more atoms leads to an increase of the membrane amplitude, which contradicts our expectation based on the model of chapter 1.3 that the cooling should become stronger. Instead, the membrane amplitude rises quickly up to a maximum value $\langle x_{\text{m}}^2(t) \rangle / \langle x_{\text{m,th}}^2(t) \rangle \approx 400 - 500$ where it stays even if the atom number grows further. As the membrane is not in a thermal state during the self-oscillation phase, I show the mean squared membrane amplitude here rather than the membrane temperature (see equation 1.53). After $5\,\text{s}$ of loading, we switch from MOT to molasses parameters. This massively changes the laser cooling dynamics (see 3.7.1), reducing the atomic temperature and density. Immediately, the membrane amplitude decreases again. Whether the amplitude reduction is solely caused by the change in atomic density, or whether the change in the laser cooling parameters themselves plays a role, cannot be distinguished by this measurement.

---

[1]The atom number in the lattice volume is recorded with the *Imaging 1b* imaging beam.

In the second-generation membrane setup optomechanical effects from the detection beam are small as the probe power is low ($P_{\text{PDH}} = 100\,\mu\text{W}$). Therefore and because I will look at very large signals in the following, I neglect the small difference between the thermal amplitude and the amplitude in presence of the weak detection beam. Throughout this chapter, I will use the measurement done with the detection beam only (green line) to calibrate the membrane amplitude axis.

We suspect from the measurement that there is a critical atom number N_{crit} above which our system becomes unstable. However, it could also be that the effect is not connected to the number of atoms, but kicks in with some delay after the start of our sequence. To rule this out and confirm the atom number dependence, a slightly different experiment was performed.

In the second experiment the MOT is loaded for a variable time to obtain different atom numbers. During this loading time the lattice is kept at very low power such that $\Omega_{\text{a}}(0) \ll \Omega_{\text{m}}$. Subsequently, the MOT loading is stopped so that the atom number stays constant. It then actually starts to decrease slowly on a timescale much longer than the self-oscillation dynamics as indicated by the gray dashed lines of the atom number plot in figure 5.3. Simultaneously to switching-off the loading, the lattice power is ramped up in 10 ms to $P_0 = 3.4\,\text{mW}$. Figure 5.3 shows exemplary traces for four different loading times. When loading the trap for 50 ms, (lightest red curve) not very many atoms are loaded. However, as soon as the lattice is turned on and atoms can couple to the membrane, one sees strong sympathetic cooling of the membrane below the optomechanical cooling level (light blue curve). When the atom number decreases after the stop of the loading, the sympathetic cooling decreases as well as we expect from our present theory, $\Gamma_{\text{sym}} \propto N$. For a loading time of 500 ms (bright red curve) the membrane amplitude does not react immediately to the turn-on of the light. Only after a while, when some atoms have been lost from the MOT, the membrane amplitude decreases. If we load even more atoms, as for the last two traces (darkest red curves), the membrane amplitude initially increases after the turn-on instead of decreasing, before it slowly decreases again when atoms are lost. Thus, it seems that the appearance of the self-oscillation is indeed connected to the number of atoms present in the lattice volume. Specifically, there is a threshold atom number above which the system becomes unstable.

From the slopes of $\langle x_{\text{m}}^2(t) \rangle$ after the turn-on of the coupling lattice, one can extract the total membrane damping rate Γ_{tot}. Note that $\Gamma_{\text{tot}} > 0$ corresponds to damping, while $\Gamma_{\text{tot}} < 0$ corresponds to amplification of the membrane oscillations. It is plotted in figure 5.4 versus the number of atoms in the lattice volume at the end of the loading time. The total membrane damping rate is the sum of the intrinsic membrane damping rate $\Gamma_{\text{m}} = 0.96\,\text{s}^{-1}$, the optomechanical damping rate $\Gamma_{\text{opt}} = 10.6\,\text{s}^{-1}$ and the sympathetic cooling rate Γ_{sym}, $\Gamma_{\text{tot}} = \Gamma_{\text{m}} + \Gamma_{\text{opt}} + \Gamma_{\text{sym}}$. The optomechanical damping rate Γ_{opt} has been inferred from the temporal average of the measurement without atoms using equation 1.59. Of the three terms in Γ_{tot} only the last one depends on N. However, the atom number dependence is strikingly different from the linear dependence we expect from from equation 1.127. In section 5.3.3 I will show that the observed dependence $\Gamma_{\text{tot}}(N)$ can be modeled
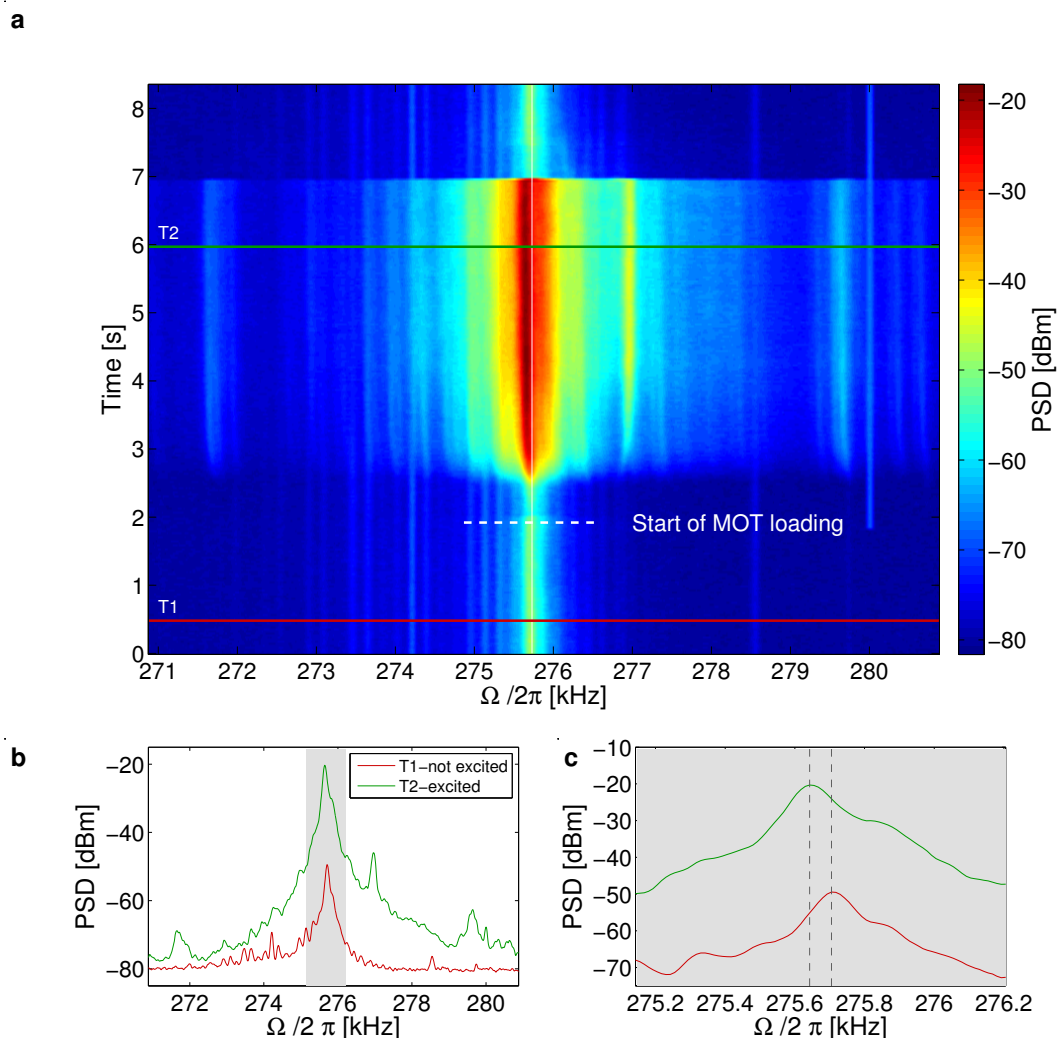
Figure 5.5: a) Membrane spectrum $S_x(\Omega)$ versus time in units of electrical power. The white dashed line marks the start of the MOT-loading. The red and the green line before the MOT loading and during the excitation mark times for exemplary spectra shown in b) and c). The vertical white line is plotted as a guide to the eye. b) Exemplary membrane spectra for excited and non-excited case referring to the times marked by the red and the green line in plot a). c) Zoom into the gray region of plot b). Experimental settings: atom-laser detuning $\Delta_{\mathrm{LA}} = -2\pi \times 960\,\mathrm{MHz}$, lattice power: $P_0 = 4.6\,\mathrm{mW}$, reflectivity: $R = 29\%$, atomic center frequency: $\Omega_{\mathrm{a}}(0) = 2\pi \times 480\,\mathrm{kHz}$, laser-cavity detuning: $\Delta = -0.037\kappa$. A new spectrum was recorded every $30\,\mathrm{ms}$ with a frequency resolution of $12.5\,\mathrm{Hz}$ and a measurement bandwidth of $50\,\mathrm{Hz}$. The data is averaged over 29 identical experiments.
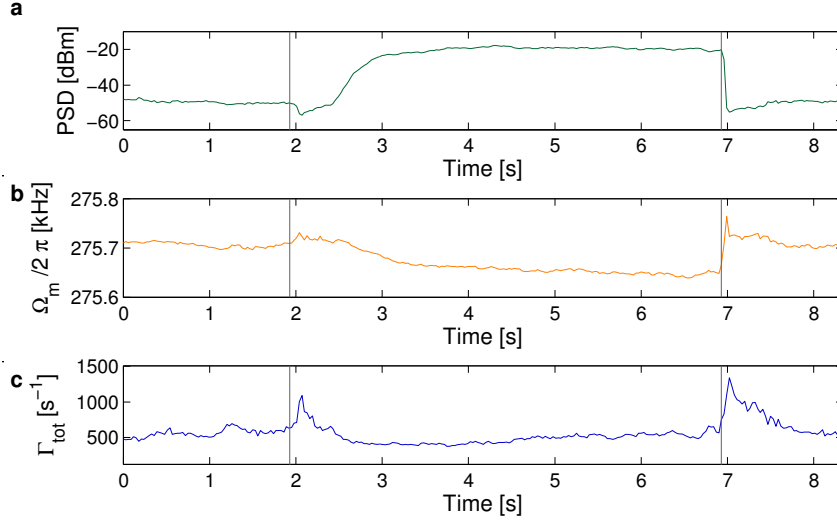
Figure 5.6: The plots show a) the membrane amplitude, b) the center frequency, and c) the linewidth of the central peak extracted from Lorentzian fits to the spectrum in figure 5.5. The two vertical black lines mark the start of the MOT-loading and the transition to molasses parameters, respectively.

by including a delay in the atom-membrane coupling.

5.2.2 Frequency domain

The measurements shown before were done in the time domain with no spectral information. To learn in which way the membrane spectrum changes when the system self-oscillates, the first experiment was repeated, and in addition to the temporal also the spectral information was recorded using a real-time spectrum analyzer. Figure 5.5 a) shows how the membrane spectrum evolves with time. The recording starts slightly before the start of the MOT-loading, which is marked by the white dashed line at $\approx 2\,\mathrm{s}$. In the initial part, below the white line, one sees the membrane signal in absence of atoms. The membrane amplitude shortly decreases after the MOT loading starts and then it increases drastically. After $5\,\mathrm{s}$ the laser cooling settings are changed from MOT to molasses settings which drastically reduces the membrane amplitude. Plot b) compares a spectrum taken without atoms (red line) to a spectrum taken during the excited phase of the membrane (green line). Plot c) shows a zoom into the gray area in plot b). Besides being of much larger amplitude, the maximum of the green line is displaced by $62.5\,\mathrm{Hz}$ towards lower frequencies compared to the maximum of the red line.

Figure 5.6 illustrates the results of Lorentzian fits to each line of the spectrum in figure 5.5 a). It shows the fitted amplitude of the central peak, its frequency Ω_m and the linewidth Γ_tot, respectively. One sees that the central frequency moves towards lower frequencies when the membrane becomes excited, and that it jumps
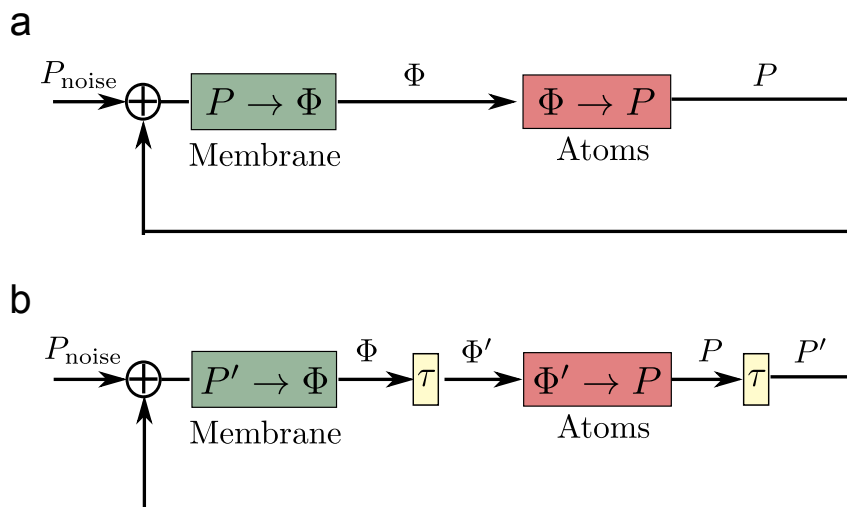
a

b

Figure 5.7: Box schematic of the coupled atom-membrane system. The black lines indicate the lattice light which travels from atoms to membrane and vice versa. P and Φ are fluctuations of the power and the phase of the light. The figure illustrates that the coupled system forms a closed loop, in which the membrane converts power modulations of the light into phase modulations and the atoms convert phase modulations into power modulations. a) without delay b) with delay.

back immediately when the setting are changes to molasses cooling. The measured linewidth Γ_{tot} in absence of atoms is ($\approx 550\,\mathrm{s}^{-1}$) is much broader than the $\approx 10\,\mathrm{s}^{-1}$ expected from the previous measurement due to slow shot to shot fluctuations in the center frequency. The membrane frequency is shifted by $\delta\Omega_{\mathrm{m}} \approx -2\pi \times 1\,\mathrm{kHz}$ due to the optical spring effect. As the lattice power is not stabilized on the membrane side of the setup, the optical spring effect drifts by $\pm 5\%$ in between measurements, which strongly broadens the narrow line. Still, one sees how the damping rate increases when atoms are loaded and then reduces again. Qualitatively, this matches the behavior seen in figure 5.4. Further one sees a strong increase in damping as soon as the laser-cooling settings are switched to molasses cooling.

5.3 Theory of a coupled atom-membrane system with delay

So far we model the atom-membrane system as two coupled and damped harmonic oscillators, of which one, the membrane, experiences a fluctuating thermal force $F_{\mathrm{th}}(t)$ due to the coupling to its support (see section 1.3). In this model, the dynamics of the position of the atomic center-of-mass and the position of the membrane

are described by the equations of motion given in equation 1.117

$$\begin{aligned}
Nm\ddot{x}_{\mathrm{a}}(t) &= -\Gamma_{\mathrm{a}}Nm\dot{x}_{\mathrm{a}}(t) - Nm\Omega_{\mathrm{a}}^2 x_{\mathrm{a}}(t) - Kx_{\mathrm{m}}(t)\,, \\
M\ddot{x}_{\mathrm{m}}(t) &= -\Gamma_{\mathrm{m}}M\dot{x}_{\mathrm{m}}(t) - M\Omega_{\mathrm{m}}^2 x_{\mathrm{m}}(t) - \eta^2 t^2 Kx_{\mathrm{a}}(t) + F_{\mathrm{th}}(t)\,,
\end{aligned} \qquad (5.1)$$

with coupling spring constant $K = \hbar g_{\mathrm{N}}/x_{\mathrm{m},0}x_{\mathrm{a},0}$, where $x_{\mathrm{m},0} = \sqrt{\hbar/2M\Omega_{\mathrm{m}}}$ and $x_{\mathrm{a},0} = \sqrt{\hbar/2Nm\Omega_{\mathrm{a}}}$ are the quantum mechanical zero-point amplitudes of the membrane motion and the atomic center-of-mass motion. Note that here and in the following two equations I use the symbol t for the time and amplitude transmission of the optical path between atoms and membrane. The difference is clear from the context.

This coupled system forms a closed loop as illustrated in figure 5.7 a) similar to a control circuit in electronics [153]. The schematic drawing depicts the power modulations P generated by the motion of the atomic ensemble (see section 1.1.6), the phase modulations Φ generated by a motion of the membrane (see section 1.2.2) and ingoing random power fluctuations P_{noise} coming e.g. from technical laser noise. The formal connections between the power and phase modulations, P and Φ, and the amplitudes of atoms and membrane, x_{a} and x_{m} will be derived in the last part of this chapter. A closed-loop system can become unstable if there is a delay in the system in combination with a too high gain. In our system the latter can occur if the coupling strength is large. Figure 5.7 b) shows the same system in presence of a delay in the coupling between atoms and membrane.

Let's go through the loop step by step to see why the delay can induce self-oscillations. As mentioned above, a motion of the membrane causes a modulation of the phase of the laser light which travels to the atoms. The atomic motion gets influenced by this phase modulation and in turn imprints its motion as a power modulation onto the light which travels back to the membrane. This power modulation affects the motional state of the membrane which closes the loop. If some noise at a given frequency Ω enters the system, e.g. in form of a power modulation in front of the membrane, this noise signal travels through the loop and comes back with a certain phase and amplitude. If the phase, which the noise signal collects, equals an integer multiple of 2π, and if in addition the amplitude of the noise after one round trip is larger than the ingoing amplitude (corresponding to a gain larger than one), the noise signal gets amplified in every loop. Membrane and atoms will then oscillate with larger and larger amplitude at the noise frequency. The equations of motion 5.1 do not allow the collected phase to be 2π for any noise frequency and therefore do not give rise to such instabilities as I will show further down in this chapter. However, a delay in the interaction between atoms and membrane adds a phase-shift $\Omega\tau$ and can induce instable behavior.

5.3.1 Stability analysis of equations of motion with delay

For the moment I ignore the question of the origin of the delay. I simply investigate the coupled system in a situation in which the forces which the atoms exert on the

membrane and vice versa are delayed by a time τ. The equations of motion will then modify to

$$
\begin{aligned}
Nm\ddot{x}_{\mathrm{a}}(t) &= -\Gamma_{\mathrm{a}}Nm\dot{x}_{\mathrm{a}}(t) - Nm\Omega_{\mathrm{a}}^2 x_{\mathrm{a}}(t) - Kx_{\mathrm{m}}(t-\tau)\,, \\
M\ddot{x}_{\mathrm{m}}(t) &= -\Gamma_{\mathrm{m}}M\dot{x}_{\mathrm{m}}(t) - M\Omega_{\mathrm{m}}^2 x_{\mathrm{m}}(t) - \eta^2 t^2 K x_{\mathrm{a}}(t-\tau)\,.
\end{aligned}
\tag{5.2}
$$

Note that I removed the thermal force $F_{\mathrm{th}}(t)$ in the equations above for the stability analysis because we want to learn whether the atom-membrane system itself without any input has unstable solutions or not. If unstable solutions exist, adding the thermal input force will excite these solutions.

To analyze the stability of the system, I look for the solutions of the differential equations 5.2 and make the ansatz

$$
\begin{aligned}
x_{\mathrm{a}}(t) &= x_{\mathrm{a}}(s)e^{st}\,, \\
x_{\mathrm{m}}(t) &= x_{\mathrm{m}}(s)e^{st}\,, \quad s \in \mathbb{C}\,.
\end{aligned}
\tag{5.3}
$$

From the ansatz it is obvious that a solution will be unstable if the real part of s is positive. In this case the solution will diverge.

Plugging the ansatz 5.3 into equation 5.2 leads to

$$
\begin{aligned}
(s^2 + s\Gamma_{\mathrm{a}} + \Omega_{\mathrm{a}}^2)x_{\mathrm{a}}(s) &= -\frac{K}{Nm}e^{-s\tau}x_{\mathrm{m}}(s)\,, \\
(s^2 + s\Gamma_{\mathrm{m}} + \Omega_{\mathrm{m}}^2)x_{\mathrm{m}}(s) &= -\frac{\eta^2 t^2 K}{M}e^{-s\tau}x_{\mathrm{a}}(s)\,.
\end{aligned}
\tag{5.4}
$$

Solving the the first equation for $x_{\mathrm{a}}(s)$,

$$
x_{\mathrm{a}}(s) = -\frac{K}{Nm}\frac{e^{-s\tau}}{s^2 + s\Gamma_{\mathrm{a}} + \Omega_{\mathrm{a}}^2}x_{\mathrm{m}}(s)\,,
\tag{5.5}
$$

and plugging it into the second equation gives

$$
\left(s^2 + s\Gamma_{\mathrm{m}} + \Omega_{\mathrm{m}}^2 - \frac{\eta^2 t^2 K^2}{MNm}\frac{e^{-2s\tau}}{s^2 + s\Gamma_{\mathrm{a}} + \Omega_{\mathrm{a}}^2}\right)x_{\mathrm{m}}(s) = 0\,.
\tag{5.6}
$$

I multiply the whole equation by $s^2 + s\Gamma_{\mathrm{a}} + \Omega_{\mathrm{a}}^2$ to remove the s dependence in the denominator:

$$
\left((s^2 + s\Gamma_{\mathrm{m}} + \Omega_{\mathrm{m}}^2)(s^2 + s\Gamma_{\mathrm{a}} + \Omega_{\mathrm{a}}^2) - \frac{\eta^2 t^2 K^2}{MNm}e^{-2s\tau}\right)x_{\mathrm{m}}(s) = 0\,.
\tag{5.7}
$$

To fulfill this equation for solutions $x_{\mathrm{m}}(s) \neq 0$, the term in the parentheses has to become zero.

$$
(s^2 + s\Gamma_{\mathrm{m}} + \Omega_{\mathrm{m}}^2)(s^2 + s\Gamma_{\mathrm{a}} + \Omega_{\mathrm{a}}^2) - \frac{\eta^2 t^2 K^2}{MNm}e^{-2s\tau} = 0\,.
\tag{5.8}
$$

To make statements about the stability of the system, it is not necessary to know the exact positions of the roots of the function on the left hand side. It is enough to know whether the real part of all roots is negative. If the delay τ is small compared to the time scale of the atom and membrane dynamics $\Omega_{\mathrm{a/m}}\tau \ll 1$, one can replace the exponential term by a first order approximation, $e^{-2s\tau} \approx 1 - 2s\tau$. The function on the left side of equation 5.8 then becomes a polynomial

$$
\begin{aligned}
(s^2 + s\Gamma_{\mathrm{m}} + \Omega_{\mathrm{m}}^2)(s^2 + s\Gamma_{\mathrm{a}} + \Omega_{\mathrm{a}}^2) - \frac{\eta^2 t^2 K^2}{MNm}(1 - 2s\tau) &= 0 \\
\Leftrightarrow s^4 + (\Gamma_{\mathrm{a}} + \Gamma_{\mathrm{m}})s^3 + (\Omega_{\mathrm{a}}^2 + \Omega_{\mathrm{m}}^2 + \Gamma_{\mathrm{a}}\Gamma_{\mathrm{m}})s^2 & \\
+(\Gamma_{\mathrm{m}}\Omega_{\mathrm{a}}^2 + \Gamma_{\mathrm{a}}\Omega_{\mathrm{m}}^2 + 8\eta^2 t^2 g_N^2 \Omega_{\mathrm{a}}\Omega_{\mathrm{m}}\tau)s + \Omega_{\mathrm{a}}\Omega_{\mathrm{m}}(\Omega_{\mathrm{a}}\Omega_{\mathrm{m}} - 4\eta^2 t^2 g_N^2) &= 0 \,, \ (5.9)
\end{aligned}
$$

where in the last step I replaced $K^2/NmM = 4g_N^2 \Omega_{\mathrm{a}}\Omega_{\mathrm{m}}$. The polynomial form allows us to apply the Hurwitz criterion ([153], section 8.3.2), which tells from the coefficients of a polynomial whether all roots will have negative real parts without determining the roots explicitly.

Hurwitz criterion [153, 154]: All roots of the polynomial

$$
p(s) = a_n s^n + a_{n-1}s^{n-1} + a_{n-2}s^{n-2} + ... + a_0 \tag{5.10}
$$

have a negative real part if $a_i > 0 \,, i = 0, 1, ..., n$, and if the determinant

$$
M_n = \begin{vmatrix}
a_{n-1} & a_{n-3} & a_{n-5} & ... & ... & ... & 0 \\
a_n & a_{n-2} & a_{n-4} & ... & ... & ... & 0 \\
0 & a_{n-1} & a_{n-3} & ... & ... & ... & 0 \\
0 & a_n & a_{n-2} & ... & ... & ... & 0 \\
. & . & . & . & . & . & . \\
. & . & . & . & . & . & . \\
. & . & . & . & . & . & . \\
. & . & . & . & . & a_1 & . \\
. & . & . & . & . & a_2 & a_0
\end{vmatrix} \tag{5.11}
$$

and all "north western" sub-determinants M_i, $i = 1...n - 1$ (which are generated by erasing the last $n - i$ columns and rows) are positive.

For our fourth order polynomial the matrix reads

$$
M_4 = \begin{vmatrix}
a_3 & a_1 & 0 & 0 \\
a_4 & a_2 & a_0 & 0 \\
0 & a_3 & a_1 & 0 \\
0 & a_4 & a_2 & a_0
\end{vmatrix} \,, \tag{5.12}
$$
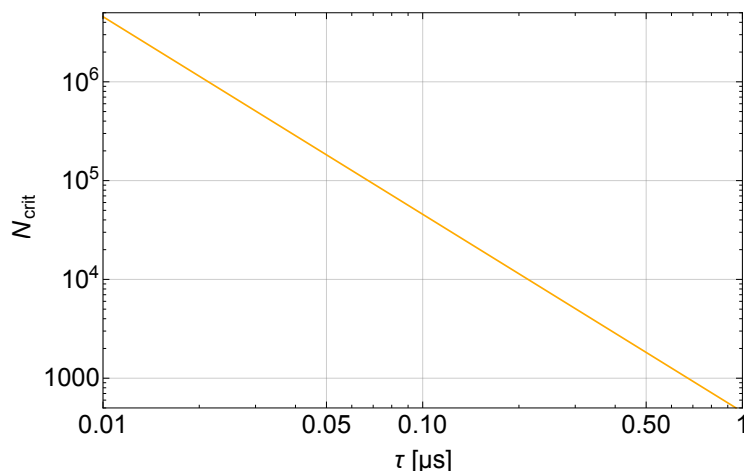
Figure 5.8: Critical atom number versus delay. The curve shows the delay dependence of the critical atom number calculated from the Hurwitz criterion for $M = 120\,\text{ng}$, $F = 600$, $r_{\text{m}}=0.4$, $\Omega_{\text{a}} = \Omega_{\text{m}} = 2\pi \times 275\,\text{kHz}$, $\Gamma_{\text{m}} = 10\,\text{s}^{-1}$, $\Gamma_{\text{a}} = 1000\,\text{s}^{-1}$, $\eta^2 = 1$, $t^2 = 0.55$. A larger membrane damping rate Γ_{m} has been assumed to take optomechanical damping into account.

with

$$
\begin{aligned}
a_4 &= 1\,, \\
a_3 &= \Gamma_{\text{a}} + \Gamma_{\text{m}}\,, \\
a_2 &= \Omega_{\text{a}}^2 + \Omega_{\text{m}}^2 + \Gamma_{\text{m}}\Gamma_{\text{a}}\,, \\
a_1 &= \Gamma_{\text{m}}\Omega_{\text{a}}^2 + \Gamma_{\text{a}}\Omega_{\text{m}}^2 + 8\eta^2 t^2 g_N^2 \Omega_{\text{a}}\Omega_{\text{m}}\tau\,, \\
a_0 &= \Omega_{\text{a}}\Omega_{\text{m}}(\Omega_{\text{a}}\Omega_{\text{m}} - 4\eta^2 t^2 g_N^2)\,.
\end{aligned}
\tag{5.13}
$$

Application of the Hurwitz criterion leads to the following stability criteria:

$$
\begin{aligned}
C_1 : \quad & a_i & > 0\,, \\
C_2 : \quad & a_3 a_2 & > a_4 a_1\,, \\
C_3 : \quad & a_3 a_2 a_1 & > a_4 a_1^2 + a_3^2 a_0\,.
\end{aligned}
\tag{5.14}
$$

The first condition C_1 holds as long as $\Omega_{\text{a}}\Omega_{\text{m}} > 4\eta^2 t^2 g_N^2$, which is very well fulfilled in our system. In an intuitive picture, this condition means that the major part of the potential seen by the oscillators has to come from the restoring force and not from the coupling.

Moreover, we see that if all coefficients are positive, fulfilling condition C_3 implies that condition C_2 is fulfilled as well. Thus, condition C_3 is the relevant one for our system. Solving condition C_3 for the number of atoms N, gives a condition

$N < N_{\mathrm{crit}}$, which the atom number has to fulfill to keep the system stable. For $\Gamma_{\mathrm{m}} \ll (\Gamma_{\mathrm{a}}, \Omega_{\mathrm{a}}, \Omega_{\mathrm{m}}, \tau\Omega_{\mathrm{a}}^2)$ and $\Gamma_{\mathrm{m}}\tau \ll 1$, and using equation 1.119 this critical atom number can be written as

$$N_{\mathrm{crit}} \approx \frac{\Gamma_{\mathrm{a}}^2 + 2\tau(\Gamma_{\mathrm{a}} - \Gamma_{\mathrm{m}})(\Omega_{\mathrm{a}}^2 - \Omega_{\mathrm{m}}^2) + \Gamma_{\mathrm{a}}\sqrt{\Gamma_{\mathrm{a}}^2 + 4\tau^2(\Omega_{\mathrm{m}}^2 - \Omega_{\mathrm{a}}^2)^2}}{32\eta^2 t^2 g_1^2 \tau^2 \Omega_{\mathrm{a}} \Omega_{\mathrm{m}}} \,, \tag{5.15}$$

with g_1 being the coupling strength of a single atom. For $\tau \to 0$ the term on the right side diverges. In this case the system is stable for all N. And indeed, the inequality shows that a finite delay in the coupling is accompanied by a critical, maximum atom number N_{crit}, above which the system becomes unstable. This fits to the experimental observation of a critical atom number visible in figure 5.4. Figure 5.8 shows how the critical atom number depends on the delay for our system parameters. We see that a $100\,\mathrm{ns}$ delay, which is rather short compared to the oscillation period of the system $T = 1/(275\,\mathrm{kHz}) = 3.64\,\mu\mathrm{s}$, requires an atom number of $\approx 5 \times 10^4$. This is easily reached in our system.

5.3.2 Modified sympathetic cooling rate

The stability criterion, that is discussed above, tells us whether the system is stable or not. It does not make statements about the damping respectively heating rate which the membrane experiences. One can extract the membrane damping rate from the effective membrane susceptibility in presence of the atoms and the delay, similar to the derivation done in section 1.2.4. I do this by comparing the modified membrane susceptibility to the susceptibility of the uncoupled membrane

$$\chi_{\mathrm{m}}(\Omega) = [M(\Omega_{\mathrm{m}}^2 - \Omega^2 + i\Omega\Gamma_{\mathrm{m}})]^{-1} \,. \tag{5.16}$$

Note that the membrane frequency Ω_{m} is equal to the zero-crossing of $\mathrm{Re}\,\chi_{\mathrm{m}}[\Omega]^{-1}$ and the damping rate Γ_{m} is equal to $\mathrm{Im}\,\chi_{\mathrm{m}}[\Omega_{\mathrm{m}}]^{-1}/M\Omega_{\mathrm{m}}$. This assignment must also hold in the coupled, delayed case. Therefore, I determine the effective damping rate by evaluating the imaginary part of the membrane susceptibility at the zero crossing of its real part. The complete calculation is presented in appendix A. By Fourier transforming the equations of motion one finds for the effective membrane susceptibility in presence of the atoms and a small delay ($\Omega_{\mathrm{a/m}}\tau \ll 1$)

$$\chi_{\mathrm{m,eff}}(\Omega) = \left[M\left(\Omega_{\mathrm{m}}^2 - \Omega^2 + i\Omega\Gamma_{\mathrm{m}} - \frac{\eta^2 t^2 K^2(1 - 2i\tau\Omega)}{NmM(\Omega_{\mathrm{a}}^2 - \Omega^2 + i\Omega\Gamma_{\mathrm{a}})} \right) \right]^{-1} \,. \tag{5.17}$$

Note that except for a factor M the susceptibility equals the term in parentheses in equation 5.6 for $s = i\Omega$ and in the limit $\Omega\tau \ll 1$. The expression I find for the new global membrane damping rate $\Gamma_{\mathrm{tot}} = \Gamma_m + \Gamma_{\mathrm{sym}}$ with a modified sympathetic damping term Γ_{sym} is quite complicated. It can be simplified in the case of resonant
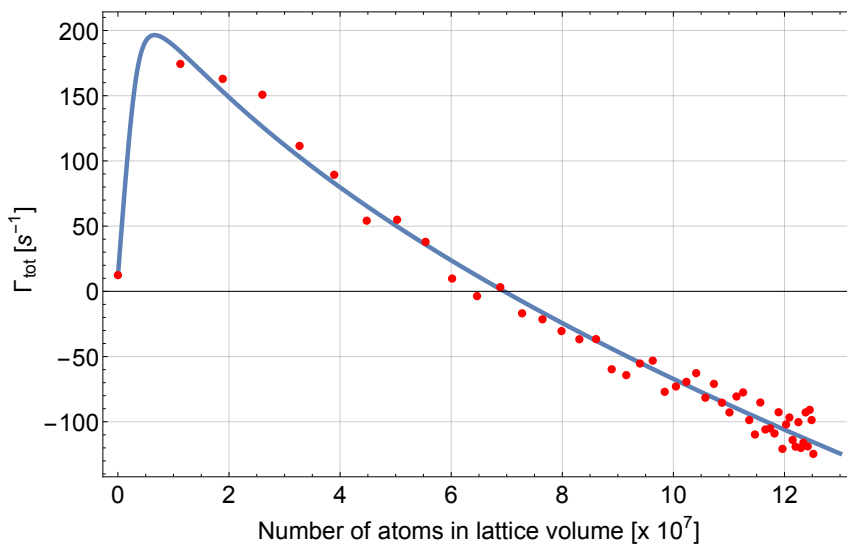
Figure 5.9: The plot shows a fit of the model in equation 5.19 to the data from the experiment described in the beginning of the chapter (see figure 5.4). The system parameters are summarized in table 5.1.

coupling $\Omega_a = \Omega_m$ and by making the following assumptions

$$
\begin{aligned}
\Gamma_a \tau &\ll \frac{1}{2}, \\
\Gamma_a &\ll \Omega_a, \\
\Gamma_a &\ll 6\tau\Omega_a^2, \\
\Gamma_a^3 &\ll 24\eta^2 t^2 g_N^2 \tau \Omega_a^2.
\end{aligned} \tag{5.18}
$$

The modified sympathetic damping rate then reads

$$
\begin{aligned}
\Gamma_{\text{sym}} &= \frac{1}{9\Gamma_a(4\eta^2 t^2 g_N^2 - \Gamma_a^2)} [48\eta^2 t^2 g_N^4 + 12\eta^2 t^2 g_N^2 \Gamma_a^2 - 6\Gamma_a^4 \\
&\quad - 3^{\frac{1}{3}}(36\eta^2 t^2 g_N^2 \Gamma_a \tau \Omega_a - \sqrt{\dots})(36\eta^2 t^2 g_N^2 \Gamma_a \tau \Omega_a + \sqrt{\dots})^{\frac{1}{3}} \\
&\quad - 3^{\frac{2}{3}}(4\eta^2 t^2 g_N^2 - \Gamma_a^2)(36\eta^2 t^2 g_N^2 \Gamma_a \tau \Omega_a + \sqrt{\dots})^{\frac{2}{3}}],
\end{aligned} \tag{5.19}
$$

$$
\text{where} \quad \sqrt{\dots} = \sqrt{(36\eta^2 t^2 g_N^2 \Gamma_a \tau \Omega_a)^2 - 3(4\eta^2 t^2 g_N^2 - \Gamma_a^2)^3}. \tag{5.20}
$$

5.3.3   Fit to measured total damping rate

The modified expression for Γ_{sym} can be used to fit the data from figure 5.4. Most of the parameters in equation 5.19 can be measured independently. They are listed in table 5.1. Furthermore, the number of resonant atoms, which participate in the

Parameter	Value
Effective membrane mass M	$117\,\mathrm{ng}$
Membrane reflectivity r_m	0.4
Cavity finesse F	570
Mechanical frequency Ω_m	$2\pi \times 275\,\mathrm{kHz}$
Mechanical damping rate Γ_m	$11.5\,\mathrm{s}^{-1}$
Transmission of optical path t^2	0.5
Cavity incoupling efficiency η^2	1

Table 5.1: Independently measured system parameters. Γ_m includes the optomechanical damping rate.

coupling, is set to $N_\mathrm{r} = N_\mathrm{lat}(\pi\Gamma_\mathrm{a}/2\Omega_\mathrm{m})$ (see section 1.3.4). The unknown delay τ and the atomic damping rate in the MOT phase Γ_a are left as fit parameters. A fit of the full expression for Γ_tot to the data gives $\tau = 88(1)\,\mathrm{ns}$ and $\Gamma_\mathrm{a} = 337(10)\,\mathrm{s}^{-1}$, setting the fraction of resonant atoms to $\pi\Gamma_\mathrm{a}/2\Omega_\mathrm{m} = 3 \times 10^{-4}$. If find reasonable looking fits also for slightly higher and lower fractions of resonant atoms up to two times larger (fitresults: $\tau = 61(1)\,\mathrm{ns}$, $\Gamma_\mathrm{a} = 326(8)\,\mathrm{s}^{-1}$) or five times smaller (fitresults: $\tau = 217(5)\,\mathrm{ns}$, $\Gamma_\mathrm{a} = 428(27)\,\mathrm{s}^{-1}$). Note that within this parameter range the assumptions I made to derive the expression for Γ_sym are justified.

5.3.4 Conclusion

In this section we learned that in presence of a delay in the coupling between atoms and membrane there is a critical atom number above which the system becomes unstable. Strictly speaking not the delay but the phase-shift induced by the delay, $2\Omega_\mathrm{m}\tau$, generates the instability. The modified sympathetic cooling rate of the coupled system with delay allows to model the measured data nicely. This suggests that indeed some delay with a duration of $\tau = 88(1)\,\mathrm{ns}$ is responsible for the self-oscillations. The origin of the delay is not entirely clear yet. In the following sections I will present further experiments and theoretical modeling that aim at identifying the mechanism which causes the delay.

5.4 Retardation between the systems

The most obvious source of a delay in our system is the finite distance between the atoms and the membrane. In the experiments presented in the beginning of the chapter the atoms and the membrane were separated by $6.5\,\mathrm{m}$ involving $5\,\mathrm{m}$ of fiber in which the speed of light is even slower. With a refractive index of $n \approx 1.5$ inside the fiber one finds $\tau_\mathrm{distance} = (l_\mathrm{freespace} + nl_\mathrm{fiber})/c = 30\,\mathrm{ns}$, where c is the speed of light. Further the membrane rests inside the cavity, so information from the atoms needs an extra time $\tau_\mathrm{cavity} = \kappa^{-1} = 0.6\,\mathrm{ns}$ to enter the cavity. Summed up, information needs $\tau = \tau_\mathrm{distance} + \tau_\mathrm{cavity} = 33.5\,\mathrm{ns}$ to travel between atoms and
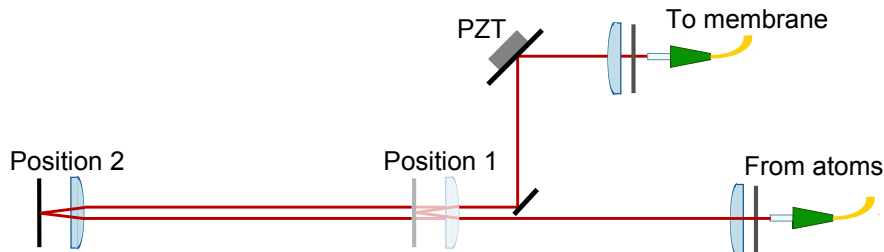
Figure 5.10: Free space part of the setup used to vary the propagation distance.

membrane via light. This seems not too far away from the $\tau = 88\,\text{ns}$ found from the fit in the last section. Motivated by this observation, we started to do experiments with varying distances between atoms and membrane to see whether the threshold atom number is influenced by this as expected from figure 5.8.

5.4.1 Varying the propagation distance

In a first attempt we varied the distance between atoms and membrane simply by replacing the optical fiber between the systems with shorter and longer ones. However, changing the fiber involves recoupling the light into the cavity, which is very time-demanding. To speed up the measurement, we decided to use a setup which is better adapted to the task of changing the length quickly without changing the beam at the membrane or atomic side. In the surroundings of membrane and atoms the setup from figure 5.1 was not changed. Only the fiber between atoms and membrane part was removed and replaced by two short (1 m and 2 m) fibers and the free space setup shown in figure 5.10. In the free space part a movable cat-eye element, which reflects an identical but displaced mode, allows to change the beam path length quickly. The reflected beam is coupled into the fiber towards the membrane. When changing the cat-eye position, only a slight realignment of the cat-eye back-mirror position is necessary to re-optimize the membrane-fiber coupling.

Figure 5.11 shows the results of experiments similar to the first experiment presented in this chapter (figure 5.2). The lattice is running continuously and we observe the membrane signal during the loading phase of the MOT $(0 - 5\,\text{s})$ and the subsequent molasses phase. The laser power is significantly higher than in the prior experiments $P_0 = 11.4\,\text{mW}$ and the amount of reflected power is lower $R = 0.10$, corresponding to $\Omega_\text{a}(0) = 2\pi \times 581\,\text{kHz}$. The traces show measurements taken with the cat-eye at position 1 (red traces, total atom-membrane light traveling time 25 ns) and position 2 (blue traces, total traveling time 40 ns). One sees that the red signals rise at slightly later times. Therefore, this configuration must have a slightly higher critical atom number. However, the time shift is extremely small although we varied
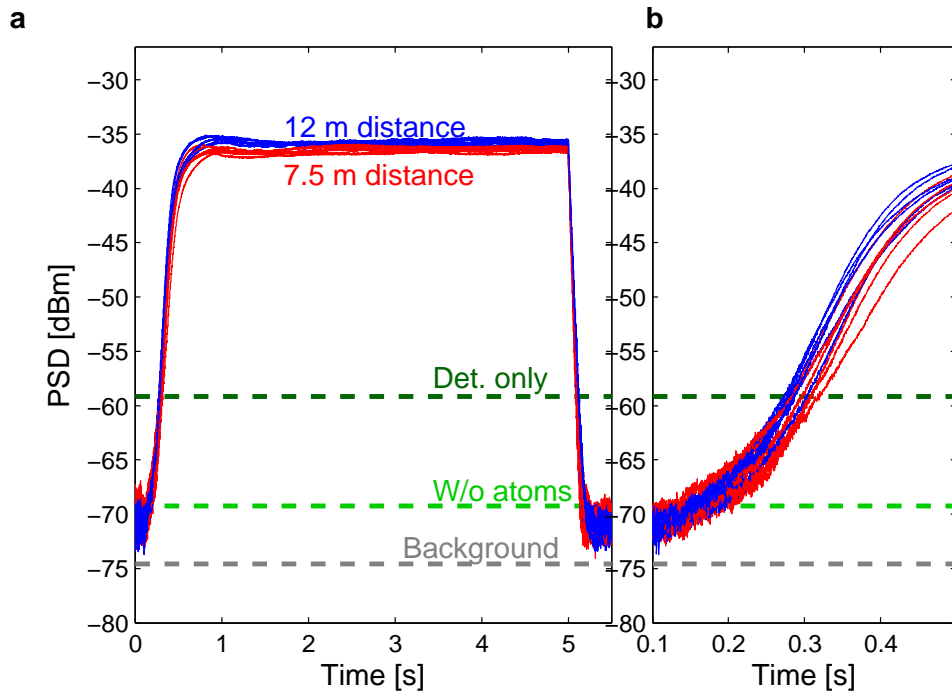
Figure 5.11: a) The traces show the membrane self-oscillation recorded with different propagation lengths between atoms and membrane. Red: cat-eye at position 1 (7.5 m distance, 25 ns traveling time). Blue: cat-eye at position 2 (12 m distance, 40 ns traveling time). Plot b) is a zoom into the initial section of plot a). The laser detuning is $\Delta_{\mathrm{LA}} = -2\pi \times 960\,\mathrm{MHz}$ and the cavity detuning is $\Delta = -0.06\kappa$. Each trace is averaged over 20 identical experimental runs.
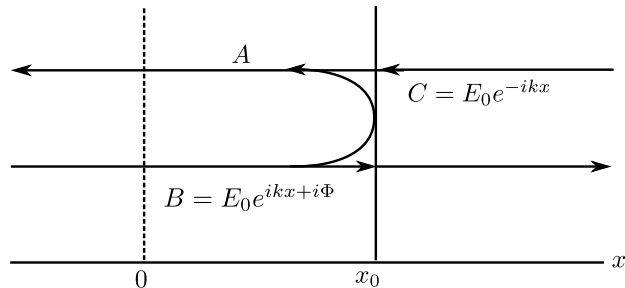
Figure 5.12: Schematic drawing of reflecting element and field amplitudes.

the delay by almost a factor 2. The mean values of the times at which the traces for position 1 and 2 cross the detection light level differ by 10.8 ± 5.5 ms. Over this short time-scale the atom number changes only by $2.7 \pm 1.4\%$ as can be inferred from the loading curve in figure 5.3. According to figure 5.8 and equation 5.15 the critical atom number should change by more than a factor of two when the delay doubles. In contrast, we see changes of the atom number on the percent level. From this observation I conclude that the run-time delay between the two systems has an effect on the stability of the system, but also that it is not the main effect which causes the instability in our system. There must be another dominant process which makes changes in the run-time delay less relevant.

Note that the fit to the data of figure 5.9 resulted in a global delay of τ of 88(1) ns. The run-time variation of 15 ns, which we implemented, is a non-negligible fraction of the fitted delay and should generate on detectable difference in the threshold atom number according to equation 5.15. However, we also have to note that the experimental situations in the length-variation experiment and the experiment in figure 5.9 were not exactly the same. The lattice power in the length-variation experiment was three times higher and the lattice reflectivity more than two times lower. The high power was chosen because it made the self-oscillation signal more stable and reproducible. If an additional delay mechanism was present which strongly depends on this power or the reflectivity, the global delay in the length-variation experiment might have been much higher than 88 ns so that additional delays of 15 ns became irrelevant.

5.4.2 Non-atom-induced instability

When performing the distance variation measurements, we noted that for atom-membrane distances larger than 10 m the membrane was driven even without atoms from time to time as illustrated in figure 5.13 a). In contrast to the self-oscillation in presence of atoms, this effect appeared and disappeared in a random manner. We

attribute this to tiny reflections in the beam path. The phase of the beam coming from the membrane is modulated at the membrane frequency. If a small fraction of this beam is reflected, it will interfere with the incoming laser beam turning the phase modulations into power modulations, which act back on the motion of the membrane. If the reflecting surface is positioned at a finite distance from the membrane, this feedback arrives delayed. This can drive the membrane into self-oscillations if the amplitude is high enough. Figure 5.12 visualizes the reflecting element at position x_0 and the optical fields around it. The system can be described by the transfer matrix formalism introduced in section 1.1.6. There is an incoming field from the right $C(x) = E_1 e^{-ikx}, E_0 \in \mathrm{R}$ and an incoming field from the left $B(x) = E_0 e^{ikx+i\Phi}$. The field from the left carries a small additional phase $\Phi \ll 2\pi$ originating from the motion of the membrane, $\Phi = (4/\kappa)Gx_{\mathrm{m}}$.

The field A which travels back to the membrane is a superposition of the transmitted part of C and the reflected part of B, see eqn. 1.31, 1.33 and 1.35. If the reflectivity of the reflecting element is small ($|\mathfrak{r}|^2 \ll 1$), the transmission coefficient becomes almost one ($\mathfrak{t} \approx 1$) and the reflectivity becomes purely imaginary so that we can write it as $\mathfrak{r} = ir$ with $r \in \mathbb{R}$. One can then write $A(x_0)$ as

$$A(x_0) \;\; = C(x_0) + irB(x_0) \;\; = E_1 e^{-ikx_0} + irE_0 e^{ikx_0+i\Phi} \, . \tag{5.21}$$

The power of the beam which travels to the membrane is proportional to the modulus squared of $A(x_0)$,

$$\begin{aligned} P \propto |A(x_0)|^2 \;\; &= \;\; E_1^2 + E_0 r^2 - 2E_0 E_1 r \sin(2kx_0 + \Phi) \\ &\approx \;\; E_1^2 + E_0^2 r^2 - 2E_1 E_0 r \sin(2kx_0) - 2E_1 E_0 r \cos(2kx_0)\Phi \, , \end{aligned} \tag{5.22}$$

where the sine has been developed to first order in the small parameter Φ in the last line. A sinusoidal modulation of $\Phi \propto x_{\mathrm{m}}$, due to the motion of the membrane, causes a sinusoidal power modulation of the beam (last term). As the radiation pressure force on the membrane is proportional to the ingoing power, there will be a feedback part in the force proportional to the membrane's own amplitude. If this feedback part has to travel for a time τ_{rt} between membrane and mirror, it arrives delayed, $F_{\mathrm{m}}(t) = (4G/\kappa)P_{\mathrm{membrane\,pos}}(t) = (4G/\kappa)P_{\mathrm{mirror\,pos}}(t - \tau_{\mathrm{rt}}) = -\gamma x_{\mathrm{m}}(t - 2\tau_{\mathrm{rt}}) \approx -\gamma x_{\mathrm{m}}(t) + 2\tau_{\mathrm{rf}}\gamma \dot{x}_{\mathrm{m}}(t)$ with backaction strength $\gamma = (4G/\kappa)^2 \cos(2kx_0)\sigma_{\mathrm{L}}\epsilon_0 E_1 E_0 r/k$. Note that once more only the power modulation is considered for the force and the constant first three terms of the power have been neglected. The last equality shows how the delayed feedback leads to a membrane-velocity-dependent term in the force on the membrane which causes damping if the sign of γ is negative, and antidamping if the sign of γ is positive. The term proportional to $x_{\mathrm{m}}(t)$ leads to a slight change in the membrane frequency analog to the similar term discussed in section 1.3 and can usually be neglected. Sign and amplitude of γ depend on the exact position of the reflector with respect to the membrane equilibrium position x_0. As the distances in our lab are not stable to the length scale of the optical wavelength, this position will vary on a slow timescale, resulting in the random appearance and disappearance of an instability without atoms on a time scale of seconds as visible in figure 5.13
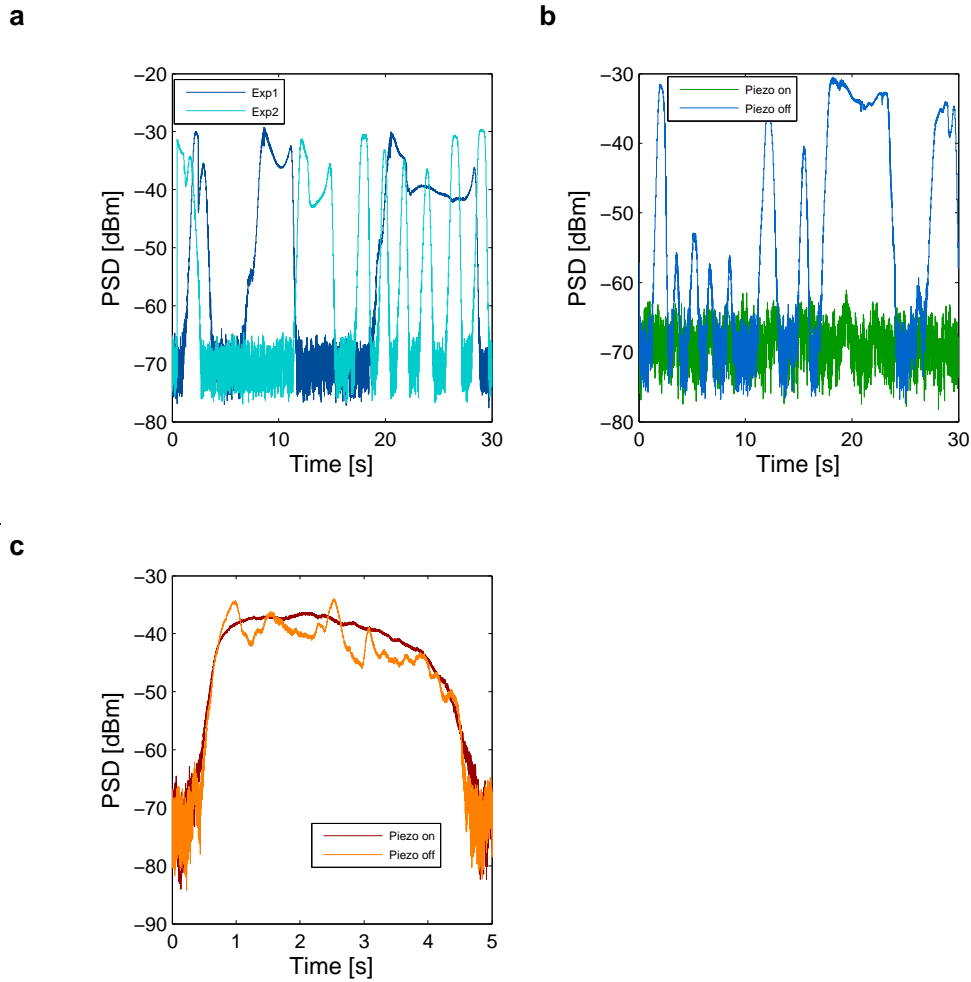
Figure 5.13: Plot a) shows two exemplary traces of the mean squared membrane amplitude (uncalibrated) versus time in presence of the coupling light and an artificial reflection of $r^2 = 10^{-5}$. Plot b) compares a third measurement of the same kind (blue) to a measurement in which in addition one of the mirrors was moved periodically by a PZT (green). Plot c) compares the situation of PZT on and off for a measurement done with atoms, without the artificial reflection and with the cat-eye at position 2.

a). Note that in contrast to the position of a reflecting surface, the position of the atoms with respect to the membrane is fixed because they are trapped in the lattice. If the position of one of the mirrors in the setup drifts slowly over a few optical wavelengths, the atoms follow the motion and their distance to the membrane stays fixed.

I tried to find the origin of the back reflection by sending light in opposite direction through our setup. The largest reflection I saw was $r^2 = 2 \times 10^{-5}$ and originated from the outcoupling lens of the coupling fiber on the membrane setup, see figure 2.5. Other reflections were not detectable on top of this 10^{-5} signal, so that they must be significantly smaller. Reflections on this low level are hard to avoid even when using antireflection-coated optics and therefore will cause problems in any long-distance atom-membrane-coupling experiment.

However, one can average the effect away due to the sinusoidal dependence of the backaction strength γ on the position of the reflecting element x_0. If one moves x_0 periodically over several optical wavelengths, the cosine-term will average to zero. The modulation has to be fast compared to the heating rate which the membrane experiences, if the cosine-term has a finite value. Also, it has to be slow compared to the axial trapping frequency of the atoms to avoid atom loss from the trap. To test this idea, we implemented an artificial reflection of $r^2 = 10^{-5}$ far away from the membrane by inserting a glass plate under a small tilt in the beam path close to the atoms. Further, we placed one of the mirrors in the path between atoms and membrane on a piezo element (PZT) as shown in figure 5.10.

Figure 5.13 a) shows the behavior of the membrane in presence of the coupling beam and the 10^{-5} reflection for the case when the PZT is switched off. Figure 5.13 b) compares a measurement taken with PZT off to a measurement in which the PZT mirror was moving back and forth over approximately one wavelength with $3\,\text{kHz}$ frequency. The motion of the mirror entirely suppresses the instability. The fluctuations one still sees on the membrane amplitude signal are on the level of the expected thermal fluctuations at this lattice power. Figure 5.13 c) compares the situation with PZT turned on and off in an experiment with atoms done with the cat-eye at position 2 and without the artificial reflection. The self-oscillation due to the atoms remains, nicely illustrating the concept of the atoms as a reflecting element whose position with respect to the membrane is interferometrically stable. The motion of the piezo also makes this signal much calmer. Indeed, all traces in figure 5.11 have been recorded with a moving piezo mirror.

5.4.3 Conclusion

In this section the influence of the propagation delay between atoms and membrane on the stability of the coupled system was investigated. We find that changing the distance between atoms and membrane changes the threshold atom number slightly. However, the effect is so small that it cannot be the major mechanism which causes the unstable behavior. Still, the run-time delay explains the instability which we see for separations larger then $10\,\text{m}$ in measurements without atoms. We attribute the

origin of this non-atom induced instability to delayed feedback from tiny reflections in the beam path. As some finite reflections will always be present in an optical setup, this driving mechanism is a problem for any long-distance coupled atom-membrane system. We found a way to strongly suppress this instability by moving one of the mirrors periodically with a PZT element. The PZT motion removes the effect of spurious optical reflections but keeps the feedback from the atoms intact.

5.5 Influence of system parameters

To get a better overview of the instable behavior, several system parameters were varied. Measurements with different sign and different magnitude of the lattice detuning Δ_{LA}, varying lattice powers P_0 and different powers in the MOT repump beam P_{repump} were performed.

5.5.1 Red versus blue-detuned lattice

Figure 5.14 compares time-resolved membrane traces of two experiments with identical settings but different detuning of the light from the atomic transition. In one case the lattice was red-detuned from the $F = 2 \leftrightarrow F' = 3$ transition by $\Delta_{\mathrm{LA}} = -2\pi \times 960\,\mathrm{MHz}$ and in the other case blue-detuned by $\Delta_{\mathrm{LA}} = +2\pi \times 770\,\mathrm{MHz}$ from the $F = 2 \leftrightarrow F' = 3$ transition. As we saw in section 1.1.6, the backaction of the atoms onto the light field depends on the atomic polarizability $\alpha \simeq -|d_{\mathrm{eg}}|^2/(\epsilon_0 \hbar \Delta_{\mathrm{LA}})$, which has been derived in section 1.1.1 equation 1.8 for a two-level atom. For the more realistic multilevel atom depicted in figure 5.15 the polarizabilities of the transitions to the three hyperfine excited states $F' = 1, 2, 3$ have to be added up $\alpha_{\mathrm{tot}} \simeq \sum_{i=1,2,3} -|d_{\mathrm{i2}}|^2/(\epsilon_0 \hbar \Delta_{\mathrm{i}})$. For the experimental configuration described above this results in a difference of only 3% in the total polarizabilities α_{tot} and therefore almost equal dispersive atom-light interaction in the red and in the blue-detuned case, resulting in equal axial trapping frequencies. However, the light shifts of the atomic levels (see equation 1.19) and also the lattice scattering rate (see equation 1.23) differ strongly as the atoms accumulate at the maxima of the lattice intensity in the red case and at the minima in the blue case. In this experiment the intensity in the maxima is 8.5 times higher than in the minima.

In figure 5.14 we see that in both realizations the atoms initially cause sympathetic cooling. Surprisingly, the sympathetic cooling is stronger in the red-detuned case although the numbers of atoms in the lattice volume are very similar. This indicates that the atom-light coupling in the red-detuned case is stronger. In the blue-detuned case, this cooling goes on and becomes stronger when the laser cooling parameters are switched from MOT to molasses. In contrast, in the red-detuned case, self-oscillations occur. The bottom row shows the corresponding number of atoms in the lattice volume for the two cases. One sees that the measured atom number in the lattice volume is slightly lower in the anti-trapping blue case. However, the self-oscillation in the red-detuned case starts when the atom number exceeds
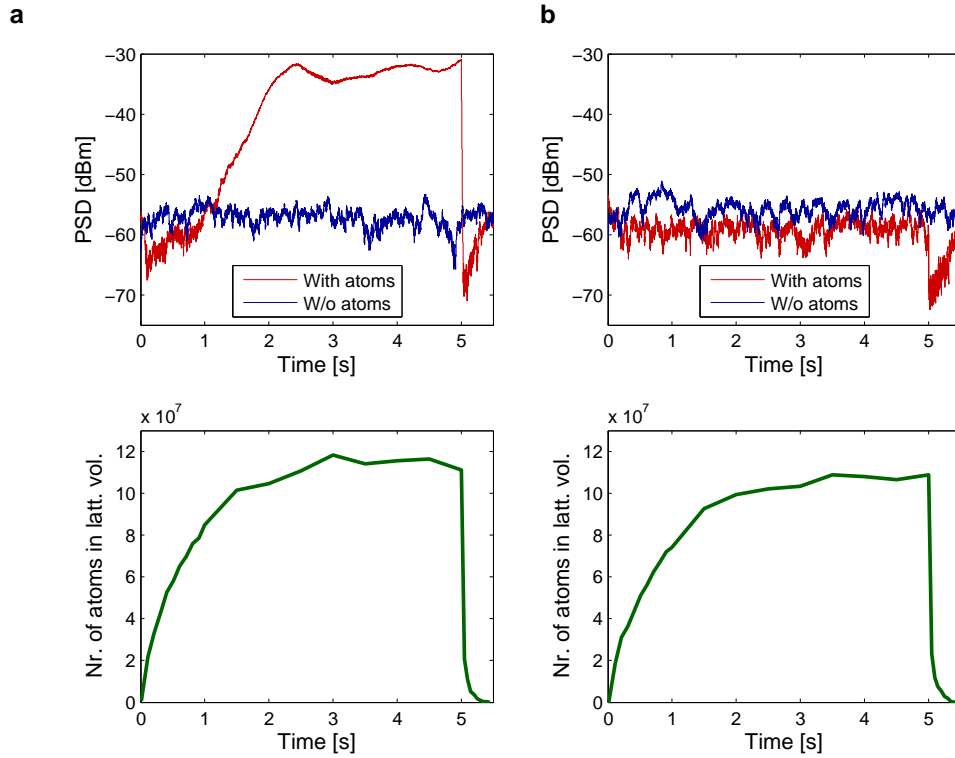
Figure 5.14: Comparison of the self-oscillation effect in red- and blue-detuned lattice. Upper plots: mean squared membrane amplitude (uncalibrated) versus time. Lower plots: corresponding atom number in lattice volume versus time. a) Red-detuned lattice ($\Delta_{\mathrm{LA}} = -2\pi \times 960\,\mathrm{MHz}$). b) Blue-detuned lattice ($\Delta_{\mathrm{LA}} = +2\pi \times 770\,\mathrm{MHz}$). In both measurements the ingoing power is $P_0 = 3\,\mathrm{mW}$, the lattice detuning is $\Delta = -0.04\,\kappa$ and the power reflectivity $R = 0.24$.
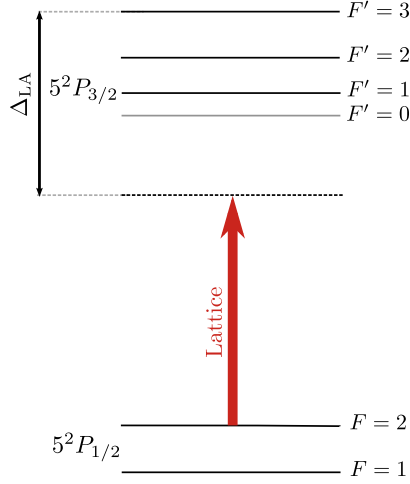
Figure 5.15: Hyperfine manifold of the ^{87}Rb D$_2$-line and lattice laser.

$\approx 9 \times 10^7$, which is reached only slightly later also in the blue-detuned case. The experiment was repeated for several lattice powers. Repetitively, ones sees a stronger initial sympathetic cooling effect followed by self-oscillations in the red lattice and no self-oscillations during the MOT phase in the blue case.

The reason for the stronger atom-light coupling in the red case, which leads to the stronger initial cooling and to the occurrence of self-oscillation, most likely lies in the different light shifts. In the red-detuned case, the ac-Stark shift of the coupling laser shifts the levels of the $|F = 2, m_F = 2\rangle \leftrightarrow |F' = 3, m'_F = 3\rangle$ MOT laser cooling transition apart by $2.5\,\Gamma$. The MOT cooling detuning, thus, locally increases from $3.5\,\Gamma$ to $6\,\Gamma$, so that the light scattering rate reduces. In section 3.7 we saw that the temperature and the density of our MOT are strongly limited by reabsorbtion of scattered laser light. As soon as the light scattering rate is reduced, for instance when we switch from MOT to molasses cooling, the temperature of the atoms quickly decreases as depicted in figure 3.6. Hence, via the light shift, the red-detuned lattice light creates an effective dark spot [155] with locally reduced atomic temperature T, modified atomic number density distribution n_a and damping rate Γ_a. As the temperature in our MOT is much larger than the lattice modulation depth ($T_{\mathrm{MOT}} = 2 - 5\,\mathrm{mK}$, $V_m = 240\,\mu\mathrm{K}$ for resonant atoms $\Omega_a = \Omega_m$), a reduction of the temperature increases the number of trapped atoms which take part in the coupling. In contrast, in the blue-detuned case, the coupling laser shifts the levels of the cooling transitions together by $0.4\,\Gamma$, and, therefore, even slightly decreases the MOT cooling detuning and increases the scattering rate. Thus, in the blue case the atoms in the lattice volume are most likely hotter. Therefore, less atoms are trapped in the lattice and take part in the coupling with the membrane. This explains the smaller initial sympathetic cooling effect and the absence of self-oscillations in the
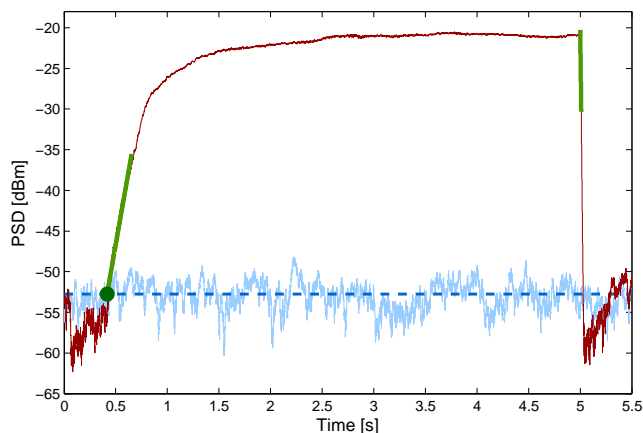
Figure 5.16: The figure shows an exemplary experimental trace of the lattice parameter variation experiment. The mean squared membrane amplitude (uncalibrated) is plotted as a function time. Red: with atoms, light blue: w/o atoms, dotted blue: average value of light blue line. The green dot marks the time at which the red curve crosses the dotted blue line. From loading curves as shown in figure 5.2 and 5.3, I extract the atom number corresponding to that time. As the number of atoms in the lattice volume depends on the lattice parameters, I recorded the loading for all lattice parameters. The left green line shows a linear fit to the red curve from which the heating rate is extracted. The green line on the right also shows a linear fit to the red data, from which the cooling rate during the molasses phase is extracted. During the measurements the cavity detuning was $\Delta = -0.06\kappa$ and the overall lattice reflectivity was $R = 22\%$.

blue-detuned case.

5.5.2 Lattice parameter dependence

During the measurements on propagation delays, we realized that the MOT-loading time at which the self-oscillation starts depends strongly on the power of the lattice beam and its detuning from the atomic transition. Therefore, we did experiments in which these two parameters were varied. To compare meaningful quantities of the different experimental runs, we extracted the atom number in the lattice volume at which the membrane mean squared amplitude $\langle x_m^2(t) \rangle$ starts to exceed the value at which it equilibrates in absence of atoms. I refer to this atom number as N_{crit} in the following. Further we determined the rate at which the membrane amplitude rises once N_{crit} is reached, Γ_{ex}, and the sympathetic cooling rate $\Gamma_{\mathrm{sym,mol}}$ at which the membrane amplitude decreases again when we switch from MOT to molasses cooling. These quantities are illustrated in figure 5.16.

Figure 5.17 and figure 5.18 display N_{crit} and Γ_{ex} as function of the ingoing lattice
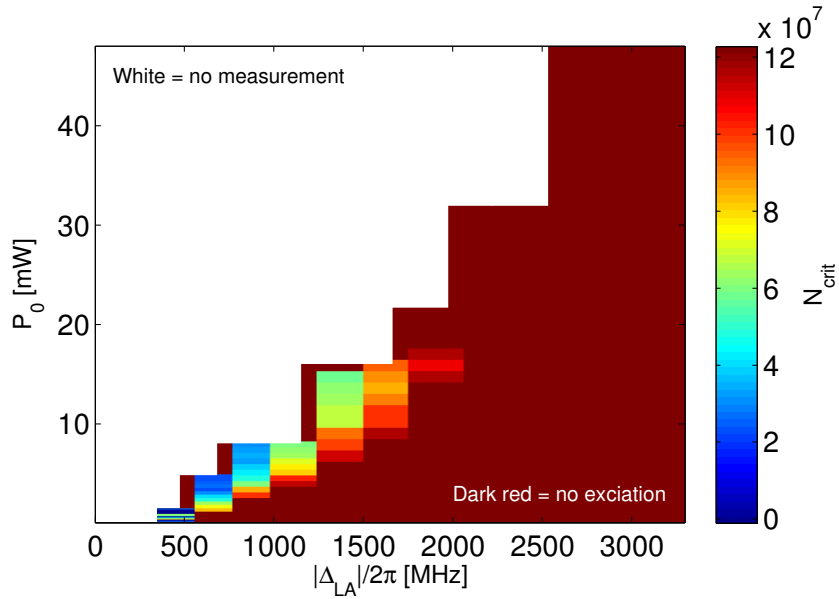
Figure 5.17: The plot shows the threshold atom number N_{crit} (color coded) vs. the power in the coupling lattice P_0 and the detuning of the coupling lattice $|\Delta_{\mathrm{LA}}|/2\pi$ from the $F = 2 \leftrightarrow F' = 3$ transition. All detunings are red detunings.
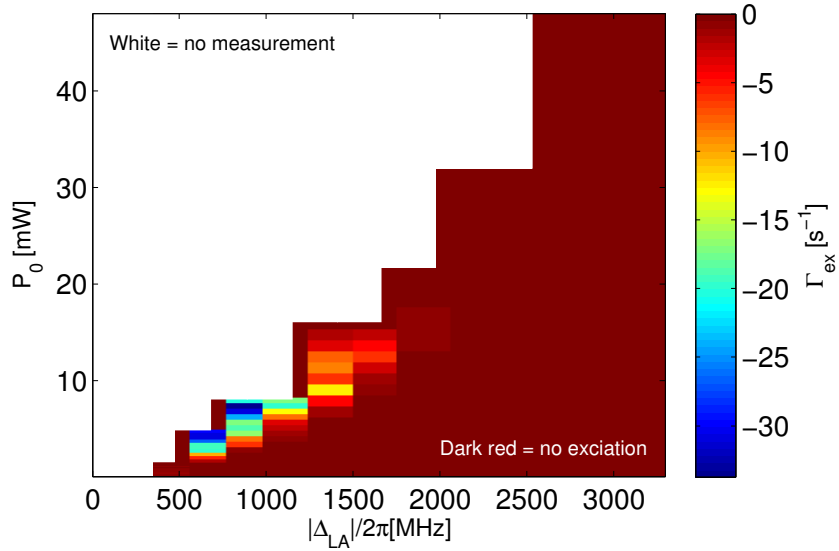
Figure 5.18: The plot shows the excitation rate Γ_{ex} (color coded) vs. the power in the coupling lattice P_0 and the detuning of the coupling lattice $|\Delta_{\mathrm{LA}}|/2\pi$ from the $F = 2 \leftrightarrow F' = 3$ transition. All detunings are red detunings.
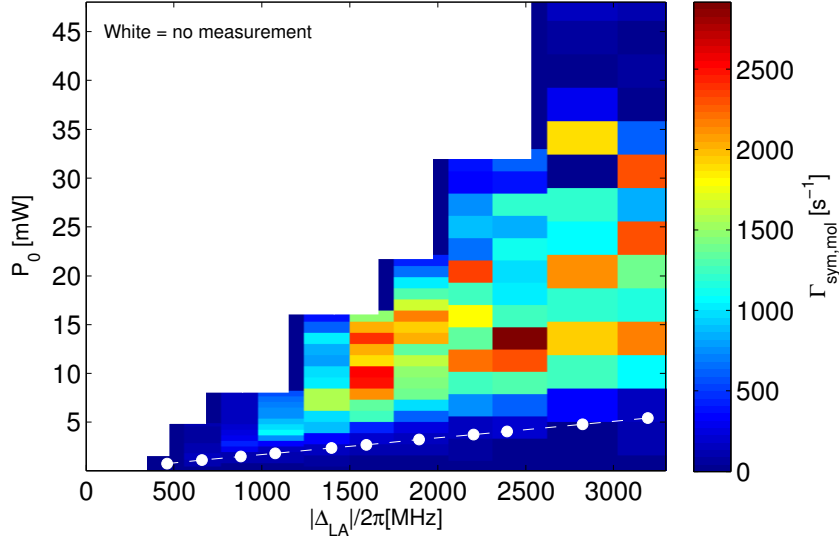
Figure 5.19: The figure depicts $\Gamma_{\text{sym,mol}}$ (color coded) during the molasses phase vs. the power in the coupling lattice P_0 and the detuning of the coupling lattice to the atomic transition $|\Delta_{\text{LA}}|/2\pi$. All detunings are red detunings. The white curve marks the linear dependence between the minimum power that is needed for sympathetic cooling and the detuning.

beam power, P_0, and the different red detunings from the $F = 2 \leftrightarrow F' = 3$ transition, Δ_{LA}. One sees that self-oscillations occur only for the smallest detunings. For a given small detuning, the threshold atom number reduces and the excitation rate rises with rising lattice power. This might be due to the atomic temperature effects described in the last paragraph. At larger lattice power the local temperature of the atoms in the lattice volume is most likely lower. Thus, a larger fraction is trapped in the lattice and takes part in the coupling. As a consequence, the total number of atoms in the lattice volume needed for the self-oscillations N_{crit} reduces and the excitation rate Γ_{ex} rises.

For increasing detuning Δ_{LA}, the self-oscillations start at larger and larger power P_0. From the resonance condition a linear scaling of the onset of the effect is expected $\Omega_{\text{m}} = \Omega_{\text{a}} \sim \sqrt{P_0/\Delta_{\text{LA}}}$ (see next paragraph). The dependence of the minimum power for self-oscillation on the detuning in the figures 5.17 and 5.18 looks rather quadratic, indicating that at larger detuning more atoms need to participate in the coupling to generate instable behavior. In section 5.7 I will introduce a model which predicts exactly this behavior.

The minimal power for which sympathetic cooling in the molasses phase can be seen in figure 5.19 depends linearly on the lattice detuning. This is expected from the theory in absence of delay. The axial oscillation frequency depends on the trap depth, which is proportional to P_0/Δ_{LA}. There is a minimum threshold trap depth,
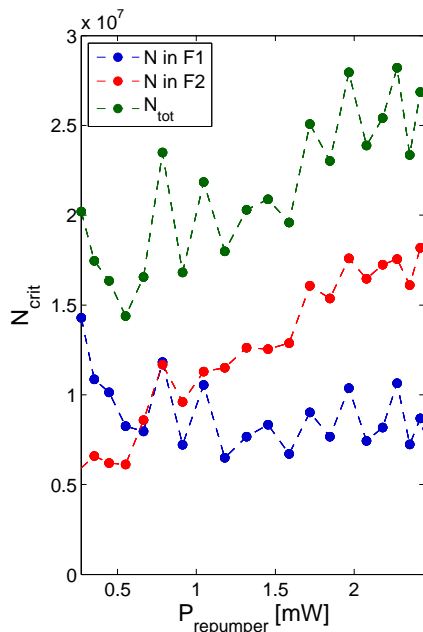
Figure 5.20: Total critical atom number N_{crit} and the contribution to N_{crit} from atoms in the $F = 1$ and $F = 2$ states vs. the power in the repumper beam. Experimental parameters: $\Delta = -0.06\kappa$, $\Delta_{\mathrm{LA}} = -2\pi \times 900\,\mathrm{MHz}$, $P_0 = 6.8\,\mathrm{mW}$, $R = 27\%$, $\Omega_{\mathrm{a}}(0) = 2\pi \times 596\,\mathrm{kHz}$.

which has to be reached in order to make the most tightly trapped atoms in the center of the beam resonant with the membrane, $\Omega_{\mathrm{a}}(0) = \Omega_{\mathrm{m}}$, see section 1.3.4. The power needed to reach this threshold trap depth depends linearly on the detuning, which can be seen in the plot. In fact, the white line in figure 5.19 has been used to calibrate the axial trapping frequency of the lattice potential (see section 3.4) via the membrane frequency Ω_{m}.

5.5.3 Repump power dependence

Lastly, the influence of the scattering rate of the MOT repump light was investigated by varying the power of the repump beams. As in the experiment before, the critical atom number in the lattice volume was determined. In addition to the critical total atom number, also the critical atom number in the $F = 2$ state was measured in this new experiment.

The imaging laser is resonant with the $F = 2 \leftrightarrow F = 3$ transition. Thus, it will always only detect the atoms which are in the $F = 2$ state. To count all atoms, the ones which stay in the $F = 1$ ground state at the end of the sequence are pumped into the $F = 2$ state by the repump light during the time of flight period (TOF) between the end of the experiment and the imaging sequence. To count the atoms

in $F = 2$ alone, one simply has to turn off the repump laser at the end of the experiment. From the difference of the total atom number and the atom number in $F = 2$, also the number of atoms in the $F = 1$ state can be inferred.

The green trace in figure 5.20 a) shows how the critical total atom number for the self-oscillation depends on the power in the repump beam. The red and blue trace show how many of these atoms are in $F = 2$ and $F = 1$. We see that more atoms are needed to make the system unstable if the repump power is higher. Again, this might be related to the temperature of the atoms. A reduction of the repump power reduces the fraction of atoms in the $F = 2$ hyperfine ground state and thus the MOT cooling light scattering rate and the temperature of the cloud. If the corresponding increase in the fraction of atoms trapped in the lattice exceeds the reduction of coupling atoms due to the growing $F = 1$ population, the total atom number in the lattice volume needed for self-oscillations decreases. Remarkably, the contribution of atoms in $F = 1$ to the critical atom number is flat.

5.5.4 Summary

This section investigated the dependence of the self-oscillation phenomenon on several system parameters. Many observations can be explained by a varying fraction of atoms which take part in the coupling for different parameter settings. The nonlinear dependence of the turn-on power of the self-ocillations on the lattice detuning and the fact that the self-oscillations disappear completely for detunings larger than $|\Delta_{\mathrm{LA}}| = 2\pi \times 2000\,\mathrm{MHz}$ remain unexplained and thus give hints at the origin of the effect.

5.6 Atomic backaction onto the light

Even if the exact mechanism which causes the delay is still unknown, the measurements we did up to this point strongly hint that the most relevant process occurs on the atomic side of the system. One should thus be able to see this in an open-loop experiment which investigates the atomic back-action on the light field.

5.6.1 Measurement setup

To investigate this, we performed measurements in which we mimicked the phase-shift caused by the membrane with a fiber electro-optic modulator (EOM) and examined the atomic backaction onto the light. The setup is sketched in figure 5.21. Laser light enters the setup from the right. After passing the atoms, a small fraction (3%) is picked up and sent to a photodiode (PD). The main part of the light propagates twice through a fiber EOM before it interacts with the atoms again. Due to strong optical losses in the fiber EOM, the power reflectivity in this setup drops to $R = 0.06$. A lock-in amplifier sinusoidally drives the fiber EOM at a frequency Ω, which imprints a phase modulation onto the light traveling back to the atoms. This modulates the location of the potential minima of the standing-wave optical
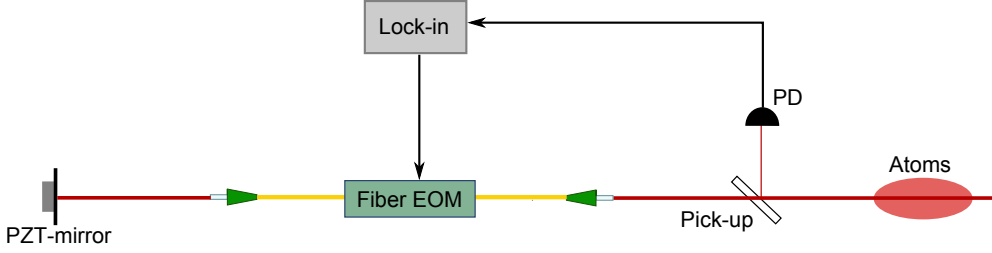
Figure 5.21: Setup for measuring the atomic backaction on the light field.

lattice. The atomic motion is affected by this modulation and, in turn, modulates the power of the laser beams as discussed in section 1.1.6, which is recorded by the PD (power to voltage conversion factor $\beta = 350 \,\mathrm{V/W}$). The PD-voltage is fed back into the lock-in amplifier, which measures its amplitude and the phase with respect to the phase of the outgoing voltage signal.

5.6.2   Expected behavior from existing theory

Before I get to the measurements, I want to briefly discuss the behavior expected from the existing theory without delay, as this kind of measurement was not done before in our lab. The calculation is based on the transfer matrix formalism presented in 1.1.6. It is similar to the calculation presented in section 5.4.2 with the difference that, here, the position of the atoms can be altered by phase shifts on the light, whereas the position of the fixed reflector in section 5.4.2 was independent of the phase of the light.

Again, I refer to the situation shown in figure 5.12 with ingoing fields $C(x) = E_1 \exp(-ikx)$ and $B(x) = E_0 \exp(ikx + i\Phi)$. Now, $x_0 = x_\mathrm{a}$ is the position of the atoms. Once more, the zero point of the coordinate system has been chosen so that the intensity $|C(x) + B(x)|^2$ is maximum at $x = 0$ if $\Phi = 0$. Now, the phase Φ is the phase added to the light by the fiber EOM. If the EOM is off, $\Phi = 0$, and if the laser is red-detuned, the light field will pull the atoms towards $x = 0$. In chapter 1.1.6, equation 1.42, we learned that for ingoing fields $B(x)$ and $C(x)$, as above, with intensities $I_{0(1)} = \frac{\epsilon_0}{2} c |E_{0(1)}|^2$ and for $|\zeta| \ll 1$, $\Delta_\mathrm{LA}/\Gamma_\mathrm{a} \gg 1$ and $kx_\mathrm{a}, \Phi \ll 2\pi$, the force exerted on the atoms by the light field is given by

$$
\begin{aligned}
F_a(x_\mathrm{a}) &= -8k\sigma_\mathrm{L} \operatorname{Re} \zeta \frac{\sqrt{I_0 I_1}}{c} \left(x_\mathrm{a} + \frac{\Phi}{2k} \right) \\
&= -Nm\Omega_\mathrm{a}^2 \left(x_\mathrm{a} + \frac{\Phi}{2k} \right) .
\end{aligned}
\tag{5.23}
$$

Further, in section 1.1.6 we found for the power modulation of the beam which

leaves the atomic ensemble towards the left (see equation 1.46)

$$
\begin{aligned}
P &= -4k\sigma_{\mathrm{L}}\sqrt{I_0 I_1}\,\mathrm{Re}\,\zeta\left(x_{\mathrm{a}} + \frac{\Phi}{2k}\right) \\
&= -\frac{c}{2}Nm\Omega_{\mathrm{a}}^2\left(x_{\mathrm{a}} + \frac{\Phi}{2k}\right).
\end{aligned}
\tag{5.24}
$$

In presence of an additional damping term, for instance originating in laser cooling, the equations of motion for the position of the atom reads

$$
Nm\ddot{x}_{\mathrm{a}} = -\Gamma_{\mathrm{a}}Nm\dot{x}_{\mathrm{a}} - Nm\Omega_{\mathrm{a}}^2\left(x_{\mathrm{a}} + \frac{\Phi}{2k}\right).
\tag{5.25}
$$

Fourier transforming and solving for $\tilde{x}_{\mathrm{a}}(\Omega)$ gives

$$
\tilde{x}_{\mathrm{a}}(\Omega) = -\frac{\Omega_{\mathrm{a}}^2}{2k}\left(\Omega_{\mathrm{a}}^2 - \Omega^2 + i\Gamma_{\mathrm{a}}\Omega\right)^{-1}\tilde{\Phi}(\Omega).
\tag{5.26}
$$

This expression gives the complex amplitude of the atomic motion which is induced by a phase modulation of a certain frequency and amplitude.

One can plug this expression for the atomic amplitude into the Fourier transformed expression for the power modulations

$$
\begin{aligned}
\tilde{P}(\Omega) &= -\frac{c}{2}Nm\Omega_{\mathrm{a}}^2\left(\tilde{x}_{\mathrm{a}}(\Omega) + \frac{\tilde{\Phi}(\Omega)}{2k}\right) \\
&= -\frac{c}{2}\frac{Nm\Omega_{\mathrm{a}}^2}{2k}\left(1 - \frac{\Omega_{\mathrm{a}}^2}{\Omega_{\mathrm{a}}^2 - \Omega^2 + i\Gamma_{\mathrm{a}}\Omega}\right)\tilde{\Phi}(\Omega).
\end{aligned}
\tag{5.27}
$$

The power modulation in equation 5.27 is the quantity which we measure in the lab via the photodiode and the lock-in amplifier. The lock-in gives out the quadratures or phase and amplitude of PD voltage caused by the power modulation in equation 5.27.

Figure 5.22 a) - d) depicts the calculated amplitude and phase of the power modulation versus the modulation frequency Ω. The model is plotted for two parameter sets, which differ in the ratio of Γ_{a} to Ω_{a}. In the left column $\Gamma_{\mathrm{a}}/\Omega_{\mathrm{a}}$ is 0.07, in the right column the ratio is 0.55. The parameters used for the plot are listed in the figure caption. For both parameter sets one sees that for very small modulation frequencies Ω the amplitude is negligible. In this case the atoms follow the motion of the intensity maxima of the standing wave adiabatically so that $x_{\mathrm{a}} = -\Phi/2k$ and, therefore, the power modulation in equation 5.24 is zero. Furthermore, the amplitude has a peak at the frequency of the atoms Ω_a as expected. Over the resonance the phase drops from $0°$ to $-180°$. For large damping, as in the right column, the phase does not reach $0°$ degrees before the resonance because the damping term pulls the phase to $-90°$ at small frequencies. At frequencies much higher than Ω_{a}, the motion of the atoms does not react to the fast phase modulation Φ any more. They stay located at the potential minimum of the temporally averaged potential.
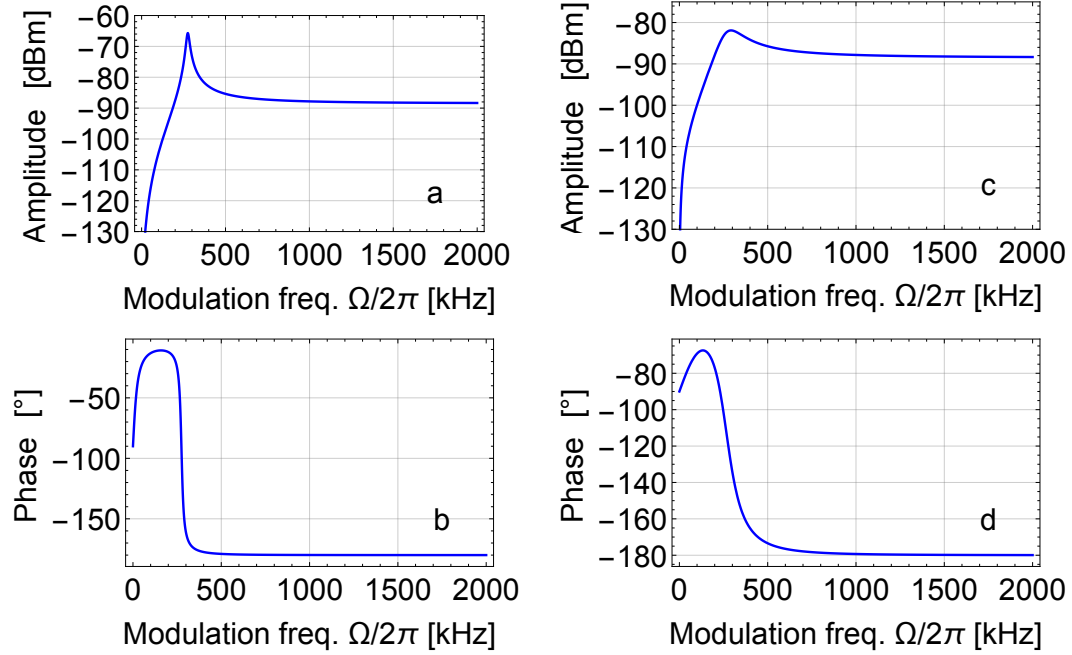
Figure 5.22: The plots show phase [b) and d)] and amplitude [a) and c)] of the power modulation caused by a periodic phase modulation at frequency Ω for $N = 2 \times 10^5$, $\Omega_a = 2\pi \times 275\,\mathrm{kHz}$, $\Phi_{\mathrm{rms}} = 0.232$ and $\Gamma_a = 2\pi \times 20\,\mathrm{kHz}$ [a) and b)] or $\Gamma_a = 2\pi \times 150\,\mathrm{kHz}$ [c) and d)] according to equation 5.27. The amplitude has been adapted to the electrical power which the lock-in measures $P_{\mathrm{el}} = (\beta r_{\mathrm{PU}} P_{\mathrm{opt}})^2 / R$ with $r_{\mathrm{PU}} = 0.03$ being the reflectivity of the pick-up plate, $\beta = 350 V/W$ the power-to-voltage conversion factor and $R = 50\,\Omega$ the input impedance of the lock-in. Thus, we can directly compare the theory to the data.
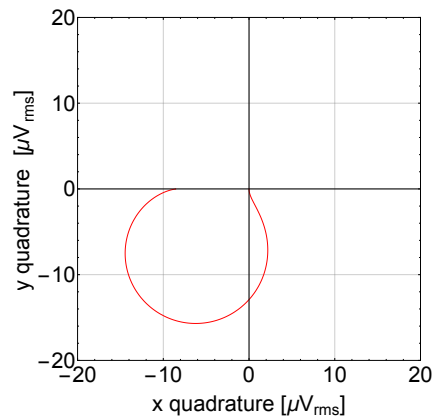
Figure 5.23: The plot shows the quadratures corresponding to the second parameter set from figure 5.22.

However, as they are a reflecting element, they still generate a power modulation on the beam which travels towards the fiber EOM, similar as described in section 5.4.2. The amplitude of the power modulation now stays constant for increasing modulation frequency. Note that the phase of the power modulation never falls below $-180°$ in the model. The measured data will strongly deviate from this.

Figure 5.23 shows the quadratures of the power modulation in equation 5.27 for the second parameters set. In principle, the figure carries the same information, but I found it helpful to look at the measured data also in this representation. Thus, I also show the quadratures here to be able to compare them to the measurements.

5.6.3 Application of the stability criterion

One can use the measurements of the atomic backaction to learn about the stability of the system under the assumption that the membrane behaves as expected from standard optomechanics theory. Via the backaction measurements, we have access to the quantity $[\tilde{P}(\Omega)/\tilde{\Phi}(\Omega)]_{\mathrm{a}}$, the factor with which the atoms convert phase modulations into power modulations at a given frequency Ω. Assuming that the membrane behaves as expected, one can calculate the phase modulation it imprints on the light when it is subject to a given power fluctuation, $[\tilde{\Phi}(\Omega)/\tilde{P}(\Omega))]_{\mathrm{m}}$. As described earlier, the coupled system will start to self-oscillate if a noise signal entering the loop, as depicted in figure 5.7, becomes amplified and collects a phase delay of 2π when it propagates through the loop once. In this case, the product $t^2 e^{-2i\Omega\tau}[\tilde{P}(\Omega)/\tilde{\Phi}(\Omega)]_{\mathrm{a}} \times [\tilde{\Phi}(\Omega)/\tilde{P}(\Omega)]_{\mathrm{m}}$ has a phase of $360°$ and an amplitude bigger than one. Here, also the reduction of the power modulation due to optical losses ($t^2 = \sqrt{R} = 0.25$ for the measurements in this chapter) and the run-time delay ($\tau = 30\,\mathrm{ns}$ in a typical coupling experiment) have been taken into account.

Calculation of $[\tilde{\Phi}(\Omega)/\tilde{P}(\Omega)]_{\mathbf{m}}$

To calculate the membrane response $[\tilde{\Phi}(\Omega)/\tilde{P}(\Omega)]_{\mathrm{m}}$, we remember from section 1.2.2 that the phase-shift per small membrane motion x_{m} is

$$\Phi = \frac{\mathrm{d}\Phi}{\mathrm{d}\Delta}\frac{\mathrm{d}\omega_{\mathrm{c}}}{\mathrm{d}x_{\mathrm{m}}}x_{\mathrm{m}} = \frac{4G}{\kappa}x_{\mathrm{m}} \tag{5.28}$$

and that the membrane susceptibility is given by

$$\chi_{\mathrm{m}}(\Omega) = \frac{\tilde{x}_{\mathrm{m}}(\Omega)}{\tilde{F}(\Omega)} = [M(\Omega_{\mathrm{m}}^2 - \Omega^2 + i\Gamma_{\mathrm{m}}\Omega)]^{-1}, \tag{5.29}$$

Thus, for the Fourier transform of Φ one can write

$$\tilde{\Phi}(\Omega) = \frac{4G}{\kappa}\tilde{x}_{\mathrm{m}}(\Omega) = \frac{4G}{\kappa}\frac{1}{M(\Omega_{\mathrm{m}}^2 - \Omega^2 + i\Gamma_{\mathrm{m}}\Omega)}\tilde{F}(\Omega) \tag{5.30}$$

Moreover, we remember (see equation 1.89 and 1.91) that the radiation pressure force modulation F_{rad} caused by a modulation of the power in front of the cavity P
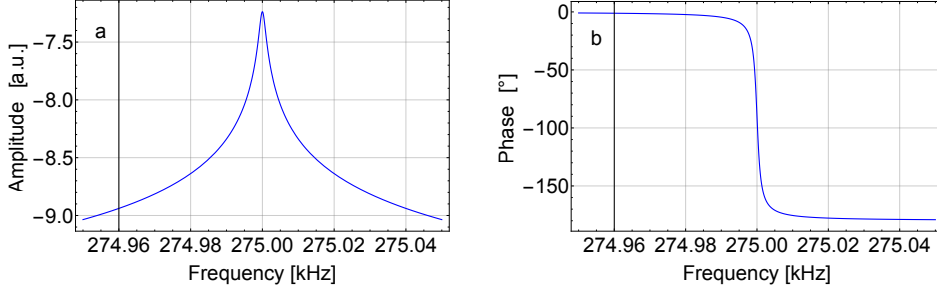
Figure 5.24: The figure illustrates the frequency response of the membrane backaction onto the light given by equation 5.33. Figure a) shows the amplitude in arbitrary logarithmic units and figure b) the phase.

is given by

$$F_{\text{rad}} = \hbar G \bar{n}_{\text{c}} = \frac{4G}{\kappa \omega_{\text{c}}} P \,, \tag{5.31}$$

so that $\tilde{\Phi}(\Omega)$ becomes

$$\tilde{\Phi}(\Omega) = \left(\frac{4G}{\kappa}\right)^2 \frac{1}{\omega_{\text{c}}} \frac{1}{M(\Omega_{\text{m}}^2 - \Omega^2 + i\Gamma_{\text{m}}\Omega)} \tilde{P}(\Omega) \,. \tag{5.32}$$

The power-to-phase conversion factor of the membrane in frequency space hence reads

$$
\begin{aligned}
\left[\frac{\tilde{\Phi}(\Omega)}{\tilde{P}(\Omega)}\right]_{\text{m}} &= \left(\frac{4G}{\kappa}\right)^2 \frac{1}{\omega_{\text{c}}} \frac{1}{M(\Omega_{\text{m}}^2 - \Omega^2 + i\Gamma_{\text{m}}\Omega)} \\
&= \left(\frac{4G}{\kappa}\right)^2 \frac{1}{\omega_{\text{c}}} \frac{1}{2\Omega_{\text{m}}M(\Omega_{\text{m}} - \Omega + i\Gamma_{\text{m}}/2)} \,,
\end{aligned}
\tag{5.33}
$$

where I did a Lorentz approximation in the last step, which is justified if $|\Omega_{\text{m}} - \Omega| \approx \Gamma_{\text{m}} \ll \Omega_{\text{m}}$. Figure 5.24 illustrates phase and amplitude of the membrane power to phase fluctuation conversion factor. Note that also here the phase never reaches $-180°$. The combined phase lag of the atomic oscillator and the membrane oscillator can therefore not exceed $360°$. An additional phase-shift e.g. from a delay is needed for this.

Stability criterion

The only frequencies at which the power to phase conversion factor on the membrane side $[\tilde{\Phi}(\Omega)/\tilde{P}(\Omega)]_{\text{m}}$ has a finite value lie within in a small window of width $\approx \Gamma_{\text{m}}$ around the membrane frequency Ω_{m}. Thus, if the system oscillates, it will oscillate at a frequency in this window. Due to the much larger atomic linewidth $\Gamma_{\text{a}} \gg \Gamma_{\text{m}}$, the conversion factor on the atomic side $[\tilde{P}(\Omega)/\tilde{\Phi}(\Omega)]_{\text{a}}$ can be assumed to be constant

within the small frequency window around Ω_{m}. As $\Gamma_{\mathrm{m}}\tau \ll 1$, also the factor $e^{-2i\Omega\tau}$ is constant to good approximation in the relevant frequency window. For statements about the stability of the coupled system it is therefore enough to measure the phase ϕ_{a} and the amplitude of the atomic conversion factor $[\tilde{P}(\Omega_{\mathrm{m}})/\tilde{\Phi}(\Omega_{\mathrm{m}})]_{\mathrm{a}} = |\tilde{P}(\Omega_{\mathrm{m}})/\tilde{\Phi}(\Omega_{\mathrm{m}})|_{\mathrm{a}} \exp(i\phi_{\mathrm{a}})$ at the membrane frequency, and to take the propagation phase at Ω_{m}, $\phi_{\mathrm{p}} = -2\Omega_{\mathrm{m}}\tau$, into account.

For an instability the combined phase of the product $t^2 e^{-2i\Omega_{\mathrm{m}}\tau}[\tilde{P}(\Omega_{\mathrm{m}})/\tilde{\Phi}(\Omega_{\mathrm{m}})]_{\mathrm{a}}\times [\tilde{\Phi}(\Omega)/\tilde{P}(\Omega)]_{\mathrm{m}}$ needs to be $-360°$. If for example the sum of the phase of the atomic backaction ϕ_{at} and the propagation phase ϕ_{p} is $-270°$, the critical $-360°$ point is reached at the membrane frequency Ω_{m}, at which the phase of membrane backaction is $-90°$ and the membrane backaction is maximal. If $\phi_{\mathrm{at}} + \phi_{\mathrm{p}}$ is less or more than $-270°$, the critical frequency will slightly deviate from Ω_{m} and the membrane backaction amplitude will be reduced.

From the condition

$$\phi_{\mathrm{at}} + \phi_{\mathrm{p}} + \arg([\tilde{\Phi}(\Omega_{\mathrm{crit}})/\tilde{P}(\Omega_{\mathrm{crit}})]_{\mathrm{m}}) = -2\pi , \tag{5.34}$$

one can find the critical frequency Ω_{crit} close to Ω_{m} at which the system will oscillate if the gain is high enough. One finds

$$\Omega_{\mathrm{crit}} = \Omega_{\mathrm{m}} - \frac{\Gamma_{\mathrm{m}}}{2}\cot\phi_{\mathrm{a}}' , \tag{5.35}$$

where $\phi_{\mathrm{a}}' = \phi_{\mathrm{a}} + \phi_{\mathrm{p}}$ is the atomic phase shifted by the propagation phase. The amplitude of the membrane backaction at this frequency is given by

$$\left|\frac{\tilde{\Phi}(\Omega_{\mathrm{crit}})}{\tilde{P}(\Omega_{\mathrm{crit}})}\right|_{\mathrm{m}} = \left|\frac{\tilde{\Phi}(\Omega_{\mathrm{m}})}{\tilde{P}(\Omega_{\mathrm{m}})}\right|_{\mathrm{m}} \frac{1}{\sqrt{1 + \cot^2\phi_{\mathrm{a}}'}} , \tag{5.36}$$

with

$$\left|\frac{\tilde{\Phi}(\Omega_{\mathrm{m}})}{\tilde{P}(\Omega_{\mathrm{m}})}\right|_{\mathrm{m}} = \left(\frac{4G}{\kappa}\right)^2 \frac{1}{\omega_{\mathrm{c}}}\frac{1}{\Omega_{\mathrm{m}}\Gamma_{\mathrm{m}}M} . \tag{5.37}$$

From the stability condition

$$\left|\frac{\tilde{\Phi}(\Omega_{\mathrm{crit}})}{\tilde{P}(\Omega_{\mathrm{crit}})}\right|_{\mathrm{m}} \times t^2 \left|\frac{\tilde{P}(\Omega_{\mathrm{m}})}{\tilde{\Phi}(\Omega_{\mathrm{m}})}\right|_{\mathrm{a}} < 1 , \tag{5.38}$$

one finds that the amplitude of the atomic backaction for a given phase ϕ_{a} of this backaction at Ω_{m} has to stay below

$$\begin{aligned}
\left|\frac{\tilde{P}(\Omega_{\mathrm{m}})}{\tilde{\Phi}(\Omega_{\mathrm{m}})}\right|_{\mathrm{a,max}} &= \frac{1}{t^2}\left|\frac{\tilde{\Phi}(\Omega_{\mathrm{crit}})}{\tilde{P}(\Omega_{\mathrm{crit}})}\right|_{\mathrm{m}}^{-1} \\
&= \frac{1}{t^2}\left|\frac{\tilde{\Phi}(\Omega_{\mathrm{m}})}{\tilde{P}(\Omega_{\mathrm{m}})}\right|_{\mathrm{m}}^{-1}\sqrt{1 + \cot^2\phi_{\mathrm{a}}'} \tag{5.39}
\end{aligned}$$

Thus, if we know the phase of the atomic backaction at Ω_m, we can calculate the maximally allowed amplitude and check whether the measured value lies below or above. From the the phase and the maximum amplitude, one can also determine the maximum quadratures along ϕ'_at

$$
\begin{aligned}
X(\Omega_\mathrm{m})_{\mathrm{a,max},\phi'_\mathrm{at}} &= \left|\frac{\tilde{P}(\Omega_\mathrm{m})}{\tilde{\Phi}(\Omega_\mathrm{m})}\right|_\mathrm{max} \cos\phi'_\mathrm{a} = \frac{1}{t^2}\left|\frac{\tilde{\Phi}(\Omega_\mathrm{m})}{\tilde{P}(\Omega_\mathrm{m})}\right|_\mathrm{m}^{-1}\sqrt{1+\cot^2\phi'_\mathrm{a}}\cos\phi'_\mathrm{a}, \\
Y(\Omega_\mathrm{m})_{\mathrm{a,max},\phi'_\mathrm{at}} &= \left|\frac{\tilde{P}(\Omega_\mathrm{m})}{\tilde{\Phi}'(\Omega_\mathrm{m})}\right|_\mathrm{max} \sin\phi'_\mathrm{a} = \frac{1}{t^2}\left|\frac{\tilde{\Phi}(\Omega_\mathrm{m})}{\tilde{P}(\Omega_\mathrm{m})}\right|_\mathrm{m}^{-1}.
\end{aligned}
\tag{5.40}
$$

Interestingly the critical Y-quadrature is independent of ϕ'_a. Summing up, I find that our coupled system is unstable if the amplitude of the atomic backaction at the membrane frequency ($\Omega_\mathrm{crit} \approx \Omega_\mathrm{m}$) exceeds $\left|\frac{\tilde{P}(\Omega_\mathrm{m})}{\tilde{\Phi}(\Omega_\mathrm{m})}\right|_\mathrm{a,max}$, or correspondingly if the Y-quadrature of the atomic backaction at Ω_m rotated by ϕ_p is larger than $\frac{1}{t^2}\left|\frac{\tilde{\Phi}(\Omega_\mathrm{m})}{\tilde{P}(\Omega_\mathrm{m})}\right|_\mathrm{m}^{-1}$. For $F = 570$, $\Gamma_\mathrm{opt} = 15\,\mathrm{s}^{-1}$, $\tilde{\Phi}_\mathrm{rms}(\Omega_\mathrm{m}) = 0.23$, and $R = \sqrt{0.06}$ as in the experiments of this section, I find $Y(\Omega_\mathrm{m})_{\mathrm{max},\phi'_\mathrm{at}} = 3.3\,\mu\mathrm{V}_\mathrm{rms}$. Note that the critical $-360°$ point cannot be reached in the existing model without delay as the phases of both, the atomic backaction, figure 5.22, and the membrane backaction, figure 5.24, stay above $-180°$. As mentioned above, an additional phase-shift e.g. from a delay is needed to realize a global phase lag of $360°$.

5.6.4   Measurements

Finally, I present our measurements of the atomic backaction. Several of them deviate strongly from the theoretical behavior without delays. In particular many traces show much larger phase lags, which is not surprising as some delay must be present in the system. Via the stability analysis presented above, one can judge from these measurements of the open loop behavior on the atomic side whether the coupled system will be unstable if we close the loop.

Signal in absence of atoms

Every reflecting element in the beam path causes a power modulation in the beam on the PD due to interference between the phase modulated reflected beam and the incoming beam as described in the section on run-time delay, see figure 5.12 and equation 5.23. The phase of this power modulation jumps randomly between $0°$ and $180°$ as the position of the reflecting elements drifts slowly, which randomly changes the sign of the cosine in equation 5.23. The plots a) and b) of figure 5.25 depict this effect. One sees that on top of the $180°$ jumps the phase decreases with a slope of $90°/2\,\mathrm{MHz}$ due to a global delay caused by propagation delays of the optical setup, propagation of the electrical signals in the BNC cables and all other delays in the electronics involved. We use this knowledge to calibrate the subsequent
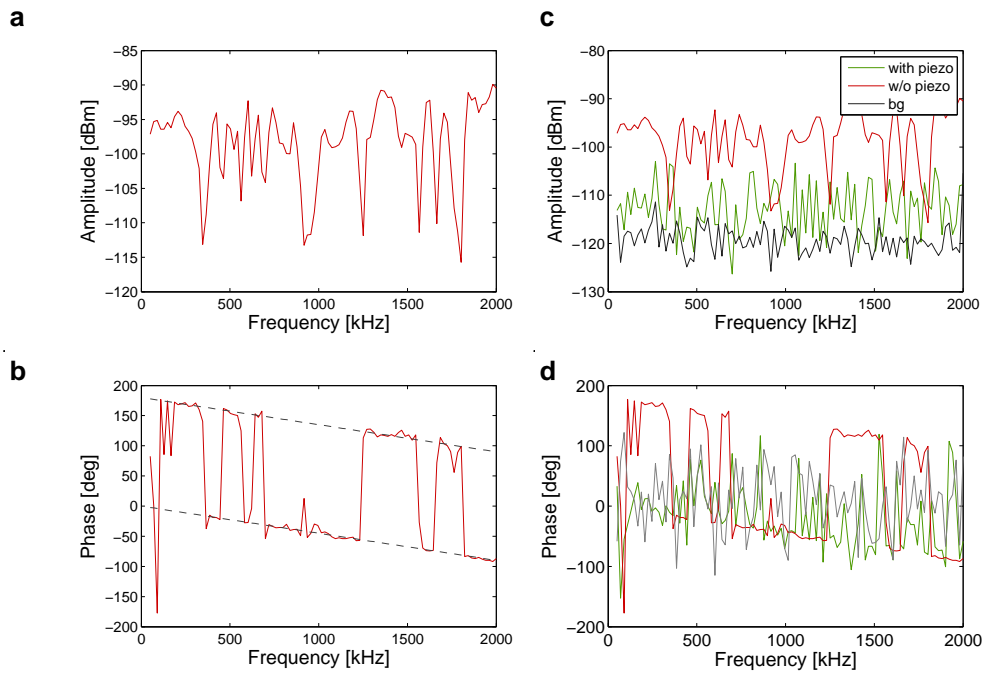
Figure 5.25: a) and b) Phase and amplitude of the power modulation generated by a reflecting element in the beam path in a measurement without atoms and without piezo. The amplitude is given in units of electrical power over the $50\,\Omega$ input impedance of the lock-in. The linear dependence of the phase on the frequency (dashed lines) is used to calibrate the delay of the measurement setup. c) and d) compare the same data to data taken in a measurement with operating piezo.

measurements as we want to isolate the delays created within the atomic ensemble. The non-atomic reflections cause a signal of significant amplitude. To reduce this, we turn on the piezo attached to the back mirror, see figure 5.21, so that the position x_0 of the reflector with respect to the end mirror moves periodically. If we perform our measurements more slowly than the oscillation timescale of the piezo, the power modulation caused by non-atomic reflecting elements will average to zero, similar as described in the propagation delay section. Plot c) and d) of figure 5.25 compare a measurement done with piezo turned off to a measurement done with piezo turned on. All measurements have been done with a filter bandwidth of the lock-in of 18 Hz, so that the measurement time, 55 ms, was much longer than the oscillation period of the piezo $T = 1/3 \,\mathrm{kHz} = 0.33 \,\mathrm{ms}$. One sees that the amplitude of the signal reduces by around 15dB almost to the background level (gray trace). In all measurements that I will show in the following the piezo was turned on.

Variation of atom number during MOT phase

The first experiment is similar to the experiment from the beginning of this chapter, in which the number of atoms in the lattice volume was varied by loading the MOT for different times, see 5.3. Again the MOT is loaded for a specific variable time. During this time the lattice beam is at very low power ($P = 110 \,\mu\mathrm{W}$), so that $\Omega_\mathrm{a}(0) \ll \Omega_\mathrm{m}$. Subsequently, the lattice is ramped up (in 10 ms) to $P_0 = 9.12 \,\mathrm{mW}$ so that $\Omega_\mathrm{a}(0) > \Omega_\mathrm{m}$. Shortly afterwards the lock-in amplifier is triggered to measure the backaction of the atoms for 50 ms at a given modulation frequency Ω. As the atomic lifetime in the MOT is seconds, the atom number in the MOT stays nearly constant during these 50 ms. Then, the experiment is repeated with a different loading time and/or a different modulation frequency Ω.

Figure 5.26 shows amplitude and phase of the power modulation for different MOT loading times and correspondingly different atom numbers in the lattice volume. The technical phase lag of $45°/\mathrm{MHz}$ has been substracted from the phase measurement, so that the signal shows the bare effect from the atoms. Figure 5.27 shows the corresponding quadratures of the electrical voltage. Here the red dot marks the measurement at the membrane frequency. If the red dot lies within the gray area, the coupled system will become unstable according to the criterion discussed in the last subsection.

The measured amplitude behavior in figure 5.26 a) is in qualitative agreement with the prediction in figure 5.22. An initial peak is followed by a plateau at large frequencies. Both figures also show that the system must be stable for the smallest loading time as the trace never enters the gray region. This is in agreement with our earlier observations that the self-oscillation only kicks in after a certain threshold loading time. Moreover, the shape of the quadrature signal of this measurement has a lot of qualitative agreement with the theory signal. It starts at around $-90°$ and then approaches $-180°$. However, there is a loop in the trace, which is not predicted by the theory. In the phase plot in figure 5.26 this is visible as a going up and down of the phase. In the second, orange trace the loop almost touches the center of the
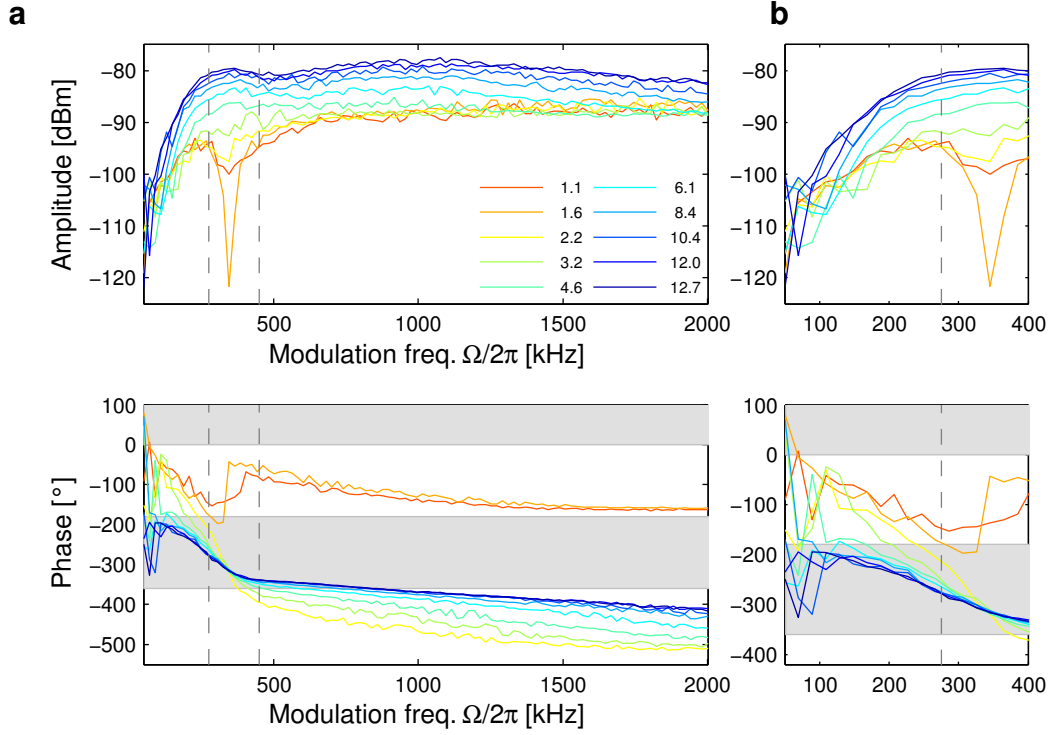
Figure 5.26: The plots show the frequency response of the atomic backaction for different MOT loading times. The legend displays the corresponding number of atoms in the lattice volume in units of 10^7 atoms. The upper graph in figure a) shows the amplitude and the lower plot the phase of the power modulation on the light caused by the backaction of the atoms. The phase is referenced to the phase of the modulation on Φ and the amplitude is given in units of electrical power. Figure b) shows a zoom to the low frequency region of figure a). The dashed lines mark the membrane frequency $\Omega_\mathrm{m}/2\pi = 275\,\mathrm{kHz}$ and the expected maximal atomic frequency $\Omega_\mathrm{a}(0)/2\pi = 449\,\mathrm{kHz}$. The gray color marks the area in which the coupled system in principle can become unstable if the gain is high enough. Experimental parameters: atom-laser detuning $\Delta_\mathrm{LA} = -2\pi \times 1\,\mathrm{GHz}$, power reflectivity $R = 0.06$.
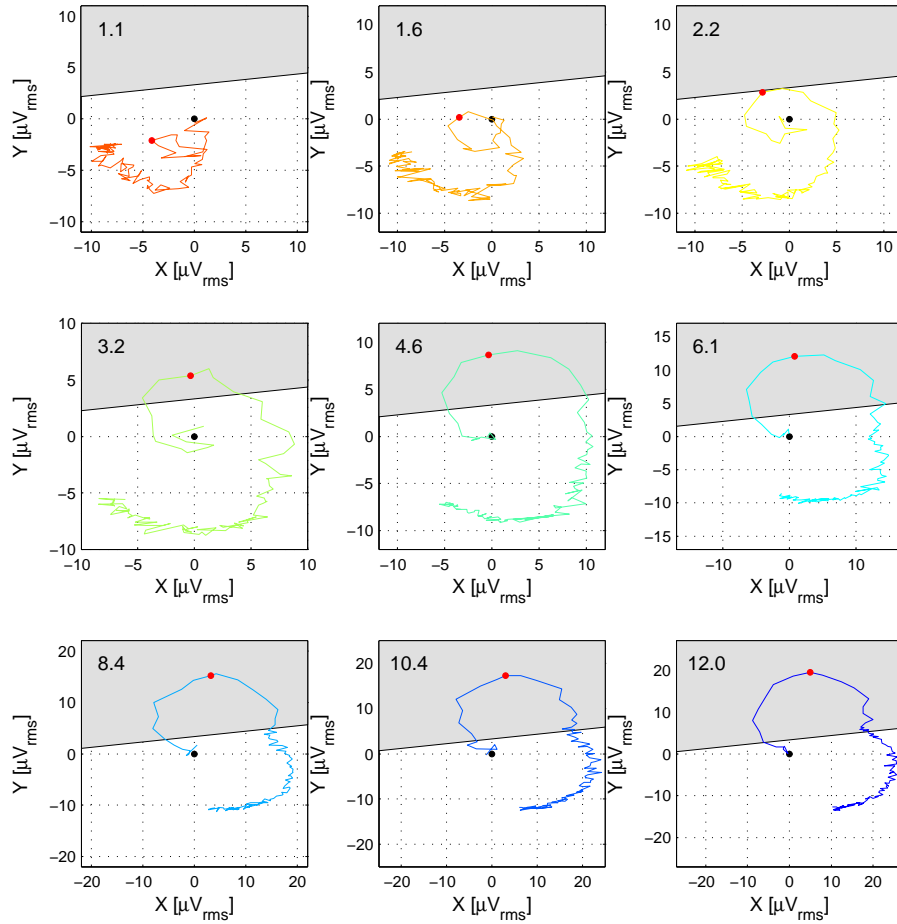
Figure 5.27: The plots show the quadratures corresponding to the frequency response shown in figure 5.26. The numbers show the loaded atom number in units of 10^7 atoms. The red dot marks the measurement at the membrane frequency and the gray area the instability region. The critical quadrature region has been tilted with respect to 5.40 by the finite propagation phase $\phi_\mathrm{p} = 5.2°$, which is typically present in our coupling experiments.

coordinate system, which corresponds to the prominent dip in the corresponding amplitude plot. This loop in the quadrature plot is located away from the origin for the smallest atom number. For increasing atom number, it moves closer to the origin and starts to wind around the zero point, which drastically influences the phase behavior.

For atom numbers exceeding 3.2×10^7 the red dot lies in the gray area, predicting an instability in the coupled system in agreement with our previous observations. The phase behavior is extremely different from the theoretically expected one for the large atom numbers. The phase lag at the membrane frequency gets as large as $270°$ exceeding the theoretical maximum of $180°$ by much more than the phase shift $2\Omega_\mathrm{m}\tau = 17°$ from the $\tau = 88\,\mathrm{ns}$ delay fitted in figure 5.9. However, it has to be noted that the current experiment and the experiment from figure 5.9 differ in the power reflectivity R and the ingoing power P_0 and can therefore not be compared directly.

Variation of atom number during molasses phase

In all measurements on the self-oscillation effect we observed an immediate reduction of the membrane amplitude as soon as we switched from MOT to molasses cooling. Therefore, I repeated the backaction measurement with molasses-cooled atoms. For this, the time of the lattice ramp-up and the subsequent measurement was shifted to a certain time after the start of the molasses phase. Figure 5.28 shows the frequency response of the atomic backaction for different molasses times. The signals are small but the phases are well-defined. The amplitude reduces with increasing molasses time because the optical depth quickly decreases. None of the traces enters the gray instability regions, and qualitatively the measured signals agree with the expectations from the model without delay. This is in agreement with our observation that the self-oscillation vanishes in the molasses phase. Note that the amplitude levels of all molasses measurements, which quantify the strength of the atom-light coupling, stay below the signal levels of the first MOT measurements in figure 5.26, which do not penetrate the instability region either. Self-oscillation might, thus, be absent in the molasses regime because the atom-light interaction is too weak.

Variation of the laser detuning - red

As we observed a strong dependence of the self-oscillation effect on the lattice parameters, we repeated the experiment for different red detunings of the coupling lattice. In this experiment the laser power was kept constant and the MOT was running permanently. Figure 5.29 shows the results of the measurement. One sees that the signal amplitude rises with decreasing detuning. This makes sense as the power modulations depend on the atomic polarizability $\zeta \sim N/\Delta_\mathrm{LA}$ (see equation 5.24), which increases for decreasing detuning Δ_LA. Furthermore, as discussed in section 5.5.1, the number of atoms trapped in the lattice modulation wells might rise for decreasing detuning as the increasing light shift leads to colder temperatures in the lattice
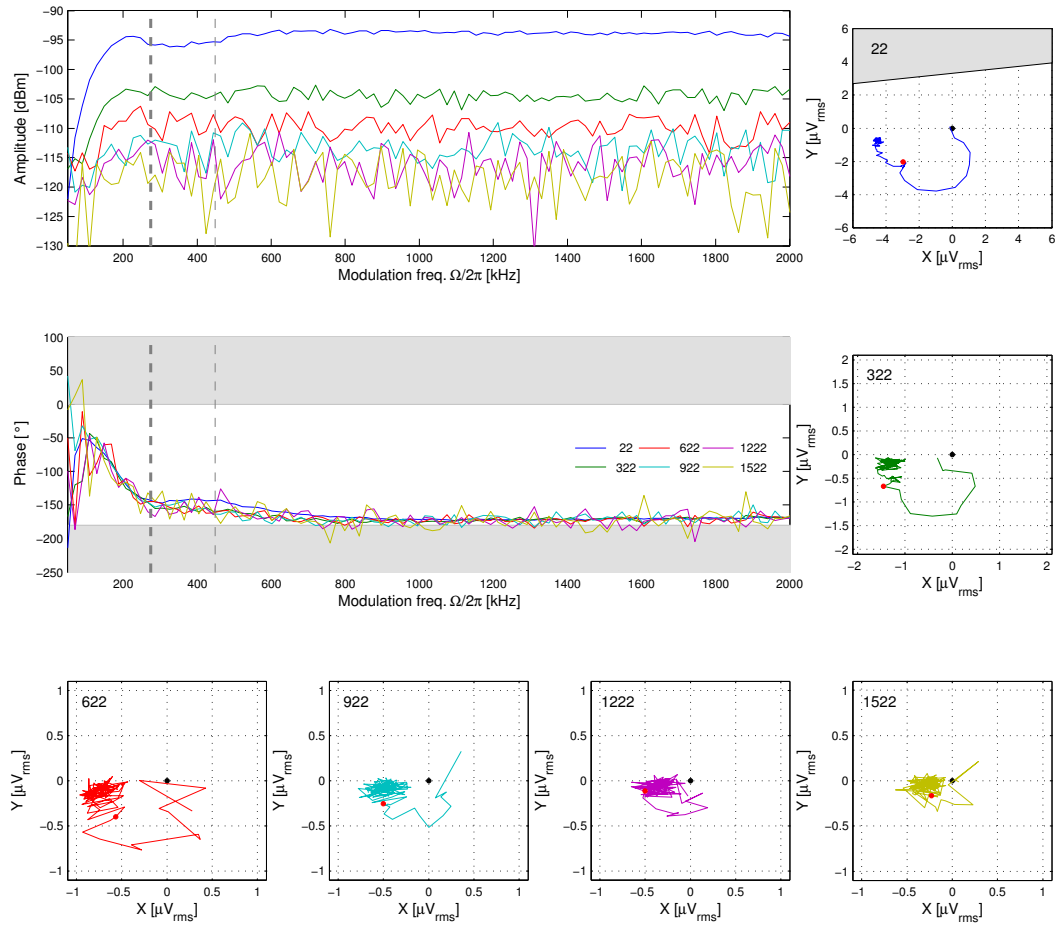
Figure 5.28: The large plots show amplitude and phase of the frequency response during the molasses phase. The small plots show the corresponding quadratures. The legend and the numbers in the quadrature plots display the molasses time in ms. The measurements look qualitatively similar to the theoretical prediction for an atomic oscillator without delay in figure 5.22.
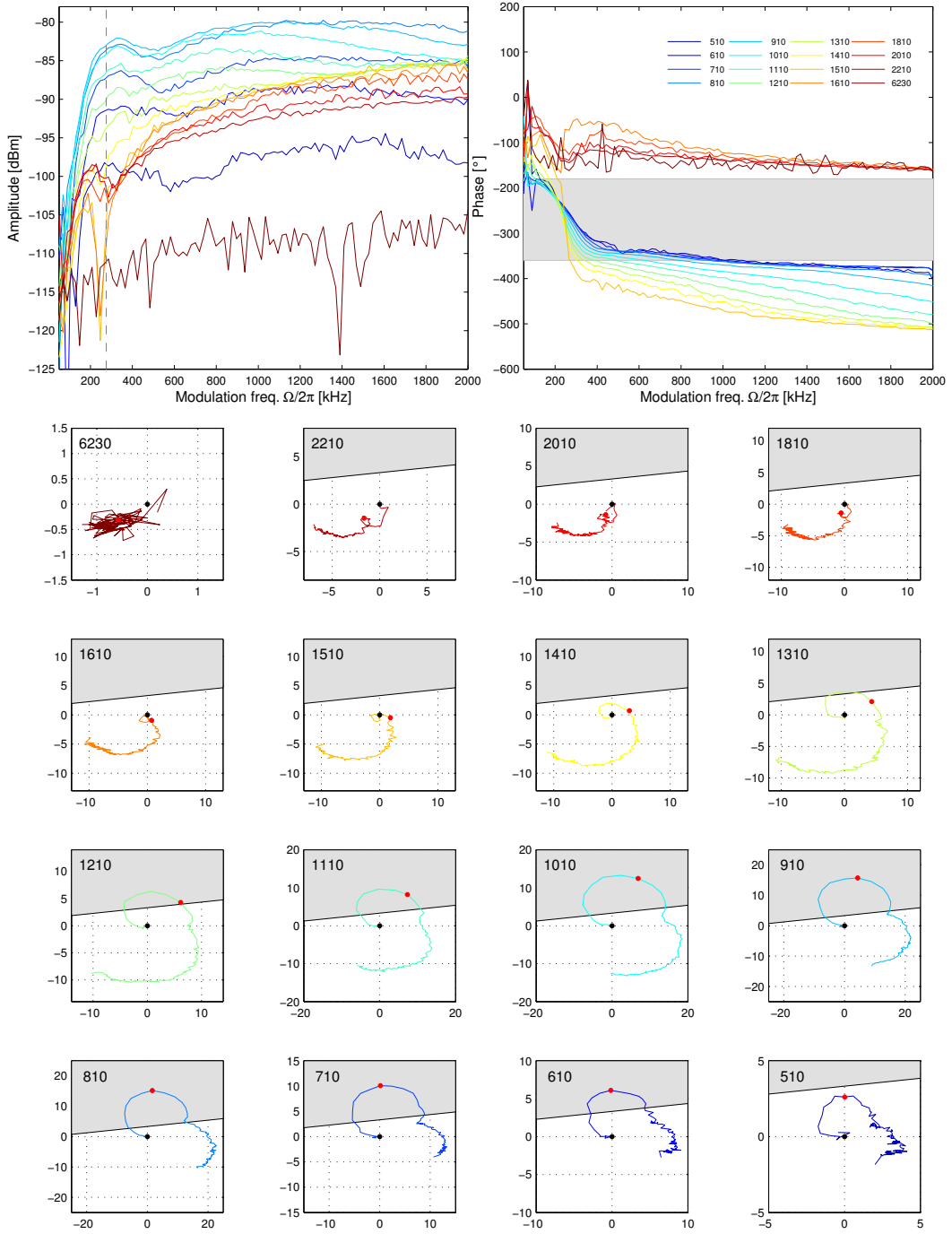
Figure 5.29: Plots on top: amplitude and phase of the freq. response for different red detunings. Small plots: corresponding quadratures. The axes of the quadrature plots show r.m.s. voltage in μV. Axis labels are left away for better visibility. The legend and the numbers in the quadrature plots show the absolute value of the detuning of the coupling lattice from the $F = 2 \leftrightarrow F' = 3$ transition $|\Delta_{\mathrm{LA}}|/2\pi$ in MHz. Exp. parameters: ingoing power $P_0 = 9.12\,\mathrm{mW}$, reflectivity $R = 0.06$.
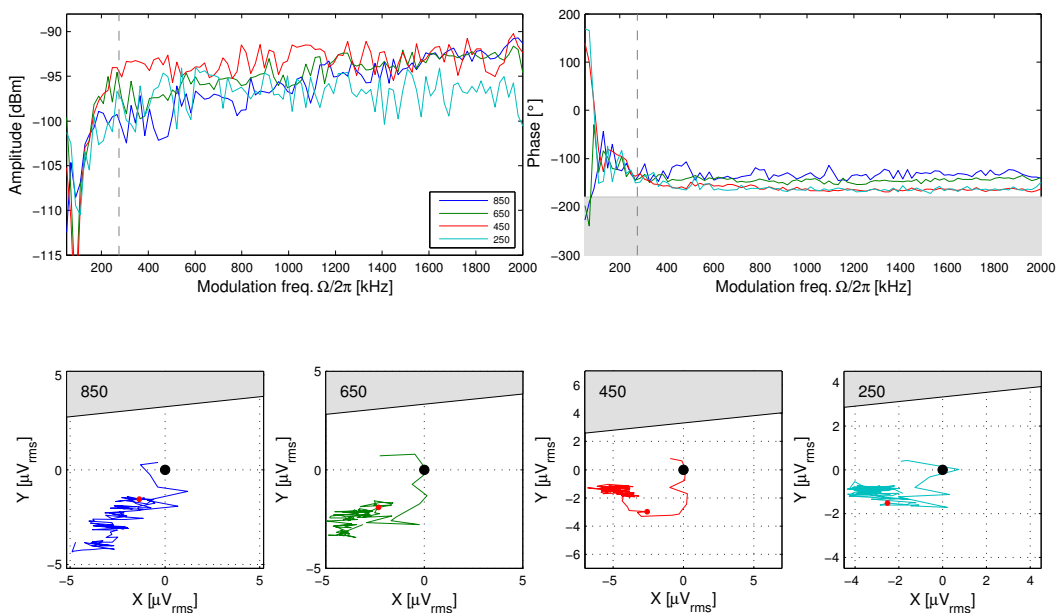
Figure 5.30: Figure a) and b) show amplitude and phase of the frequency response for different blue detunings at the laser from the atomic transition, figures c)-f) the corresponding quadratures. The legend and the numbers in the quadrature show the absolute value of the detuning of the coupling lattice from the $F = 2 \leftrightarrow F' = 3$ transition $|\Delta_{\text{LA}}/2\pi|$ in MHz.

volume. Surprisingly, for detunings below $\Delta_{\text{LA}} = 2\pi \times 910\,\text{MHz}$, the signal amplitude decreases again. A reduction of the atom number due to the increased lattice scattering rate at small detuning (see equation 1.23) might explain this. However, the phase behavior of the traces at very small detunings differs strongly from the behavior at large detuning even if the signal amplitudes are comparable (compare e.g. the 2010 MHz and 610 MHz measurements). This indicates that not simply the number of trapped atoms is changing. In this measurement atom number effects and detuning effects are connected, which makes it hard to analyze the data.

Still, the measurement allows to make some remarks. Firstly, it predicts stability for large detunings and instability for small detunings consistent with the measurements on lattice parameter dependence (see figure 5.17). Secondly, for large detunings the loop with unknown origin appears again. It approaches the zero point for decreasing detuning and winds around it for detunings smaller than 1610 MHz.

Variation of the laser detuning - blue

Lastly, figure 5.30 shows results of the same measurement as before but with blue detunings. For all measurements the signal stays in the stability region. The phase responses for different blue detunings roughly overlap, going from $-90°$ towards

$-180°$. The measurements look qualitatively similar to the expectation without delay and to the measurements performed during the molasses phase. This fits to the prior observations that we do not see any self-oscillations when the lattice is blue-detuned. Note that also here, the signal levels are small, indicating that self-oscillations do not appear in blue lattices because the atom-light coupling is too small as discussed already in section 5.5.1.

5.6.5 Summary

In this section I described measurements of the atomic backaction onto the coupling laser light. It was the first time in our lab that we directly measured this backaction. The measurements give valuable information about the atom-light interactions of our coupled atom-membrane system. Especially in the context of the self-oscillation, the backaction measurement is a useful tool as we suspect the atoms to be responsible for the phase delay.

The measurements show that in regimes in which no instability is observed in the coupled system, namely in the molasses phase, for small atom numbers and large lattice detunings or in experiments with blue detuning, the atomic backaction shows no sign of a delay. On the contrary, measurements in the MOT phase, with large atom number and small red detuning, show extremely large phase lags in the atomic backaction. In this parameter regime the backaction measurements predict instable behavior, which is consistent with our prior observations. Thus, the measurements show that the retardation which causes the instability arises within the atomic ensemble. Strictly speaking, there is no real delay in the system. We observe a phase-shift with respect to the expected behavior $\Delta\phi_{\mathrm{at}} = \phi_{\mathrm{at,theo}} - \phi_{\mathrm{at}}$, that can be assigned to an effective delay $\tau_{\mathrm{at}} = \Delta\phi_{\mathrm{at}}/\Omega_{\mathrm{m}}$. As already mentioned in the beginning of section 5.3, it is the phase-shift induced by a delay that matters for the stability of the system.

5.7 Collective atomic effects in an asymmetric lattice

In section 1.1.6 I claimed that if $|\Delta_{\mathrm{LA}}| \gg \Gamma_{\mathrm{a}}$, the atomic ensemble can be described as one single beamsplitter and I used this description to derive the equations of motion of the coupled atom-membrane system. In the parameter regime of small detunings $\Delta_{\mathrm{LA}} \approx -2\pi \times 1\,\mathrm{GHz}$, in which the instability studied in this chapter occurs, this one-beamsplitter-assumption is not necessarily well-fulfilled. In [78] Asbóth et al. study the atom-light interaction in a one-dimensional lattice and explicitly take the distribution of the atoms over several lattice wells into account. They find that the lattice can become unstable if the atomic polarizability ζ given in equation 1.30 is large and the lattice is asymmetric, meaning that one lattice beam is stronger than the other. Inspired by their observations and the preceding backaction measurements, I repeated the numerical simulation done in [78] and extended it to simulate the backaction measurements. Interestingly, I find that light-mediated interaction between the atoms in different wells of an asymmetric lattice can lead to

146
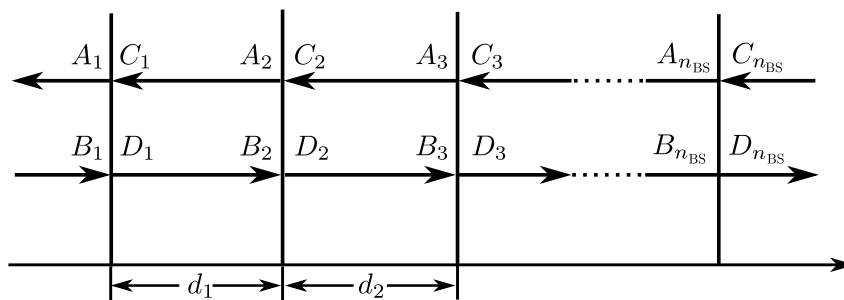
Figure 5.31: New model of atoms in optical lattice taking the distribution over several lattice wells into account. The atomic ensemble is described as a stack of beamsplitters.

large phase shifts in the atomic backaction onto the light. This makes such collective atomic effects a strong candidate for being the origin of the self-oscillation.

Collective effects in atomic ensembles mediated by the atomic backaction on laser light have been observed in optical cavities [156]. The presence of a cavity strongly enhances the atom-light interaction. If a cold atomic ensemble in a linear cavity is strongly driven by a perpendicular laser beam, the coupling of atoms at different positions to the cavity mode leads to a self-organization of the atoms in a checkerboard lattice [157, 158]. In an experiment with a BEC this self-organisation mechanism was even exploited to realize a phase transition between a super-fluid and a self-organized phase [159, 160]. In a ring cavity the backaction of atoms can lead to the conceptually related phenomenon of collective recoil lasing [161, 162]. Atoms in a unidirectionally pumped high-finesse ring cavity scatter light also into the back-propagating cavity mode. The dipole force generated by light in this cavity mode pulls the atoms towards positions at which the backwards scattering is stronger. This mechanism results in an exponential gain of the back-propagating field mode amplitude and an accumulation of the atoms at the antinodes of the emerging moving optical lattice.

In free-space experiments the atom-light coupling is typically too weak to induce collective effects. However, the following simulations show that in an asymmetric lattice light-mediated atom-atom interactions can matter for realistic experimental parameters. I will sketch the model and present the results of the numerical simulations in the following.

5.7.1 Model

The atomic ensemble is modeled as an array of n_{BS} beamsplitters with transfer matrices $M_{\mathrm{BS},i}, i \in (1...n_{\mathrm{BS}})$ as given in equation 1.36. The beamsplitters are separated by distances d_i corresponding to the free-space transfer matrices $M_{\mathrm{d},i}$ introduced in equation 1.67 as depicted in figure 5.31. As in section 1.1.6, the lattice is created by two laser beams with amplitudes $C(x) = E_1 e^{-ikx}$ from the right and

147

$B(x) = E_0 e^{ikx+i\Phi(t)}$ from the left and intensities $I_i = \epsilon_0 c|E_i|^2/2$. The lattice is asymmetric, $E_0 = \sqrt{R}E_1$ ($\sqrt{R} \leq 1$), and the phase on the beam from the left is modulated with frequency Ω, $\Phi(t) = \Phi_0 \cos(\Omega t)$.

5.7.2 Numerical simulation

At the start of the simulation (t=0) each atomic ensemble is displaced by a small, random displacement $\xi_i(t=0)$ from its steady state position x_i^s

$$x_i(t=0) = x_i^s + \xi_i(t=0) \,. \tag{5.41}$$

The initial displacement $\xi_i(t=0)$ is a uniformly distributed random variable between $-\xi_{\text{initial}}$ and ξ_{initial}, with $\xi_{\text{initial}} = 5 \times 10^{-4}\lambda$. To determine the steady state positions x_i^s, the asymmetric radiation pressure is taken into account as well as the reduction of the lattice constant d in presence of atoms for red and blue detuning [78]

$$
\begin{aligned}
\text{red:} \quad d &= \frac{\lambda}{2}\left(1 - \frac{\chi^+}{\pi}\right), \\
\text{blue:} \quad d &= \frac{\lambda}{2}\left(1 - \left|\frac{\chi^-}{\pi}\right|\right),
\end{aligned}
\tag{5.42}
$$

with

$$\chi^{\pm} = \arcsin\left(\frac{\zeta\sqrt{4+\mathcal{A}} \pm \zeta\sqrt{4-\zeta^2\mathcal{A}^2}}{2(1+\zeta^2)}\right). \tag{5.43}$$

The parameter $\mathcal{A}$ quantifies the asymmetry of the lattice

$$\mathcal{A} = \frac{I_1 - I_0}{\sqrt{I_1 I_0}} \,. \tag{5.44}$$

These analytic expressions for the reduced lattice constant hold for non-dissipative atomic ensembles only ($\zeta \in \mathbb{R}$). Therefore, I restrict my simulations to this case and neglect the imaginary part of the atomic polarization $\text{Im}\,\zeta$. In principle, the simulation can also be performed for dissipative material. Only the starting displacements will be slightly different from ξ_{initial} in this case. If $\text{Im}\,\zeta \ll \text{Re}\,\zeta$, the deviation is small and not relevant for the result of the simulation. In fact, for the parameters used in this chapter, I do not see a significant difference in the results of the simulations if I use the full complex polarizability ζ to calculate the beamsplitter matrices $M_{\text{BS},i}$.

For each timestep the global outgoing fields A_1 and $D_{n_{\text{BS}}}$ as well as the fields at the position of each atomic beamsplitter are calculated using the transfer matrix method. Via equation 1.39, the force on each atomic pancake F_i is determined. Subsequently, the position of each atom in the next timestep is calculated from the corresponding equation of motion

$$m_{\text{BS}}\ddot{x}_i = -m_{\text{BS}}\Gamma_a \dot{x}_i + F_i \,. \tag{5.45}$$
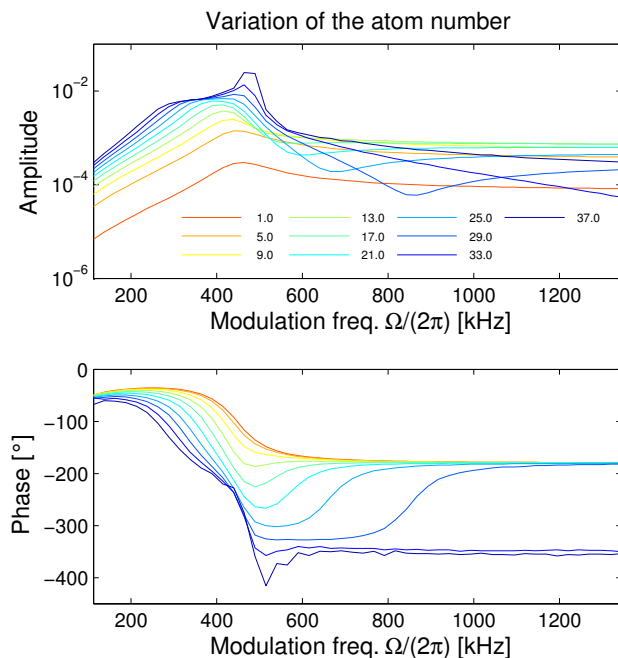
Figure 5.32: Simulated atomic response for variable atom number. The plot shows the amplitude and the phase of the relative power modulation of the outgoing beam $(P_{\text{left}} - \langle P_{\text{left}} \rangle)/\langle P_{\text{left}} \rangle$ for various atom numbers. The legend displays the atom number in units of 10^7 atoms. The phase is referenced to the phase of the ingoing modulation. The simulation has been performed for ingoing power $P_1 = \pi w_0^2 I_1/2 = 9.12\,\text{mW}$, atom-laser detuning $\Delta_{\text{LA}} = -2\pi \times 1\,\text{GHz}$, beam waist $w_0 = 280\,\mu\text{m}$, reflectivity $R = 0.06$, $n_{\text{BS}} = 10$ pancakes, atomic damping $\Gamma_{\text{a}} = \Omega_{\text{a}}(0)/4 = 7 \times 10^5\,\text{s}^{-1}$ and driving amplitude $\Phi_0 = 10^{-3} \times 2\pi$.

Here $m_{\text{BS}} = N_{\text{BS}}m$ is the mass of the $N_{\text{BS}} = N/n_{\text{BS}}$ atoms in one lattice well.

If the phase of the beam from the left Φ is modulated ($|\Phi_0| > 0$) at a frequency Ω, the phase and the amplitude of the resulting power fluctuations of the outwards going beam to the left $P_{\text{left}} = I_{\text{left}}\pi w_0^2/2$ ($I_{\text{left}} = \epsilon_0 c|A_1|^2/2$) are evaluated once the simulation is completed. For this evaluation only the outgoing power P_{left} after the initial transient time $T_{\text{damp}} = 1/\Gamma_{\text{a}}$ is taken into account.

5.7.3   Results of the simulation

Atom number dependence

Figure 5.32 shows the simulated backaction of the atomic ensemble onto the light for parameters similar to the ones of the experiment presented in figure 5.26. Concretely, the ingoing power P_1, the detuning Δ_{LA}, the beam waist w_0 and the reflectivity R have been set to the same values (see figure caption). The atomic damping rate has
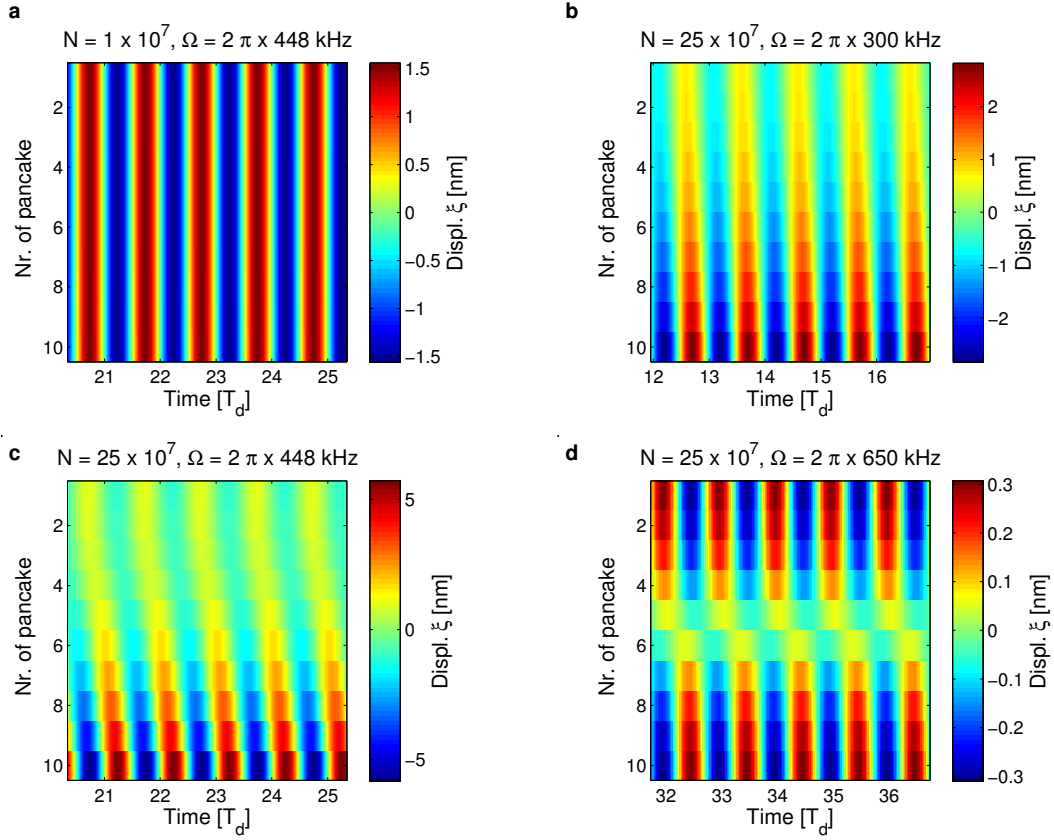
Figure 5.33: Exemplary atomic traces corresponding to different points in figure 5.32. The plots depict how the displacement $\xi_i(t) = x_i(t) - x_i^s$ of each atom from its steady state position (color coded) evolves with time. The time is given in units of the drive period $T_d = 2\pi/\Omega$. The titles show the atom number N and the drive frequency Ω.

been set to $\Gamma_a = \Omega_a(0)/4$ to simulate the strong inhomogeneous broadening in the experiment. Here, $\Omega_a(0) = 2\pi \times 448\,\mathrm{kHz}$ is the trapping frequency in the low atom-light coupling limit given by equation 1.21. Moreover, the total number of atoms N is varied over a similar regime as in figure 5.26. The N atoms are distributed over $n_{\mathrm{BS}} = 10$ beamsplitters. For atom numbers larger than $N = 37 \times 10^7$ the lattice becomes unstable.

For small atom numbers (red and orange trace) the curves follow the prediction of the single beamsplitter model depicted in figure 5.22 as expected. For increasing atom number, the amplitude of the relative power modulations $(P_{\mathrm{left}} - \langle P_{\mathrm{left}} \rangle)/\langle P_{\mathrm{left}} \rangle$ increases. Surprisingly, the peak moves towards lower frequencies and broadens. Simultaneously the phase of the backaction starts to penetrate the region below $-180°$ enabling the occurrence of self-oscillations in the coupled system. For very

large atom numbers (dark blue traces), a new second peak appears slightly to the right of the initial atomic resonance and the phase drops in two steps as low as $-360°$.

Figure 5.33 shows a couple of exemplary atomic traces corresponding to different points in figure 5.32. Plot a) shows how the displacements of the atomic ensembles from their steady state positions $\xi_i(t) = x_i(t) - x_i^s$ evolve with time if the atom number is small ($N = 1 \times 10^7$). All beamsplitters oscillate with the same phase set by the ingoing modulation as expected in the absence of atom-atom interaction. For large atom numbers, the behavior is fundamentally different. The plots b) - d) show the evolution of the displacement $\xi(t)$ of $N = 25 \times 10^7$ (slightly higher than the maximum atom number in our experiment) atoms for driving frequencies b) below resonance ($\Omega = 2\pi \times 300\,\text{kHz}$) c) at resonance ($\Omega = 2\pi \times 448\,\text{kHz}$) and d) above resonance ($\Omega = 2\pi \times 650\,\text{kHz}$). The beamsplitters do not oscillate in phase any more but the motional phases of the individual beamsplitters are strongly correlated. Plot b) and d) show very different collective modes. In b) the phase and the amplitude vary linearly over the atomic ensemble. In d) there is a region in the middle in which the atoms hardly oscillate. Here, the oscillations at the edges are equally large but opposite in phase. Plot c) shows the transition between the two modes in b) and d).

Thus, the modified model predicts that collective effects between the atomic beamsplitters in an asymmetric lattice lead to phase-shifts in the atomic backaction onto the light in a parameter regime similar as in our experiment. Any phase-shift with respect to the single beamsplitter model can lead to instable behavior as discussed in section 5.6.3. Collective atomic effects might therefore be the origin of the self-oscillations.

The simulation in figure 5.32 does not exactly reproduce the measured frequency response of figure 5.26. This can be due to the fact that the model of the atomic ensemble is greatly simplified. Already in chapter 4, the radial density distribution of the atomic ensemble had to be taken into account to model the data. In the self-oscillation experiments of the current chapter, the coupling lattice is surrounded by the MOT cooled cloud and the MOT magnetic field gradients are turned on. The MOT temperature is high ($> 1\,\text{mK}$), but very likely the light-shift induced by the coupling lattice locally modifies the atomic temperature, the density profile and the atomic damping rate as discussed in section 5.5.1. With our current setup we are not able to precisely determine the local properties of the atoms in the coupling lattice volume in presence of the surrounding MOT cloud. This makes it difficult to model radial distributions in this case. Still, two very important features, the occurrence of atomic backaction phases below $-180°$ and the fact that this behavior becomes more pronounced for increasing atom number, are in agreement in data and simulation.
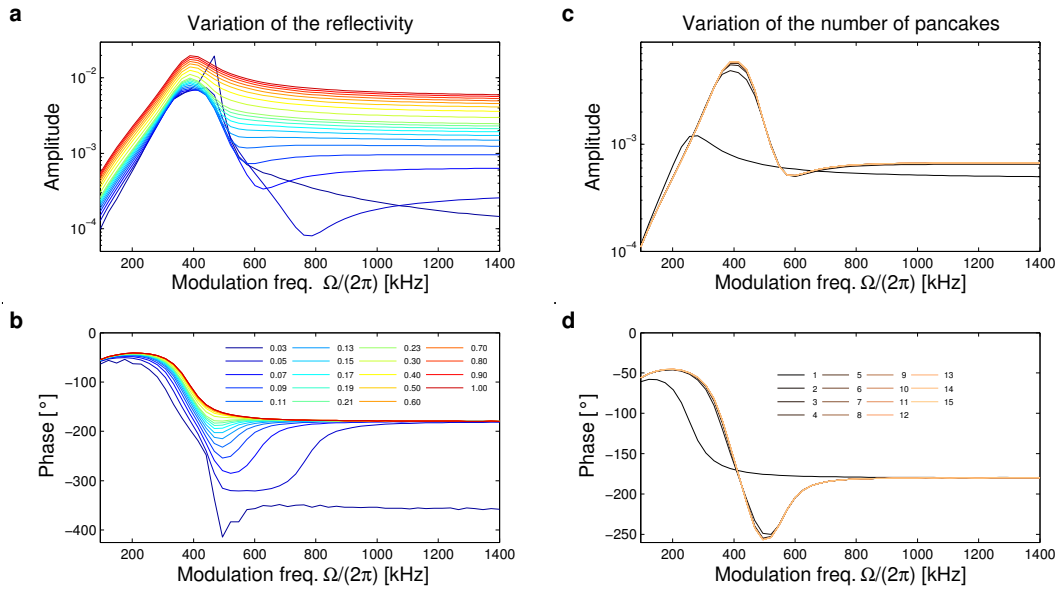
Figure 5.34: a) and b) Simulated frequency response for variable reflectivity R. $N = 25 \times 10^7$. The ingoing power P_1 is adjusted such that the trapping frequency stays at $\Omega_a(0) = 2\pi \times 448\,\text{kHz}$. c) and d) Simulated frequency response for different numbers of pancakes. $N = 20 \times 10^7$. a) and c) Amplitude, b) and d) phase of the relative power fluctuations of the leftwards traveling beam as in figure 5.32. All parameters which are not mentioned explicitly are given in the caption of figure 5.32.
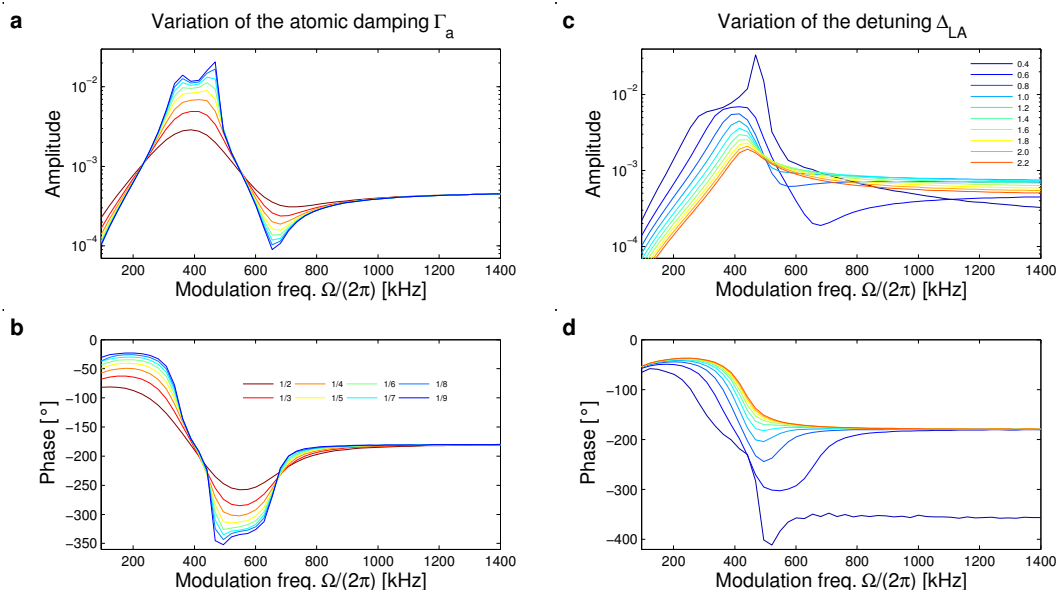
Figure 5.35: a) and b) Simulated frequency response for different atomic damping rates Γ_a. The legend shows the ratio between the atomic damping rate and the oscillation frequency $\Gamma_a/\Omega_a(0)$. $N = 25 \times 10^7$. c) and d) Simulated frequency response for different red atomic detunings $\Delta_{LA} < 0$. The legend displaces $|\Delta_{LA}/2\pi|$ in GHz. $N = 15 \times 10^7$. The ingoing power P_1 is adjusted such that the trapping frequency stays at $\Omega_a(0) = 2\pi \times 448\,\mathrm{kHz}$. a) and c) Amplitude, b) and d) phase of the relative power fluctuations of the leftwards traveling beam as in figure 5.32. All parameters which are not mentioned explicitly are given in the caption of figure 5.32.

Dependence on the asymmetry, number of pancakes, atomic damping and detuning

To get more insights into the collective behavior, several system parameters have been varied in the simulation. Figure 5.34 a) and b) show amplitude and phase of the atomic frequency response for different reflectivities R. For $R = 1$ the behavior equals the expectation from the single beamsplitter model (figure 5.22). For all driving frequencies the atomic beamsplitters move in phase as in figure 5.33 a). Thus, no collective effects are present in the symmetric lattice. Figure 5.34 a) and) clearly shows that this behavior changes and becomes more and more pronounced for decreasing reflectivity. In figure 5.34 c) and d) the number of the atomic beamsplitters is varied between $n_{BS} = 1..15$. One sees a drastic difference when going from one to two beamsplitters. For one beamsplitter no collective effects can occur and the response is given by the single beamsplitter model as expected. For $n_{BS} > 2$ the collective behavior immediately kicks in and saturates quickly. For $n_{BS} > 4$ no
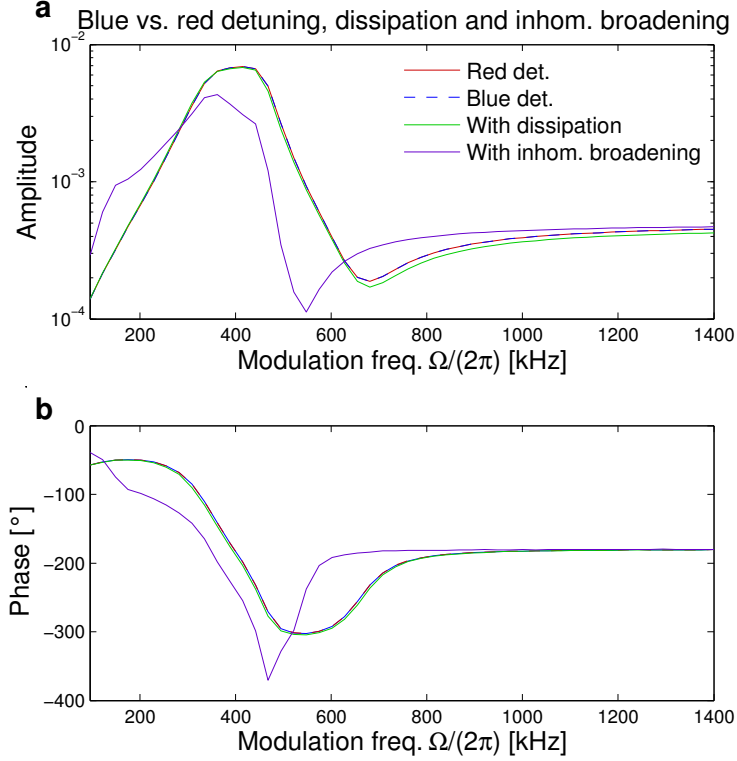
Figure 5.36: Amplitude a) and phase b) of the simulated relative power modulations of the leftward traveling beam at a given modulation frequency Ω for different configurations. Red: $\Delta_{\mathrm{LA}} = -2\pi \times 1\,\mathrm{GHz}$, $\Gamma_{\mathrm{a}} = \Omega_{\mathrm{a}}(0)/4$. Blue dashed: $\Delta_{\mathrm{LA}} = 2\pi \times 1\,\mathrm{GHz}$, $\Gamma_{\mathrm{a}} = \Omega_{\mathrm{a}}(0)/4$. Green: As red, but also $\mathrm{Im}\,\zeta$ is taken into account. Purple: As red, but with radial distribution of 50 atomic ensembles with $\Gamma_{\mathrm{a}} = \Omega_{\mathrm{a}}(0)/10$. $N = 25 \times 10^7$ in all plots. All parameters which are not explicitly mentioned are the same as in figure 5.32.

significant difference between the traces can be observed any more. Note that in the experiment the atoms occupy $n_{\mathrm{BS}} = 2R_{\mathrm{a}}/(\lambda/2) \approx 10^4$ potential wells. Such large numbers were not simulated because the computation time would have been too long.

Figure 5.35 a) and b) shows the behavior for varying atomic damping Γ_{a}. At low damping ($\Gamma_{\mathrm{a}} \approx \Omega_{\mathrm{a}}(0)/9$, blue traces) one clearly sees the presence of two distinct peaks in the amplitude plot corresponding to the two different spatial modes in figure 5.33. For larger damping the amplitude strongly reduces and the phase behavior washes out.

In figure 5.35 c) and d) the atomic detuning Δ_{LA} is varied. The ingoing power P_1 is adjusted so that $\Omega_{\mathrm{a}}(0)$ stays constant. A smaller detuning increases the atomic polarizability $\zeta \sim \frac{1}{\Delta_{\mathrm{LA}}}$ (see equation 1.30), which increases the atomic backaction

onto the light field. Therefore, the signal is larger for smaller detunings and stronger influenced by the collective effects.

Finally figure 5.36 compares two simulations which only differ in the sign of the detuning (red and dashed blue trace). The curves lie on top of each other meaning that the collective behavior is the same in the red and the blue case. The absence of self-oscillations in the blue case in the experiment is due to the fact that less atoms take part in the coupling in a blue-detuned lattice as discussed in section 5.5.1. Figure 5.36 further shows the result of a simulation in which also the imaginary part of the atomic polarizability $\operatorname{Im} \zeta$ and, therefore, dissipation has been taken into account (green trace). As mentioned above, the difference is negligible. Lastly, a plot is shown for which the radial distribution of trapping frequencies in an atomic ensemble with constant density distribution has been taken into account (purple trace). For this it is assumed that light from different radial regions hits the photo-detector at different positions so that the voltage signal is the sum of the signals from the different radial regions. The purple trace shows the summed signal of 50 equally dense atomic packets at different radial positions (thus seeing different lattice intensities) with atomic damping rates of $\Gamma_a = \Omega_a(0)/10$. Compared to the traces without this inhomogeneous broadening and $\Gamma_a = \Omega_a(0)/4$ the resonance peak is slightly deformed, of comparable width and at a lower frequency. The minimal phase is reduced and the behavior on the right side of $\Omega_a(0)$ is sharper due to the reduced Γ_a. As mentioned above, the correct radial density and damping rate distribution in the middle of the MOT cloud are not known so that an exact modeling of the inhomogeneous broadening is very difficult. Specifically it is not guaranteed that the density profile is flat as in chapter 4 for the reasons discussed in section 5.5.1.

5.7.4 Discussion

The numerical simulation presented above showed that large atomic polarizabilities in asymmetric lattices lead to light-induced interactions between the atoms in different potential wells. If the atomic motion is driven via a modulation of the phase of one ingoing beam, the atomic backaction onto the light in presence of these atom-atom-interactions strongly deviates from the single beamsplitter behavior. Especially the phase lag of the backaction can be much larger than 180°. This acts as an effective delay in the coupled atom-membrane system and is therefore very likely the origin of the self-oscillations.

Due to the lack of knowledge about the exact atomic parameters in the lattice volume, precise modeling of the measured atomic backaction onto the light is difficult. Still, the modeled parameter dependence of the collective atomic backaction is qualitatively consistent with our measurements. It shows the desired atom number dependence and can be much larger than the propagation delay, so that the latter can become irrelevant. Further, the collective effects are stronger for smaller detunings Δ_{LA} as they scale with the atomic polarizability $\zeta \sim N/\Delta_{LA}$. Thus, for larger detunings and fixed atomic frequency $\Omega_a(0) \sim \sqrt{P_0/\Delta_{LA}}$ the atom number needed for the same collective backaction effects is larger. If the fraction of trapped

atoms in the lattice increases with rising lattice power, this qualitatively explains the lattice parameter dependence observed in section 5.5.2.

5.8 Summary and final conclusion

In this chapter I investigated self-oscillations, which appear in the atom-membrane system under certain experimental conditions.

I studied the dependence of this instability on several system parameters and found that a larger atom number and a smaller atom-light detuning Δ_{LA} make the system less stable.

The effect can be explained by a retardation in the coupling, which drives the system into limit cycle oscillations if the coupling strength is large. From the equations of motion in presence of a delay, I derived a modified sympathetic cooling rate. The model allows to fit the measured atom number dependence with a delay of $\tau = 88(1)$ ns. This retardation exceeds the propagation time between atom and membrane by a factor of three.

From the theoretical investigation we learned that any retardation in the coupling, even the small propagation delay between atoms and membrane, limits the sympathetic cooling performance. Possibly some of the sympathetic cooling experiments presented in the preceding chapter 4 were delay-limited. For sympathetic cooling into the quantum ground state, it is therefore crucial to minimize the distance between the atomic and membrane-cavity setup as well as the lifetime of photons in the cavity.

In the parameter regime exploited in this chapter, the main contribution to the retardation in the coupling arises from an effective delay in the backaction of the atoms onto the light. This could be shown by direct measurements of this backaction. These show large phase lags at the membrane frequency, which can be assigned to an effective retardation. Numerical simulations suggest that, most likely, the phase lags are caused by collective effects within the atomic ensemble. Such backaction mediated collective effects have been observed in optical cavities [161, 160, 158], but are not well studied in free space systems. In our experiments, the membrane oscillator acts as a sensitive probe for this small atomic light-matter interactions, demonstrating the possibilities of the hybrid system for sensing and signal transduction. To optimize the performance in sympathetic cooling experiments this effective atomic backaction delay can be suppressed simply by choosing a large atom-light detuning.

Chapter 6

Conclusions and outlook

This thesis presented experiments with a hybrid system, in which the motion of laser-cooled atoms is coupled to the vibrations of a membrane oscillator in a cavity. During the course of this thesis both subsystems were carefully characterized.

We used the coupling to cool the fundamental membrane vibration at $\Omega_\mathrm{m} = 2\pi \times 276\,\mathrm{kHz}$ from room temperature to $T_\mathrm{sym} = 0.4(2)\,\mathrm{K}$. Thus, during this thesis we realized for the first time an atom-membrane system which can be exploited for a useful task. In previous experiments the coupling had been too weak to alter the membrane properties significantly [28, 54, 29].

During the course of this thesis we learned that a delay in the coupling can have a significant impact on the behavior of the system. It drives the system into limit cycle oscillations if the coupling is large, which limits the sympathetic cooling performance.

We identified several sources of delays in our system. Under certain experimental conditions, the atomic backaction on the light is retarded, most likely due to light-mediated collective atomic effects within the ensemble. In this case the membrane acts as a sensitive probe for the collective atomic light-matter interaction. This shows the potential of the hybrid system for signal transduction or sensing applications. If desired, e.g. for sympathetic cooling, the effect can be suppressed by choosing a large atom-light detuning. The second source of the delay is the propagation time between atoms and membrane consisting of the bare propagation time between the atoms and the cavity and the lifetime of the cavity. This finite delay will always be present and has to be taken into account in any ground state cooling experiment. By using a fiber of suitable length the corresponding phase shift could be set to 2π and thus rendered irrelevant. We are currently investigating whether this delay-coupling can even by exploited in an experiment in the quantum regime e.g. for the creation of atom-membrane entanglement via two-mode squeezing.

For experiments in the quantum regime the atom-membrane quantum cooperativity C_qu has to be enhanced. In our current system it is limited to $C_\mathrm{qu} \approx 10^{-5}$ by the large phonon occupation of the membrane's thermal bath n_bath and laser noise on the membrane side as well as the large atomic inhomogeneous broadening on the
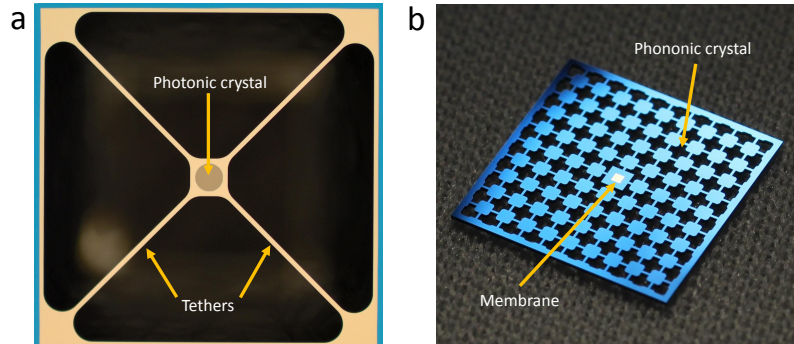
Figure 6.1: a) Tether membrane with photonic crystal. Most of the membrane material is removed to reduce the membrane mass. A photonic crystal structure on the membrane increases the membrane reflectivity. b) Standard Si_3N_4 membrane (golden square in the middle) embedded in a phononic crystal (blue structure).

atomic side. During the writing of this thesis optimization processes on the atomic and membrane side of the setup have been started, which I briefly present in the remaining paragraphs.

Further, we are currently investigating new coupling schemes which address the internal state of the atomic ensemble [163, 164, 72, 73]. This will allow us to use higher frequency mechanical oscillators, which are affected less by laser noise. Moreover, the internal states of the atoms can be prepared and detected with higher precision than the motional states, offering new possibilities for quantum operation.

Already after the current optimization steps on the atomic and membrane side, our hybrid atom-membrane system should be ready for operation in the quantum regime [69]. The system will then open the door to the preparation of non-classical motional states via optomechanical coupling to the atomic ensemble e.g. by the creation of atom-light entanglement [71, 72]. Ultimately, this will enable quantum signal transduction and precision sensing [165] applications as well as tests of quantum mechanical predictions in the regime of large masses [10, 11, 12].

Next generation membrane oscillators and cryogenic pre-cooling

To optimize the optomechanical coupling on the membrane side we are currently testing several types of new membranes. A very promising approach are so called tether membranes [166], see figure 6.1 a). In these structures most of the Si_3N_4 membrane material is removed. A small piece in the middle is attached to the frame
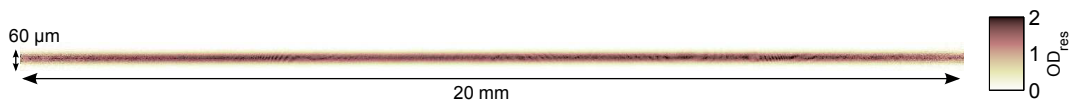
Figure 6.2:   Absorption image of the atomic ensemble in the dipole trap. The plot shows the resonant optical depth of 3×10^7 atoms seen from the side. The atoms form a straight line. The entire width of the ensemble cannot even be recorded because it exceeds the size of our imaging beam. The image was recorded after $1\,\mathrm{ms}$ of TOF.

only by four thin tethers. The resulting low frequency oscillator ($\Omega_\mathrm{m} = 2\pi \times 185\,\mathrm{kHz}$) has a very small mass ($2\,\mathrm{ng}$), which increases the single photon optomechanical coupling rate $g_0 = Gx_\mathrm{m,0}$. Due to the tethers, the membrane is well-isolated from the environment. We observed Q-factors of up to 15×10^6. The small mass and the high quality factor make these membranes very attractive for optomechanics experiments. The group of Simon Gröblacher in Delft combines tether membranes with photonic crystal structures [166]. This drastically increases the membrane reflectivity ($r_\mathrm{m} > 0.999$) enabling the usage of these membranes as vibrating endmirrors in optomechanical cavities. They provided us with a set of structures optimized for operation at $\lambda = 780\,\mathrm{nm}$. Unfortunately, the optical modes of the cavities built with these photonic crystals deviate strongly from the TEM_{00} mode. This will strongly reduce the efficiency in an atom-membrane coupling experiment so that the structures in their current status are not yet ready for the usage in a hybrid system. Fine tuning of the photonic crystal parameters might solve this problem.

   Further, we investigate membranes which are embedded in a phononic crystal, see figure 6.1. These membranes are purchased from Norcada and based on a design by the Regal group in Boulder [123] (see also [120]). A periodic structure in the membrane frame creates a phononic bandgap around the frequency of the membrane mode. This shields the mechanical mode of interest from the environment. The Q-factors which we observed with these membranes are not higher than the ones of the standard Norcada membranes, but they are more robust so that mounting the membrane is easier. In addition the background noise floor is lower, improving the signal to noise ratio of the membrane detection. A membrane cavity system using a phononic crystal membrane with a bandgap around the 33-mode at $\Omega_\mathrm{m,33} = 2\pi \times 4.7\,\mathrm{MHz}$ is currently being set up. Besides using mirrors of slightly higher reflectivity resulting in a higher cavity finesse, the new cavity is built cryo-compatible and will be placed into a cryostat at $4\,\mathrm{K}$ to reduce the thermal phonon occupation. With this new system we expect to achieve an membrane cooperativity close to the maximum value of $C_\mathrm{m} = 1$ enabling ground state cooling by classical feedback.

An elongated atomic ensemble in a dipole trap

The major limitation on the atomic side of our setup is currently the large inhomogenous broadening of the atomic ensemble. We can prepare atomic ensembles
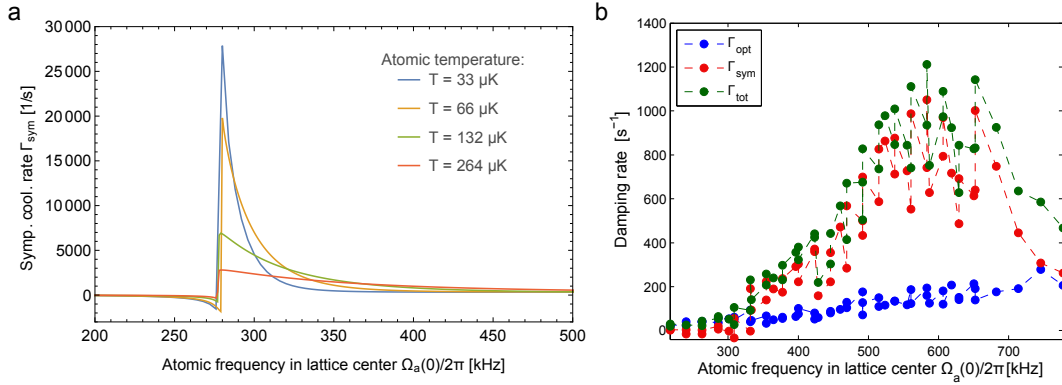
Figure 6.3: Sympathetic cooling experiment with a cigar-shaped atomic ensemble a) Theoretical expectation of sympathetic cooling rate for $N = 3 \times 10^7$ atoms and atomic temperatures as given in the legend. Further parameters: $M = 110\,\mathrm{ng}$, $F = 700$, $\Omega_\mathrm{m} = 2\pi \times 276\,\mathrm{kHz}$, $\Gamma_\mathrm{m} = 0.9\,\mathrm{s}^{-1}$, $r_\mathrm{m} = 0.4$, $\eta = 1$, $t = 0.68$, $\Gamma_\mathrm{a} = 500\,\mathrm{s}^{-1}$, $\tau = 30\,\mathrm{ns}$. b) Result of a first sympathetic cooling experiment with atomic ensemble loaded from the dipole trap. The measured sympathetic cooling rate Γ_sym is plotted against the separately calibrated frequency in the lattice center $\Omega_\mathrm{a}(0)$. The resonance is displaced towards higher frequencies and very broad indicating that the transfer from the dipole trap into the lattice is not fully adiabatic yet.

with optical depths of $OD_\mathrm{res} \approx 100$, but as the atoms populate the entire lattice profile, the number of resonantly coupled atoms is strongly reduced. This limits the atomic cooperativity to $C_\mathrm{a} \approx 2 \times 10^{-3}$.

To overcome this limitation, we recently set up a far-detuned optical dipole trap. It allows to produce thin cigar-shaped atomic ensembles much better suited for atom-membrane coupling experiments. Currently we trap 3×10^7 atoms in the dipole trap and manage to transfer almost all of them into the coupling lattice. The resulting cloud in the lattice is $2\,\mathrm{cm}$ long and only $60\,\mu\mathrm{m}$ wide ($1/e^2$ diameter and length), see figure 6.2. It has a temperature of $33\,\mu\mathrm{K}$. Due to the absence of the surrounding molasses or MOT cooled cloud we can now for the first time directly access the properties of the atoms in the coupling lattice volume. From the measured temperature and atom number we calculate a peak optical depth of the atomic ensemble of $OD_\mathrm{res,max} = 4300$. Averaged over the current optical lattice beam area ($w_0 = 115\,\mu\mathrm{m}$) this gives an optical depth and correspondingly atomic cooperativity of $C_\mathrm{a} = OD_\mathrm{res} = \sigma_0 N/\sigma_\mathrm{L} = 280$. When combining the novel cryogenic cavity setup with the new atomic ensemble, we thus expect to observe an atom-membrane quantum cooperativity of $C_\mathrm{qu} = 4C_\mathrm{m}C_\mathrm{a} = 1120$ in absence of losses. This will place our coupled atom-membrane system deep into the quantum regime.

Figure 6.3 shows the results of a first sympathetic cooling experiment with the new atomic ensemble and the "old" second-generation membrane-cavity setup. In
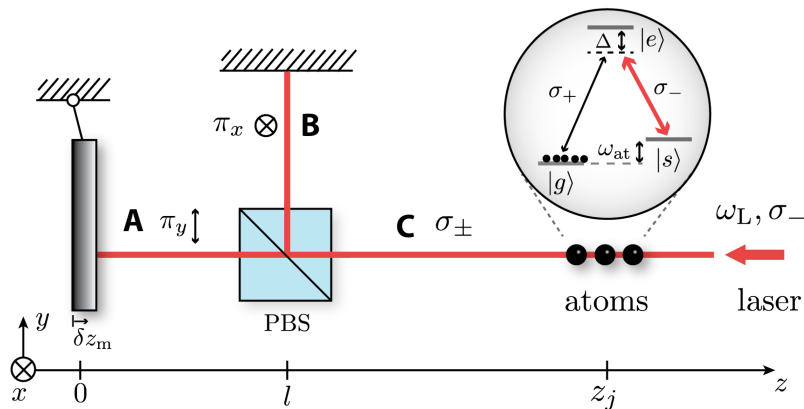
Figure 6.4: Mirror coupled to the internal states of a distant atomic ensemble. A laser at frequency ω_L from the left pumps the system. The polarizing beam-splitter cube translates a motion of the mirror into a polarization rotation at the position of the atoms. Transitions between the atomic ground states modify the radiation pressure on the membrane. Figure adapted from [163].

the experiment we first prepared a cigar-shaped cloud in the dipole trap and then transferred it into the coupling lattice by slowly ramping up the coupling lattice power. The resonance is shifted strongly towards higher center frequencies and much broader than the theoretical expectation of the left. This indicates that the transfer from the from the dipole trap into the lattice is not yet fully adiabatic.

Coupling to the internal states of the atoms

In a recent paper the Zoller group, in collaboration with Klemens Hammerer from Hannover and our group, proposes a coupling scheme between a mechanical oscillator and the internal states of an atomic ensemble [163]. Figure 6.4 sketches the proposed scenario. The atomic ensemble is modeled as N Λ-type three-level systems with two ground states, $|e\rangle$ and $|g\rangle$, which are separated by ω_at. The coupling of the ground states to the excited state $|e\rangle$ is polarization-dependent. The system is driven by a σ^--polarized laser beam from the right, which pumps the atoms initially into the $|g\rangle$ ground state. In a Michelson-interferometer-like setup, a polarizing beam splitter cube (PBS) splits the light into two equal linearly-polarized components. Arm A is terminated by the mechanical oscillator, the other arm B by a fixed mirror. If the oscillator is in its equilibrium position, the two arm lengths are equal and the reflected light at the position of the atoms is purely σ^--polarized. A motion of the mechanical oscillator induces a phase shift of the reflected light in arm A, which is translated into a polarization rotation at the PBS. If the membrane vibration is resonant to the atomic transition $\omega_\mathrm{m} \approx \omega_\mathrm{at}$, the reflected σ^+ polarized light at the

sideband frequency $\omega_L + \omega_{at}$ can induce a two-photon transition $|s\rangle \leftrightarrow |g\rangle$. Vice versa, if an atom makes a transition between the ground states, additional σ^+ light at the sideband frequency is emitted. Behind the PBS this light interferes with the main laser beam and modifies the radiation pressure on the oscillator.

Vogell *et al.* show that the interaction can be described by an effective Hamiltonian between the membrane displacement and a collective spin wave in the atomic ensemble

$$H_{eff} = -\frac{\hbar g_{eff}}{2}(a_m + a_m^\dagger)(S_0 + S_0^\dagger) \,. \tag{6.1}$$

Here $a_m(a_m^\dagger)$ is the annihilation (creation) operator of the membrane mode and $S_0(S_0^\dagger)$ the annihilation (creation) operator of the collective spin wave mode

$$S_0 = \frac{1}{\sqrt{N}} \sum_j \sigma_{gs}^j \,, \tag{6.2}$$

where $\sigma_{gs}^j = |g\rangle \langle s|^j$ is the transition operator of the jth atom. Further, g_{eff} is the atom-membrane coupling constant

$$g_{eff} = 2\sqrt{N} g_m g_a = \sqrt{\frac{N}{2}} \frac{\Omega_+ \Omega_-}{\Delta} k_L l_m \,. \tag{6.3}$$

Here $\Omega_+(\Omega_-)$ is the Rabi frequency resulting from the drive laser field amplitude and the dipole matrix element of the $\sigma_+(\sigma_-)$ transition and $l_m = \sqrt{\hbar/2M\omega_m}$ is the zero-point amplitude of the membrane vibration.

To be able to realize this effective Hamiltonian a number of technical requirements have to be fulfilled. Firstly, to prevent coupling to multiple atomic spin waves, the atoms have to be positioned at certain locations within the σ_- standing wave by an external lattice. Further, to avoid atom-atom interaction via the backreflected light an additional phase-shifter on the atomic side of the PBS is required (not drawn in figure 6.4), which shifts the phase of the σ_+-light by $\pi/4$.

For a membrane-in-the-middle optomechanics system, the coupling strength in this internal state coupling scheme exceeds the coupling strength achievable in the motional coupling scheme, which was discussed in this thesis, by one single-atom Lamb-Dicke factor $g_{eff}/g_{motion} = 1/k_L l_{at}$ [163], where $l_{at} = \sqrt{\hbar/2m\omega_{at}}$. Vogell *et al.* show the atomic diffusion rate increases by $(k_L l_{lat})^2$ so that the atom-membrane cooperativity given in equation 1.139 remains unchanged.

Even if no higher cooperativities can be achieved, the internal state coupling scheme is very appealing. Coupling to the motion of the atomic ensemble limits the mechanical resonator frequency to the sub-MHz regime. In the internal states scheme this constraint is absent as the resonance condition is given by the energy splitting between the two ground states $|g\rangle$ amd $|s\rangle$. The atomic Zeemann-sublevels can be split easily by a magnetic field offering the possibility to couple to MHz oscillators. If the atomic hyperfine ground states are addressed, also coupling to GHz oscillators can be realized. Furthermore, the internal state of atoms can be prepared and manipulated and detected with a much higher fidelity than the center-of-mass-motion, offering more possibilities for coherent quantum control in the hybrid system.

Appendix A

Sympathetic cooling rate in presence of delay

The following lines show how a modified sympathetic cooling rate can be derived from the equations of motion of the coupled system in presence of a delay. I consider two coupled and damped harmonic oscillators, the atomic center of mass motion, x_a, and the membrane motion, x_m. The coupling term acts delayed by τ. Further one of the oscillators, x_m, experiences a fluctuating thermal force F_{th}. The equations of motion of this system are

$$
\begin{aligned}
Nm\ddot{x}_a(t) &= -\Gamma_a Nm\dot{x}_a(t) - Nm\Omega_a^2 x_a(t) - Kx_m(t-\tau)\,, &\text{(A.1)}\\
M\ddot{x}_m(t) &= -\Gamma_m M\dot{x}_m(t) - M\Omega_m^2 x_m(t) - Kx_a(t-\tau) + F_{th}(t)\,,
\end{aligned}
$$

where N is the number of atoms, m the atomic mass, M the membrane mass, Ω_a the frequency of the atomic center of mass motion, Ω_m the membrane frequency, Γ_a the atomic damping rate, Γ_m the membrane damping rate and $K = \hbar g_N/x_{m,0}x_{a,0}$ the coupling spring constant. For simplicity I neglect optical losses. To include inefficient cavity incoupling and optical losses on the way between atoms and membrane, the K in the second equation has to be multiplied with $\eta^2 t^2$ as presented in section 1.3.

Fourier transforming the equations of motion one obtains

$$
\begin{aligned}
\tilde{x}_a(\Omega) &= \chi_a(\Omega)[-K\exp(-i\tau\Omega)\tilde{x}_m(\Omega)] \quad\text{and}\\
\tilde{x}_m(\Omega) &= \chi_m(\Omega)[\tilde{F}_{th} - K\exp(-i\tau\Omega)\tilde{x}_a(\Omega)]\,, &\text{(A.2)}
\end{aligned}
$$

with the mechanical susceptibilities

$$
\begin{aligned}
\chi_a(\Omega) &= [Nm(\Omega_a^2 - \Omega^2 + i\Omega\Gamma_a)]^{-1} \quad\text{and}\\
\chi_m(\Omega) &= [M(\Omega_m^2 - \Omega^2 + i\Omega\Gamma_m)]^{-1}\,. &\text{(A.3)}
\end{aligned}
$$

If we eliminate $\tilde{x}_a(\Omega)$ from the equations A.2 we find for the membrane amplitude

$$
\begin{aligned}
\tilde{x}_m(\Omega) &= \frac{\tilde{F}_{th}}{\chi_m^{-1}(\Omega) - K^2\exp(-i2\tau\Omega)\chi_a(\Omega)}\,,\\
&= \chi_{m,eff}(\Omega)\tilde{F}_{th}\,, &\text{(A.4)}
\end{aligned}
$$
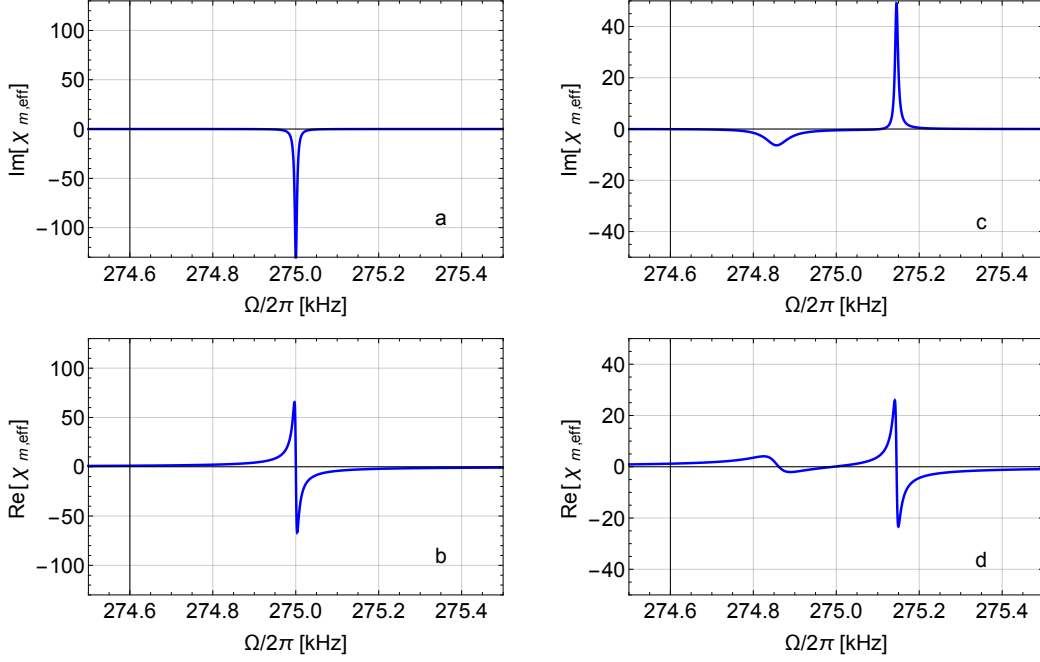
Figure A.1: Real and imaginary part of the effective membrane susceptibility $\chi_{\mathrm{m,eff}}$ in presence of a delay in the coupling between atoms and membrane for a), b) 10 atoms and c),d) 10^4 atoms.

with an effective membrane susceptibility

$$
\begin{aligned}
\chi_{\mathrm{m,eff}}(\Omega) &= \left[M \left(\Omega_{\mathrm{m}}^2 - \Omega^2 + i\Omega\Gamma_{\mathrm{m}} - \frac{K^2 \exp(-i2\tau\Omega)}{NmM(\Omega_{\mathrm{a}}^2 - \Omega^2 + i\Omega\Gamma_{\mathrm{a}})} \right) \right]^{-1} , \\
&\simeq \left[M \left(\Omega_{\mathrm{m}}^2 - \Omega^2 + i\Omega\Gamma_{\mathrm{m}} - \frac{K^2(1 - 2i\tau\Omega)}{NmM(\Omega_{\mathrm{a}}^2 - \Omega^2 + i\Omega\Gamma_{\mathrm{a}})} \right) \right]^{-1} . \quad \text{(A.5)}
\end{aligned}
$$

The last equations holds for small delays, such that $2\tau\Omega \ll 1$. I will assume this in the following.

The effective membrane susceptibility is the starting point of the derivation of the modified sympathetic cooling rate Γ_{sym}. Equation. A.3 reveals that the central frequency of the oscillators $\Omega_{\mathrm{m}}(\Omega_{\mathrm{a}})$ is given by the zero point of the real part of the inverse susceptibilities and that the damping rates $\Gamma_{\mathrm{m}}(\Gamma_{\mathrm{a}})$ are given by the imaginary part of the inverse susceptibility divided by $\Omega M(\Omega Nm)$. This dependence must hold also for the modified membrane susceptibility $\chi_{\mathrm{m,eff}}$. Thus, all we have to do is to find the zero point of $\mathrm{Re}[\chi_{\mathrm{m,eff}}(\Omega)^{-1}]$, called $\Omega_{\mathrm{m,eff}}$ in the following, and then to evaluate $\mathrm{Im}[\chi_{\mathrm{m,eff}}(\Omega)^{-1}]/\Omega M$ at $\Omega_{\mathrm{m,eff}}$ to find the total damping rate $\Gamma_{\mathrm{tot}} = \Gamma_{\mathrm{m}} + \Gamma_{\mathrm{sym}}$ of the membrane mode in presence of atoms and delay.

Before starting the calculation we have a look at the real and imaginary part of the effective susceptibility $\chi_{\mathrm{m,eff}}$ itself. Note that zero points of $\mathrm{Re}[\chi_{\mathrm{m,eff}}(\Omega)^{-1}] \equiv \mathrm{Re}[a + ib] = a \,, (a, b \in \mathbb{R})$ are also zero points of $\mathrm{Re}[\chi_{\mathrm{m,eff}}(\Omega)] = a/(a^2 + b^2)$ and

that $\text{Im}[\chi_{\text{m,eff}}(\Omega_{\text{m,eff}})^{-1}] = b = -(\text{Im}[1/ib])^{-1} = -1/\text{Im}[\chi_{\text{m,eff}}(\Omega_{\text{m,eff}})]$, so that the imaginary part of $\chi_{\text{m,eff}}(\Omega_{\text{m,eff}})$ has opposite sign to the damping rate Γ_{tot}. Figure A.1 shows real and imaginary part of $\chi_{\text{m,eff}}(\Omega)$ for a small atom number ($N = 10$, left column) and for a big atom number ($N = 10^4$, right column). Upper and lower plot in the left column look qualitatively still the same as imaginary and real part of the bare membrane susceptibility $\chi_{\text{m}}(\Omega)$ (equation A.3). On closer inspection one finds that the small coupling to the atoms broadens the peak in the imaginary part plot and moves this peak as well as the zero point in the real part plot slightly towards higher frequencies. For strong coupling to the atoms (right column) two peaks are visible in the plot of $\text{Im}[\chi_{\text{m,eff}}(\Omega)]$, a sign of normal mode splitting due to strong coupling. For intermediate atom numbers (not shown in the figure) the two peaks are of equal negative sign. However, for a certain threshold atom number, the imaginary part of the right mode changes its sign from negative to positive as shown in the right column of figureA.1. Thus, this mode changes its damping rate from positive to negative.

It is exactly such a behavior of switching from positive to negative damping with increasing atom number which we observe with our membrane. Therefore, I will investigate the real part zero crossing of $\text{Re}[\chi_{\text{m,eff}}(\Omega)^{-1}] = \Omega_{\text{m,eff}}$ and corresponding damping rate $\Gamma_{\text{tot}} = \text{Im}[\chi_{\text{m,eff}}(\Omega_{\text{m,eff}})^{-1}]/\Omega_{\text{m,eff}}M$ for the right mode in the following.

For real and imaginary part of the inverse effective membrane susceptibility in equation A.5 in one finds

$$\text{Re}[\chi_{\text{m,eff}}(\Omega)^{-1}] = M\left[\Omega_{\text{m}}^2 - \Omega^2 + \frac{4g_N^2\Omega_{\text{a}}\Omega_{\text{m}}[(1 + 2\Gamma_{\text{a}}\tau)\Omega^2 - \Omega_{\text{a}}^2]}{\Gamma_{\text{a}}^2\Omega^2 + (\Omega^2 - \Omega_{\text{a}}^2)^2}\right] , \qquad (A.6)$$

$$\text{Im}[\chi_{\text{m,eff}}(\Omega)^{-1}] = M\Omega\left[\Gamma_{\text{m}} + \frac{4g_N^2\Omega_{\text{a}}\Omega_{\text{m}}[\Gamma_{\text{a}} + 2\tau(\Omega_{\text{a}}^2 - \Omega^2)]}{\Gamma_{\text{a}}^2\Omega^2 + (\Omega^2 - \Omega_{\text{a}}^2)^2}\right] . \qquad (A.7)$$

Applying the procedure described above to determine the sympathetic cooling rate $\Gamma_{\text{sym}} = \Gamma_{\text{tot}} - \Gamma_{\text{m}}$, leads to a very longish expression even for resonant coupling $\Omega_{\text{a}} = \Omega_{\text{m}}$, namely

$$\Gamma_{\text{sym}} = \frac{c}{d} \quad \text{with} \qquad (A.8)$$

$$
\begin{aligned}
c = \ & -8g_N^2 t^{1/3}\Omega_{\text{a}}^2[-3t^{1/3}\Gamma_{\text{a}} + 2^{2/3}t^{2/3}\tau - 2t^{1/3}\Gamma_{\text{a}}^2\tau + 2\times 2^{1/3}\Gamma_{\text{a}}^4\tau \\
& +6\times 2^{1/3}\tau\Omega_{\text{a}}^2[g_N^2(4 + 8\Gamma_{\text{a}}\tau) - \Gamma_{\text{a}}^2]] \quad \text{and} \\
d = \ & \frac{2^{1/3}}{3}\sqrt{\cdot}t^{1/3} + \frac{2^{2/3}}{3}\sqrt{\cdot}\Gamma_{\text{a}}^2 + 16g_N^2t^{2/3}\Omega_{\text{a}}^2 - 4\times 2^{1/3}g_N^2t^{1/3}\Gamma_{\text{a}}^2\Omega_{\text{a}}^2 \\
& +2t^{2/3}\Gamma_{\text{a}}^2\Omega_{\text{a}}^2 + 2^{1/3}t^{1/3}\Gamma_{\text{a}}^4\Omega_{\text{a}}^2 + 32g_N^2t^{2/3}\Gamma_{\text{a}}\tau\Omega_{\text{a}}^2 \\
& -8\times 2^{1/3}g_N^2t^{1/3}\Gamma_{\text{a}}^3\tau\Omega_{\text{a}}^2 + 2^{2/3}\Gamma_{\text{a}}^4\Omega_{\text{a}}^2[g_N^2(4 + 8\Gamma_{\text{a}}\tau) - \Gamma_{\text{a}}^2] \\
& +72\times 2^{1/3}g_N^2t^{1/3}\Gamma_{\text{a}}\tau\Omega_{\text{a}}^4 \\
& +6\times 2^{2/3}\Omega_{\text{a}}^4[\Gamma_{\text{a}}^4 - 4g_N^2\Gamma_{\text{a}}^2(2 + \Gamma_{\text{a}}\tau) + 16g_N^4(1 + 2\Gamma_{\text{a}}\tau)^2] , \qquad (A.9)
\end{aligned}
$$

where

$$\sqrt{\cdot} = \sqrt{\Gamma_\mathrm{a}^2[-2\Gamma_\mathrm{a}^5 + 9\Gamma_\mathrm{a}[\Gamma_\mathrm{a}^2 - 4g_N^2(1 + 2\Gamma_\mathrm{a}\tau)]\Omega_\mathrm{a}^2 + 216g_N^2\tau\Omega\mathrm{a}^4]^2 \cdots}$$
$$\overline{\cdots - 4[\Gamma_\mathrm{a}^4 + 3[-\Gamma_\mathrm{a}^2 + g_N^2(4 + 8\Gamma_\mathrm{a}\tau)]\Omega_\mathrm{a}^2]^3} \tag{A.10}$$

and

$$t = \sqrt{\cdot} - 2\Gamma_\mathrm{a}^6 + 9\Gamma_\mathrm{a}^2\Omega_\mathrm{a}^2[\Gamma_\mathrm{a}^2 - 4g_N^2(1 + 2\Gamma_\mathrm{a}\tau)] + 216g_N^2\Gamma_\mathrm{a}\tau\Omega_\mathrm{a}^4. \tag{A.11}$$

One can simplify these expressions using the following assumptions

$$\begin{aligned}
\Gamma_\mathrm{a}\tau &\ll \frac{1}{2}, \\
\Gamma_\mathrm{a} &\ll \Omega_\mathrm{a}, \\
\Gamma_\mathrm{a} &\ll 6\tau\Omega_\mathrm{a}^2, \\
\Gamma_\mathrm{a}^3 &\ll 24g_N^2\tau\Omega_\mathrm{a}^2.
\end{aligned} \tag{A.12}$$

Of these assumptions the second one is certainly true in our system and with this plus the assumption that the delay is small ($\Omega_\mathrm{m}\tau \ll 1$) the first assumption is also true. In our parameter regime ($\tau > 50\,\mathrm{ns}$, $\Gamma_\mathrm{a} < 10^3\,\mathrm{s}^{-1}$, $N > 10^3$) the last two assumptions are fulfilled as well.

Using the assumptions the expressions above reduce to

$$\begin{aligned}
\sqrt{\cdot} &\simeq \sqrt{\Gamma_\mathrm{a}^2(216g_N^2\tau\Omega_\mathrm{a}^4)^2 - 4(3\Omega_\mathrm{a}^2(4g_N^2 - \Gamma_\mathrm{a}^2))^3}, \\
t &\simeq \sqrt{\cdot} + 216g_N^2\tau\Omega_\mathrm{a}^4, \\
c &\simeq -8g_N^2 t^{1/3}\Omega_\mathrm{a}^2(-3t^{1/3}\Gamma_\mathrm{a} + 2^{2/3}t^{2/3}\tau + 6\times 2^{1/3}\tau(4g_N^2 - \Gamma_\mathrm{a}^2)\Omega_\mathrm{a}^2), \\
d &\simeq \frac{2^{1/3}}{3}\sqrt{\cdot}\,t^{1/3} + 16g_N^2 t^{2/3}\Omega_\mathrm{a}^2 + 2t^{2/3}\Gamma_\mathrm{a}^2\Omega_\mathrm{a}^2 + 72\times 2^{1/3}g_N^2 t^{1/3}\Gamma_\mathrm{a}\tau\Omega_\mathrm{a}^4 \\
&\quad + 6\times 2^{2/3}\Omega_\mathrm{a}^4(\Gamma_\mathrm{a}^2 - 4g_N^2)^2.
\end{aligned} \tag{A.13}$$

With these approximations Mathematica is able to further simplify the global expression $\Gamma_\mathrm{sym} = c/d$ to

$$\begin{aligned}
\Gamma_\mathrm{sym} = \;& \frac{1}{9\Gamma_\mathrm{a}(4g_N^2 - \Gamma_\mathrm{a}^2)}[48g_N^4 + 12g_N^2\Gamma_\mathrm{a}^2 - 6\Gamma_\mathrm{a}^4 \\
& - 3^{\frac{1}{3}}(36g_N^2\Gamma_\mathrm{a}\tau\Omega_\mathrm{a} - \sqrt{\cdots})(36g_N^2\Gamma_\mathrm{a}\tau\Omega_\mathrm{a} + \sqrt{\cdots})^{\frac{1}{3}} \\
& - 3^{\frac{2}{3}}(4g_N^2 - \Gamma_\mathrm{a}^2)(36g_N^2\Gamma_\mathrm{a}\tau\Omega_\mathrm{a} + \sqrt{\cdots})^{\frac{2}{3}}] \quad \text{where}
\end{aligned} \tag{A.14}$$

$$\sqrt{\cdots} = \sqrt{(36g_N^2\Gamma_\mathrm{a}\tau\Omega_\mathrm{a})^2 - 3(4g_N^2 - \Gamma_\mathrm{a}^2)^3}. \tag{A.15}$$

To include optical losses, all factors g_N^2 in the expression have to be multiplied by $\eta^2 t^2$.

Appendix B

Acronyms

NV	Nitrogen-vacancy
BEC	Bose-Einstein condensate
MIM	Membrane-in-middle
MOT	Magneto optical trap
EOM	Electro-optic modulator
PSD	Power spectral density
PDH	Pound-Drever-Hall
EIT	Electromagnetically-induced transparency
AR	Anti-reflection coated
TA	Tapered amplifier
PD	Photo diode
PBS	Polarizing beam splitter
BS	Beam splitter
AOM	Acousto-optic modulator
VCO	Voltage-controlled oscillator
DC	Direct Current
IFL	Interference-filter laser
PZT	Piezo element
LO	Local oscillator
PID	Proportional-integral-derivative
OD	Optical depth
CCD	Charged-coupled device
ND	Neutral density
RF	Radio frequency
OC	Optical circulator
MIT	Magnetically-induced transparency
FSR	Free spectral range

List of Figures

List of Tables

Bibliography

[1] J. Sakurai, *Modern Quantum Mechanics* (Addison-Wesley Publishing Company, Inc., Boston) (1994).

[2] H. J. Metcalf and P. van der Straten, *Laser cooling and trapping of atoms* (Springer-Verlag, New York Berlin Heidelberg) (1999).

[3] D. Leibfried, R. Blatt, C. Monroe, and D. Wineland, *Quantum dynamics of single trapped ions*, Rev. Mod. Phys. **75**, 281 (2003).

[4] D. Rugar, R. Budakian, H. J. Mamin, and B. W. Chui, *Single spin detection by magnetic resonance force microscopy*, Nature **430**, 329 (2004).

[5] C. M. Caves, K. S. Thorne, R. W. P. Drever, V. D. Sandberg, and M. Zimmermann, *On the measurement of a weak classical force coupled to a quantum-mechanical oscillator. i. issues of principle*, Rev. Mod. Phys. **52**, 341 (1980).

[6] K. Stannigel, P. Rabl, A. S. Sørensen, P. Zoller, and M. D. Lukin, *Optomechanical transducers for long-distance quantum communication*, Phys. Rev. Lett. **105**, 220501 (2010).

[7] P. Rabl, S. J. Kolkowitz, F. H. L. Koppens, J. G. E. Harris, P. Zoller, and M. D. Lukin, *A quantum spin transducer based on nanoelectromechanical resonator arrays*, Nature Physics **6**, 602 (2010).

[8] R. W. Andrews, R. W. Peterson, T. P. Purdy, K. Cicak, R. W. Simmonds, C. A. Regal, and K. W. Lehnert, *Bidirectional and efficient conversion between microwave and optical light*, Nature Physics **10**, 321 (2014).

[9] T. Bagci, A. Simonsen, S. Schmid, L. G. Villanueva, E. Zeuthen, J. Appel, J. M. Taylor, A. Sorensen, K. Usami, A. Schliesser, and E. S. Polzik, *Optical detection of radio waves through a nanomechanical transducer*, Nature **507**, 81 (2014).

[10] M. Arndt and K. Hornberger, *Testing the limits of quantum mechanical superpositions*, Nature Physics **10**, 271 (2014).

[11] S. Nimmrichter, K. Hornberger, and K. Hammerer, *Optomechanical sensing of spontaneous wave-function collapse*, Phys. Rev. Lett. **113**, 020405 (2014).

[12] M. Aspelmeyer, T. J. Kippenberg, and F. Marquardt, *Cavity optomechanics*, Rev. Mod. Phys. **86**, 1391 (2014).

[13] O. Arcizet, P.-F. Cohadon, T. Briant, M. Pinard, and A. Heidmann, *Radiation-pressure cooling and optomechanical instability of a micromirror*, Nature **444**, 71 (2006).

[14] S. Gröblacher, K. Hammerer, M. R. Vanner, and M. Aspelmeyer, *Observation of strong coupling between a micromechanical resonator and an optical cavity field*, Nature **460**, 724 (2009).

[15] J. D. Thompson, B. M. Zwickl, A. M. Jayich, F. Marquardt, S. M. Girvin, and J. G. E. Harris, *Strong dispersive coupling of a high-finesse cavity to a micromechanical membrane*, Nature **452**, 72 (2008).

[16] D. J. Wilson, C. A. Regal, S. B. Papp, and H. J. Kimble, *Cavity Optomechanics with Stoichiometric SiN Films*, Phys. Rev. Lett. **103**, 207204 (2009).

[17] M. Underwood, D. Mason, D. Lee, H. Xu, L. Jiang, A. B. Shkarin, K. Børkje, S. M. Girvin, and J. G. E. Harris, *Measurement of the motional sidebands of a nanogram-scale oscillator in the quantum regime*, Phys. Rev. A **92**, 061801 (2015).

[18] J. D. Teufel, T. Donner, D. Li, J. W. Harlow, M. S. Allman, K. Cicak, A. J. Sirois, J. D. Whittaker, K. W. Lehnert, and R. W. Simmonds, *Sideband cooling of micromechanical motion to the quantum ground state*, Nature **475**, 359 (2011).

[19] M. Yuan, V. Singh, Y. M. Blanter, and G. A. Steele, *Large cooperativity and microkelvin cooling with a three-dimensional optomechanical cavity*, Nature Commun. **6**, (2015).

[20] E. E. Wollman, C. U. Lei, A. J. Weinstein, J. Suh, A. Kronwald, F. Marquardt, A. A. Clerk, and K. C. Schwab, *Quantum squeezing of motion in a mechanical resonator*, Science **349**, 952 (2015).

[21] J.-M. Pirkkalainen, E. Damskägg, M. Brandt, F. Massel, and M. A. Sillanpää, *Squeezing of quantum noise of motion in a micromechanical resonator*, Phys. Rev. Lett. **115**, 243601 (2015).

[22] E. Verhagen, S. Deleglise, S. Weis, A. Schliesser, and T. J. Kippenberg, *Quantum-coherent coupling of a mechanical oscillator to an optical cavity mode*, Nature **482**, 63 (2012).

[23] J. Gieseler, B. Deutsch, R. Quidant, and L. Novotny, *Subkelvin parametric feedback cooling of a laser-trapped nanoparticle*, Phys. Rev. Lett. **109**, 103603 (2012).

[24] P. Asenbaum, S. Kuhn, S. Nimmrichter, U. Sezer, and M. Arndt, *Cavity cooling of free silicon nanoparticles in high vacuum*, Nature Commun. **4**, (2013).

[25] N. Kiesel, F. Blaser, U. Delic, D. Grass, R. Kaltenbaek, and M. Aspelmeyer, *Cavity cooling of an optically levitated submicron particle*, Proceedings of the National Academy of Sciences **110**, 14180 (2013).

[26] J. Millen, P. Z. G. Fonseca, T. Mavrogordatos, T. S. Monteiro, and P. F. Barker, *Cavity cooling a single charged levitated nanosphere*, Phys. Rev. Lett. **114**, 123602 (2015).

[27] J. Chan, T. P. M. Alegre, A. H. Safavi-Naeini, J. T. Hill, A. Krause, S. Groblacher, M. Aspelmeyer, and O. Painter, *Laser cooling of a nanomechanical oscillator into its quantum ground state*, Nature **478**, 89 (2011).

[28] D. Hunger, S. Camerer, T. W. Hänsch, D. König, J. P. Kotthaus, J. Reichel, and P. Treutlein, *Resonant coupling of a Bose-Einstein condensate to a micromechanical oscillator*, Phys. Rev. Lett. **104**, 143002 (2010).

[29] S. Camerer, M. Korppi, A. Jöckel, D. Hunger, T. W. Hänsch, and P. Treutlein, *Realization of an Optomechanical Interface Between Ultracold Atoms and a Membrane*, Phys. Rev. Lett. **107**, 223001 (2011).

[30] T. P. Purdy, D. W. C. Brooks, T. Botter, N. Brahms, Z.-Y. Ma, and D. M. Stamper-Kurn, *Tunable cavity optomechanics with ultracold atoms*, Phys. Rev. Lett. **105**, 133602 (2010).

[31] F. Brennecke, S. Ritter, T. Donner, and T. Esslinger, *Cavity Optomechanics with a Bose-Einstein Condensate*, Science **322**, 235 (2008).

[32] A. D. O'Connell, M. Hofheinz, M. Ansmann, R. C. Bialczak, M. Lenander, E. Lucero, M. Neeley, D. Sank, H. Wang, M. Weides, J. Wenner, J. M. Martinis, and A. N. Cleland, *Quantum ground state and single-phonon control of a mechanical resonator*, Nature **464**, 697 (2010).

[33] J. D. Teufel, J. W. Harlow, C. A. Regal, and K. W. Lehnert, *Dynamical backaction of microwave fields on a nanomechanical oscillator*, Phys. Rev. Lett. **101**, 197203 (2008).

[34] T. Faust, J. Rieger, M. J. Seitner, J. P. Kotthaus, and E. M. Weig, *Coherent control of a classical nanomechanical two-level system*, Nature Physics **9**, 485 (2013).

[35] R. W. Peterson, T. P. Purdy, N. S. Kampel, R. W. Andrews, P.-L. Yu, K. W. Lehnert, and C. A. Regal, *Laser cooling of a micromechanical membrane to the quantum backaction limit*, Phys. Rev. Lett. **116**, 063601 (2016).

[36] J. D. Teufel, D. Li, M. S. Allman, K. Cicak, A. J. Sirois, J. D. Whittaker, and R. W. Simmonds, *Circuit cavity electromechanics in the strong-coupling regime*, Nature **471**, 204 (2011).

[37] T. A. Palomaki, J. W. Harlow, J. D. Teufel, R. W. Simmonds, and K. W. Lehnert, *Coherent state transfer between itinerant microwave fields and a mechanical oscillator*, Nature **495**, 210 (2013).

[38] T. P. Purdy, R. W. Peterson, and C. A. Regal, *Observation of radiation pressure shot noise on a macroscopic object*, Science **339**, 801 (2013).

[39] D. W. C. Brooks, T. Botter, S. Schreppler, T. P. Purdy, N. Brahms, and D. M. Stamper-Kurn, *Non-classical light generated by quantum-noise-driven cavity optomechanics*, Nature **488**, 476 (2012).

[40] A. H. Safavi-Naeini, S. Groblacher, J. T. Hill, J. Chan, M. Aspelmeyer, and O. Painter, *Squeezed light from a silicon micromechanical resonator*, Nature **500**, 185 (2013).

[41] F. Lecocq, J. B. Clark, R. W. Simmonds, J. Aumentado, and J. D. Teufel, *Quantum nondemolition measurement of a nonclassical state of a massive object*, Phys. Rev. X **5**, 041037 (2015).

[42] P. Treutlein, C. Genes, K. Hammerer, M. Poggio, and P. Rabl, *Cavity Optomechanics*, chapter Hybrid Mechanical Systems, pp. 327–351 (Springer-Verlag, Berlin Heidelberg) (2014).

[43] D. Hunger, S. Camerer, M. Korppi, A. Jöckel, T. Hänsch, and P. Treutlein, *Coupling ultracold atoms to mechanical oscillators*, Comptes Rendus Physique **12**, 871 (2011).

[44] O. Arcizet, V. Jacques, A. Siria, P. Poncharal, P. Vincent, and S. Seidelin, *A single nitrogen-vacancy defect coupled to a nanomechanical oscillator*, Nature Physics **7**, 879 (2011).

[45] S. Kolkowitz, A. C. Bleszynski Jayich, Q. P. Unterreithmeier, S. D. Bennett, P. Rabl, J. G. E. Harris, and M. D. Lukin, *Coherent sensing of a mechanical resonator with a single-spin qubit*, Science **335**, 1603 (2012).

[46] J. Teissier, A. Barfuss, P. Appel, E. Neu, and P. Maletinsky, *Strain coupling of a nitrogen-vacancy center spin to a diamond mechanical oscillator*, Phys. Rev. Lett. **113**, 020503 (2014).

[47] P. Ovartchaiyapong, K. W. Lee, B. A. Myers, and A. C. B. Jayich, *Dynamic strain-mediated coupling of a single diamond spin to a mechanical resonator*, Nature Commun. **5**, (2014).

178

[48] B. Pigeau, S. Rohr, L. Mercier de Lepinay, A. Gloppe, V. Jacques, and O. Arcizet, *Observation of a phononic mollow triplet in a multimode hybrid spin-nanomechanical system*, Nature Commun. **6**, (2015).

[49] A. Barfuss, J. Teissier, E. Neu, A. Nunnenkamp, and P. Maletinsky, *Strong mechanical driving of a single electron spin*, Nature Physics **11**, 820 (2015).

[50] I. Yeo, P.-L. de Assis, A. Gloppe, E. Dupont-Ferrier, P. Verlot, N. S., Malik, E. Dupuy, J. Claudon, J.-M. Gerard, A. Auffeves, G. Nogues, S. Seidelin, J.-P. Poizat, O. Arcizet, and M. Richard, *Strain-mediated coupling in a quantum dot-mechanical oscillator hybrid system*, Nature Nanotechn. **9**, 106 (2014).

[51] M. Montinaro, G. Wüst, M. Munsch, Y. Fontana, E. Russo-Averchi, M. Heiss, A. F. i Morral, R. J. Warburton, and M. Poggio, *Quantum dot opto-mechanics in a fully self-assembled nanowire*, Nano Letters **14**, 4454, pMID: 25010118 (2014).

[52] J.-M. Pirkkalainen, S. U. Cho, J. Li, G. S. Paraoanu, P. J. Hakonen, and M. A. Sillanpaa, *Hybrid circuit cavity quantum electrodynamics with a micromechanical resonator*, Nature **494**, 211 (2013).

[53] J.-M. Pirkkalainen, S. Cho, F. Massel, J. Tuorila, T. Heikkila, P. Hakonen, and M. Sillanpaa, *Cavity optomechanics mediated by a quantum two-level system*, Nature Commun. **6**, (2015).

[54] Y.-J. Wang, M. Eardley, S. Knappe, J. Moreland, L. Hollberg, and J. Kitching, *Magnetic resonance in an atomic vapor excited by a mechanical resonator*, Phys. Rev. Lett. **97**, 227602 (2006).

[55] A. Jöckel, A. Faber, T. Kampschulte, M. Korppi, M. T. Rakher, and P. Treutlein, *Sympathetic cooling of a membrane oscillator in a hybrid mechanical-atomic system*, Nature Nanotechn. **10**, 55 (2015).

[56] C. Montoya, J. Valencia, A. A. Geraci, M. Eardley, J. Moreland, L. Hollberg, and J. Kitching, *Resonant interaction of trapped cold atoms with a magnetic cantilever tip*, Phys. Rev. A **91**, 063835 (2015).

[57] S. Chu and W. D. Cohen-Tannoudji, Claude N. Phillips, *Nobel lectures*, Rev. Mod. Phys. **70**, 685 (1998).

[58] S. Chu, *Cold atoms and quantum control*, Nature **416**, 206 (2002).

[59] I. Bloch, J. Dalibard, and W. Zwerger, *Many-body physics with ultracold gases*, Rev. Mod. Phys. **80**, 885 (2008).

[60] M. H. Anderson, E. J. R., M. R. Matthews, C. E. Wieman, and E. A. Cornell, *Observation of Bose-Einstein condensation in a dilute atomic vapor*, Science **269**, 198 (1995).

[61] K. B. Davis, M.-O. Mewes, M. R. Andrews, N. J. van Druten, D. S. Durfee, D. M. Kurn, and W. Ketterle, *Bose-Einstein condensation in a gas of sodium atoms*, Phys. Rev. Lett. **75**, 3969 (1995).

[62] R. Wynands and S. Weyers, *Atomic fountain clocks*, Metrologia **42**, S64 (2005).

[63] A. Peters, K. Y. Chung, and S. Chu, *High-precision gravity measurements using atom interferometry*, Metrologia **38**, 25 (2001).

[64] C. F. Ockeloen, R. Schmied, M. F. Riedel, and P. Treutlein, *Quantum metrology with a scanning probe atom interferometer*, Phys. Rev. Lett. **111**, 143001 (2013).

[65] I. M. Georgescu, S. Ashhab, and F. Nori, *Quantum simulation*, Rev. Mod. Phys. **86**, 153 (2014).

[66] M. Saffman, T. G. Walker, and K. Mølmer, *Quantum information with rydberg atoms*, Rev. Mod. Phys. **82**, 2313 (2010).

[67] L.-M. Duan and C. Monroe, *Colloquium : Quantum networks with trapped ions*, Rev. Mod. Phys. **82**, 1209 (2010).

[68] K. Hammerer, K. Stannigel, C. Genes, P. Zoller, P. Treutlein, S. Camerer, D. Hunger, and T. W. Hänsch, *Optical lattices with micromechanical mirrors*, Phys. Rev. A **82**, 021803 (2010).

[69] B. Vogell, K. Stannigel, P. Zoller, K. Hammerer, M. T. Rakher, M. Korppi, A. Jöckel, and P. Treutlein, *Cavity-enhanced long-distance coupling of an atomic ensemble to a micromechanical membrane*, Phys. Rev. A **87**, 023816 (2013).

[70] J. S. Bennett, L. S. Madsen, M. Baker, H. Rubinsztein-Dunlop, and W. P. Bowen, *Coherent control and feedback cooling in a remotely coupled hybrid atom–optomechanical system*, New J. Phys. **16**, 083036 (2014).

[71] C. Genes, H. Ritsch, M. Drewsen, and A. Dantan, *Atom-membrane cooling and entanglement using cavity electromagnetically induced transparency*, Phys. Rev. A **84**, 051801 (2011).

[72] K. Hammerer, M. Aspelmeyer, E. S. Polzik, and P. Zoller, *Establishing Einstein-Poldosky-Rosen Channels between Nanomechanics and Atomic Ensembles*, Phys. Rev. Lett. **102**, 020501 (2009).

[73] A. Carmele, B. Vogell, K. Stannigel, and P. Zoller, *Opto-nanomechanics strongly coupled to a rydberg superatom: coherent versus incoherent dynamics*, New J. Phys. **16**, 063042 (2014).

[74] C. Cohen-Tannoudji, *Les Houches, Session LIII,1990 Fundamental System in Quantum Optics*, chapter Atomic motion in laser light (Elservier Science Publishers, Amsterdam) (1992).

[75] R. Grimm, M. Weidemüller, and Y. B. Ovchinnikov, *Optical Dipole Traps for Neutral Atoms*, Advances In Atomic, Molecular, and Optical Physics **42**, 95 (2000).

[76] I. H. Deutsch, R. J. C. Spreeuw, S. L. Rolston, and W. D. Phillips, *Photonic band gaps in optical lattices*, Phys. Rev. A **52**, 1394 (1995).

[77] A. Xuereb, P. Domokos, J. Asbóth, P. Horak, and T. Freegarde, *Scattering theory of cooling and heating in optomechanical systems*, Phys. Rev. A **79**, 053810 (2009).

[78] J. K. Asboth, H. Ritsch, and P. Domokos, *Optomechanical coupling in a one-dimensional optical lattice*, Phys. Rev. A **77**, 063424 (2008).

[79] D. J. Wilson, *Cavity Optomechanics with High-Stress Silicon Nitride Films*, Ph.D. thesis, California Institute of Technology (2012).

[80] A. M. Jayich, J. C. Sankey, B. M. Zwickl, C. Yang, J. D. Thompson, S. M. Girvin, A. A. Clerk, F. Marquardt, and J. G. E. Harris, *Dispersive optomechanics: a membrane inside a cavity*, New J. Phys. **10**, 095008 (2008).

[81] J. Dalibard and C. Cohen-Tannoudji, *Laser cooling below the doppler limit by polarization gradients: Simple theoretical models*, Journal of the Optical Society of America B Optical Physics **6**, 2023 (1989).

[82] D. A. Steck, *Rubidium 87 d line data*, http://steck.us/alkalidata (2002).

[83] C. Cohen-Tannoudji, J. Dupont-Roc, and G. Grynberg, *Atom-Photon Interaction - Basic Processes and Applications* (John Wiley & Sons, Inc., Hoboken, New Jersey) (1992).

[84] C. Cohen-Tannoudji, J. Dupont-Roc, and G. Grynberg, *Photons and Atoms: Introduction to Quantum Electrodynamics* (John Wiley & Sons, Inc., Hoboken, New Jersey) (1989).

[85] A. Xuereb, *Optical Cooling Using the Dipole Force*, Ph.D. thesis, University of Southampton, Faculty of Physical and Applied Sciences, School of Physics and Astronomy (2011).

[86] W. Demtröder, *Experimentalphysik 1* (Springer Verlag, Berlin Heidelberg) (2015).

[87] F. Schwabl, *Quantenmechanik* (Springer Verlag, Berlin Heidelberg) (2007).

[88] A. Wachter and H. Hoeber, *Repetitorium Theoretische Physik* (Springer Verlag, Berlin Heidelberg) (2005).

[89] L. You and M. Holland, *Ballistic expansion of trapped thermal atoms*, Phys. Rev. A **53**, R1 (1996).

[90] W. Ketterle, D. S. Durfee, and S. D. M. Kurn, *Making, probing and understanding Bose-Einstein condensates*, in M. Inguscio, S. Stringari, and C. E. Wieman (editors), *Bose-Einstein Condensation in Atomic Gases (Proceedings of the International School of Physics "Enrico Fermi," Course CXL)* (IOS Press) (1999).

[91] W. Nolting, *Grundkurs Theoretische Physik 3 - Elektrodynamik* (Springer-Verlag, Berlin Heidelberg) (2013).

[92] A. M. K. L.D. Landau, L. P. Pitaevskii and E. Lifshitz, *Theory of Elasticity* (Elsevier Ldt., Amsterdam) (1986).

[93] J. Sólnes, *Stochastic Processes and Random Vibration: Theory and Practice* (John Wiley & Sons, Inc., Hoboken, New Jersey) (1997).

[94] H. B. Callen and T. A. Welton, *Irreversibility and generalized noise*, Phys. Rev. **83**, 34 (1951).

[95] P. R. Saulson, *Thermal noise in mechanical experiments*, Phys. Rev. D **42**, 2437 (1990).

[96] M. B.E.A.Saleh, *Fundamentals of Photonics* (John Wiley & Sons, Inc., Hoboken, New Jersey) (2007).

[97] A. Zeilinger, *General properties of lossless beam splitters in interferometry*, American Journal of Physics **49**, 882 (1981).

[98] A. Jöckel, *Sympathetic cooling of a membrane oscillator in a hybrid mechanical-atomic system*, Ph.D. thesis, Departement Physik, Universität Basel (2014).

[99] A. A. Clerk, M. H. Devoret, S. M. Girvin, F. Marquardt, and R. J. Schoelkopf, *Introduction to quantum noise, measurement, and amplification*, Rev. Mod. Phys. **82**, 1155 (2010).

[100] C. Gardiner and P. Zoller, *Quantum Noise* (Springer-Verlag, Berlin Heidelberg) (2004).

[101] F. Marquardt, J. P. Chen, A. A. Clerk, and S. M. Girvin, *Quantum theory of cavity-assisted sideband cooling of mechanical motion*, Phys. Rev. Lett. **99**, 093902 (2007).

[102] I. Wilson-Rae, N. Nooshi, J. Dobrindt, T. J. Kippenberg, and W. Zwerger, *Cavity-assisted backaction cooling of mechanical resonators*, New J. Phys. **10**, 095007 (2008).

[103] P. Rabl, C. Genes, K. Hammerer, and M. Aspelmeyer, *Phase-noise induced limitations on cooling and coherent evolution in optomechanical systems*, Phys. Rev. A **80**, 063819 (2009).

[104] A. M. Jayich, J. C. Sankey, K. Børkje, D. Lee, C. Yang, M. Underwood, L. Childress, A. Petrenko, S. M. Girvin, and J. G. E. Harris, *Cryogenic optomechanics with a Si_3N_4 membrane and classical laser noise*, New J. Phys. **14**, 115018 (2012).

[105] E. D. Black, *An introduction to pound-drever-hall laser frequency stabilization*, American Journal of Physics **69**, 79 (2001).

[106] I. Wilson-Rae, N. Nooshi, W. Zwerger, and T. J. Kippenberg, *Theory of ground state cooling of a mechanical oscillator using dynamical backaction*, Phys. Rev. Lett. **99**, 093901 (2007).

[107] C. Genes, D. Vitali, P. Tombesi, S. Gigan, and M. Aspelmeyer, *Ground-state cooling of a micromechanical oscillator: Comparing cold damping and cavity-assisted cooling schemes*, Phys. Rev. A **77**, 033804 (2008).

[108] J. P. Gordon and A. Ashkin, *Motion of atoms in a radiation trap*, Phys. Rev. A **21**, 1606 (1980).

[109] M. Fleischhauer, A. Imamoglu, and J. P. Marangos, *Electromagnetically induced transparency: Optics in coherent media*, Rev. Mod. Phys. **77**, 633 (2005).

[110] T. Lauber, *A compact and stable membrane-optomechanical system*, Master's thesis, Departement Physik, Universität Basel (2013).

[111] M. Korppi, *Optomechanical Coupling between Ultracold Atoms and a Membrane Oscillator*, Ph.D. thesis, Departement Physik, Universität Basel (2013).

[112] T. P. Purdy, R. W. Peterson, P.-L. Yu, and C. A. Regal, *Cavity optomechanics with Si_3N_4 membranes at cryogenic temperatures*, New J. Phys. **14**, 115021 (2012).

[113] T. Westphal, D. Friedrich, H. Kaufer, K. Yamamoto, S. Goßler, H. Müller-Ebhardt, S. L. Danilishin, F. Y. Khalili, K. Danzmann, and R. Schnabel, *Interferometer readout noise below the standard quantum limit of a membrane*, Phys. Rev. A **85**, 063806 (2012).

[114] A. Jöckel, M. T. Rakher, M. Korppi, S. Camerer, D. Hunger, M. Mader, and P. Treutlein, *Spectroscopy of mechanical dissipation in micro-mechanical membranes*, Applied Physics Letters **99**, 143109 (2011).

[115] C. W. C.Y. Wang, *Structural vibration: exact solutions for strings, membranes, beams, and plates.* (CRC Press, Boca Raton, Florida) (2014).

[116] S. Chakram, Y. S. Patil, L. Chang, and M. Vengalattore, *Dissipation in ultrahigh quality factor sin membrane resonators*, Phys. Rev. Lett. **112**, 127201 (2014).

[117] J. C. Sankey, C. Yang, B. M. Zwickl, A. M. Jayich, and J. G. E. Harris, *Strong and tunable nonlinear optomechanical coupling in a low-loss system*, Nature Physics **6**, 707 (2010).

[118] G. D. Cole, I. Wilson-Rae, K. Werbach, M. R. Vanner, and M. Aspelmeyer, *Phonon-tunnelling dissipation in mechanical resonators*, Nature Commun. **2**, 231 (2011).

[119] T. Faust, J. Rieger, M. J. Seitner, J. P. Kotthaus, and E. M. Weig, *Signatures of two-level defects in the temperature-dependent damping of nanomechanical silicon nitride resonators*, Phys. Rev. B **89**, 100102 (2014).

[120] Y. Tsaturyan, A. Barg, A. Simonsen, L. G. Villanueva, S. Schmid, A. Schliesser, and E. S. Polzik, *Demonstration of suppressed phonon tunneling losses in phononic bandgap shielded membrane resonators for high-q optomechanics*, Opt. Express **22**, 6810 (2014).

[121] I. Wilson-Rae, *Intrinsic dissipation in nanomechanical resonators due to phonon tunneling*, Phys. Rev. B **77**, 245418 (2008).

[122] P.-L. Yu, T. P. Purdy, and C. A. Regal, *Control of material damping in high-q membrane microresonators*, Phys. Rev. Lett. **108**, 083603 (2012).

[123] P.-L. Yu, K. Cicak, N. S. Kampel, Y. Tsaturyan, T. P. Purdy, R. W. Simmonds, and C. A. Regal, *A phononic bandgap shield for high-q membrane microresonators*, Applied Physics Letters **104**, 023510 (2014).

[124] Q. P. Unterreithmeier, T. Faust, and J. P. Kotthaus, *Damping of nanomechanical resonators*, Phys. Rev. Lett. **105**, 027205 (2010).

[125] S. S. Verbridge, H. G. Craighead, and J. M. Parpia, *A megahertz nanomechanical resonator with room temperature quality factor over a million*, Applied Physics Letters **92**, 013112 (2008).

[126] I. Wilson-Rae, R. A. Barton, S. S. Verbridge, D. R. Southworth, B. Ilic, H. G. Craighead, and J. M. Parpia, *High-q nanomechanics via destructive interference of elastic waves*, Phys. Rev. Lett. **106**, 047205 (2011).

[127] S. Schmid, K. D. Jensen, K. H. Nielsen, and A. Boisen, *Damping mechanisms in high-q micro and nanomechanical string resonators*, Phys. Rev. B **84**, 165307 (2011).

[128] D. R. Southworth, R. A. Barton, S. S. Verbridge, B. Ilic, A. D. Fefferman, H. G. Craighead, and J. M. Parpia, *Stress and silicon nitride: A crack in the universal dissipation of glasses*, Phys. Rev. Lett. **102**, 225503 (2009).

[129] V. P. Adiga, B. Ilic, R. A. Barton, I. Wilson-Rae, H. G. Craighead, and J. M. Parpia, *Approaching intrinsic performance in ultra-thin silicon nitride drum resonators*, Journal of Applied Physics **112**, 064323 (2012).

[130] B. M. Zwickl, W. E. Shanks, A. M. Jayich, C. Yang, A. C. Bleszynski Jayich, J. D. Thompson, and J. G. E. Harris, *High quality mechanical and optical properties of commercial silicon nitride membranes*, Applied Physics Letters **92**, 103125 (2008).

[131] M. Mader, *Characterisation of Silicon Nitride MMembrane for Optomechanical Experiments*, Master's thesis, Fakultät für Physik, Ludwig-Maximilian Universität München (2010).

[132] G. Buser, *Dipole-trapped atoms at high optical depth for atom-light quantum interfaces*, Master's thesis, Universität Basel (2016).

[133] M. T. Rakher, R. J. Warburton, and P. Treutlein, *Prospects for storage and retrieval of a quantum-dot single photon in an ultracold ^{87}rb ensemble*, Phys. Rev. A **88**, 053834 (2013).

[134] J.-P. Jahn, M. Munsch, L. Béguin, A. V. Kuhlmann, M. Renggli, Y. Huo, F. Ding, R. Trotta, M. Reindl, O. G. Schmidt, A. Rastelli, P. Treutlein, and R. J. Warburton, *An artificial rb atom in a semiconductor with lifetime-limited linewidth*, Phys. Rev. B **92**, 245439 (2015).

[135] K. Dieckmann, R. J. C. Spreeuw, M. Weidemüller, and J. T. M. Walraven, *Two-dimensional magneto-optical trap as a source of slow atoms*, Phys. Rev. A **58**, 3891 (1998).

[136] B. Höltkemeier, *2D-MOT as a source of a cold atom target*, Master's thesis, Departement of Physics and Astronomy, University of Heidelberg (2011).

[137] T. Arpornthip, C. A. Sackett, and K. J. Hughes, *Vacuum-pressure measurement using a magneto-optical trap*, Phys. Rev. A **85**, 033420 (2012).

[138] D. Hunger, *A Bose-Einstein condensate coupled to a micromechanical oscillator*, Ph.D. thesis, Fakultät für Physik, Ludwig-Maximilians-Universität München (2010).

[139] M. F. Riedel, *Multi-particle entanglement on an atom chip*, Ph.D. thesis, Fakultät für Physik, Ludwig-Maximilian-Universität München (2010).

[140] L. Ricci, M. Weidemüller, T. Esslinger, A. Hemmerich, C. Zimmermann, V. Vuletic, W. König, and T. Hänsch, *A compact grating-stabilized diode laser system for atomic physics*, Optics Communications **117**, 541 (1995).

[141] D. W. Preston, *Doppler-free saturated absorption: Laser spectroscopy*, American Journal of Physics **64**, 1432 (1996).

[142] X. Zhu and D. T. Cassidy, *Modulation spectroscopy with a semiconductor diode laser by injection-current modulation*, J. Opt. Soc. Am. B **14**, 1945 (1997).

[143] S. Zürcher, *Set up and Characterization of a Diode Laser System for ultra cold Atom Experiments*, Master's thesis, Departement Physik, Universität Basel (2012).

[144] W. Demtröder, *Experimentalphysik 2* (Springer-Verlag, Berlin Heidelberg) (2013).

[145] P. Boehi, *Coherent manipulation of ultracold atoms with microwave nearfields*, Ph.D. thesis, Ludwigs-Maximilians-Universität München (2010).

[146] C. Ockeloen, *Quantum Metrology with a Scanning Probe Atom Interferometer*, Ph.D. thesis, Departement Physik, Universität Basel (2014).

[147] C. J. Cooper, G. Hillenbrand, J. Rink, C. G. Townsend, K. Zetie, and C. J. Foot, *The temperature of atoms in a magneto-optical trap*, Europhysics Letters (EPL) **28**, 397 (1994).

[148] T. Walker, D. Sesko, and C. Wieman, *Collective behavior of optically trapped neutral atoms*, Phys. Rev. Lett. **64**, 408 (1990).

[149] D. W. Sesko, T. G. Walker, and C. E. Wieman, *Behavior of neutral atoms in a spontaneous force trap*, J. Opt. Soc. Am. B **8**, 946 (1991).

[150] A. J. Kerman, V. Vuletic, C. Chin, and S. Chu, *Beyond optical molasses: 3d raman sideband cooling of atomic cesium to high phase-space density*, Phys. Rev. Lett. **84**, 439 (2000).

[151] M. H. Anderson, W. Petrich, J. R. Ensher, and E. A. Cornell, *Reduction of light-assisted collisional loss rate from a low-pressure vapor-cell trap*, Phys. Rev. A **50**, R3597 (1994).

[152] D. Offenberg, C. B. Zhang, C. Wellers, B. Roth, and S. Schiller, *Translational cooling and storage of protonated proteins in an ion trap at subkelvin temperatures*, Phys. Rev. A **78**, 061401 (2008).

[153] J. Lunze, *Regelungstechnik 1* (Springer-Verlag, Berlin Heidelberg) (2014).

[154] J. Raisch, *Grundlagen der Regelungstechnik*, Vorlesungsskript (2015/2016).

[155] W. Ketterle, K. B. Davis, M. A. Joffe, A. Martin, and D. E. Pritchard, *High densities of cold atoms in a dark spontaneous-force optical trap*, Phys. Rev. Lett. **70**, 2253 (1993).

[156] H. Ritsch, P. Domokos, F. Brennecke, and T. Esslinger, *Cold atoms in cavity-generated dynamical optical potentials*, Rev. Mod. Phys. **85**, 553 (2013).

[157] P. Domokos and H. Ritsch, *Collective cooling and self-organization of atoms in a cavity*, Phys. Rev. Lett. **89**, 253003 (2002).

[158] A. T. Black, H. W. Chan, and V. Vuletić, *Observation of collective friction forces due to spatial self-organization of atoms: From rayleigh to bragg scattering*, Phys. Rev. Lett. **91**, 203001 (2003).

[159] D. Nagy, G. Szirmai, and P. Domokos, *Self-organization of a Bose-Einstein condensate in an optical cavity*, The European Physical Journal D **48**, 127 (2008).

[160] K. Baumann, C. Guerlin, F. Brennecke, and T. Esslinger, *Dicke quantum phase transition with a superfluid gas in an optical cavity*, Nature **464**, 1301 (2010).

[161] D. Kruse, C. von Cube, C. Zimmermann, and P. W. Courteille, *Observation of lasing mediated by collective atomic recoil*, Phys. Rev. Lett. **91**, 183601 (2003).

[162] S. Slama, S. Bux, G. Krenz, C. Zimmermann, and P. W. Courteille, *Superradiant rayleigh scattering and collective atomic recoil lasing in a ring cavity*, Phys. Rev. Lett. **98**, 053603 (2007).

[163] B. Vogell, T. Kampschulte, M. T. Rakher, A. Faber, P. Treutlein, K. Hammerer, and P. Zoller, *Long distance coupling of a quantum mechanical oscillator to the internal states of an atomic ensemble*, New J. Phys. **17**, 043044 (2015).

[164] F. Bariani, S. Singh, L. F. Buchmann, M. Vengalattore, and P. Meystre, *Hybrid optomechanical cooling by atomic Λ systems*, Phys. Rev. A **90**, 033838 (2014).

[165] E. S. Polzik and K. Hammerer, *Trajectories without quantum uncertainties*, Annalen der Physik **527**, A15 (2015).

[166] R. A. Norte, J. P. Moura, and S. Gröblacher, *Mechanical resonators for quantum optomechanics experiments at room temperature*, Phys. Rev. Lett. **116**, 147202 (2016).

Danksagung

Diese Arbeit wäre ohne die Unterstützung und Mitwirkung vieler Menschen nicht möglich gewesen, denen ich an dieser Stelle herzlich dafür danken möchte. Insbesondere danke ich

Philipp Treutlein für die Aufnahme in seine Arbeitsgruppe, die hervorragende Betreuung und das große Vertrauen. In den zahlreichen Diskussionen hat deine Fähigkeit komplizierte physikalische Sachverhalte intuitiv verständlich zu erklären oft den Knoten in meinem Kopf gelöst. Ich danke dir auch dafür, dass du deinen Doktoranden die Möglichkeit gibst, eine Vielzahl von Konferenzen zu besuchen.

Claus Zimmermann für die Übernahme des Zweitgutachtens.

den Kollegen des Atom-Membran-Experiments, Maria Korppi, Andreas Jöckel, Tobias Kampschulte, Matthew Rakher, Thomas Lauber und Lucas Beguin, für die gute Zusammenarbeit, die vielen Diskussionen und die schönen Momente außerhalb des Labors. Maria Korppi danke ich außerdem für den Aufbau des ersten Cavity Systems, Andreas Jöckel für die Planung des Atomsetups, die Einführung in das Experiment zu Beginn meiner Arbeit, seine vielen guten technischen Ideen und seine gute Laune, Matthew Rakher für seine theoretischen Beiträge zur Atom-Membran Kopplung, Thomas Lauber für den Aufbau des zweiten Cavity Systems, Tobias Kampschulte für seine große physikalische Intuition, von der ich viel lernen konnte, und die gute Zusammenarbeit bei der Suche nach der Ursache der Selbstoszillationen, Lucas Beguin für seine Motivation theoretische Fragen von Grund auf mit Zettel und Bleistift zu beantworten, die mich zu der ein oder anderen Rechnung motiviert hat. Den neuen Mitarbeitern im Labor Thomas Karg, Gianni Buser und Janik Wolters wünsche ich viel Erfolg und spannende Quantenexperimente mit Membranen und Quantendots.

den aktuellen und ehemaligen Kollegen aus dem Nachbarlabor Andrew Horsley, Roman Schmied, Caspar Ockeloen, Baptiste Allard, Guan-Xiang-Du, Matteo Fadel und Tilmann Zibold für die freundliche Atmosphäre in der Arbeitsgruppe.

den Theoretikern in Innsbruck und Hannover insbesondere Berit Vogell, Kai Stannigel, Peter Zoller und Klemens Hammerer, deren Arbeiten für unser Verständnis